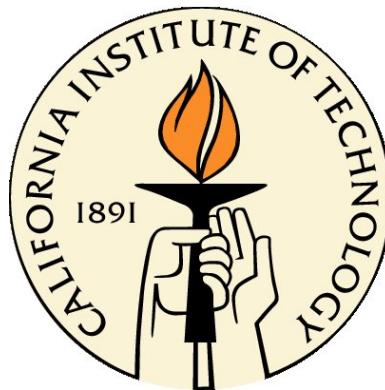


Multiscale and Multiphysics Computational Frameworks for Nano- and Bio-Systems

Thesis by
Hyungjun Kim

In Partial Fulfillment of the Requirements
for the Degree of
Doctor of Philosophy



California Institute of Technology
Pasadena, California

2009
(Defended May 4, 2009)

© 2009

Hyungjun Kim

All Rights Reserved

I dedicate this PhD thesis to God and my loving parents.

Acknowledgments

I would like to express my gratitude to Prof. Bill Goddard, who guided me to become an independent researcher during my PhD journey. He allowed me the freedom to spend my time on many different projects, trained me to solve various problems, and let me have a broad scientific scope with sharp instinct and creative ideas. His wide range of research interests and enthusiasm for science always provided plenty of insights and thoughts, which, I believe will be a great asset to me as I continue my research life.

Prof. Seung Soon Jang, at Georgia Institute of Technology, taught me a lot of simulation techniques and tips, along with his systematic way of thinking to tackle scientific problems, during his days at Caltech. Even after he moved to Gatech, he continues to be my mentor about science and non-science, and I really appreciate his invaluable advice.

I also appreciate Prof. Eok Kyun Lee, who was my undergraduate advisor. He introduced me to computational and theoretical chemistry, and furthermore, he first taught me how to figure out and solve science problems. I am always indebted to him for his warm encouragement and support.

My committee members, Prof. Vincent McKoy, Prof. Mark Davis, Prof. Jack Beauchamp, and Prof. Jim Heath, have provided useful insights and guidance through the candidacy, proposal, and thesis defense. Moreover, it has been an honor for me to work on several projects with them.

I also thank Dr. Isik Kanik and Dr. Luther Beegle at Jet Propulsion Laboratory (JPL) for supporting me during the IMS project. Their fruitful discussions helped me successfully complete our project. It was a great thrill for me to have a chance to collaborate with NASA.

While working at the MSC, it was a pleasure to have many friends and colleagues who shared a similar interest. I want to thank all MSC members, especially, Sergey Zybin and Julius Su who helped me a lot on the energetic material project and the eFF project with their kind advice. I would also like to thank my friend, Mu-Jeng Cheng, for engaging in scientific discussions as well as listening to my random complaints. I owe a lot of coffees to Jiyong Heo, Sang Soo Han and Soo-Kyung Kim, too.

Finally, I wish to thank Hugh Kim and Young Shik Shin, who gave me many insights on the experiments while conducting our lipid projects. And last but not least, I am truly grateful for all the scientific, mental, and sometimes physical help from all other friends at KAIST and Caltech.

Abstract

Multiscale and multiphysics simulation strategy is important to investigate complex problems in nature because it provides a systematic method to understand underpinning physics of the systems depending on the size. In this thesis, we discuss how such multiscale and multiphysics simulation framework can explain and rationalize the experimental observations in several nano- and bio-systems. Furthermore, we exhibit the computational simulation methods that play major roles to rationally design novel materials with desired properties in next generation nano electronic devices, alternative energy materials, life science, and so on.

Chapter 1 reviews the significance of multiscale and multiphysics simulation strategy. In this chapter, we briefly discuss the multiscale and multiphysics natures in nano- and bio-systems, and detailed examples are contained in the next chapters. Chapter 2 introduces an electric field induced conformational change mechanism, which is responsible for the unique current-voltage (I - V) behavior of nano device, negative differential resistance (NDR). In Chapter 3, the on/off kinetics of the Stoddart-Heath rotaxane-based programmable molecular electronic switch is discussed in terms of the free energy quantities. Chapter 4 explores sodium diffusion through the aluminum-doped zeolite BEA system, and the effect of water uptake amount is thoroughly discussed. This has importance for the application of zeolite to proton exchange membranes for fuel cells (PEMFC). In Chapters 5 and 6, the ion mobilities of tertiary and quaternary ammonium cations (precursors for lipids), and phosphatidylcholine (PC) lipid cations are investigated, respectively. In order to compute the ion mobilities of the precursors and entire lipids, we develop a modified trajectory (TJ) method dealing with the complicated integrals of interaction terms. QM and MD simulations are performed to determine the structures and charge distributions. In Chapter 7, we study how the model lung system of lipid monolayer with surfactant protein B (SP-B) responds to ozone introduction. In parallel with the field induced droplet ionization (FIDI) mass spectrometry study, MD simulations identify the distinct ozone reaction mechanism at the interface, and the role of SP-B at the pulmonary surfactant (PS) system on the oxidative stresses.

From these studies, we suggest various multiscale and multiphysics modeling approaches depending on the characteristics of systems and objectives. These efforts allow us to overcome the limited time- and length-scales of the monoscale simulations. In addition, we expect that an establishment

of such multiscale modeling procedures will invoke interdisciplinary studies by tightly combining the developments occurring independently across fields.

Contents

Acknowledgments	iv
Abstract	v
1 Introduction	1
2 Negative Differential Resistance of Oligo (Phenylene Ethynylene) Self-Assembled Monolayer Systems: The Electric Field Induced Conformational Change Mechanism	8
2.1 Abstract	8
2.2 Introduction	8
2.3 Simulation Details	10
2.3.1 Computational Details of QM Calculations	10
2.3.2 Conductivities of P and T Conformations (NEGF Calculations)	10
2.3.3 Coarse-Grained NN Interacting Hamiltonian	10
2.3.4 Extracting NN Model Parameters from QM/FF Energies	11
2.3.5 Coarse-Grained MC Simulations	13
2.4 Results and Discussion	13
2.4.1 Two Conformations of AN-OPE	13
2.4.2 Electrical Conductivities of P and T	15
2.4.3 Response to Constant External Field	21
2.4.4 NDR for Time Dependent Electric Field	24
2.5 Conclusions	27
2.6 Acknowledgments	27
Bibliography	28
3 Free Energy Barrier for Molecular Motions in Bistable [2]Rotaxane Molecular Electronic Devices	30
3.1 Abstract	30

3.2	Introduction	31
3.3	Simulation Details	33
3.3.1	Potential of Mean Force from Constrained Molecular Dynamics Simulation	33
3.3.2	Constrained Molecular Dynamics Simulation	35
3.3.3	Force Field and MD Parameters	36
3.4	Results and Discussion	38
3.4.1	Charge Scheme: Adiabatic Approximation	38
3.4.2	Free Energy Profiles from PMF Calculations	39
3.4.2.1	ΔG_{T2D}	39
3.4.2.2	$\Delta G_{\text{T2D}}^{\ddagger}$ and $\Delta G_{\text{D2T}}^{\ddagger}$ for Neutral Case	41
3.4.2.3	$\Delta G_{\text{T2D}}^{\ddagger}$ and $\Delta G_{\text{D2T}}^{\ddagger}$ for Oxidized Cases	42
3.4.2.4	Effect of Coulombic Energy and van der Waals Energy	42
3.5	Conclusions	45
3.6	Acknowledgments	46
	Bibliography	47
4	Sodium Diffusion through Aluminum-Doped Zeolite BEA System: Effect of Water Solvation	52
4.1	Abstract	52
4.2	Introduction	52
4.3	Simulation Details	55
4.3.1	Force Field	55
4.3.2	Grand Canonical Monte Carlo (GCMC) method and Molecular Dynamics (MD) Simulation	55
4.3.3	Construction of Models and Calculation of Properties	56
4.4	Results and Discussion	56
4.4.1	Water Absorption	56
4.4.2	Structure of Water in Zeolite	58
4.4.3	Effect of Water Contents on Sodium Diffusion	60
4.4.4	Effect of Temperature on Sodium Diffusion	63
4.5	Conclusions	65
4.6	Acknowledgments	68
	Bibliography	69

5	Experimental and Theoretical Investigation into the Correlation between Mass and Ion Mobility for Choline and Other Ammonium Cations in N₂	72
5.1	Abstract	72
5.2	Introduction	73
5.3	Experimental Section	75
5.3.1	Chemicals and Reagents	75
5.3.2	Electrospray Ionization Ion Mobility Spectrometer	75
5.3.3	Computational Modeling	76
5.4	Results	77
5.4.1	Mass-Mobility Correlation of Ammonium Cations	77
5.4.2	Tertiary and Quaternary Ammonium Cations with Similar Molecular Weights	79
5.4.3	Functional Group Isomers of Ammonium Cations	81
5.4.4	Collision Cross-Sections of Ions in N ₂ via the Trajectory Method	81
5.5	Discussion	83
5.5.1	Classical Ion-Neutral Collision Model	83
5.5.2	Computational Trajectory Method	84
5.5.3	Ion-Quadrupole Potential	84
5.5.4	Ion-Induced Dipole Potential	84
5.5.5	Van der Waals Potential	86
5.5.6	Mass-Mobility Correlation	86
5.6	Conclusions	89
5.7	Acknowledgments	90
	Bibliography	91
6	Structural Characterization of Unsaturated Phospholipids Using Traveling Wave Ion Mobility Spectrometry	94
6.1	Abstract	94
6.2	Introduction	95
6.3	Experimental Section	96
6.3.1	Chemicals and Reagents	96
6.3.2	Electrospray Ionization Traveling Wave Ion Mobility Mass Spectrometer . . .	97
6.3.3	Collision Cross-Section Calibration	97
6.3.4	Computational Modeling	99
6.4	Results	99
6.4.1	Saturated Phosphatidylcholine Cations	99
6.4.2	Unsaturated Phosphatidylcholine Cations	101

6.4.3	Sodiated Phosphatidylcholine Cations	101
6.4.4	Estimated Collision Cross-Sections of Ions Using T-Wave Calibration	103
6.4.5	Determination of Collision Cross-Sections of Ions	104
6.4.6	Calculated Collision Cross-Sections of Ions Using the Trajectory Method	106
6.5	Discussion	106
6.5.1	Effect of Drift Gas on Ion Mobility	106
6.5.2	Geometrical Effect on the Collision Cross-Sections of Phosphatidyl- choline Cations	108
6.5.3	Mass-Mobility Correlations of Phosphatidylcholine Cations	109
6.5.4	Characterizing Unsaturated Phosphatidylcholines from Mass-Mobility Corre- lation	111
6.6	Conclusions	113
6.7	Acknowledgments	115
Bibliography		116
7	Interfacial Reactions of Ozone with Lipids and Proteins in a Model Lung Surfac- tant System	119
7.1	Abstract	119
7.2	Introduction	120
7.3	Methods	121
7.3.1	Chemicals and Reagents	121
7.3.2	Online FIDI-MS Technique and Heterogeneous Oxidation by O ₃	121
7.3.3	Molecular Dynamic Simulations	123
7.4	Results and Discussion	125
7.4.1	Interfacial Reaction of POPG with O ₃	125
7.4.2	Interfacial Oxidation of SP-B ₁₋₂₅	126
7.4.3	Oxidation of SP-B ₁₋₂₅ in POG Monolayer by O ₃	128
7.4.4	Interactions of SP-B ₁₋₂₅ in a Lipid Monolayer	128
7.5	Conclusions	132
7.6	Acknowledgments	134
Bibliography		135
A	Discussions on Coarse-Graining of Time- and Length-Scale in Monte Carlo Sim- ulations for AN-OPE SAM	138
A.1	Time-Scale	138
A.2	Length-Scale	138

B	Effect of Molecular Fluctuations on the Electrical Conductivity of AN-OPE SAM	140
C	NDR in Other OPE-derivative Systems	143
C.1	Bare OPE	143
C.2	Nitro OPE	143
D	Conversion Factor between External Electric Field and Bias Voltage	147
E	Mulliken Charge Distributions of Bistable [2]Rotaxane Molecular Switch Depending on CBPQT⁴⁺ Ring's Position	148
F	Consideration of Metric Effect on the Bistable [2]Rotaxane Molecule during the Constant MD Simulations using Fixman's Theorem	156
G	Time for Consumption of POPG	158
H	Bulk-phase Ozonolysis	159
H.1	Methods	159
H.1.1	Chemicals and Reagents	159
H.1.2	Bulk-phase O ₃ Reaction	159
H.1.3	Fenton Reaction	159
H.2	Results and Discussion	160
	Bibliography	165

List of Figures

1.1	Multiscale and Multiphysics paradigm simulation strategy.	2
1.2	Multiscale and Multiphysics characteristics in nano electronic systems. At electron size scale, electrical conductivity depends on the quantum states of the molecules. At molecular size scale, classical interactions determine the molecular conformation, which affects its quantum state. At device size scale, hundreds of molecules are assembled to build a mesoscale junction and these are packaged into a device component.	3
1.3	Multiscale and Multiphysics characteristics in bio systems. At electron size scale, chemical reactions, which are governed by huge QM effects (e.g., electron/proton transfer), regulate the molecular architecture of the protein for an effective functionality. At molecular scale, CM describes the interactions, such as hydrophobic interaction, among the bio components of proteins, lipids, etc. Large scale motion of the membrane, such as endo- or exo-vesiculation, is in the regime of hydrodynamic descriptions, and this affects the dynamics of a cell.	4
2.1	(a) Energies of various conformations of AN-OPE relative to the AP conformation computed with a 1.2 V/Å external field from FF calculations (black histograms) and NN model calculations (orange histograms). (b) Energies of various conformations of AN-OPE relative to the AP conformation computed with no external field from FF calculations (black histograms), NN model calculations (orange histograms), and QM calculations (green histograms).	12
2.2	Torsional strain energy $E_i^{torsion}$ as a function of twisting angle χ from QM (PBE) on the isolated molecule. The energy at $\chi = 4^\circ$ (corresponding to P) is 0.01 kcal/mol higher than the ground state energy at $\chi = 0^\circ$. The energy at $\chi = 160^\circ$ (which corresponds to T) is 0.23 kcal/mol higher than the energy at $\chi = 0^\circ$, leading the 0.22 kcal/mol higher $E_i^{torsion}$ of T compared to $E_i^{torsion}$ of P.	13

2.3	(a) Optimized geometry for the low field structure (P) of AN-OPE SAM. Here [0001] is the surface normal and the views are along z -axis (upper middle), y -axis (lower middle), and x -axis (lower right). The left picture is a perspective along the axis of one plane of molecules. The hydrogen bonding network is aligned along the $[11\bar{2}0]$ direction. (b) Optimized geometry for the high field structure (T) of AN-OPE SAM. Here [0001] is the surface normal and the views are along z -axis (upper middle), y -axis (lower middle), and x -axis (lower right). The left picture is a perspective along the axis of one plane of molecules. The hydrogen bonding network is aligned along the $[10\bar{1}0]$ direction.	14
2.4	Density of state (DOS) and transmission function $T(E)$ of P structure (a) and T structure (b). The top electrode is located 12 Å above from the bottom electrode. . .	16
2.5	(a) Current through P conformation, I_P and current through T conformation, I_T versus the bias voltage V determined from the NEGF calculations using the DOS and $T(E)$ of Figure 2.4. (b) Conductivity of P conformation, σ_P and conductivity of T conformation, σ_T versus the bias voltage V determined. The top electrode is located 12 Å above from the bottom electrode. σ_P is ~ 10 times larger than σ_T	17
2.6	Density of state (DOS) and transmission function $T(E)$ of P structure (a) and T structure (b). The top electrode is located 20 Å above from the bottom electrode. . .	18
2.7	(a) Current through P conformation, I_P and current through T conformation, I_T versus the bias voltage V determined from the NEGF calculations using the DOS and $T(E)$ of Figure 2.6. (b) Conductivity of P conformation, σ_P and conductivity of T conformation, σ_T versus the bias voltage V determined. The top electrode is located 20 Å above from the bottom electrode. σ_P is ~ 163 times larger than σ_T	19
2.8	Conductivities depending on the twisting angle are extracted from the previous study [36], which are the results from NEGF calculations. (a) Semi-log plots of I - V curves shows that the slope decrease as the twist angle approaches to 90° , which means that the tunneling barrier from the bottom electrode to top electrode, Φ_B increases as the the π - π orbital overlap decreases. (b) Since the conductivity is dominated by the π - π orbital overlap, we assumed that the conductivity between two phenyl rings, $\sigma_i = 1/R_i$ is proportional to $\cos^4(\chi_i)$. From simple calculation leads the total conductivity tot to be proportional to the $\cos^4(\chi_1) \cos^4(\chi_2) / (\cos^4(\chi_1) + \cos^4(\chi_i))$, which shows good agreement with the NEGF results.	20

- 2.9 (a) Snapshots during P-to-T transition from MC simulation with $1.2 \text{ V}/\text{\AA}$ external field. The first nucleation is occurred at 55,184 MCS, then, the $[11\bar{2}0]$ line propagates until 55,214 MCS. More nucleation and propagation along $[11\bar{2}0]$ are taken place, and finally, the full system is transformed by 1,008,706 MCS. We note that increased bias voltage yields a faster P-to-T transition. (b) Time dependence of P and T populations and electrical conductivity through the SAM during P-to-T transition. (c) Snapshots during T-to-P transition from MC simulation without an external field. The first nucleation is occurred at 486,389 MCS, then, the $[11\bar{2}0]$ line propagates until 486,410 MCS. More nucleation and propagation along $[11\bar{2}0]$ are taken place, and finally, the full system is transformed by 2,377,335 MCS. (d) Time dependence of P and T populations and electrical conductivity through the SAM during T-to-P transition. 22
- 2.10 (a) P-to-T transition; (b) T-to-P transition; Top panels show the temperature dependence of the propagation rate along $[11\bar{2}0]$, $k_{[11\bar{2}0]}$. Middle panels show the probability, $P(t)$ of exhibiting no nucleation by time, t for the case when the nucleation is initiated next to another $[11\bar{2}0]$ line. The dotted lines is an exponential fit of $P(t)$. This leads to a nucleation rate of $\tau = 5,583 \text{ MCS}$ for the P-to-T transition and $\tau = 72,926 \text{ MCS}$ for the T-to-P transition. Bottom panels show the probability, $P(t)$ of exhibiting no nucleation by time, t for the case when the nucleation is initiated in the absence of next $[11\bar{2}0]$ line. The exponential fit leads to a nucleation rate of $\tau_0 = 274,193 \text{ MCS}$ for the P-to-T transition and $\tau_0 = 357,135 \text{ MCS}$ for the T-to-P transition. 23
- 2.11 (a) Current-voltage (I - V) curves calculated at 300 K from MC simulations combined with the I - V results of the Green's function calculations. Results for three sweeping rates are shown: S (blue line): $1 \times 10^{-8} \text{ V/MCS}$, M (red line): $4 \times 10^{-8} \text{ V/MCS}$, and F (black line): $2 \times 10^{-7} \text{ V/MCS}$. Inset is the experimental I - V curves from the reference [9] with 3 different sweeping rates: S (blue line) : 21 mV/sec, M (red line) : 83 mV/sec, and F (black line) : 415 mV/sec. (b) The sweep rate dependence of the integral of the current from the peak to the valley during NDR, Q_F from current simulation (left panel) and experiment [9] (right panel). 25
- 3.1 Structural formula of the two co-conformations of a bistable [2]rotaxane fragment used in this study. 32
- 3.2 (a) Backbone of the rotaxane molecule simulated in this study. (b) CBPQT⁴⁺ ring positions along the backbone (unit: \AA). 34

3.3	Charges for the initial nine structures obtained from QM with Mulliken analysis. In addition, we included two more structures beyond each station of the TTF and the DNP, using charges identical to those for the equilibrium CBPQT ⁴⁺ @TTF and CBPQT ⁴⁺ @DNP cases, respectively. Ten more structures were generated on the basis of these eleven structures. The position of the CBPQT ⁴⁺ ring for each additional structure was obtained using the arithmetic average of the two adjacent cases from the eleven structures. The charges were also averaged.	35
3.4	Probability density function of kinetic energy KE ($= mv^2/2$) is from the MD simulation of the CBPQT ⁴⁺ ring@TTF (blue line) at 300 K. Here the time step was 0.01 fs and the total simulation time was 3 ns after 500 ps of equilibration. The black dashed line compares with the Maxwell-Boltzmann distribution of the energy, $2 \left(\text{KE}/\pi (k_B T)^3 \right)^{1/2} \exp(-\text{KE}/k_B T)$, for $T = 300$ K.	37
3.5	Probability density function of KE _x ($= mv_x^2/2$; blue line), KE _y ($= mv_y^2/2$; green line), and KE _z ($= mv_z^2/2$; red line) are computed from the MD simulation of the CBPQT ⁴⁺ ring@TTF (blue line), which are identical to each other. These are compared with the Maxwell-Boltzmann distribution of KE _i , $\sqrt{1/(\pi \text{KE}_i k_B T)} \exp(-\text{KE}_i/k_B T)$ at 300 K. ($i \in \{x, y, z\}$; black dashed line)	37
3.6	Change of mean force as a function of simulation time. In each case this follows 500 ps of equilibration time. This plot shows two representative cases: the CBPQT ⁴⁺ ring@TTF (TTF) and the CBPQT ⁴⁺ ring@DNP (DNP).	38
3.7	Change of potential of mean force as a function of ring position along the backbone. The blue curve allows the charge to change adiabatically as the ring moves along the dumbbell, which is the reliable result. The other two curves show the error obtained when the charges are fixed: the green curve uses fixed charges from the ring@TTF; the red curve uses a fixed charge from the ring@DNP.	39
3.8	(a) Change of the mean force as a function of ring position along the backbone. (b) Change of the potential of mean force as a function of ring position along the backbone. The green vertical lines denote the ring@TTF (8.90 Å) and ring@DNP (47.70 Å).	40
3.9	Change of Coulombic interaction energy as a function of the ring position: (a) neutral state; (b) oxidation state +1; (c) oxidation state +2.	44
3.10	Change of van der Waals interaction energy as a function of the ring position: (a) neutral state; (b) oxidation state +1; (c) oxidation state +2.	45
3.11	Variations in the total charge on the ring as a function of the ring position for the neutral case.	46

- 4.1 Atomistic structure for the primitive periodic cell with composition of $\text{Na}_8\text{Al}_8\text{Si}_{248}\text{O}_{512}$. This shows green balls are aluminum and magenta balls are sodium. (a) Minimized aluminosilicate zeolite BEA structures without H_2O , (b) snapshot of zeolite BEA structures after the GCMC simulation for 298.15 K and 101.3250 kPa, and (c) snapshot of zeolite BEA structures after 4 ns NPT MD simulation at 298.15 K and 101.3250 kPa. 54
- 4.2 Dashed line is the least-squares fitted to $f(x) = a \tanh(bx)$, where $a = 46.19$ molecules/unit cell and $b = 0.753$ (1/kPa). We obtain a vapor pressure of 3.578 kPa for the point at which the water uptake reaches to 99 % of the maximum loading uptake. 57
- 4.3 Predicted temperature-dependence of water uptake at 101.3250 kPa when the zeolite BEA has no aluminum doping (red curve) and $\text{Si}/\text{Al} = 30$ (blue curve). The presence of aluminum-doped sites as well as sodium ions enhance the water uptake amount especially in the high temperature. 58
- 4.4 (a) Probability of finding additional water molecules at a specific distance from each water molecule. This is obtained as the product of pair correlation functions of water oxygens, $g_{O(\text{water})-O(\text{water})}$ with water density ρ and $4\pi r^2$. (b) Water coordination number (CN) of water molecule as a function of pressure. The CN of water molecule is obtained from the integration of curve a up to first minimum, which is at 3.7 Å. The saturated value of CN of the absorbed phase (~ 3.8) is smaller than the CN of the bulk phase (4.5). 59
- 4.5 (a) Probability of finding sodium ions at a specific distance from each water molecule. This is obtained as the product of pair correlation functions of sodium atoms and water oxygen, $g_{\text{Na}-O(\text{water})}$ with water density ρ and $4\pi r^2$. (b) Water coordination number (CN) of sodium ions as a function of pressure. The CN of water molecule is obtained from the integration of curve a up to first minimum, which is at 3.5 Å. The saturated value of CN of the absorbed phase (~ 5.0) is same to the CN of the bulk phase. . . . 61
- 4.6 Log-log plot of mean square displacements (MSD) vs time at 298.15 K and 101.3250 kPa based on a trajectory of 12 ns. Initially the MSD shows $\text{MSD} \propto t^{1/2}$ up to $t \approx 20$ ps, but the times $> \sim 2$ ns, we see normal 3D Fickian behavior ($\text{MSD} \propto t$). The Fickian regime leads to a diffusion coefficient of $D = 1.233 \times 10^{-7}$ cm^2/s 62

- 4.7 Dependence of diffusion coefficient of sodium ion on water coordination number (CN) of sodium ion. The diffusion coefficients were calculated from three partitioned trajectories of 12 ns NPT simulations (each partition has 4 ns length), and the error bars were evaluated from the diffusion coefficients obtained from the three partitioned trajectories. This represents pressures from 0.1013 to 101.3250 kPa at 298.15 K. At a pressure of ~ 2.0 kPa, we find an abrupt change in the water CN. When the sodium ion is solvated by > 4.5 water molecules, its diffusion coefficient increases abruptly by a factor of 3.5. The dashed line is to guide the eye. 63
- 4.8 Time dependence of the distances of one sodium ion to all 8 aluminum atoms of the zeolite membrane. The distance to each aluminum atom is shown with a different color. (a) Vapor pressure is 101.3250 kPa (good solvation regime) at 298.15 K. This shows that it took 2 ns for the Na to hop from a position 4.8 Å from the purple Al to a position 7.5 Å from the black Al. Here a distance of 4.8 Å indicates one water shell between the Na and the Al, while 7.5 Å indicates separate water shells around each; (b) vapor pressure is 0.1013 kPa (poor solvation regime) at 298.15 K. In this case the Na remains at 4 Å from the Al which indicates that the Na remains coordinated to the O of the Al. 64
- 4.9 Dependence of the sodium diffusion coefficient on the temperature for a vapor pressure of 101.3250 kPa. The diffusion coefficients were calculated from three partitioned trajectories of 12 ns NPT simulations (each partition has 4 ns length), and the error bars were evaluated from the diffusion coefficients obtained from the three partitioned trajectories. Up to 373.15 K, the diffusion coefficient increases with increasing temperature, whereas it decreases beyond 373.15 K due to the depletion of the water solvation. 66
- 4.10 Arrhenius plots of diffusion coefficient from each solvation regime: the red squares are for the poor solvation regime and the blue diamond is for the good solvation regime. The solid black line is a linear fitting of each regime. This leads to $D_{300K} = 3.762 \times 10^{-8}$ cm²/s and $E_{act} = 3.810$ kcal/mol for the poor solvation regime and $D_{300K} = 1.512 \times 10^{-7}$ cm²/s and $E_{act} = 3.540$ kcal/mol for the good solvation regime, and the equation of each fitted line and R2 value are inset in the figure. 67

- 5.1 Examples of the ion mobility spectra taken in this study. Shown are two spectra taken in 730 Torr N_2 . The electric field strength and the temperature of the drift tube were 292 V/cm and 473 K, respectively. The dash curve is a spectrum taken with pure solvent being introduced to the electrospray needle while the solid curve is a spectrum of solvent and 300 μ M *N,N*-dimethylammoniummethanol. The two spectra were smoothed (10 point adjacent averaging) and shifted in intensity by an additive constant to avoid overlap. The *N,N*-dimethylammoniummethanol feature is indicated in the figure. The unlabeled features correspond to ionized solvent (water, methanol, acetic acid) and atmospheric constituents ionized through proton transfer (due to the open nature of the ESI-IMS instrument). 78
- 5.2 Plot of K_0^{-1} for 3° and 4° ammonium cations drifting in N_2 versus ion mass. Experimentally determined data for 3° ammonium and 4° ammonium cations are shown as asterisks and solid squares, respectively. The solid line is the fit of the 12 – 4 potential model to the ammonium cation data set. DFT optimized structure of each numerically or alphabetically labeled ion is shown above. Optimized geometries are obtained at B3LYP/6-31G** level. The hydrogen bonds are indicated with dashed lines. 80
- 5.3 (a) Plot of experimentally determined collision cross-sections (Ω_D) of abiotic amino acid cations [14] and carboxylic acid anions [15] in N_2 versus theoretically determined Ω_D using the modified TJ method for N_2 drift gas. Abiotic amino acid cation data are shown as solid squares and carboxylic acid anion data are shown as empty circles. The solid line is $y = x$. (b) Plot of experimentally determined collision cross-sections (Ω_D) of 3° and 4° ammonium cations in N_2 versus theoretically determined Ω_D using the modified TJ method for N_2 drift gas. 3° ammonium cation data are shown as asterisks and 4° ammonium cation data are shown as solid squares. Each ion is labeled with the appropriate identifying number and alphabet shown in Figure 5.1. The solid line is $y = x$ 82
- 5.4 Plots of theoretically determined collision cross-sections (Ω_D) (a) with potential from van der Waals and ion-induced dipole ($VDW + IID$) interactions over the theoretical Ω_D with original pairwise potential, van der Waals + ion-induced dipole + ion-quadrupole ($VDW + IID + IQ$) interactions, and (b) with potential from van der Waals potential (VDW) over the theoretical Ω_D with potential from van der Waals and ion-induced dipole ($VDW + IID$) interactions of 3° and 4° ammonium cations, abiotic amino acid cations, and carboxylic acid anions in N_2 versus ion mass. The ammonium cation data, the abiotic amino acid cation, and carboxylic acid anion data are shown as solid squares, empty circles, and asterisks, respectively. 85

5.5	Plots of theoretically determined collision cross-sections (Ω_D) of 3° and 4° ammonium cations, abiotic amino acid cations, and carboxylic acid anions in N ₂ versus ion mass. The calculated Ω_D of the molecular ions only with van der Waals (<i>VDW</i>) interaction with N ₂ are shown as empty squares (left <i>y</i> -axis). The calculated Ω_D of the molecular ions with original pairwise potential, van der Waals + ion-induced dipole + ion-quadrupole (<i>VDW + IID + IQ</i>) interactions, with N ₂ are shown as solid circles (right <i>y</i> -axis).	87
5.6	Plot of the total shape asymmetry (AS) of the ammonium cations versus ion mass. The ammonium cations with no oxygen atom are shown as solid squares. The ions containing one oxygen atom and two oxygen atoms are shown as empty triangles and empty circles, respectively. The DFT optimized structure of each numerically or alphabetically labeled ion is shown in Figure 5.2.	89
6.1	(a) Plot of drift time of saturated phosphatidylcholine (PC) cations in traveling wave ion mobility spectrometer versus ion mass. Experimentally determined data for symmetric PC and asymmetric PC cations are shown as solid squares and empty circles, respectively. The black dash and red solid lines are the linear fit to the symmetric PC cation data set and to both symmetric and asymmetric PC cation data set, respectively. (b) Plot of drift time of PC cations spanning mass range 700–800 Da in traveling wave ion mobility spectrometer versus ion mass. Experimentally determined data for saturated PC and unsaturated PC cations are shown as solid squares and empty circles, respectively. The black dash and red solid lines are the linear fit to the saturated PC cation data set and to both saturated and unsaturated PC cation data set, respectively. (c) Plot of drift time of protonated and sodiated PC cations in traveling wave ion mobility spectrometer versus ion mass. Experimentally determined data for protonated PC and sodiated PC cations are shown as solid squares and empty circles, respectively. The black dash and red solid lines are the linear fit to the protonated PC cation data set and to both protonated and sodiated PC cation data set, respectively.	102
6.2	(a) Plot of corrected empiric cross-sections versus effective drift times for 14 peptides and 4 phosphatidylcholines (PC). For each peptide and PC the singly charged cation is used. Linear trend and power trend lines are shown as solid and dash lines, respectively. (b) A plot of the estimated cross-sections versus the ion mass for PC cations investigated in this study. The estimated collision cross-sections from linear trend and power trend are shown as solid squares and empty circles, respectively.	105

- 6.3 (a) Time profile of the distance between the carbon atoms at the end of each acyl chain of 18:0-18:0 phosphatidylcholine during 200 ps of the molecular dynamics simulation. The fluctuation is ranging from $\sim 5 \text{ \AA}$ to $\sim 25 \text{ \AA}$ with the time period of 5 – 20 ps. Approximately 17 times of fluctuation is observed from this trajectory. (b) Plot of experimentally determined collision cross-sections (Ω_D) of phosphatidylcholine (PC) cations in N_2 against theoretically determined Ω_D using the modified TJ method for N_2 drift gas. The theoretical Ω_D is obtained by averaging Ω_D for 200 structures from MD simulations. The solid line is $y = x$. (c) Plot of theoretical Ω_D in He over theoretical Ω_D in N_2 versus mass of PC cations. 107
- 6.4 (a) Plots of theoretically determined collision cross-sections (Ω_D) and surface areas of phosphatidylcholine (PC) cations in N_2 versus ion mass. The calculated average Ω_D of the 200 ion conformations are shown as solid squares (left y -axis). The calculated surface areas of PC cations in N_2 at 300 K are shown as empty circles (right y -axis). (b) Plots of experimentally evaluated Ω_D and surface areas of phosphatidylcholine (PC) cations in N_2 versus ion mass. The Ω_D of PC cations are shown as solid squares (left y -axis). The calculated surface areas of PC cations in N_2 at 300 K and 400 K are shown as empty circles and empty triangle, respectively (right y -axis). 110
- 6.5 (a) MD simulated structures of saturated phosphatidylcholine cations at minimum energy state (E_0) are shown. The structures of the closest Ω_D to the experimental values are also shown along with corresponding relative energy values (E^*). (b) Plot of experimentally determined collision cross-sections (Ω_D) of phosphatidylcholine (PC) cations in N_2 against theoretically determined Ω_D at E_0 and E^* using the modified TJ method for N_2 drift gas. The solid line is $y = x$ 112
- 6.6 MD simulated structures of unsaturated phosphatidylcholine cations at minimum energy state (E_0) are shown. The structures of the closest Ω_D to the experimental values are also shown along with corresponding relative energy values (E^*). Unsaturated acyl chain is colored in yellow. 114

- 7.1 Illustration of FIDI-MS methodology for studies of interfacial reactions. (a) A quiescent hanging droplet of analyte-containing solution is formed on the end of a capillary. All electrical components remain at ground as the droplet is formed and reacts in a field-free environment. (b) The droplet is exposed to gas-phase reactants for a variable period of time to allow for heterogeneous reactions between gas-phase and solution-phase species. (c) After a reaction period, a pulsed electric field stretches the neutral droplet until it emits stream of positively and negatively charged submicron droplets in opposite directions. Ionized reactants and products from heterogeneous reactions enter the capillary inlet of the mass analyzer. Either positive or negative ions can be sampled. 122
- 7.2 Structures of POPG, POG, and SP-B₁₋₂₅ investigated in this study. 123
- 7.3 (a) Heterogeneous reaction of POPG with O₃ as a function of time. In the absence of ozone, the negative ion FIDI-MS spectrum of POPG is dominated by the singly deprotonated POPG peak at m/z 748. POPG is depleted after 15 s of the exposure and oxidation products are dominated by deprotonated hydroxyhydroperoxide (HHP) at m/z 672. The aldehyde, carboxylic acid, and methoxyhydroperoxide products are observed at m/z 638, m/z 654, and m/z 686, respectively. The secondary ozonide (SOZ) and sodiated alcohol products show up in the spectra at m/z 796 and m/z 662, respectively. (b) Summary of heterogeneous oxidation of POPG with O₃ at the air-liquid interface. R' is H for water and CH₃ for methanol. 124
- 7.4 (a) Air-liquid interfacial oxidation of SP-B₁₋₂₅ by O₃ as a function of time. In the absence of ozone, the positive ion FIDI-MS spectrum of SP-B₁₋₂₅ is dominated by the doubly protonated SP-B₁₋₂₅ peak at m/z 1465. The products at m/z 1481 and m/z 1489 correspond to doubly protonated SP-B₁₋₂₅ with two oxygen atoms and with three oxygen atoms, respectively, appear after the droplet is exposed to O₃ for 5 s. The triply oxygenated product at m/z 1489 dominates the FIDI-MS spectrum after exposing the droplet to O₃ for 10 s. No further oxidation of the peptide is observed up to 30 s of exposure. (b) FIDI-MS² of doubly charged triply oxygenated SP-B₁₋₂₅ product from heterogeneous oxidation yields an exclusive fragment at m/z 1457 resulting from the elimination of hydrosulfinylmethane (CH₄SO). (c) The oxidation mechanisms of Trp by ozonolysis and hydrolysis with hydrolysis mechanism of Met in peptide. (d) Air-liquid interfacial oxidation of SP-B₁₋₂₅ by O₃ in the POG monolayer as a function of time. Doubly protonated SP-B₁₋₂₅ products with two oxygen atoms and with three oxygen atoms appear after the droplet is exposed to O₃ for 10 s. The triply oxygenated product dominates the FIDI-MS spectrum after exposing the droplet to O₃ for 15 s and no further oxidation of the peptide is observed up to 30 s of exposure. 126

- 7.5 Atomic density profiles of POPG monolayer systems (solid lines) and POG monolayer systems (dotted lines) as a function of Δz , where the air/liquid interface is 0, and proceeding left to right from the water to the lipid layer. The lipid surface densities are (a) $55 \text{ \AA}^2/\text{lipid}$, (b) $60 \text{ \AA}^2/\text{lipid}$, (c) $65 \text{ \AA}^2/\text{lipid}$, and (d) $70 \text{ \AA}^2/\text{lipid}$. Blue lines denote the density profiles of oxygen atoms of water molecules, black lines denote that of saturated carbons of lipid acyl chains, and red lines denote that of unsaturated carbons of lipid acyl chains. 129
- 7.6 (a) Final snapshot after 2.0 ns of MD simulation of SP-B₁₋₂₅ in a POG monolayer at $60 \text{ \AA}^2/\text{lipid}$. The peptide is shown in rainbow color (C-terminal: red, N-terminal: blue). Lipids, water molecules, and chloride are shown in purple, cyan, and red, respectively. (b) AA hydrophobicities [46] (top) and Δz of C_α of each residue averaged during the last 0.5 ns of a 2.0 ns duration MD simulation (bottom) are plotted as a function of amino acid residue number. The air/water interface is located near $\Delta z = 0$. (c) Atomic density profiles of SP-B₁₋₂₅ in POG monolayer at $60 \text{ \AA}^2/\text{lipid}$ as a function of Δz during the last 0.5 ns of the 2.0 ns MD simulation. Blue dash line denotes the density profiles of oxygen atoms of water molecules. Black and red dash lines denote those of separately summed saturated and unsaturated carbons of lipid acyl chains, respectively. Wine, magenta, cyan, and olive solid lines denote the 100 times scaled density profiles of the C_α carbon of Cys₈, Trp₉, Cys₁₁, Met₂₁ residues, respectively. 130
- 7.7 (a) The xy -projected density profiles of saturated carbon atoms of lipid acyl chains from MD simulations is shown with colors and the averaged positions of C_α carbons of SP-B₁₋₂₅ in the POG monolayer is shown with a black line (each residue is shown with cross). (b) Top view of final snapshot after 2.0 ns of MD simulation of SP-B₁₋₂₅ in a POG monolayer at $60 \text{ \AA}^2/\text{lipid}$. The peptide is shown in rainbow color (C-terminal: red, N-terminal: blue). Lipids and water molecules are shown in gray and cyan, respectively. Black spheres denote unsaturated carbon atoms of lipid acyl chains, and orange spheres denote hydroxyl oxygen atoms. 131

- 7.8 (a) Final snapshot after 2.0 ns MD simulation of SP-B₁₋₂₅ in POPG monolayer at 60 Å²/lipid is shown at top panel. The peptide is shown in rainbow color (C-terminal: red, N-terminal: blue), lipids in gray, water molecules in cyan, and chloride ions in red. Lower left and right show that Arg residues and Lys residues (displayed with sticks) are interacting with phosphate groups of lipids, respectively. (Phosphorous atoms are in magenta.) (b) AA index for hydrophobicity scale [46] (top) and Δz of C α of each residue averaged during the last 0.5 ns trajectory of 2.0 ns duration MD simulations (bottom) are plotted as a function of amino acid residue number. The air/water interface is located near $\Delta z = 0$. (c) Atomic density profiles of SP-B₁₋₂₅ in POPG monolayer at 60 Å²/lipid as a function of Δz during the last 0.5 ns of the 2.0 ns MD simulation. Blue dash line denotes the density profiles of oxygen atoms of water molecules. Black and red dash lines denote those of saturated and unsaturated carbons of lipid acyl chains, respectively. Wine, magenta, cyan, and olive solid lines denote the 100 times scaled density profiles of the C α carbon of Cys₈, Trp₉, Cys₁₁, and Met₂₁ residues, respectively. 133
- 7.9 The xy -projected density profiles of saturated carbon atoms of lipid acyl chains is shown with colors and the averaged positions of C α carbons of SP-B₁₋₂₅ in the POPG monolayer is shown with a black line (each residue is shown with cross). 134
- A.1 Total time taken for the complete P-to-T transition, $t_{\text{P-to-T}}$ by varying the area of the periodic simulation cell as $10 \times 10 = 100$, $30 \times 30 = 900$, $40 \times 40 = 1600$, $50 \times 50 = 2500$, and $60 \times 60 = 3600$. Black line denotes the change of $t_{\text{P-to-T}}$ under the external field of $F = 1.2 \text{ V/\AA}$, red line denotes the change of $t_{\text{P-to-T}}$ scaled by 10 under the external field of $F = 1.0 \text{ V/\AA}$, and blue line denotes the change of $t_{\text{P-to-T}}$ scaled by 15 under the external field of $F = 0.95 \text{ V/\AA}$. The $t_{\text{P-to-T}}$ value is converged at the area of 900–1600 and 2500–3600 when $F = 1.2 \text{ V/\AA}$ and 1.0 V/\AA , respectively. When $F = 0.95 \text{ V/\AA}$, the $t_{\text{P-to-T}}$ value is not converged until the area of 3600. This infers that we need much larger simulation cell to get the right converged value of $t_{\text{P-to-T}}$ as the F approaches to the critical field, $F_c = 0.56 \text{ V/\AA}$. Otherwise, we will get the overestimated value of $t_{\text{P-to-T}}$ near F_c 139
- B.1 (top panel) Electrical conductivity through the AN-OPE is estimated based on the twisting angles from MD simulations with (10×10) unit cell. (bottom panels) The final snapshot after each step is shown with the populations of χ_1 and χ_2 , which are averaged during the last 0.5 ns dynamics. 142

C.1	(a) Optimized geometry for the low field structure (P) of N-OPE SAM. Here [0001] is the surface normal and the views are along z -axis (upper middle), y -axis (lower middle), and x -axis (lower right). The left picture is a perspective along the axis of one plane of molecules. The weak hydrogen bonding network is aligned along the $[11\bar{2}0]$ direction. (b) Optimized geometry for the high field structure (T) of N-OPE SAM. Here [0001] is the surface normal and the views are along z -axis (upper middle), y -axis (lower middle), and x -axis (lower right). The left picture is a perspective along the axis of one plane of molecules. The weak hydrogen bonding network is aligned along the $[10\bar{1}0]$ direction.	145
C.2	(a) Energies of various conformations of N-OPE relative to the AP conformation computed with a $0.6 \text{ V}/\text{\AA}$ external field from FF calculations (black histograms). (b) Energies of various conformations of N-OPE relative to the AP conformation computed with no external field from FF calculations (black histograms), and QM calculations (green histograms).	146
E.1	Structures of a) backbone part and b) CBPQT ⁴⁺ ring part with numbered atoms. The assigned numbers on the atoms are associated with the partial charge distribution data shown in Tables E.1, E.2, and E.3.	149
H.1	(a) Quadruply charged SP-B ₁₋₂₅ and oxidized products from (b) the bulk-phase O ₃ reaction and (c) the Fenton reaction with intact SP-B ₁₋₂₅ . (d) Triply charged SP-B ₁₋₂₅ and oxidized products from (e) the bulk-phase O ₃ reaction and (f) the Fenton reaction are also shown.	160
H.2	(a) The ESI mass spectrum of the trypsin digests of SP-B ₁₋₂₅ in positive mode. (b) The ESI mass spectrum of the trypsin digests of the oxidized SP-B ₁₋₂₅ from the bulk-phase O ₃ reaction in positive mode. (c) The negative mode ESI mass spectrum of the trypsin digests of the oxidized SP-B ₁₋₂₅ from the bulk-phase O ₃ reaction.	161
H.3	(a) The CID spectrum of cationic IQAMIPK + 3O at m/z 817 from the tryptic digest of the oxidized SP-B ₁₋₂₅ . (b) The CID of cationic FPIPLPYCWLCR + 8O at m/z 1636 from the tryptic digest of the oxidized SP-B ₁₋₂₅ . (c) The CID of anionic FPIPLPYCWLCR + 8O at m/z 1634 from the tryptic digest of the oxidized SP-B ₁₋₂₅	162
H.4	ESI-MS ² of triply oxygenated products of quadruply protonated SP-B ₁₋₂₅ from (a) bulk-phase O ₃ application, and from (b) the Fenton reaction. M denotes a parent ion, which is triply oxygenated SP-B ₁₋₂₅	163

List of Tables

2.1	AN-OPE Interaction Energies, U_{ij} , for Monte Carlo (MC) Calculations	11
3.1	Free Energy Barriers, Rate Constants, and Relaxation Half-Lives from DNP toward TTF (DNP \rightarrow TTF) at 298 K (All Simulation Results from this Work)	43
4.1	Vapor Pressures, Water Uptake/Cell, Water Coordination Numbers of the Water Molecule (up to 3.7 Å Cutoff), Water Coordination Numbers of the Sodium Ion (up to 3.5 Å Cutoff), and Diffusion Coefficients from NPT MD at Temperature of 298.15 K	62
4.2	Temperature, Water Uptake/Cell, and Diffusion Coefficients at Constant Pressure Condition of 101.3250 kPa	66
5.1	Drift Times, Reduced Mobilities, and Collision Cross-Sections of Ammonium Cations in N ₂ Drift Gas	81
5.2	Critical Impact Parameter, b^* , Langevin Capture Cross-Section, Ω_L , and Mean Relative Kinetic Energies, KE, during the Experiments with Experimentally Determined Hard-Sphere Collision Radius, R_c for Each Ammonium Cation	86
5.3	Theoretically Determined Collision Cross-Sections of 3° and 4° Ammonium Cations	87
6.1	Mass, Drift time, and Corrected Drift Time of Ion Molecule Used in This Study	98
6.2	Optimized Partial Charge Distribution of Protonated Phosphate from the DFT Calculation of Protonated Dimethyl Phosphate (The Partial Charges with Atom Types for CHARMM Force Field are Tabulated.)	100
6.3	Collision Cross-Sections of Phosphatidylcholine Cations in N ₂ Drift Gas Estimated and Evaluated using Empiric Calibration Method and Equations from Shavartsburg and Smith [27], respectively. Theoretically Determined Collision Cross-Sections in N ₂ and He are also Listed.	103
6.4	Theoretically Determined Collision Cross-Sections (Ω_D) of Phosphatidylcholine Cations at Minimum Energy State (E_0). The Differences of Ω_D ($\Delta\Omega_D$) and Potential Energy (ΔE) from the PC Structure at E_0 to Experimentally Determined Ω_D	113

E.1	Partial Charge Distribution of Neutral Rotaxane when the Center of Mass of the CBPQT ⁴⁺ Ring Moves from $z = 10.92 \text{ \AA}$ (TTF side) to $z = 44.83 \text{ \AA}$ (DNP side) . . .	150
E.2	Partial Charge Distribution of +1 Oxidized Rotaxane when the Center of Mass of the CBPQT ⁴⁺ Ring Moves from $z = 10.92 \text{ \AA}$ (TTF side) to $z = 44.83 \text{ \AA}$ (DNP side) . . .	152
E.3	Partial Charge Distribution of +2 Oxidized Rotaxane when the Center of Mass of the CBPQT ⁴⁺ Ring Moves from $z = 10.92 \text{ \AA}$ (TTF side) to $z = 44.83 \text{ \AA}$ (DNP side) . . .	154

Chapter 1

Introduction

Generally, a great number of chemical and physical problems in real life have multiscale and multiphysics features. Many observable physical quantities originate from multiple physical phenomena working cooperatively at different time- and length-scale. Interestingly, it is well known that different regimes are interpreted in terms of the different physics, which are inter-connected to each other through the “coarse-graining of the scale.” Exemplifying, quantum mechanics (QM) governs the physics between nuclei and electrons. Classical mechanics (CM) governs the atomic or molecular dynamics on the complex energy surface, which is the outcome of the quantum mechanical interactions. The material flow is described by rheology, which coarse grains the particles into a continuum. Here, the governing parameters of such rheology are determined by the inter-molecular interactions.

Computational simulation methods, along with statistical mechanics, have been employed as a useful tool to expand our knowledge of microscale events and connect them into macroscopic observances. Thanks to the development of many simulation methods at various scales and the combination of these methods within a multiscale and multiphysics simulation paradigm (Figure 1.1), computational simulation is now regarded as an indispensable tool for the new advancement in science and engineering. In a good number of cases, computer simulations efficiently supplement experiments in interpreting observations, otherwise research would be too expensive or dangerous. On the contrary, in many others, computer simulations are the only possible choice to probe the complicated phenomena. In this context, the tremendous quest for ever-higher levels of detail and realism in such simulations, contribute to the inexorable demand for new theory, methods, and computational tools.

Currently, an enormous amount of research is focused on nano- and bio-systems. Research on nano-systems is most often centered on predicting nanoscaled transport properties such as electron, thermo, and mass transportations for the application of next-generation electronic devices or alternative energy materials. Research on bio-systems has significant potential in life science and medical applications. In particular, such nano- or bio-systems have a strong multiscale and multiphysical nature within them, intriguing the quest for the development of an elaborated methodology to un-

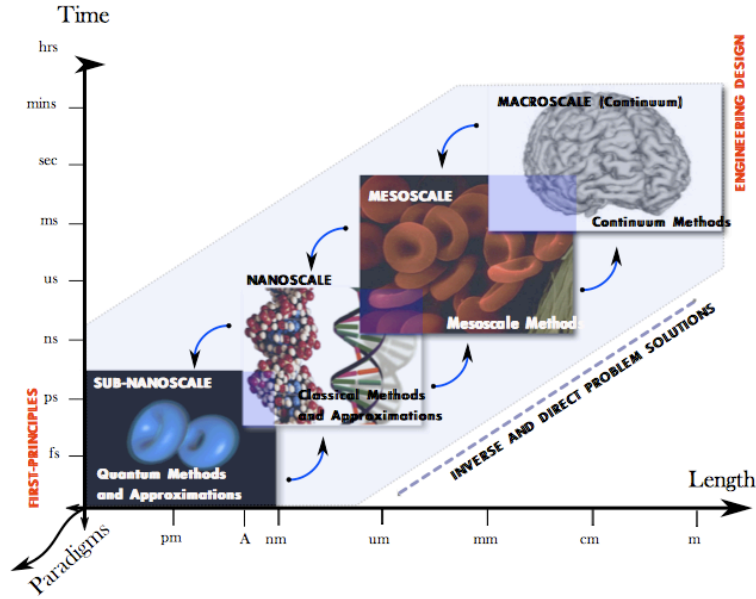


Figure 1.1: Multiscale and Multiphysics paradigm simulation strategy.

Understand the scale-dependent physics. Specifically, in nano-systems (Figure 1.2), electron transport through a molecule is strongly dependent on the energy eigen states of the molecule (QM regime), which are affected by the molecular/atomic conformations and motions (CM regime). When we design an engineering process for manufacturing electronic device such as ultimate complementary metal-oxide-semiconductor (CMOS) electronics using novel materials, continuum level theory and simulations are important. In bio-systems (Figure 1.3), lipid layers encapsulate cells and control fluidity and surface tensions, which are macroscopic/hydrodynamic regime quantities. These macroscopic changes are yielded by the inter-molecular interactions at the interface (CM region). In the lower scale, such molecular interactions are often tuned by chemical reactions such as a proton transfer, which has a strong QM effect.

Within contemporary computing power, direct use of first principle computational methods is limited by an order of ~ 1000 atoms and an order of *pico* to *nano* seconds. Thus, for managing many practical issues in using computational simulation methods which often involve a large length- and long time-span, we need to overcome the limitations in simulation scales. In this thesis, several cases of nano- and bio-systems are presented; (1) we understand them by capturing fundamental nanoscale intrinsic and extensive properties, then, (2) we define the macroscopic behavior observed from experiments based on the microscopic understandings.

The first half (Chapters 2–4) discusses the multiscale and multiphysics simulation approaches for nano-systems.

In Chapter 2, we investigate a negative differential resistance (NDR) effect observed from a metal/molecular SAM/metal junction. Amino- and nitro-substituted oligo-phenylene ethynylene

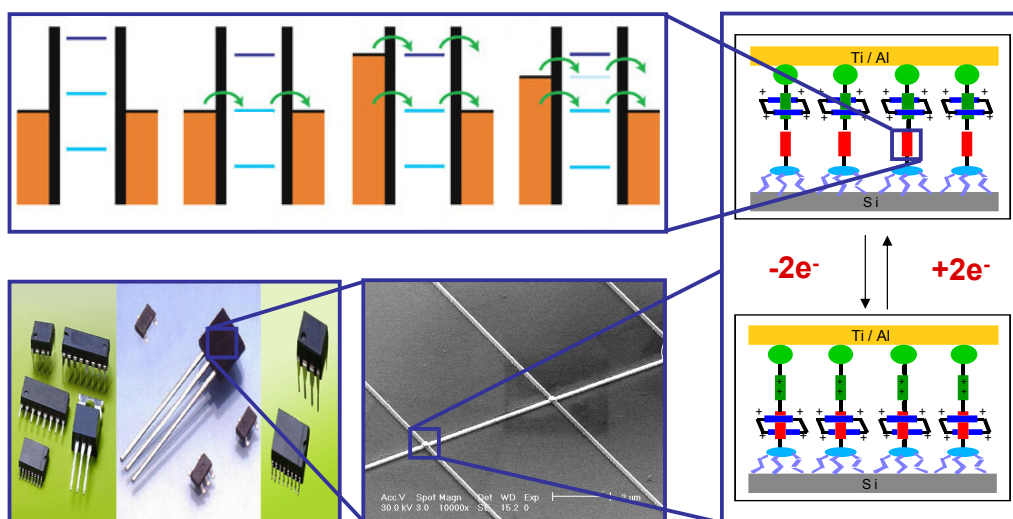


Figure 1.2: Multiscale and Multiphysics characteristics in nano electronic systems. At electron size scale, electrical conductivity depends on the quantum states of the molecules. At molecular size scale, classical interactions determine the molecular conformation, which affects its quantum state. At device size scale, hundreds of molecules are assembled to build a mesoscale junction and these are packaged into a device component.

(OPE) molecules in the self-assembled monolayer (SAM) have a large molecular dipole moment, which responds to the external electric field. Hence, applying the bias voltage induces the conformational changes of the individual molecules and thereby yield a structural transition of the SAM. Such a conformational change is in the regime where the molecular dynamics (MD) simulation is useful. However, the kinetics during the structural relaxation of the SAM requires larger scale simulation methods. On the other hand, electrical conductivities on the total I - V curve are rooted in QM. In order to manage such a complicated problem, we design a nearest neighbor (NN) model with lattice Monte Carlo (MC) simulation, whose parameters are obtained by coarse-graining QM and MD simulation results. The electrical conductivities depending on the conformations are parameterized using non-equilibrium green functional theory combined with QM.

In Chapter 3, on/off kinetics of the molecular switch, bistable [2]rotaxane is discussed. The rotaxane has been intensively studied because of its interesting properties, which are attributed to the molecular recognition between charge donor and acceptor. The shuttling motion of electron accepting cyclobis-(paraquat-*p*-phenylene) (CBPQT⁴⁺) between the charge donating stations such as tetrathiafulvalene (TTF) and 1,5-dioxynaphthalene (DNP) moieties, has brought many applications such as molecular switch in nanoelectronics and artificial muscle in nanomechanics. Therefore, comprehensive understanding of the free energy barrier required for this shuttling motion is essential. In addition, the fine control of the free energy barrier can open an application of the rotaxane system

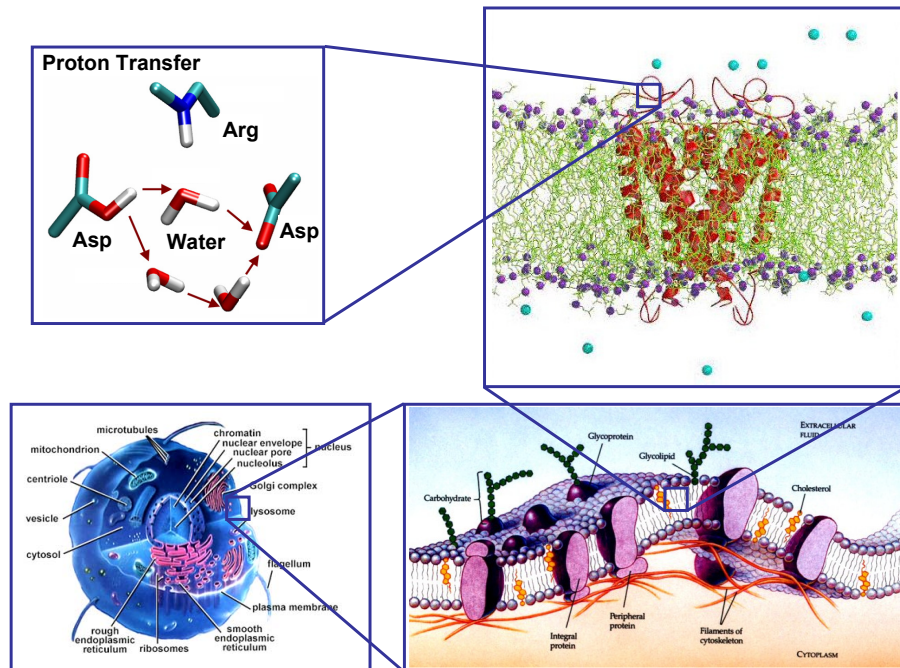


Figure 1.3: Multiscale and Multiphysics characteristics in bio systems. At electron size scale, chemical reactions, which are governed by huge QM effects (e.g., electron/proton transfer), regulate the molecular architecture of the protein for an effective functionality. At molecular scale, CM describes the interactions, such as hydrophobic interaction, among the bio components of proteins, lipids, etc. Large scale motion of the membrane, such as endo- or exo-vesiculation, is in the regime of hydrodynamic descriptions, and this affects the dynamics of a cell.

toward non-volatile flash memory devices, which has not yet achieved. Since the ring and backbone form a charge transfer complex, the local charge distribution (QM effect) strongly determines the free energy profiles for the rings shuttling. However, the time scale for the shuttling is order of μs , which is beyond the available time scale of atomistic simulations. To handle such difficulties, we perform a “blue moon sampling technique” with MD simulations, which allows an effective sampling using a series of constraint MD simulations. The change of potential energy surface depending on the charge transfer amount is reflected on the MD simulations using various Mulliken charge populations from QM calculations according to the ring’s location. The free energy barrier from the TTF station to the DNP station is evaluated as 19 kcal/mol when the system is neutral and 8 – 9 kcal/mol for the oxidation states +1 and +2, and the free energy barrier from the DNP station to the TTF station is 18 kcal/mol, 22 – 23 kcal/mol, and 32 – 33 kcal/mol for the neutral and the oxidation states +1 and +2, respectively. These values are quite comparable to the values that were obtained from various prior experiments, and greatly explain the microscopic ground for the on/off switching kinetics of the molecular switch.

In Chapter 4, the diffusion process of sodium ion in the aluminum-doped zeolite BEA system is studied. Understanding the ionic diffusion through a percolated pore of the zeolite is important for the application of the zeolite to proton exchange membranes for fuel cells (PEMFC). Especially, investigating the role of the confined water is vital because it provides a medium for transport of the ions. The amount of water swelled into the PEMFC depends on the macroscopic variables, such as pressure and temperature, where the PEMFC is working. Thus, combining the grand canonical Monte Carlo (GCMC) simulations (for the study of water uptake amount) with MD simulations (for the study of confined water structure), we investigate the effect of water on the sodium diffusion. We observe a first-order-like transition from the absorption isotherm, inferring that zeolite provides a hydrophobic environment. From MD trajectories, we observe the sodium ions diffused via a hopping mechanism among aluminum-doped sites (which are Brönsted acid sites). We figure out that, above 15 wt % hydration (good solvation regime), the solvation cage is easily formed, and dramatically increases sodium diffusion by reducing the hopping energy barrier by 25 % from the value of 3.8 kcal/mol observed in the poor solvation regime.

The second half (Chapters 5–7) discusses the multiscale and multiphysics simulation approaches for bio-systems. In particular, we scrutinize lipid systems, which have critical roles in cell structure, energy storage and metabolic control, using computational methods in collaboration with gas-phase experiments.

In Chapter 5, we study the ion mobility of a number of tertiary amine and quaternary ammonium cations in gas-phase. These tertiary amine and quaternary ammonium cations are related to the choline and its derivatives, which are precursors for lipids such as a phosphatidylcholine and sphingomyelin. For example, choline is oxidized to betaine, which is readily demethylated to yield

N,N-dimethylglycine. Decomposition of choline yields trimethylamine and dimethylamine. Ion mobility in gas phase is determined by the collision of the ion with drift gas molecules. Utilizing the kinetic theory under the assumption of binary collision, the ion mobility in gas-phase is formulated as a complex integration of interaction terms between the ion and the drift gas molecule. We develop a methodology (referred to as modified trajectory (TJ) method) for the numerical integrations of complex interaction terms for the case where the ion drifts within the N₂ buffer gas. Since the interaction terms depend on the electron distribution and molecular conformation, the gas phase structures and the charge distributions are investigated using QM calculations. Then, ion mobilities are calculated using the modified TJ method. The calculated ion mobility is in agreement with the experimental value, and it well explains the observed mass-mobility correlation of tertiary amine and quaternary ammonium cations, in terms of the asymmetry of the shape. In addition, computational numerical study allows us to identify the role of each interaction term (van der Waals interaction, ion-induced dipole interaction, ion-quadrupole interaction, charge-charge interaction) on the ion mobility at the border-line regime, which lies between the regime where the long-range interactions are dominant (small ion size) and the regime where the short-range interactions are dominant (large ion size).

In Chapter 6, we expand the ion mobility study of lipid precursors in Chapter 5 into the study of the intact lipids of phosphatidylcholines (PC). Since the PC contains a flexible acyl chain, the molecular fluctuation changes the mobility of the PC cation. Taking the molecular fluctuation effect into account, 200 conformations are sampled from the MD simulations, then, the average collision cross-section is computed using the modified TJ method for the calculation of ion mobility. Here, for the experimental section, a commercial traveling wave ion mobility spectrometry (TWIMS) has been employed. Our simulation results exhibit a good agreement with the experimental values. In particular, we reveal that the traveling wave applied in the experiments excites the ions. Since this excitation yields a less compact form of saturated PCs, while unsaturated PCs can not form such a stretched conformation due to the rigid double bonds, we observe distinct mass-mobility correlation lines for the saturated PC cations and for the unsaturated PC cations.

In Chapter 7, a model lung surfactant system composed of lipid monolayer with surfactant protein B (SP-B) is examined. Lung disease is the third leading cause of death in United States, and concerns about chronic respiratory tract disease increase significantly as the level of air pollution increases. Thus, chemical and physical comprehensions about the response of pulmonary surfactant (PS) system to ozone (O₃), one of the most common air pollutants, are required. Due to the interfacial characteristic of PS, the ozonolysis of PS can undergo different pathways according to the reaction environment, especially, depending on whether or not the reaction occurs under water-rich conditions. From the multiscale/multiphysics point of view, the ozonolysis is the result of the QM effect, but the reaction environment is determined by the location of each component,

which is the outcome of the CM interactions among the molecules. In addition, the change of physical properties of PS (e.g., surface tension) is in the regime of larger-scale physics such as hydrodynamics. In this chapter, a complete study on the response of lipid monolayer to O_3 is achieved at the air-liquid interface when O_3 is introduced from the air. The chemical composition changes during the heterogeneous O_3 reaction are analyzed using field induced droplet ionization (FIDI) mass spectrometry, which exhibits quite a different reaction pathway to the bulk-phase ozone reaction. Our MD simulation provides molecular level understanding and rationalization for the observed distinct reaction pathways.

Depending on the characteristics of systems and the objectives that we want to figure out, as exemplified in this thesis, distinct approaches are required to explain the actual observations from experiments. Based on the cases discussed here, we suggest various systematic strategies to overcome the limitations in time- and length-scales of the traditional monoscale approaches. In addition, due to the nature of multiscale and multiphysics phenomena, we expect that a concrete establishment of the fundamental multiscale modeling procedures will invoke interdisciplinary studies by tightly combining the developments occurring independently across fields.

Chapter 2

Negative Differential Resistance of Oligo (Phenylene Ethynylene) Self-Assembled Monolayer Systems: The Electric Field Induced Conformational Change Mechanism

2.1 Abstract

We investigate here a possible mechanism for the room temperature Negative Differential Resistance (NDR) in the Au/AN-OPE/RS/Hg self-assembled monolayer (SAM) system, where AN-OPE = 2'-amino, 5'-nitro oligo (phenylene ethynylene) and RS is a C14 alkyl thiolate. Kiehl and co-workers showed that this molecular system leads to NDR with hysteresis and sweep-rate-dependent position and amplitude in the NDR peak. To investigate a molecular basis for this interesting behavior, we combine first principles quantum mechanics (QM) and meso-scale lattice Monte Carlo (MC) methods to simulate the switching as a function of voltage and voltage rate, leading to results consistent with experimental observations. This simulation shows how the structural changes at the microscopic level lead to the NDR and sweep-rate dependent macroscopic I - V curve observed experimentally, suggesting a microscopic model that might aid in designing improved NDR systems.

2.2 Introduction

Esaki's discovery of the negative differential resistance (NDR) in Ge p - n diodes opened a new phase in semiconductor devices [1]. Since the NDR devices enable faster and more efficient circuits

by reducing the number of transistors required, they have many applications such as high-speed integrated circuits and low-power memories. As the scale of electronic devices is reduced toward nano-scale sizes, it would be useful to demonstrate NDR in molecular electronic systems [2, 3, 4, 5, 6, 7, 8, 9, 10, 11, 12, 13].

Derivatives of oligo (phenylene ethynylene) (OPE) have been identified as a good candidate for the molecular junctions due to its rigid and good conducting (fully conjugated) characteristics [9, 11, 12, 13, 14, 15, 16, 17, 18, 19]. Chen *et al.* reported that a SAM of amino-nitro substituted OPE (AN-OPE) between two Au electrodes exhibits NDR at 60 K with an applied voltage of ~ 2 V. The current-voltage (I - V) curve is fully reversible, but the NDR peak decays as the temperature increases. This NDR has been rationalized by the electrochemical oxidation/reduction or resonant-tunneling mechanism [15, 16, 17]. Support for this oxidation/reduction mechanism was the correspondence between the threshold potential for the electrical conductance (2.09 V) and the electrochemical potential (1.67 V) [15, 19].

The device showing NDR at room temperature (RT) is important for many practical applications [20, 21]. However, the poor reproducibility in device construction and the limited device stability have hampered extensive study on NDR. Kiehl and co-workers showed that a SAM of AN-OPE deposited on an Au electrode coupled to a Hg electrode covered with a tetradecane-thiolate (RS) leads to a well-defined and stable NDR at RT [9]. In this system, a distinct sweeping-rate-dependency in the NDR hysteresis loop was observed for a bias voltage near ~ 0.6 V. The presence of hysteresis rules out the resonant tunneling mechanism [5, 6, 7, 8, 10]. Based on the observed hysteresis and a variety of detailed features of the characteristics, they proposed a charge capture (QC) mechanism to explain the macroscopic I - V behavior. However, an atomistic level analysis of a charge capture process and other possible mechanisms has not yet been established.

Several studies suggest that the conformational change would be a plausible mechanism to explain hysteretic I - V curve [14, 22], and the external electric field can induce conformational change of the molecule in the junction [14, 23, 24, 25, 26]. Especially, Donhauser *et al.* reported STM studies in which isolated AN-OPE molecules contained in a dodecane-thiolate SAM on the Au substrate show at least two states having different conductances [14]. They showed that the transition from the high-conductance state to the low-conductance state is switched by applying external electric field. However no detailed atomic level description of the mechanism was provided.

In this chapter, we use first principle theory to analyze the sweeping-rate-dependent hysteresis of NDR observed in Kiehl's system, focusing on the possibility of electric field based conformational changes. We find that this system has two states:

- a high-conductance phase stable at low field (planar structure) and
- a low-conductance phase stable at high field (twisted structure).

The transition between the two phases is driven by the interaction between the external field and the molecular dipole moment of the middle phenylene ring in AN-OPE. This leads to consistent results with the charge capturing mechanism of Kiehl. Using coarse-grained Monte Carlo simulations, we investigated how such a molecular conformational change results in a sweep-rate-dependent hysteresis in the NDR as well as the detailed kinetics of transition.

2.3 Simulation Details

2.3.1 Computational Details of QM Calculations

To obtain the structures and energies of planar (P) and twisted (T) structures, we carried out QM calculations for a (1×1) periodic unit cell. We employed the Perdew-Burke-Ernzerhof (PBE) generalized gradient approximation exchange-correlation density-functional with a plane wave basis set (540 eV cutoff), using the Vienna Ab initio Simulation Package (VASP) [27]. Only the gamma point is sampled in reciprocal space to reduce computational cost for this large system (67 atoms per periodic cell). For the electrodes, we used 3-layer of Au (111) surface with all gold atoms fixed at their bulk value ($a = 2.8838 \text{ \AA}$) during the geometry optimization steps. The OPE molecules were anchored on the 3×3 Au (111) surface through sulfur atoms with hexagonal packing.

To understand the local electronic structure and local interactions of the AN-OPE part, we performed non-periodic QM calculations of the isolated OPE with 3 connected Au atoms, using Jaguar package [28] with PBE exchange-correlation functional and LACVP** basis set. Using the geometries from VASP calculations, we carried out the single point calculations.

2.3.2 Conductivities of P and T Conformations (NEGF Calculations)

The I - V performance of each conformation is calculated by combining Green's function theory with the DFT Hamiltonian that are determined from the SeqQuest calculation with PBE functional [29, 30]. The current is calculated using following equation:

$$I(v) = \frac{2e}{h} \int_{-\infty}^{\infty} T(E, V) [f_1(E, V) - f_2(E, V_2)] dE, \quad (2.1)$$

where $T(E, V)$ is the transmission function for the AN-OPE SAM part.

2.3.3 Coarse-Grained NN Interacting Hamiltonian

The NN interacting Hamiltonian which describes the AN-OPE SAM is

$$H = \sum_{i=1}^N (E_i^{torsion}(\chi) - D_i F) + \sum_{\text{NN}} U_{ij}, \quad (2.2)$$

Table 2.1: AN-OPE Interaction Energies, U_{ij} , for Monte Carlo (MC) Calculations

	$[10\bar{1}0]$ pair	$[01\bar{1}0]$ pair	$[11\bar{2}0]$ pair
$\{i, j\} \subset P$	-3.95	-5.00	-7.19
$\{i, j\} \subset T$	-7.66	-3.12	-0.61
$\{i \in P, j \in T\}$ or $\{i \in T, j \in P\}$	-5.70	-2.56	3.13

*All energy values are in kcal/mol.

where $E_i^{torsion}(\chi)$ is the internal torsional energy of the i -th AN-OPE molecule due to twisting the AN-OPE by an angle χ , D_i is the $[0001]$ component of the dipole moment of the i -th AN-OPE, F is the $[0001]$ component of the external electric field, U_{ij} is the intermolecular interaction energy between i -th and j -th AN-OPE, and summation over NN denotes that the summation is over nearest neighbors. There are two interactions each for three directions: $[10\bar{1}0]$, $[01\bar{1}0]$, and $[11\bar{2}0]$. To avoid double counting, however, we used just one interaction per direction.

2.3.4 Extracting NN Model Parameters from QM/FF Energies

The U_{ij} terms when $\{i, j\} \subset P$ or $\{i, j\} \subset T$ were determined from the Jaguar calculations (*vide infra*). In order to extract U_{ij} when $\{i \in P, j \in T\}$ or $\{i \in T, j \in P\}$, we need to investigate inter-OPE interaction in the packed system from a larger simulation cell containing more than one OPE. Since this is too expensive for QM calculations (268 atoms), we used a simple DREIDING Force Field [31] (FF) in which the charges are based on QM. We considered six possible packings within a (2×2) unit cell:

- AP: all P's,
- AT: all T's,
- P3T1: 3 P's and 1 T,
- P2T2_{10 $\bar{1}0$} : 2 P's and 2 T's aligned along $[10\bar{1}0]$,
- P2T2_{01 $\bar{1}0$} : 2 P's and 2 T's aligned along $[01\bar{1}0]$,
- P2T2_{11 $\bar{2}0$} : 2 P's and 2 T's aligned along $[11\bar{2}0]$,
- P1T3: 1 P and 3 T's.

The FF energies are shown at Figures 2.1a and 2.1b for when no external electric field and 1.2 V/Å external electric field is applied, respectively. Using FF energies under zero external field, the U_{ij} terms when $\{i \in P, j \in T\}$ or $\{i \in T, j \in P\}$ were fitted. Values are in Table 2.1.

The torsional energy, $E_i^{torsion}$ is estimated from the energy versus twisting angle χ curve (Figure 2.2), leading the 0.01 kcal/mol per AN-OPE when $i \in P$, and 0.23 kcal/mol when $i \in T$. The

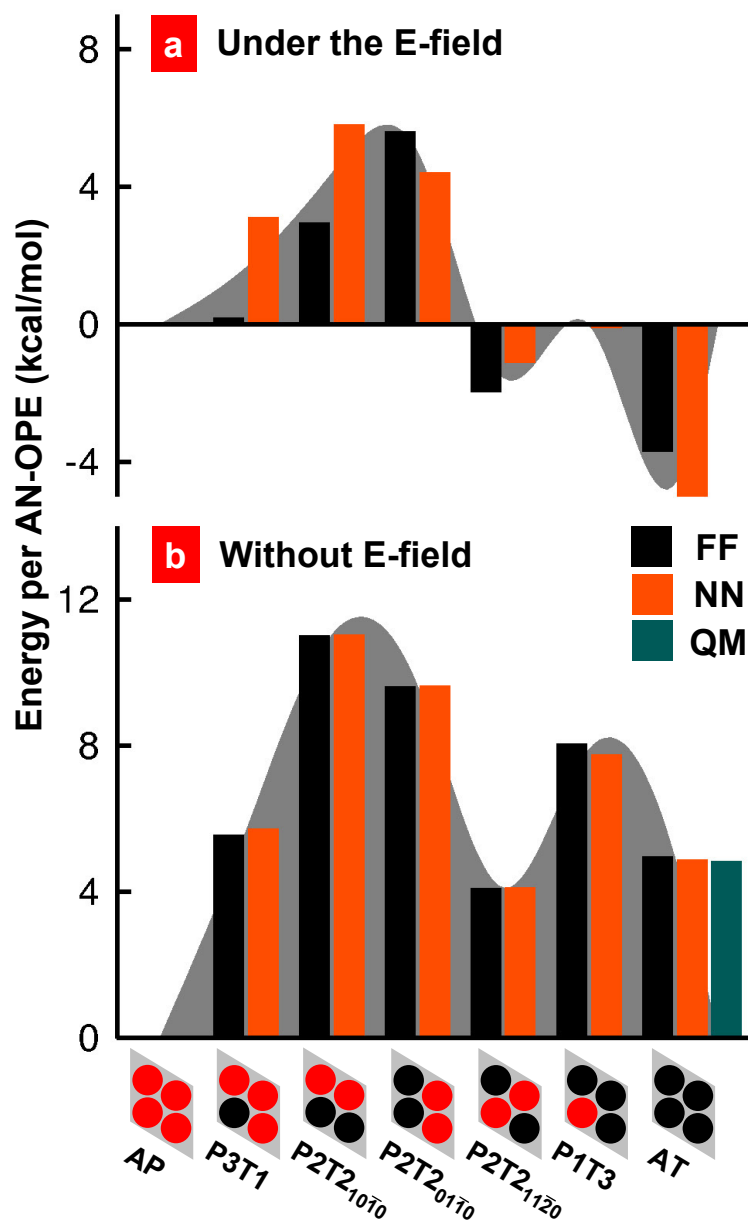


Figure 2.1: (a) Energies of various conformations of AN-OPE relative to the AP conformation computed with a 1.2 V/\AA external field from FF calculations (black histograms) and NN model calculations (orange histograms). (b) Energies of various conformations of AN-OPE relative to the AP conformation computed with no external field from FF calculations (black histograms), NN model calculations (orange histograms), and QM calculations (green histograms).

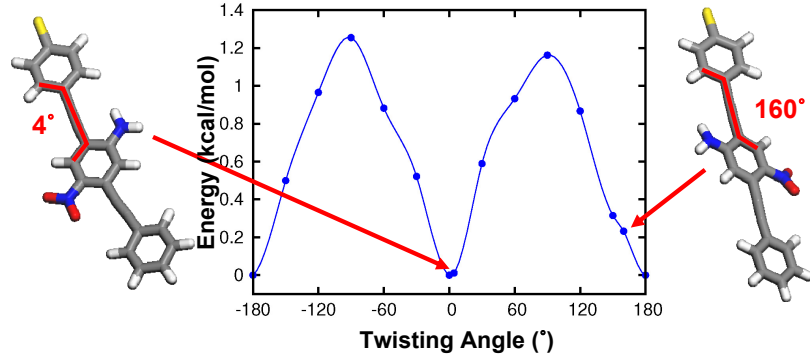


Figure 2.2: Torsional strain energy $E_i^{torsion}$ as a function of twisting angle χ from QM (PBE) on the isolated molecule. The energy at $\chi = 4^\circ$ (corresponding to P) is 0.01 kcal/mol higher than the ground state energy at $\chi = 0^\circ$. The energy at $\chi = 160^\circ$ (which corresponds to T) is 0.23 kcal/mol higher than the energy at $\chi = 0^\circ$, leading the 0.22 kcal/mol higher $E_i^{torsion}$ of T compared to $E_i^{torsion}$ of P.

D_i values were optimized to fit the energies from Hamiltonian in Equation 2.2 to FF energies under 1.2 V/Å external field. The fitted values are $D_i = 5.48$ debye per AN-OPE for P and 7.30 Debye for T, which are quite comparable to the dipoles from Mulliken charge analysis, $D_i = 5.74$ Debye per AN-OPE for P and 7.03 debye for T.

All MD simulations with DREIDING FF were performed using LAMMPS (large-scale atomic/molecular massively parallel simulator) MD code from Plimpton at Sandia [32, 33]. The equations of motion were integrated using the velocity-Verlet algorithm [34], with a time step of 1.0 fs.

2.3.5 Coarse-Grained MC Simulations

The 2-dimensional rhombic MC simulation cell containing (50×50) lattice points with periodic boundary conditions. The MC simulations used the Metropolis algorithm (our own code). Each Monte Carlo Step (MCS) is defined as 2500 MC trials with a fixed external field applied in the z -direction. Our MC simulations are similar to the study of an Ising model in a time-dependent magnetic field [35].

2.4 Results and Discussion

2.4.1 Two Conformations of AN-OPE

Figure 2.3a shows the minimized conformation of AN-OPE determined from the periodic DFT calculation. The three phenylene rings are coplanar, forming a well-conjugated structure, which we label as P (for planar). Here the lowest ring is connected to the Au electrode via a thiolate group. The middle ring (containing the functional groups) has a twist angle of $\chi = 4^\circ$ with respect to the

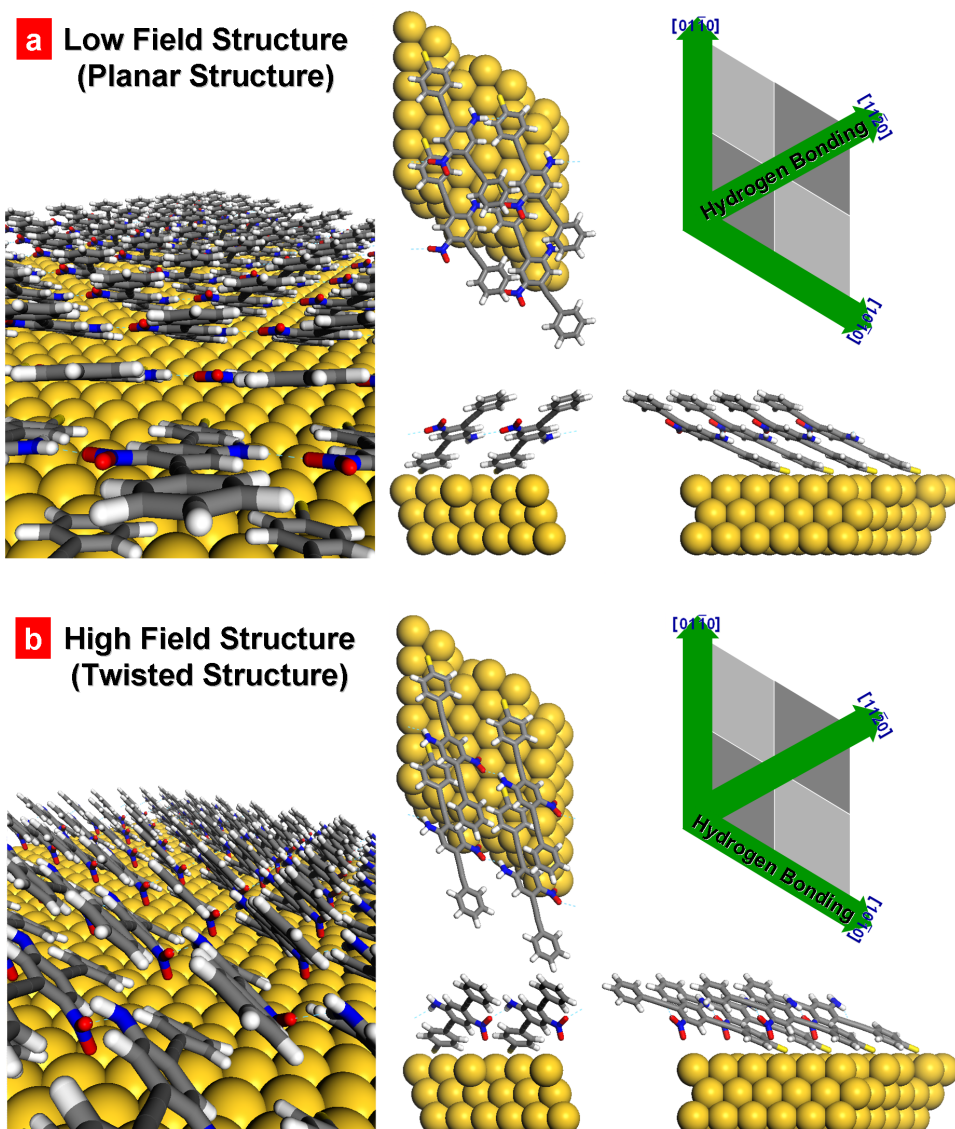


Figure 2.3: (a) Optimized geometry for the low field structure (P) of AN-OPE SAM. Here $[0001]$ is the surface normal and the views are along z -axis (upper middle), y -axis (lower middle), and x -axis (lower right). The left picture is a perspective along the axis of one plane of molecules. The hydrogen bonding network is aligned along the $[11\bar{2}0]$ direction. (b) Optimized geometry for the high field structure (T) of AN-OPE SAM. Here $[0001]$ is the surface normal and the views are along z -axis (upper middle), y -axis (lower middle), and x -axis (lower right). The left picture is a perspective along the axis of one plane of molecules. The hydrogen bonding network is aligned along the $[10\bar{1}0]$ direction.

bottom ring ($\chi = 0^\circ$ for the isolated OPE). This structure packs on the Au surface as (3×3) , with the axis of the molecule along the $[1\bar{1}00]$ direction, and a tilt angle $\theta = 66^\circ$ from the z -axis. The adjacent amino and nitro groups form hydrogen bonding (HB) networks along the $[11\bar{2}0]$ direction.

To understand the local electronic structure and local interactions of the organic molecular part, we performed a single point non-periodic QM calculation of an isolated OPE. The polar amino and nitro groups lead to a large dipole moment of 9.24 (7.22) debye with the z -axis component ($[0001]$) of 5.74 (3.55) debye, the component along $[1\bar{1}00]$ (tilt direction) of 4.44 (3.35) debye, and the component along $[11\bar{2}0]$ (HB direction) of 5.72 (5.32) debye. These dipole moments were determined from the analysis of Mulliken charges, while the values in parenthesis are from quantum mechanical wavefunctions.

The inter AN-OPE interaction energies on the SAM, U_{ij} are determined from the difference between dimer energy and doubled monomer energy:

$$U_{ij} = E_{2 \times (AN-OPE \text{ w/ } 3Au)} - 2 \times E_{AN-OPE \text{ w/ } 3Au}, \quad (2.3)$$

where we included three Au atoms connected to the sulfur atom.

The value of U_{ij} between two P's are shown at Table 2.1, especially, U_{ij} along $[11\bar{2}0]$ direction shows the largest stabilization energy of -7.19 kcal/mol, due to the HB interaction.

Figure 2.3b shows the T (for twisted) conformation, which is 4.85 kcal/mol less stable than P. The middle and terminal phenyl rings are rotated from the bottom one by $\chi = 160^\circ$. Although we note that this twist angle is not stable for the isolated AN-OPE, it becomes meta-stable in the packed system (Figure 2.2). The rotation of the middle ring changes the direction of amino/nitro groups along $[10\bar{1}0]$ from $[11\bar{2}0]$, leading the hydrogen bond network to be aligned along $[10\bar{1}0]$. The axis of the molecule is at $\theta = 71^\circ$ from the z -axis, which makes the T lies more down than the P. The height of the terminal phenyl ring of T is 7.60 Å while that of P is 8.73 Å from the Au surface. The lower height of T is comparable to the Donhausers observations from the STM experiment that exhibits ~ 3 Å lower height of low conductance phase to higher conductance phase [14].

The dipole moment of T is 8.71 (6.88) debye with the component along $[0001]$ of 7.04 (4.62) debye, a component along $[1\bar{1}00]$ (tilt direction) of -3.32 (-3.40) debye and a component along $[10\bar{1}0]$ (HB direction) of 5.12 (5.10) debye.

The value of U_{ij} between two T's shown at Table 2.1. For T conformation, U_{ij} along the $[10\bar{1}0]$ direction (HB network direction) is the most stable with the value of -7.66 kcal/mol.

2.4.2 Electrical Conductivities of P and T

The electrical conductivity, σ , was predicted using non-equilibrium Green's function (NEGF) theory for P and T structures with QM on the (1×1) unit cell. These calculations partition the tunnel-

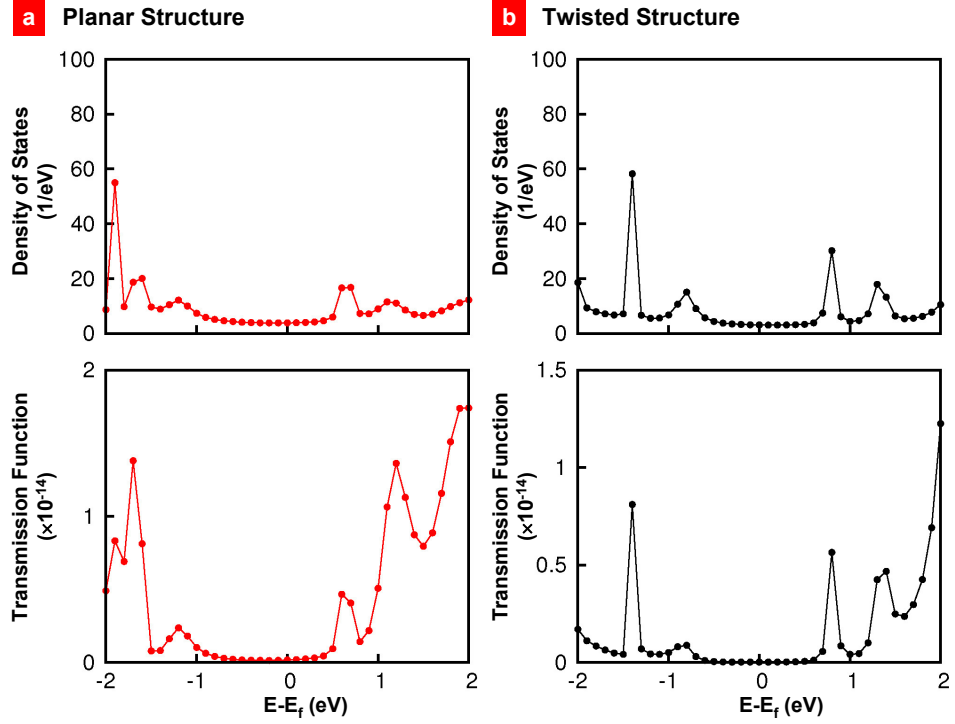


Figure 2.4: Density of state (DOS) and transmission function $T(E)$ of P structure (a) and T structure (b). The top electrode is located 12 Å above from the bottom electrode.

ing Hamiltonian using the Gaussian basis function representation. The semi-infinite electrode is calculated interactively using 3 explicit layers of Au [29].

The experiments use a top Hg electrode covered with a tetradecane-thiolate (RS), the atomic structure of which is not certain due to the amorphous character of the Hg electrode and the fluctuations in the alkyl thiol at room temperature. Instead, our calculations use a second 3-layer of Au (111) surface 12 Å above the bottom electrode. We also tested placing the top electrode in contact with the OPE, which 20 Å above the bottom electrode.

The density of states (DOS) with the transmission function $T(E)$ were computed (Figures 2.4 and 2.6), and these are used to obtain the I - V curve and the σ - V curve (Figures 2.5 and 2.7). Over the range of 0 to 1.5 V, we see that the average ratio of σ_P to σ_T is 10 for the thickness of 12 Å, and 163 for the thickness of 20 Å. Since the experimental value is ~ 13 fold larger σ_P than σ_T , we adopted the case of 12 Å.

The calculated I - V curves lead correctly to a smaller σ for the high field stable phase. The difference in σ is explained by two factors:

1. the loss of π - π orbital overlap due to the rotation of the middle phenyl ring (which contributes to the conductivity through the molecules) and

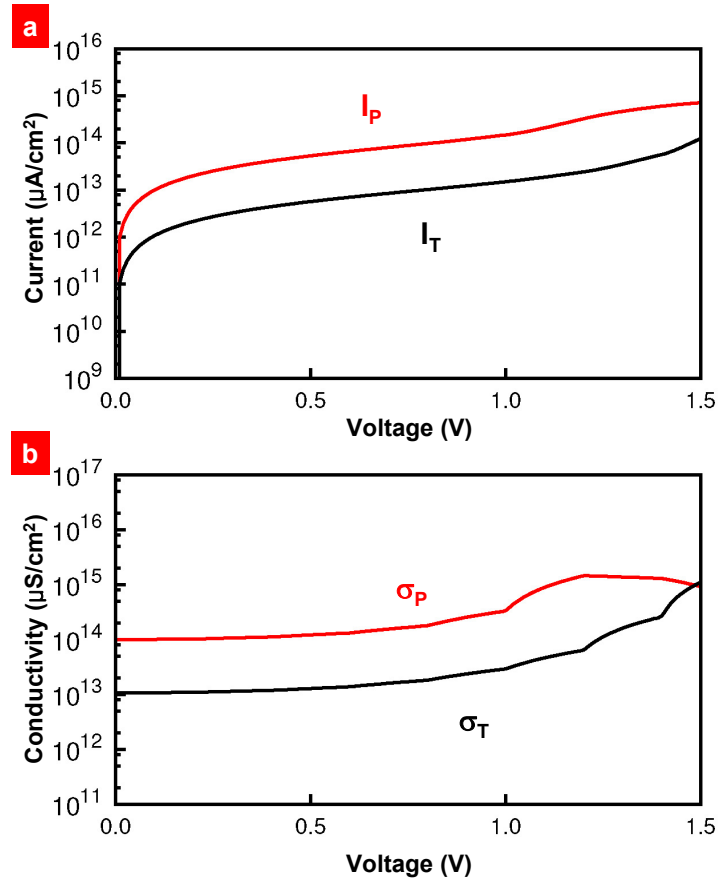


Figure 2.5: (a) Current through P conformation, I_P and current through T conformation, I_T versus the bias voltage V determined from the NEGF calculations using the DOS and $T(E)$ of Figure 2.4. (b) Conductivity of P conformation, σ_P and conductivity of T conformation, σ_T versus the bias voltage V determined. The top electrode is located 12 Å above from the bottom electrode. σ_P is ~ 10 times larger than σ_T .

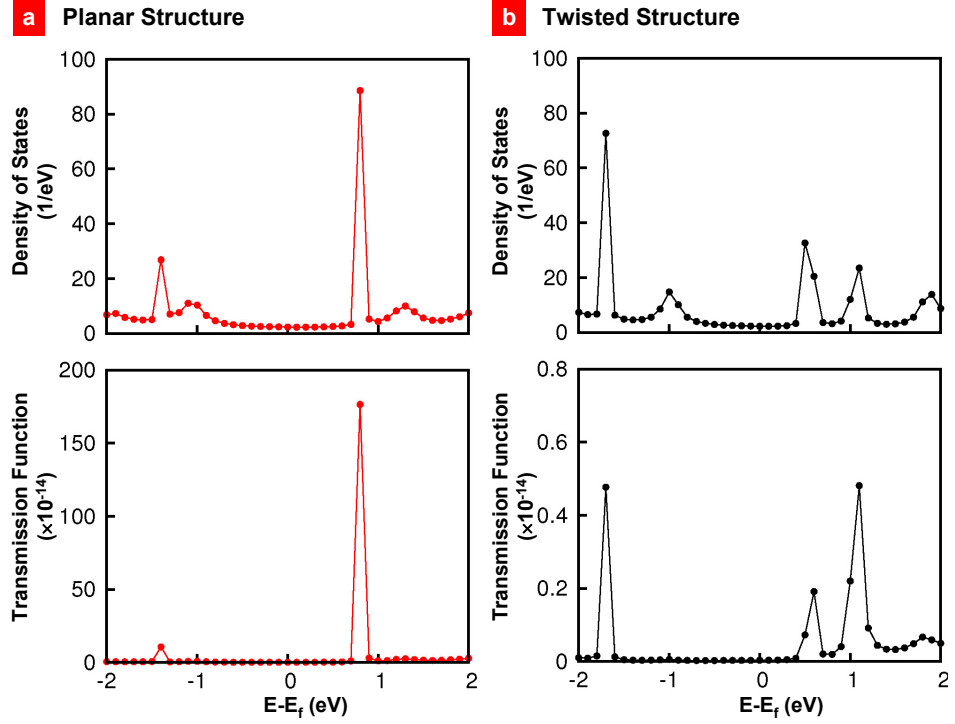


Figure 2.6: Density of state (DOS) and transmission function $T(E)$ of P structure (a) and T structure (b). The top electrode is located 20 Å above from the bottom electrode.

2. the increase of vacuum distance due to the lower height of T phase.

Previous studies showed that the rotation of the ring by χ reduces the conductivity by factor of $\cos^4 \chi$ (Figure 2.8) [36]. Thus, using the QM minimized structures, which are twisted by 4° and 160° , yield an average ratio of σ_P to σ_T by ~ 1.3 times. However, considering the distribution of angles from the MD, we find an average ratio of σ_P to σ_T of ~ 3.5 times. (Details are discussed in Appendix B.)

The minimized structures for P and T lead semi-log plots of $I-V$ curves (Figure 2.5) to show similar slopes for both phases, in disagreement with experiment showing a slope ratio of ~ 3.2 . From previous study [36], we found that the slope of the semi-log plot of $I-V$ curve strongly depends on the χ , and it decreases until almost zero when the molecule twisted with $\chi = 90^\circ$ (Figure 2.8a). This is a reasonable result since the slope of semi-log plot is related to the height of tunneling barrier, Φ_B which highly depended on the π - π orbital overlap. Therefore, consideration of the twisted structure from MD simulations, which has a significant population near 90° , well explains the distinct difference between the slopes of semi-log $I-V$ plots for both structures observed in the experiment.

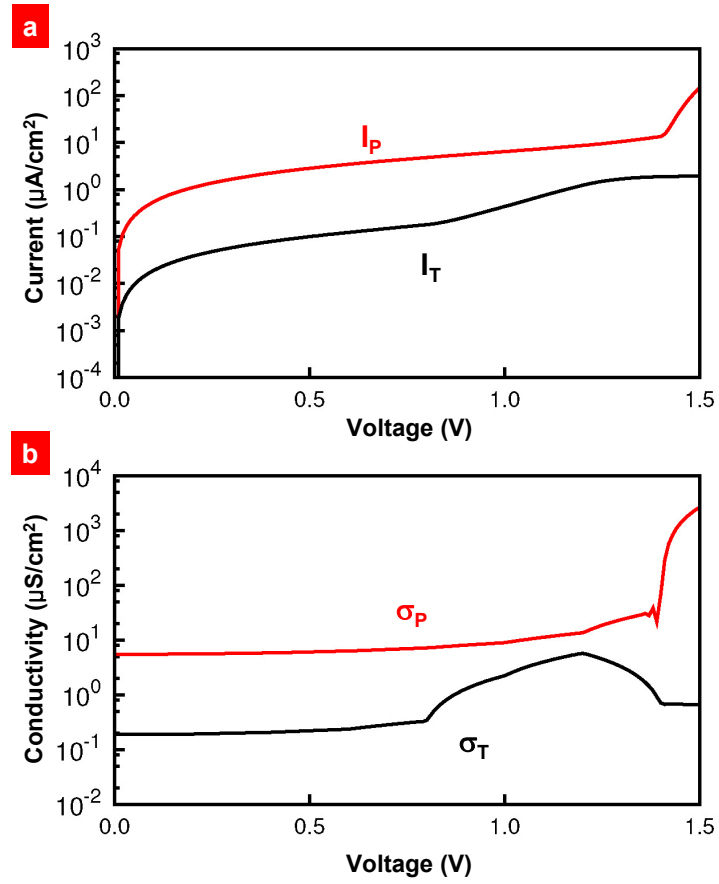


Figure 2.7: (a) Current through P conformation, I_P and current through T conformation, I_T versus the bias voltage V determined from the NEGF calculations using the DOS and $T(E)$ of Figure 2.6. (b) Conductivity of P conformation, σ_P and conductivity of T conformation, σ_T versus the bias voltage V determined. The top electrode is located 20 Å above from the bottom electrode. σ_P is ~ 163 times larger than σ_T .

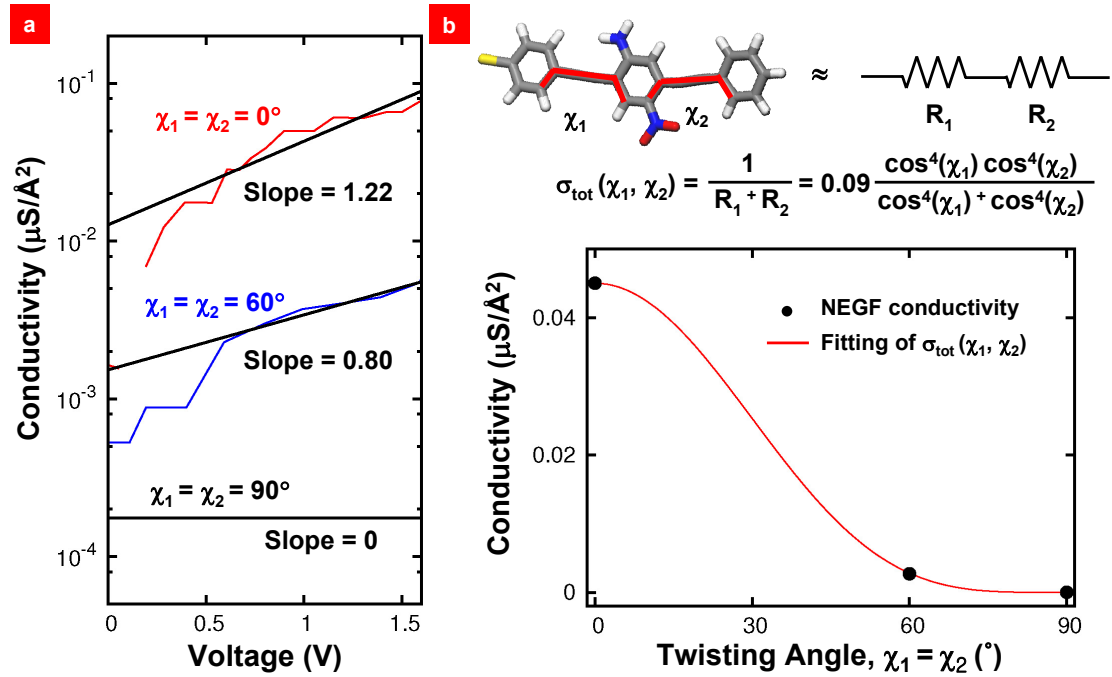


Figure 2.8: Conductivities depending on the twisting angle are extracted from the previous study [36], which are the results from NEGF calculations. (a) Semi-log plots of I - V curves shows that the slope decrease as the twist angle approaches to 90° , which means that the tunneling barrier from the bottom electrode to top electrode, Φ_B increases as the the π - π orbital overlap decreases. (b) Since the conductivity is dominated by the π - π orbital overlap, we assumed that the conductivity between two phenyl rings, $\sigma_i = 1/R_i$ is proportional to $\cos^4(\chi_i)$. From simple calculation leads the total conductivity tot to be proportional to the $\cos^4(\chi_1) \cos^4(\chi_2) / (\cos^4(\chi_1) + \cos^4(\chi_i))$, which shows good agreement with the NEGF results.

2.4.3 Response to Constant External Field

In order to describe the structural rearrangement process of the AN-OPE SAM, we use a (50×50) unit cell containing 2500 AN-OPE molecules. To describe the dynamics of such a large simulation cell, we developed a simplified nearest neighbor (NN) interaction Hamiltonian with the model parameters extracted from QM and Force Field (FF) energies (Figure 2.1). Important feature of the NN model is that the energetically favorable state changes from P to T as the external electric field increases, due to the higher dipole moment along $[0001]$ of the T phase. In this model, the critical field for which the energies of both states are same is $F_c = 0.56 \text{ V/\AA}$.

We simulated the response of the SAM of the P's to the 1.2 V/\AA external field during 1.2×10^6 Monte Carlo steps (MCS) at $T = 300 \text{ K}$. Figures 2.9a and 2.9b show the time evolution of the system starting with all P's and ending with all T's and the population change with the electrical conductivity change during this P-to-T transition, respectively. There were no T states until just before 55,184 MCS, but within the next 15 steps, half of the neighbors along $[11\bar{2}0]$ have transformed, and after another 15 steps the entire $[11\bar{2}0]$ line is transformed to the T. Then, by 405,907 MCS, totally 19 $[11\bar{2}0]$ lines have transformed, which are all neighbors to the original one. Then, at 486,389 MCS, we see that a second $[11\bar{2}0]$ swath has nucleated. By 697,272 MCS, these two have grown to 28 and 7 adjacent lines but still just two swathes, and from 697,273 MCS, they are merged into one swath. Finally, by 1,008,706 MCS the full system is transformed to T. Along with the decrease of the P population, the total conductivity through the SAM also decreases.

The analysis of the snapshots demonstrates that the time to complete the transformation of each line in $[11\bar{2}0]$ after initiation is 26.32 MCS, leading to the rate constant of propagation, $k_{[11\bar{2}0]} = 5.48 \text{ \AA/MCS}$. The $k_{[11\bar{2}0]}$ shows almost no dependence on the temperature (Figure 2.10a, top), which infers that the energy barrier for the propagation is zero or quite negligible. Thus, once one AN-OPE is switched as a nucleation, the transformation propagates quickly along the $[11\bar{2}0]$ line, which is quite reasonable in terms of the energetic stability of $\text{P}2\text{T}2_{11\bar{2}0}$ (Figure 2.1). Then, another nucleation occurs for subsequent transformation of another $[11\bar{2}0]$ line. Typically this subsequent transformation takes place right next to the precedent transformed line in the $[1\bar{1}00]$ direction.

Therefore, the nucleation is the key step governing the time scale of the transition. The middle panel of Figure 2.10a shows the probability, $P(t)$ of exhibiting no nucleation until time t . To obtain the nucleation time (τ) when we have a transformed $[11\bar{2}0]$ line already, the nucleation events initiated next to $[11\bar{2}0]$ line are analyzed among the snapshots. The nucleation process is found to be a Poisson process, in which $P(t)$ decays exponentially with time. The value of τ was obtained as 5,583 MCS by fitting of $P(t)$.

To obtain the nucleation time (τ_0) in the absence of $[11\bar{2}0]$ line, we carried out additional 50 simulations to find when the first P transforms to the T, showing that this process proceeds as a Poisson process with $\tau_0 = 274,193 \text{ MCS}$ that is ~ 50 time larger than τ (Figure 2.10a, bottom

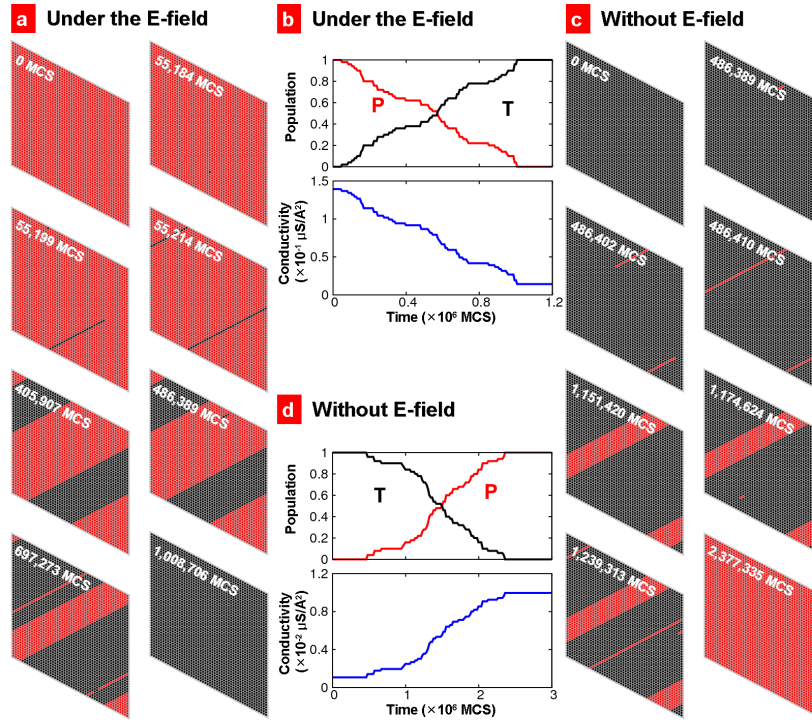


Figure 2.9: (a) Snapshots during P-to-T transition from MC simulation with $1.2 \text{ V}/\text{\AA}$ external field. The first nucleation is occurred at 55,184 MCS, then, the $[11\bar{2}0]$ line propagates until 55,214 MCS. More nucleation and propagation along $[11\bar{2}0]$ are taken place, and finally, the full system is transformed by 1,008,706 MCS. We note that increased bias voltage yields a faster P-to-T transition. (b) Time dependence of P and T populations and electrical conductivity through the SAM during P-to-T transition. (c) Snapshots during T-to-P transition from MC simulation without an external field. The first nucleation is occurred at 486,389 MCS, then, the $[11\bar{2}0]$ line propagates until 486,410 MCS. More nucleation and propagation along $[11\bar{2}0]$ are taken place, and finally, the full system is transformed by 2,377,335 MCS. (d) Time dependence of P and T populations and electrical conductivity through the SAM during T-to-P transition.

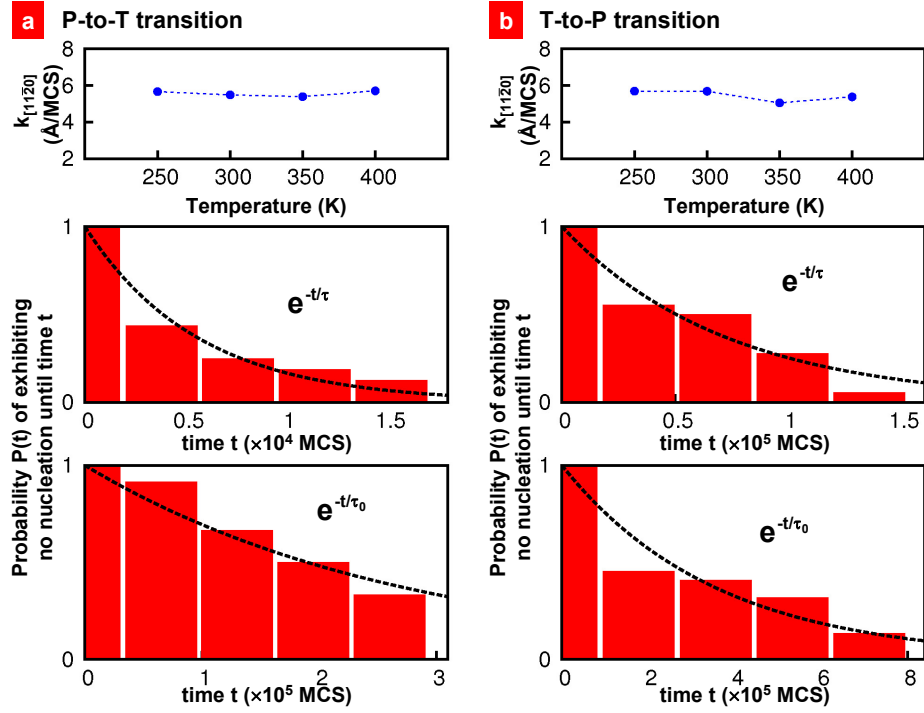


Figure 2.10: (a) P-to-T transition; (b) T-to-P transition; Top panels show the temperature dependence of the propagation rate along $[11\bar{2}0]$, $k_{[11\bar{2}0]}$. Middle panels show the probability, $P(t)$ of exhibiting no nucleation by time, t for the case when the nucleation is initiated next to another $[11\bar{2}0]$ line. The dotted lines is an exponential fit of $P(t)$. This leads to a nucleation rate of $\tau = 5,583$ MCS for the P-to-T transition and $\tau = 72,926$ MCS for the T-to-P transition. Bottom panels show the probability, $P(t)$ of exhibiting no nucleation by time, t for the case when the nucleation is initiated in the absence of next $[11\bar{2}0]$ line. The exponential fit leads to a nucleation rate of $\tau_0 = 274,193$ MCS for the P-to-T transition and $\tau_0 = 357,135$ MCS for the T-to-P transition.

panel).

Figures 2.9c and 2.9d show the time evolution of the system with no external field starting with all T's and ending with all P's and the population change with the electrical conductivity change during this T-to-P transition, respectively. The overall process is quite similar to that of P-to-T transition except for the detailed numbers. The first nucleation occurred at 486,389 MCS, and then, the neighbors along $[11\bar{2}0]$ showed fast transition to P within 21 MCS. While this swath is growing along $[1\bar{1}00]$ direction, the second and the third nucleation without next transformed line occurred at 1,174,624 MCS and 1,239,313 MCS, respectively. Finally, the full system is transformed to P by 2,377,335 MCS. During the transition, the total conductivity through the SAM increases along with the decrease of the P population.

During T-to-P transition, the average time to complete each line of $[11\bar{2}0]$ growth is 25.38 MCS, leading to $k_{[11\bar{2}0]} = 5.68 \text{ \AA}/\text{MCS}$ with no temperature dependency (Figure 2.10b, top panel).

The nucleation times are studied in the same manner with the P-to-T transition. The nucleation process follows Poisson process with the $\tau = 72,926 \text{ MCS}$ and $\tau_0 = 357,135 \text{ MCS}$ in the presence and the absence of the next transformed $[11\bar{2}0]$ line, respectively (Figure 2.10b, middle and bottom panels).

The interaction between P-T is smaller than the interaction between P-P or T-T by $\sim 8.6 \text{ kcal/mol}$ in average (Table 1), due to the loss of HB or less-favorable van der Waals interaction caused by the packing of two different conformations. This infers that the boundary of $[11\bar{2}0]$ line is energetically less stable, leading a fast transformation at the boundary. This well explains the smaller τ than τ_0 .

We also found τ during P-to-T transition is smaller than τ during T-to-P transition (which is responsible to that NDR is not shown during the backward sweep). This is because the formation of T-T HB network is accompanied with the expansion of $[11\bar{2}0]$ swath along $[1\bar{1}00]$ during the P-to-T transition, while the loss of T-T HB network is accompanied during the T-to-P transition.

2.4.4 NDR for Time Dependent Electric Field

Applying a time dependent external field, we calculated the response of the system to voltage sweeps at various sweep rates. For each sweep, the magnitude of the external field was increased linearly until $F = 1.4 \text{ V/\AA}$ (corresponding to 1.5 V bias voltage in forward sweep) and then it was decreased at the same rate until the field was 0 V/\AA (corresponding to 0 V bias voltage in backward sweep). (Appendix D discusses the conversion factor between the external electric field and the bias voltage.) The sweep rates were $1 \times 10^{-8} \text{ V/MCS}$, 4^{-8} V/MCS , and $2 \times 10^{-7} \text{ V/MCS}$. The resultant I - V curves are shown in Figure 2.11a. Although the current drops dramatically at sufficiently high voltage, similar for all cases, we found that faster sweep let the systems stay in the P phase at higher voltage, which is in a good agreement with the experimental observation. Clearly, the simulations

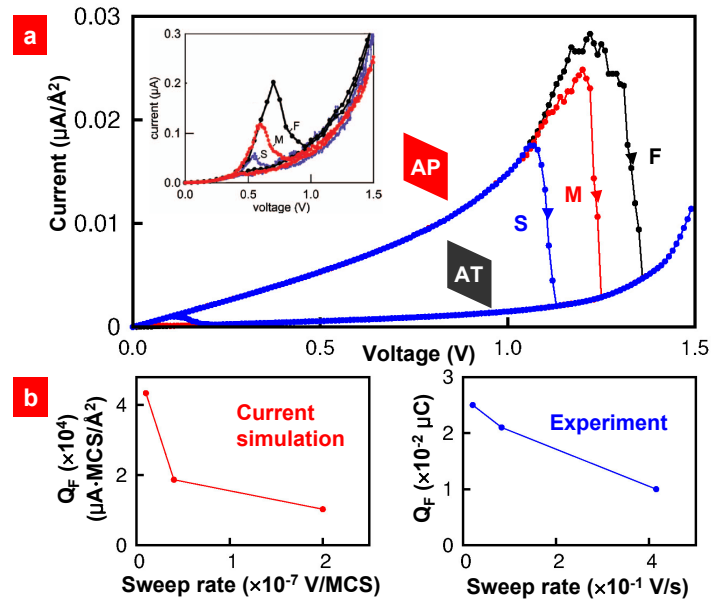


Figure 2.11: (a) Current-voltage ($I-V$) curves calculated at 300 K from MC simulations combined with the $I-V$ results of the Green's function calculations. Results for three sweeping rates are shown: S (blue line): 1×10^{-8} V/MCS, M (red line): 4×10^{-8} V/MCS, and F (black line): 2×10^{-7} V/MCS. Inset is the experimental $I-V$ curves from the reference [9] with 3 different sweeping rates: S (blue line) : 21 mV/sec, M (red line) : 83 mV/sec, and F (black line) : 415 mV/sec. (b) The sweep rate dependence of the integral of the current from the peak to the valley during NDR, Q_F from current simulation (left panel) and experiment [9] (right panel).

show both the NDR phenomena and hysteretic behavior with sweep rate dependence as observed experimentally.

We found that the P-to-T transition voltage is located at 1.1 – 1.4 V, depending on sweep rate. This can be compared to the experimental results in which the transition is completed by 0.6 to 1.0 V. During the backward sweep, the simulations found that the T state transforms back to P at ~ 0.2 V bias voltage with slower sweep rates.

To determine the total charge associated with the NDR region, we integrated the current from the peak to the valley in Figure 2.11a. This amount of charge (Q_F) flowing through the junction during NDR, is an important physical quantity that characterizes the QC model [9]. The calculated Q_F values are

- $Q_F = 4.34 \times 10^4 \mu\text{A}\cdot\text{MCS}/\text{\AA}^2$ ($\sim 1.76 \times 10^6 e/\text{AN-OPE}$), for sweep rates of 1×10^{-8} V/MCS,
- $Q_F = 1.87 \times 10^4 \mu\text{A}\cdot\text{MCS}/\text{\AA}^2$ ($\sim 7.57 \times 10^5 e/\text{AN-OPE}$), for sweep rates of 4×10^{-8} V/MCS, and
- $Q_F = 1.03 \times 10^4 \mu\text{A}\cdot\text{MCS}/\text{\AA}^2$ ($\sim 4.17 \times 10^5 e/\text{AN-OPE}$), for sweep rates of 2×10^{-7} V/MCS.

Figure 2.11b shows the sweep rate versus Q_F plots from the simulation (left panel) and from the experiment (right panel). The simulations reproduce the experimental observation that Q_F decreases with increasing sweep rate. Additionally, we find that changing the sweep rate by 20 times only changes the Q_F by 4.2 times, which is comparable to the experimental observation that the Q_F varies 2.5 times while the sweep rate changes by ~ 20 times [9].

The NDR peak from the MC simulations leads to a voltage range of ~ 0.15 V while the experimental NDR range is ~ 0.25 V. One issue is the time scale. Our MC sweep frequency was $\sim 10^{-7}$ V/MCS whereas experimental sweep frequency is $\sim 10^{-1}$ V/s. To convert from MCS to second, we compared the initial nucleation rate expressed in MCS to that expected from the transition state theory using the predicted barrier in kcal/mol. The result is 1 MCS equals $\sim 10^{-13}$ s (see Appendix A.), indicating the theoretical sweep frequency $\sim 10^6$ times the experimental sweep frequency. This faster sweep should decrease the NDR range. In addition, the small size of our periodic cell, 1620 nm^2 , compared to the experiment of $O(\text{cm}^2)$ would also tend to decrease the NDR range.

A limitation in our MC simulations is that we idealized the degrees of freedom for the molecules into two states, which consider as the perfectly crystallized phases where an infinite AN-OPEs are connected through the HB network. In order to investigate the effect of molecular fluctuations, we performed a series of MD simulations with a (10×10) unit cell (100 independent AN-OPE molecules). The MD simulations account for two aspects missing from the MC simulations:

1. The AN-OPE is allowed to have a distribution of conformations, accounting for the much lower current for χ near 90° while losing the HB network at high fields. This distribution in χ leads

to decreased current at a given voltage, leading to a lower slope in the higher-field due to the larger $\Delta\Phi_B$.

2. The AN-OPE forms a partially disordered phase with some HB along $[10\bar{1}0]$ in the low field (Appendix B). The loss of the HB network at high field decreases the hysteresis during the backward sweep since the loss of HB in the high field decreases the T-to-P transition barrier.

In addition, we found that once a disordered area is developed, it does not easily recover the P phase; hence, the development of a disordered part on the SAM yields less dramatic changes in conductivity. The experimental observation of slight current decrease with successive sweeps may result from the expansion of the disordered area during the sweep cycles.

In order to validate the suggested mechanism for NDR for AN-OPE, we investigated the possibility of NDR from the system N-OPE which contains no NH_2 group and the bare B-OPE containing no functional group. We found that the N-OPE system shows NDR behavior very similar to AN-OPE, in agreement with experiment [37]. However, we found no NDR behavior for B-OPE, also in agreement with experiment (Appendix C).

2.5 Conclusions

Summarizing, we find that a coarse-grained model based on parameters from first principles calculations leads to a mechanism for room temperature hysteretic NDR that is in qualitative agreement with experiments on AN-OPE, N-OPE, and B-OPE. This provides a plausible mechanism for understanding this phenomena which may be useful in developing new NDR systems.

2.6 Acknowledgments

The computational work was initiated with support by the National Science Foundation (NIRT, WAG). The collaboration was supported by the Microelectronics Advanced Research Corporation (MARCO, WAG and RAK) and its Focus Centers on Functional Engineered NanoArchitectonics (FENA). The facilities of the MSC (WAG) were supported by ONR-DURIP, ARO-DURIP and the facilities of the CNBT lab (SSJ) were supported by the start-up from the MSE in Georgia Tech.

Bibliography

- [1] Esaki, L. *Phys. Rev.* **1958**, 109, 603-604.
- [2] Xue, Y. Q.; Datta, S.; Hong, S.; Reifenberger, R.; Henderson, J. I.; Kubiak, C. P. *Phys. Rev. B* **1999**, 59, R7852-R7855.
- [3] Tao, N. J. *Nat. Nanotechnol.* **2006**, 1, 173-181.
- [4] Chen, J.; Reed, M. A.; Rawlett, A. M.; Tour, J. M. *Science* **1999**, 286, 1550-1552.
- [5] Selzer, Y.; Salomon, A.; Ghabboun, J.; Cahen, D. *Angew. Chem. Int. Ed.* **2002**, 41, 827.
- [6] Pitters, J. L.; Wolkow, R. A. *Nano Lett.* **2006**, 6, 390-397.
- [7] He, J.; Lindsay, S. M. *J. Am. Chem. Soc.* **2005**, 127, 11932-11933.
- [8] Salomon, A.; Arad-Yellin, R.; Shanzer, A.; Karton, A.; Cahen, D. *J. Am. Chem. Soc.* **2004**, 126, 11648-11657.
- [9] Kiehl, R. A.; Le, J. D.; Candra, P.; Hoyer, R. C.; Hoyer, T. R. *Appl. Phys. Lett.* **2006**, 88, 172102.
- [10] Guisinger, N. P.; Yoder, N. L.; Hersam, M. C. *Proc. Nat. Acad. Sci. U.S.A.* **2005**, 102, 8838-8843.
- [11] Kratochvilova, I.; Kocirik, M.; Zambova, A.; Mbindyo, J.; Mallouk, T. E.; Mayers, T. S. *J. Mater. Chem.* **2002**, 12, 2927-2930.
- [12] Rawlett, A. M.; Hopson, T. J.; Nagahara, L. A.; Tsui, R. K.; Ramachandran, G. K.; Lindsay, S. M. *Appl. Phys. Lett.* **2002**, 81, 3043-3045.
- [13] Amlani, I.; Rawlett, A. M.; Nagahara, L. A.; Tsui, R. K. *Appl. Phys. Lett.* **2002**, 80, 2761-2763.
- [14] Donhauser, Z. J.; Mantooth, B. A.; Kelly, K. F.; Bumm, L. A.; Monnell, J. D.; Stapleton, J. J.; Price, D. W.; Rawlett, A. M.; Allara, D. L.; Tour, J. M.; Weiss, P. S. *Science* **2001**, 292, 2303-2307.
- [15] Fan, F. R. F.; Lai, R. Y.; Cornil, J.; Karzazi, Y.; Bredas, J. L.; Cai, L. T.; Cheng, L.; Yao, Y. X.; Price, D. W.; Dirk, S. M.; Tour, J. M.; Bard, A. J. *J. Am. Chem. Soc.* **2004**, 126, 2568-2573.

- [16] Seminario, J. M.; Zacarias, A. G.; Tour, J. M. *J. Am. Chem. Soc.* **2000**, 122, 3015-3020.
- [17] Xiao, X. Y.; Nagahara, L. A.; Rawlett, A. M.; Tao, N. J. *J. Am. Chem. Soc.* **2005**, 127, 9235-9240.
- [18] Reed, M. A.; Chen, J.; Rawlett, A. M.; Price, D. W.; Tour, J. M. *Appl. Phys. Lett.* **2001**, 78, 3735-3737.
- [19] Chen, J.; Wang, W.; Reed, M. A.; Rawlett, A. M.; Price, D. W.; Tour, J. M. *Appl. Phys. Lett.* **2000**, 77, 1224-1226.
- [20] Sollner, T. C. L. G.; Goodhue, W. D.; Tannenwald, P. E.; Parker, C. D.; Peck, D. D. *Appl. Phys. Lett.* **1983**, 43, 588-590.
- [21] Tsuchiya, M.; Sakaki, H.; Yoshino, J. *Jpn. J. Appl. Phys., Part 2-Letters* **1985**, 24, L466-L468.
- [22] Qiu, X. H.; Nazin, G. V.; Ho, W. *Phys. Rev. Lett.* **2004**, 93, 4.
- [23] Akdim, B.; Pachter, R. *J. Phys. Chem. C* **2008**, 112, 3170-3174.
- [24] Troisi, A.; Ratner, M. A. *Nano Lett.* **2004**, 4, 591-595.
- [25] Emberly, E. G.; Kirczenow, G. *Phys. Rev. B* **2001**, 64, 125318.
- [26] Galperin, M.; Ratner, M. A.; Nitzan, A. *Nano Lett.* **2005**, 5, 125-130.
- [27] Kresse, G.; Furthmüller, J. *Phys. Rev. B* **1996**, 54, 11169-11186.
- [28] *Jaguar*, V. 6.5 ed.; Schrödinger Inc.: Portland, 2005.
- [29] Kim, Y. H.; Jang, S. S.; Jang, Y. H.; Goddard, W. A. *Phys. Rev. Lett.* **2005**, 94, 156801.
- [30] Schultz, P., *SeqQuest Project*; Sandia National Laboratories: Albuquerque, NM, 2003.
- [31] Mayo, S. L.; Olafson, B. D.; Goddard, W. A. *J. Phys. Chem.* **1990**, 94, 8897-8909.
- [32] Plimpton, S. J. *J. Comput. Phys.* **1995**, 117, 1-19.
- [33] Plimpton, S. J.; Pollock, R.; Stevens, M. *The Eighth SIAM Conference on Parallel Processing for Scientific Computing Minneapolis*; 1997.
- [34] Swope, W. C.; Andersen, H. C.; Berens, P. H.; Wilson, K. R. *J. Chem. Phys.* **1982**, 76, 637-649.
- [35] Lo, W. S.; Pelcovits, R. A. *Phys. Rev. A* **1990**, 42, 7471-7474.
- [36] Stokbro, K.; Taylor, J.; Brandbyge, M.; Ordejón, P.; *Ann. N Y. Acad. Sci.* **2003**, 1006, 212-216.
- [37] Candra, P. M.S. Dissertation, University of Minnesota, 2006.

Chapter 3

Free Energy Barrier for Molecular Motions in Bistable [2]Rotaxane Molecular Electronic Devices

Reproduced with permission from Kim, H; Goddard, W. A.; Jang S. S.; Dichtel, W. R.; Heath, J. R.; and Stoddart J. F. J. Phys. Chem. A 2009, 113, 2136. Copyright 2009 American Chemical Society.

3.1 Abstract

Donor-acceptor binding of the π -electron-poor cyclophane cyclobis(paraquat-*p*-phenylene) (CBPQT⁴⁺) with the π -electron-rich tetrathiafulvalene (TTF) and 1,5-dioxynaphthalene (DNP) stations provides the basis for electrochemically switchable, bistable [2]rotaxanes, which have been incorporated and operated within solid state devices to form ultradense memory circuits [1, 2] and nanoelectromechanical systems. The rate of CBPQT⁴⁺ shuttling at each oxidation state of the [2]rotaxane dictates critical write-and-retention time parameters within the devices, which can be tuned through chemical synthesis. To validate how well computational chemistry methods can estimate these rates for use in designing new devices, we used molecular dynamics simulations to calculate the free energy barrier for the shuttling of the CBPQT⁴⁺ ring between the TTF and the DNP. The approach used here was to calculate the potential of mean force along the switching pathway, from which we calculated free energy barriers. These calculations find a turn-on time after the rotaxane is doubly oxidized of $\sim 10^{-7}$ s (suggesting that the much longer experimental turn-on time is determined by the time scale of oxidization). The return barrier from the DNP to the TTF leads to a predicted lifetime of 2.1 s, which is compatible with experiments.

3.2 Introduction

The electrochemically switchable, bistable [2]rotaxanes [1] (Figure 3.1) developed in recent years by Stoddart and co-workers exhibit two distinct co-conformations [3, 4, 5, 6, 7]: the ground-state co-conformation, in which the cyclobis(paraquat-*p*-phenylene) (CBPQT⁴⁺) encircles the tetrathiafulvalene (TTF) station, and the metastable state co-conformation, in which the CBPQT⁴⁺ encircles the 1,5-dioxynaphthalene (DNP) station [2, 8, 9, 10, 11, 12, 13, 14, 15]. The population of the two co-conformations may be shifted away from equilibrium by temporarily oxidizing one or two electrons from the TTF units. This switching process forms the basis of using these compounds as storage elements in molecular electronic devices. Consequently, significant experimental efforts have been made to investigate the switching behavior of molecular switches [5, 6, 16, 17, 18, 19, 20, 21, 22, 23] and molecular machines [24, 25, 26, 27, 28, 29] in various environments, such as solution [5, 6, 30, 31, 32, 33, 34, 35, 36, 37], polymer electrolyte gels [38], metal surfaces [39, 40, 41] and devices [7, 16, 17]. Important experimental evidence [15] for molecular switching in these devices was the correlation of the kinetics of relaxation from the DNP to the TTF, across each of these environments. However, the rate of this process is also a function of the molecular structure, suggesting that longer storage times, or even nonvolatile memory, might be possible with the appropriate molecular design.

Computation chemistry calculations could provide an effective approach for optimizing the performance of such molecular switches, but such applications require that the accuracy of the theory be validated by comparing to well-documented experimental results. The purpose of this paper is to provide such validation. Previously, we investigated these compounds using a multiscale first principles approach combining quantum mechanics (QM) and atomistic force field (FF) methods [42, 43, 44, 45, 46, 47]. First we considered the molecules as individual species, and then we examined self-assembled monolayers bound to gold surfaces or compressed into Langmuir monolayers at the air-water interface. These studies successfully predicted a number of phenomena that were confirmed later experimentally, including the higher conductivity [47] of the DNP relative to the TTF, and the increased stability of the TTF relative to the DNP (by 2.0 kcal/mol from QM, 2.3 kcal/mol from the FF, and 1.4 – 1.6 kcal/mol from experiment) [15, 43]. In addition, on the basis of the predicted footprint of the 115 Å²/molecule for the self-assembled structure, we predicted that the surface tension of the TTF is 32 % lower than that of the DNP, an observation that was confirmed in subsequent experiments [43, 44].

In this study, we evaluated the free energy profile of the shuttling motion of the CBPQT⁴⁺ ring between the TTF and the DNP stations to determine how the nature of the rotaxane affects the switching and relaxation rates. These rates have been determined experimentally in various environments [15, 35, 40, 48], and we now want to understand the structural contributions to these

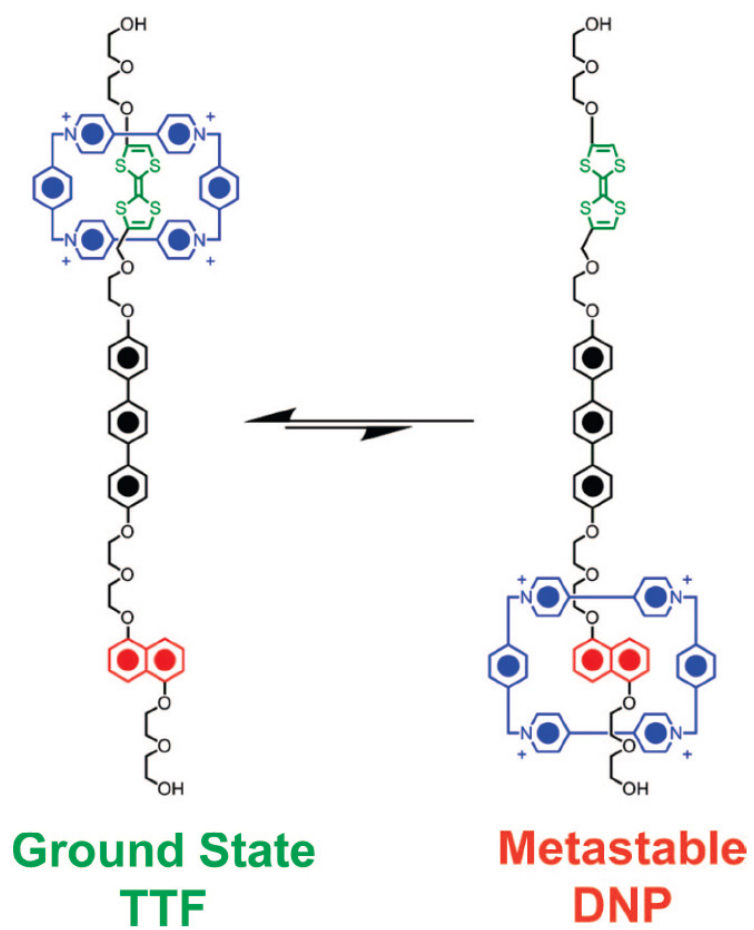


Figure 3.1: Structural formula of the two co-conformations of a bistable [2]rotaxane fragment used in this study.

rates. We seek to find a level for theoretical calculations of these rates that is both accurate and fast so that we can use theory to optimize the structural characteristics to achieve desired rates.

Rather than finding the energy barrier for a minimized reaction path connecting the two states, we used potential of mean force (PMF) to evaluate the change of free energy along the shuttling pathway of the CBPQT⁴⁺ ring between the TTF and the DNP so that we can determine the rates at the experimental temperature. We carried out these calculations for three oxidation states of the molecule relevant to the switching and thermally activated relaxation process.

3.3 Simulation Details

3.3.1 Potential of Mean Force from Constrained Molecular Dynamics Simulation

The experimental time scale for the ring to relax back from the DNP to the TTF is $10^{-1} - 10^3$ seconds [15, 34, 49], suggesting that simple molecular dynamics (MD) simulation of a few hundred nanoseconds might not be sufficiently ergodic to provide an accurate transition rate. Hence, we adopted the ‘‘Blue Moon sampling’’ technique [50, 51] of constrained MD simulations using holonomic constraints that fix the systems along the reaction coordinate. To determine the free energy barrier, we used the reaction-coordinate (R)-dependent potential of mean force (PMF), $F_{\text{rxn}}(R)$ defined as the integration of the mean force (MF) along the reaction coordinate, $-dF_{\text{rxn}}(R) dR$ [52],

$$F_{\text{rxn}}(R) = F_{\text{rxn}}(\infty) + \int_{\infty}^R \frac{dF_{\text{rxn}}(R')}{dR'} dR'. \quad (3.1)$$

Here, the MF is a measurable quantity from our simulations. To calculate the MF, we assumed that the CBPQT⁴⁺ ring moves between the TTF and the DNP along the backbone of the rotaxane (Figure 3.2a), which we assume to be in an extended conformation but with the minimized structure. This extended conformation should provide the fastest shuttling motion of the CBPQT⁴⁺ ring, being governed mainly by its interaction with the backbone. This MF does not account for the presence of folded chain conformations, so that the PMF may lack some contributions from conformational entropy.

First, we prepared the extended rotaxane backbone without the CBPQT⁴⁺ ring using quantum mechanical geometry optimization at the level of B3LYP/6-31G* (Figure 3.2a). Then, we added and optimized the CBPQT⁴⁺ ring at various fixed points on the fixed extended backbone (Figure 3.2b) using quantum mechanics. Thus, the atomic partial charges of all atoms are allowed to readjust, depending on the relative position of the charge acceptor (CBPQT⁴⁺) with respect to the charge donor (TTF and DNP).

To obtain the change of the PMF during the shuttling process, we first evaluated the MF as a

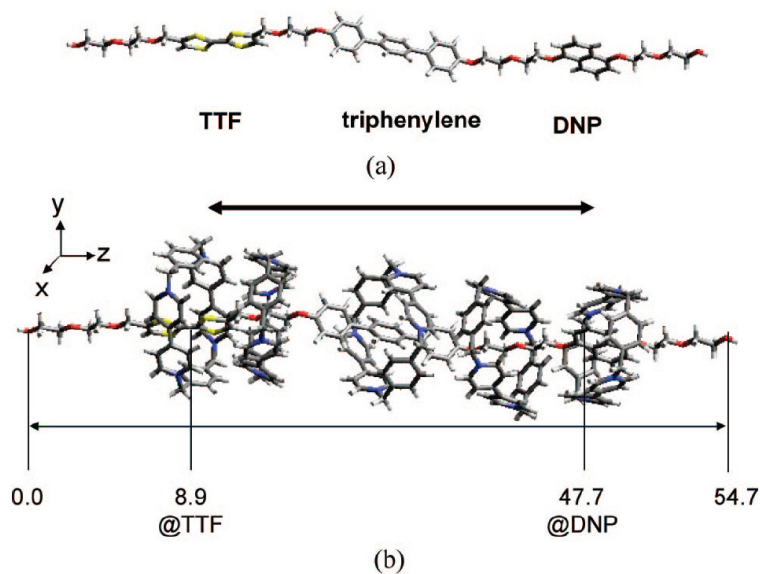


Figure 3.2: (a) Backbone of the rotaxane molecule simulated in this study. (b) CBPQT⁴⁺ ring positions along the backbone (unit: Å).

function of the position of the CBPQT⁴⁺ ring. Because the length of the backbone is 54.7 Å and the distance between the TTF and the DNP is 36.9 Å, we chose to sample the dynamics for nine independent samples, each of which has the z -coordinate (along the backbone) of the center of mass (COM) of the CBPQT⁴⁺ ring at a different position along the extended backbone, as schematically presented in Figure 3.3. Using quantum mechanics, the geometry and atomic charges were obtained from each of these nine cases.

After preparing these nine initial structures, we prepared two more structures beyond each station of the TTF and the DNP with identical charges to the CBPQT⁴⁺@TTF case and the CBPQT⁴⁺@DNP case, respectively. In addition, we constructed another ten structures in which the position and charges of the CBPQT⁴⁺ ring were calculated by arithmetically averaging the coordinates and charges of two consecutive structures in the eleven structures. Thus, a total of 21 structures were prepared for simulations.

Then, to simulate both the turning on and turning off the rotaxane switch, we investigated the effect of oxidation of rotaxane molecule on the free energy profile, for three different oxidation states: the neutral state, the +1 oxidation state, and the +2 oxidation state.

The QM calculations of the charges for the nine different structures were repeated for each of the three oxidation states: 0, +1, and +2. The atomic partial charge distributions are tabulated in the Appendix E (Tables E.1, E.2, and E.3).

All quantum mechanical computations in this study were performed using Jaguar [53].

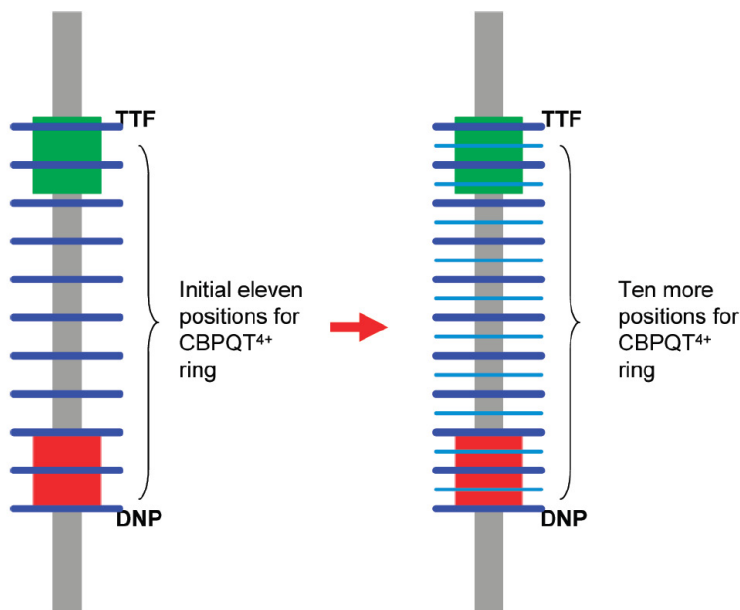


Figure 3.3: Charges for the initial nine structures obtained from QM with Mulliken analysis. In addition, we included two more structures beyond each station of the TTF and the DNP, using charges identical to those for the equilibrium $\text{CBPQT}^{4+}@\text{TTF}$ and $\text{CBPQT}^{4+}@\text{DNP}$ cases, respectively. Ten more structures were generated on the basis of these eleven structures. The position of the CBPQT^{4+} ring for each additional structure was obtained using the arithmetic average of the two adjacent cases from the eleven structures. The charges were also averaged.

3.3.2 Constrained Molecular Dynamics Simulation

Next, we carried out a constrained NVT MD simulation at 300 K for 500 ps to equilibrate each system. This MD was then continued for an additional 3 ns at 300 K (constrained NVT MD) to compute the MF. The constraint was introduced using Gauss' principle of least constraints [54] to fix only the z -component of the center of mass (COM) of the CBPQT^{4+} ring parallel to the molecular axis direction (z -axis direction as in Figure 3.2b). To ensure that our constrained dynamics produces the correct equilibrium averages without bias due to ensemble sampling, we used Fixman's theorem [55] to evaluate the metric effect originating from the holonomic constraints. We determined that the metric effect only adds a constant scalar value to the absolute free energy values, which has no influence on the relative energetics. (Details are in the Appendix F.)

We also fixed the position of the last oxygen atom at each end of the backbone to retain the extended conformation. This restricts the conformational flexibility of the system, which suppresses conformational entropic contributions to the free energy. The mean force was sampled from such constrained MD simulations.

3.3.3 Force Field and MD Parameters

We used the generic DREIDING force field [56], which was found to lead to accurate results in our previous studies on rotaxane systems [43, 44, 45]. It was also successful in our studies on various other molecular systems, such as the hydrated polymer electrolyte membranes [57, 58, 59] and the surfactant-mediated air-water interface [60, 61].

The force field has the form

$$E_{\text{total}} = E_{\text{vdW}} + E_{\text{Q}} + E_{\text{bond}} + E_{\text{angle}} + E_{\text{torsion}} + E_{\text{inversion}}, \quad (3.2)$$

where E_{total} , E_{vdW} , E_{Q} , E_{bond} , E_{angle} , E_{torsion} , and $E_{\text{inversion}}$ are the total energies, the van der Waals, electrostatic, bond stretching, angle bending, torsion, and inversion energy components, respectively, and the force field parameters are described in the original papers [56]. The atomic charges were obtained from a QM Mulliken population analysis as indicated above.

All MD simulations were performed using LAMMPS (large-scale atomic/molecular massively parallel simulator) MD code from Plimpton at Sandia [62, 63]. The equations of motion were integrated using the velocity-Verlet algorithm [64], with a time step of 0.01 fs. This unusually small time step was to ensure high quality sampling of phase space by avoiding abrupt changes in atomic positions.

The temperature was kept constant during the MD using the Berendsen thermostat with temperature damping time of 0.01 fs. To demonstrate that our MD leads to a proper canonical ensemble, the probability distribution function (PDF) of kinetic energy $\text{KE} (= mv^2/2)$ is shown in Figure 3.4. The PDF is quite close to the Maxwell-Boltzmann distribution of energy at $T = 300$ K, indicating that the simulation describes a proper canonical ensemble. Furthermore, the PDF for each component of velocity is the same and the system obeys the equipartition theorem (Figure 3.5).

Figure 3.6 shows the typical behavior of the MF as a function of simulation time for two representative systems: one is the ground state, $\text{CBPQT}^{4+}@\text{TTF}$, green color, denoted as TTF and the other is the metastable state, the CBPQT^{4+} ring on the DNP, red color, denoted as DNP. This shows that the mean force was well equilibrated for both cases.

The weakness of this blue moon sampling method is that the error in each MF measurement is integrated to obtain the PMF profile along the reaction coordinate. From block averages, we estimate the uncertainty of the MF values to be 0.04 kcal/mol/Å for $\text{CBPQT}^{4+}@\text{TTF}$ and 0.22 kcal/mol/Å for $\text{CBPQT}^{4+}@\text{DNP}$. Assuming that these errors are random and that the average value is 0.13 kcal/mol/Å, we estimate that the error of the free energy difference between two stations is $38.8 \times 0.13 / (20)^{1/2} = 1.13$ kcal/mol from integrating over the 38.8 Å distance. Similarly the error of the barrier from the DNP toward the TTF is $25.5 \times 0.13 / (14)^{1/2} = 0.89$ kcal/mol from the integration over the 25.5 Å distance. Hence, the small errors in the MF values can lead to

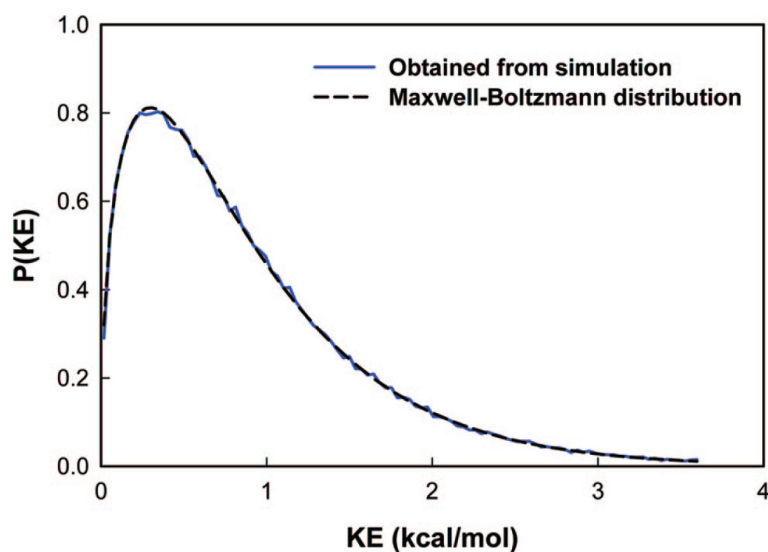


Figure 3.4: Probability density function of kinetic energy $KE (= mv^2/2)$ is from the MD simulation of the CBPQT⁴⁺ ring@TTF (blue line) at 300 K. Here the time step was 0.01 fs and the total simulation time was 3 ns after 500 ps of equilibration. The black dashed line compares with the Maxwell-Boltzmann distribution of the energy, $2 \left(KE/\pi (k_B T)^3 \right)^{1/2} \exp(-KE/k_B T)$, for $T = 300$ K.

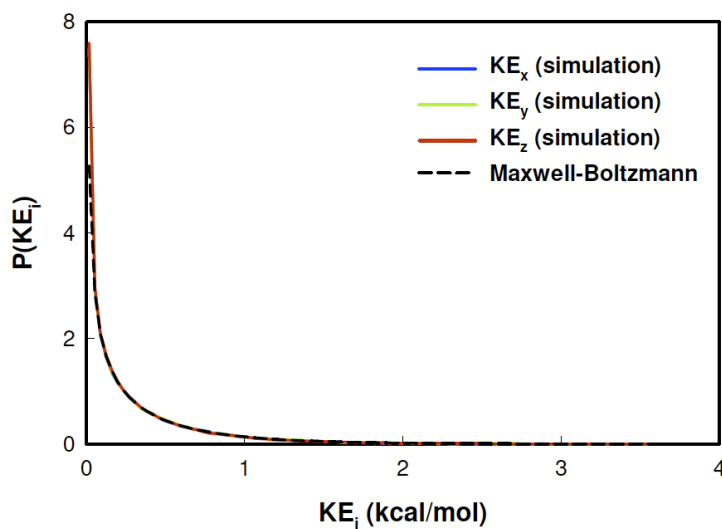


Figure 3.5: Probability density function of $KE_x (= mv_x^2/2)$; (blue line), $KE_y (= mv_y^2/2)$; (green line), and $KE_z (= mv_z^2/2)$; (red line) are computed from the MD simulation of the CBPQT⁴⁺ ring@TTF (blue line), which are identical to each other. These are compared with the Maxwell-Boltzmann distribution of KE_i , $\sqrt{1/(\pi KE_i k_B T)} \exp(-KE_i/k_B T)$ at 300 K. ($i \in \{x, y, z\}$); black dashed line)

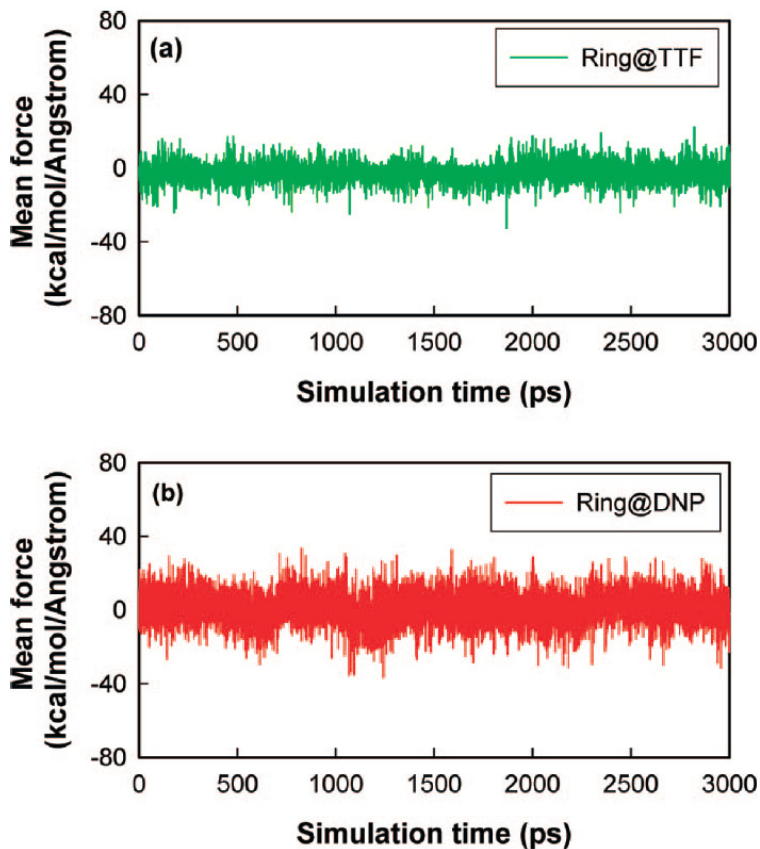


Figure 3.6: Change of mean force as a function of simulation time. In each case this follows 500 ps of equilibration time. This plot shows two representative cases: the CBPQT⁴⁺ ring@TTF (TTF) and the CBPQT⁴⁺ ring@DNP (DNP).

substantial errors in the PMF value. However, previous studies that carefully compare various PMF calculation methods show that constraint-biased sampling to determine mean forces is one of the best methods to obtain reasonable PMF values, even though, statistically, they contain large error bars [52].

3.4 Results and Discussion

3.4.1 Charge Scheme: Adiabatic Approximation

We expected that no set of fixed charges scheme would be adequate enough to describe the electrostatic interactions as the highly charged ring is moved along the backbone. Thus, as described in Section 3.3.1, we obtained atomic charges from independent QM at each position as the ring is moved along the backbone.

This assumption of adiabatically adjusted charges assumes that charge re-distribution is much faster than the time for the ring to travel along the backbone. To test the effect of these charge

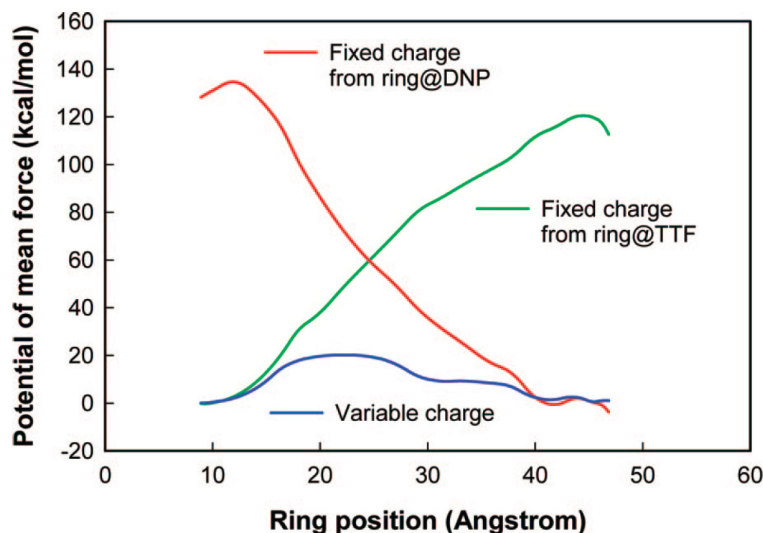


Figure 3.7: Change of potential of mean force as a function of ring position along the backbone. The blue curve allows the charge to change adiabatically as the ring moves along the dumbbell, which is the reliable result. The other two curves show the error obtained when the charges are fixed: the green curve uses fixed charges from the ring@TTF; the red curve uses a fixed charge from the ring@DNP.

re-adjustments on the PMF, Figure 3.7 shows the PMF based on three different charge schemes for the neutral rotaxane system: the green curve was obtained using the fixed charges from the ring@TTF, the red curve was obtained using the fixed charges from the ring@DNP, and the blue curve was obtained using adiabatic charges.

Clearly, the green and red curves are biased to have a minimum PMF at the position for which the charge was calculated, leading to very bad estimates of the barrier. In contrast, the energy barrier between the TTF and the DNP sites, based on the adiabatic charges, is consistent with experimental observations. Thus, we used the adiabatic charges for all oxidation states from the neutral state to the +2 state.

3.4.2 Free Energy Profiles from PMF Calculations

Sampling the MFs from the constrained MD simulations (Figure 3.8a) and integrating them along the ring position, we calculated the profile of the PMF for the shuttling motion of the CBPQT⁴⁺ ring (Figure 3.8b). We found that each oxidation state (neutral state (0), oxidized states (+1 and +2)), leads to significantly different profiles.

3.4.2.1 ΔG_{T2D}

We calculated that the most stable complex for the neutral state (black) is CBPQT⁴⁺@TTF (ring at 8.9 Å) whereas the CBPQT⁴⁺@DNP state (ring at 47.7 Å) is less stable than the TTF by

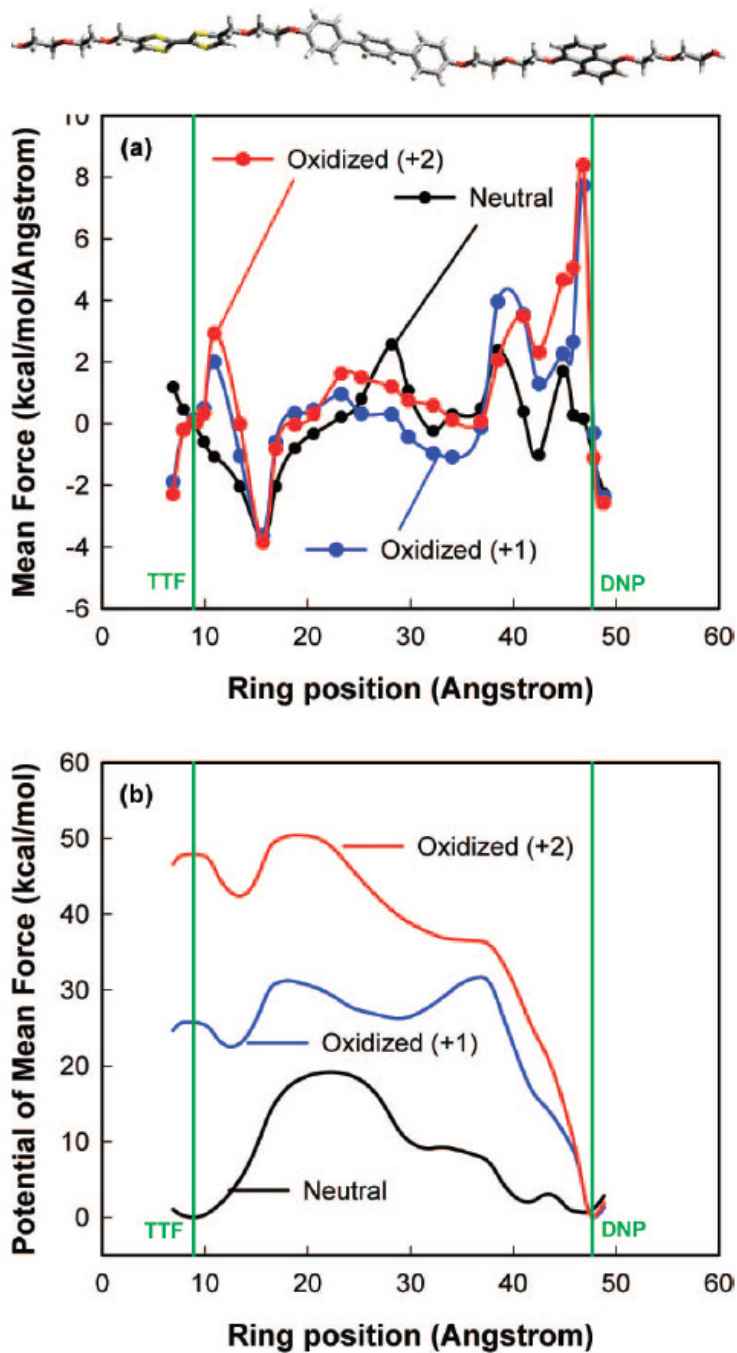


Figure 3.8: (a) Change of the mean force as a function of ring position along the backbone. (b) Change of the potential of mean force as a function of ring position along the backbone. The green vertical lines denote the ring@TTF (8.90 Å) and ring@DNP (47.70 Å).

$\Delta G_{\text{T2D}} = 1.0$ kcal/mol. This agrees with various experiments, which lead to $\Delta G_{\text{T2D}} = 1.4 - 1.6$ kcal/mol [15, 65, 66, 67, 68] on the basis of the difference in the binding free energies of the individual components of the rotaxane in the MeCN solvent. In addition, this calculation agrees with our previous computations from QM ($\Delta G_{\text{T2D}} = 2.0$ kcal/mol) [43] and Hessian-based FF calculations ($\Delta G_{\text{T2D}} = 2.3$ kcal/mol) [43]. We emphasize here that all previous experimental and theoretical studies studied ΔG_{T2D} by comparing the binding free energy of the TTF derivatives with the CBPQT⁴⁺ ring and the binding free energy of the DNP derivatives with the CBPQT⁴⁺ ring. Thus, our current calculation is the first direct measurement of the ΔG_{T2D} on a complete rotaxane.

3.4.2.2 $\Delta G_{\text{T2D}}^{\ddagger}$ and $\Delta G_{\text{D2T}}^{\ddagger}$ for Neutral Case

We calculate that the free energy barrier is $\Delta G_{\text{T2D}}^{\ddagger} = 19.03$ kcal/mol from the TTF toward the DNP, and $\Delta G_{\text{D2T}}^{\ddagger} = 18.03$ kcal/mol in the opposite direction. The relaxation barrier in the neutral state was measured for a similar bistable [2]rotaxane in which the triphenylene spacer was missing, leading to [15] (see Table 3.1)

- $\Delta G_{\text{D2T}}^{\ddagger} = 16.2$ kcal/mol ($\tau \sim 0.095$ s) in MeCN solvent,
- $\Delta G_{\text{D2T}}^{\ddagger} = 18.1$ kcal/mol ($\tau \sim 2.4$ s) in a MeCN/polymethylmethacrylate/propylene carbonate/LiClO₄ polymer matrix containing weight ratios of 70:7:20:3, and
- $\Delta G_{\text{D2T}}^{\ddagger} = 22.21$ kcal/mol ($\tau \sim 2.5 \times 10^3$ s) in the molecular switch tunnel junction.

In addition, the devices fabricated with this derivative containing the triphenylene spacer exhibit a relaxation half-life of $\tau \sim 90$ min [2] ($\Delta G_{\text{D2T}}^{\ddagger} = 22.66$ kcal/mol).

In addition, our free energy barrier is quite comparable to the barriers to circumrotation of [2]catenanes. Leigh and co-workers used NMR to determine ΔG^{\ddagger} of interlocked catenane molecules as 11 – 20 kcal/mol for various solvents and calculated the free energy barrier as 10 – 20 kcal/mol using force-field based Hessians [69, 70, 71].

Although our simulations were performed in the gas phase, the $\Delta G_{\text{D2T}}^{\ddagger}$ of 18 kcal/mol agrees well with the experimental barriers (17 – 22 kcal/mol) [15, 34, 49] for a variety of environments. This suggests that the energy barrier does not depend strongly on environment.

We did not include the counterions in this study because preliminary calculations showed that the charges would sometimes change in erratic ways due to the floppy energy landscape for the countercharges. Indeed, the good agreement with experiment for the barriers suggests that the instantaneous changes in the potential due to counterions can be neglected.

3.4.2.3 $\Delta G_{\text{T2D}}^\ddagger$ and $\Delta G_{\text{D2T}}^\ddagger$ for Oxidized Cases

Although the neutral state prefers to have the CBPQT⁴⁺ ring at the TTF, we find that the +1 and +2 oxidized states lead to a completely different energy profile (Figure 3.8b). In both cases, the DNP becomes the global minimum with the TTF destabilized by $\Delta G = 25.75$ kcal/mol for the +1 oxidation state and $\Delta G = 47.78$ kcal/mol for the +2 oxidation state.

Starting with the ring at the TTF site and oxidizing, we find that the ring moves first by ~ 5 Å to a local minimum on the ethylene oxide linker (with an energy decrease by $\Delta G = 3.25$ kcal/mol for the +1 and $\Delta G = 5.49$ kcal/mol for the +2). Then, it has a free energy barrier of $\Delta G = 8.70$ kcal/mol (+1 state) or 8.02 kcal/mol (+2 state) to continue past the triphenylene spacer and toward the DNP for oxidation states.

Using the Eyring rate equation [$1/\tau = (k_B T/h) \exp(-\Delta G^\ddagger/RT)$], the time required to overcome this barrier to move onto the DNP is 2.9×10^{-7} s for the +1 oxidation state and 9.0×10^{-8} s for the +2 oxidation state. It would be interesting to design an experiment to probe for this predicted barrier. It has been assumed that the huge Coulomb potential of the +4 ring with the +2 TTF would preclude a barrier. The origin of this barrier in the oxidized state is discussed below, which we find arises from the triphenylene spacer. We expect that there would be no barrier without this spacer.

Relative to the final state of the ring at the DNP site, the energy at the ethylene oxide linker (EO) near the TTF site is 22.52 kcal/mol higher (+1 oxidation), leading to a Boltzmann population of 10^{-17} . For the +2 oxidation state, the energy is 42.41 kcal/mol higher, leading to a population of 10^{-32} . Thus, for oxidation states +1 and +2, we expect the CBPQT⁴⁺ ring to stay on the DNP site until the system is reduced.

Indeed, there is an experimental estimate of this reverse barrier. Using a modified AFM with the ring attached, Brough *et al.* [72] measured the force exerted on the ring shuttling from the DNP to the TTF in the +2 oxidized system as 145 pN. Combining this experimental data with results from molecular mechanics simulations, they estimated the energy barrier to be 65 kcal/mol. This can be compared to our calculated barrier of 50.4 kcal/mol energy, validating the accuracy of the experiment. The maximum force measured in our simulation during the ring shuttling is 583 pN, which is similar to the experimental value of 145 pN.

3.4.2.4 Effect of Coulombic Energy and van der Waals Energy

To understand why the PMF profiles are so different between the neutral, +1, and +2 oxidation states, we calculated the change in the Coulombic interaction energy and the van der Waals (vdW) interaction energy as a function of ring position along the backbone, for these three oxidation states (Figures 3.9 and 3.10).

Table 3.1: Free Energy Barriers, Rate Constants, and Relaxation Half-Lives from DNP toward TTF (DNP \rightarrow TTF) at 298 K (All Simulation Results from this Work)

ΔG (kcal/mol)	$^a k$ (s $^{-1}$)	$^a \tau_{1/2}$ (s)	condition
18.03 \pm 1.5 (simul.)	0.33 \pm 0.83	2.1 \pm 5.4	gas phase (neutral)
16.2 \pm 0.3 (exp.[34])	7.3 \pm 3.7	0.095 \pm 0.048	(CH ₃ CN) (neutral)
18.1 \pm 0.2 (exp.[15, 34, 71])	0.3 \pm 0.10	2.4 \pm 0.082	^b polymer matrix (neutral)
22.21 \pm 0.04 (exp.[15, 34, 71])	(2.7 \pm 0.19) $\times 10^{-4}$	(2.5 \pm 0.18) $\times 10^3$	molecular-switch junction (neutral)
31.22 (simul.)	6.3 $\times 10^{-11}$	1.1 $\times 10^{10}$	gas phase (oxidation +1)
50.43 (simul.)	4.5 $\times 10^{-25}$	1.5 $\times 10^{24}$	gas phase (oxidation +2)
65 (exp. + simul.[72])	–	–	^c SAM on SiO ₂ wafers (oxidation +2)

^aValues are calculated using the Eyring equation, $1/\tau = (k_B T/h) \exp(-\Delta G^\ddagger/RT)$. ^bWeight ratio 70:7:20:3 for CH₃CN/poly(methylmethacrylate)/propylene carbonate/LiClO₄. ^cThe modified AFM tip is attached to the CBPQT⁴⁺ ring.

For the neutral state, we find that the Coulombic energy increases by 60 kcal/mol as the ring moves from the TTF to the triphenylene spacer (barrier) and then drops by 45 kcal/mol as it moves to the DNP. On the other hand, the vdW energy changes, within a range of ± 4 kcal/mol, while the ring travels from the TTF to the DNP.

This indicates that the barrier is dominated by the differential Coulombic interactions with a peak of 443 kcal/mol at $z = 28$ Å (over the spacer). We were quite surprised because we expected the barrier to be dominated by vdW repulsions due to the bulky size of the triphenylene. To understand why Coulombic interactions are so important, we plot in Figure 3.11 the total charge on the ring along the pathway, in the neutral case. We see that at the TTF or the DNP positions there is strong delocalization from the ring onto the backbone, but as the ring passes over the triphenylene spacer (at $z = 28$ Å), this charge localizes back onto the ring. Thus, we conclude that localization of the ring charge increases the Coulombic repulsion and dominates the free energy barrier. This suggests that the barrier can be modified dramatically by changing the polarity of the spacer.

We also found that as the system is oxidized, the magnitude of Coulombic repulsion increases from 380 – 445 kcal/mol for the neutral state, to 520 – 545 kcal/mol for the +1 oxidation state, and finally, to 670 – 700 kcal/mol for the +2 oxidation state. In contrast, the vdW energy changes from 165 – 173 to 165 – 172 to 164 – 171 kcal/mol as the system is oxidized. This implies that the driving force inducing the mechanical movement of the ring is the increased Coulombic repulsion due to oxidization of the rotaxane. This confirms our view since the beginning of our experiments.

However, the PMF profile (Figure 3.7b) still differs substantially from the Coulombic energy

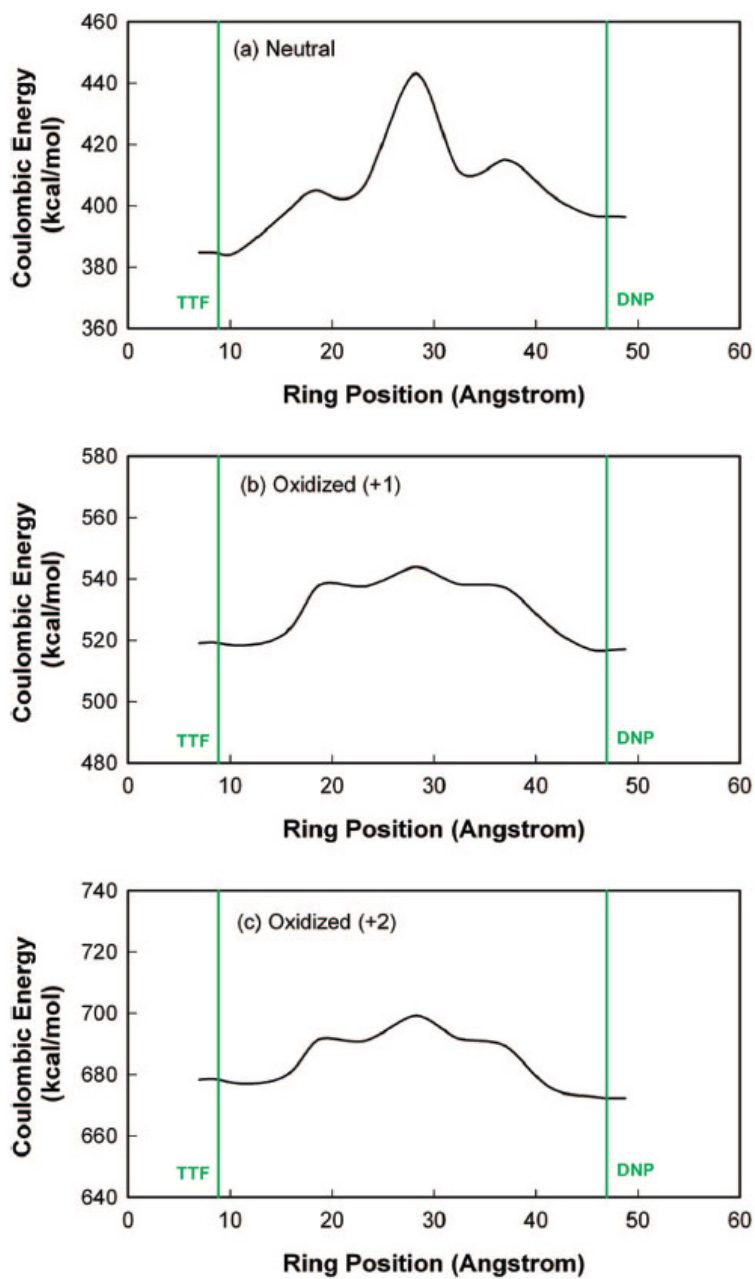


Figure 3.9: Change of Coulombic interaction energy as a function of the ring position: (a) neutral state; (b) oxidation state +1; (c) oxidation state +2.

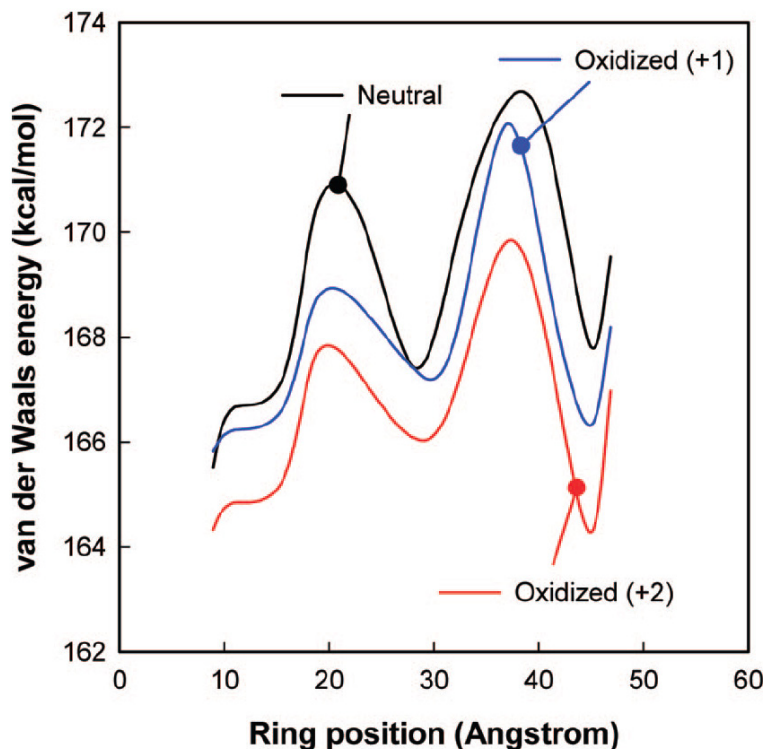


Figure 3.10: Change of van der Waals interaction energy as a function of the ring position: (a) neutral state; (b) oxidation state +1; (c) oxidation state +2.

profile (Figure 3.9). For instance, in the neutral case, the Coulombic energy difference between two stations is 12.03 kcal/mol, which is ~ 12 times larger than $\Delta G_{\text{T2D}} = 1.0$ kcal/mol, and the Coulombic energy barrier for the shuttling from the DNP to the TTF is 46.75 kcal/mol, which is ~ 2.6 times larger than $\Delta G_{\text{D2T}}^{\ddagger} = 18.03$ kcal/mol. Thus, the key features of the PMF profile are not fully explained in terms of the Coulombic energy alone. Another possible contributor to the free energy is vibrational entropy, which can be investigated directly from the MD simulation trajectory [73, 74].

3.5 Conclusions

We used constrained MD simulations to calculate the free energy profile at 300 K for the shuttling of the CBPQT^{4+} ring between the TTF and the DNP in the rotaxane molecule. This free energy profile was derived by calculating and integrating the MF acting on the ring as it is moved from one position to another position along the backbone. We found that it is particularly important to allow the charges to adjust adiabatically as the ring moves. Indeed, we find that the Coulomb interactions dominate the barriers for these systems.

We found that the free energy barrier from the DNP to the TTF is 18.03 kcal/mol for the neutral

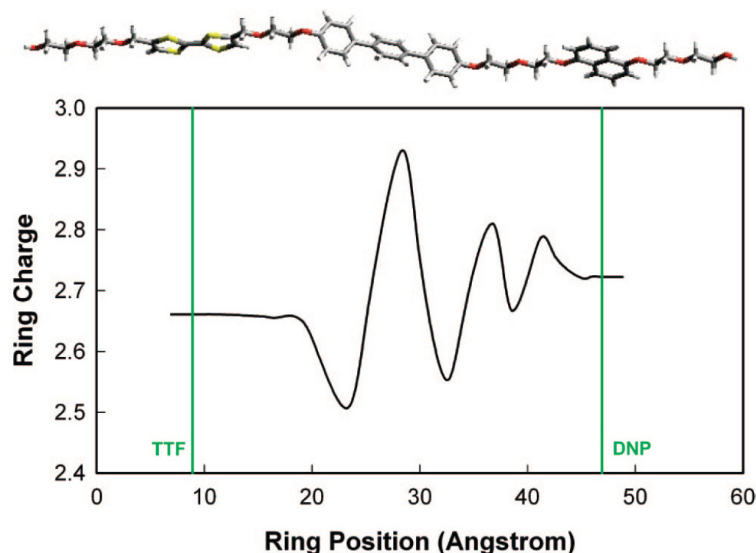


Figure 3.11: Variations in the total charge on the ring as a function of the ring position for the neutral case.

system, which agrees well with experimental values of 17 – 22 kcal/mol for various environments. We calculate that the ΔG between the TTF and the DNP positions is 1.0 kcal/mol, which compares well with experimental results of 1.4 – 1.6 kcal/mol obtained from binding energies of separate DNP and TTF systems with the CBPQT⁴⁺ ring.

These results validate the accuracy of our computational procedure. Thus, we can now use this validated technique for estimating the switching kinetics for new designs of molecular architectures.

3.6 Acknowledgments

The computational work was initiated with support by the National Science Foundation (NIRT, W.A.G.). The collaboration was supported by the Microelectronics Advanced Research Corporation (MARCO; W.A.G. and J.F.S.) and its Focus Centers on Functional Engineered NanoArchitectonics (FENA) and Materials Structures and Devices, the Moletronics Program of the Defense Advanced Research Projects Agency (DARPA; J.F.S. and J.R.H.), the Center for Nanoscale Innovation for Defense (CNID; J.F.S.), and the MARCO Materials Structures and Devices Focus Center (J.R.H.). In addition, the facilities of the MSC (W.A.G.) were supported by ONR-DURIP and ARO-DURIP.

Bibliography

- [1] Luo, Y.; Collier, C. P.; Jeppesen, J. O.; Nielsen, K. A.; DeIonno, E.; Ho, G.; Perkins, J.; Tseng, H. R.; Yamamoto, T.; Stoddart, J. F.; Heath, J. R. *ChemPhysChem* **2002**, 3, 519-525.
- [2] Green, J. E.; Choi, J. W.; Boukai, A.; Bunimovich, Y.; Johnston-Halperin, E.; DeIonno, E.; Luo, Y.; Sheriff, B. A.; Xu, K.; Shin, Y. S.; Tseng, H.-R.; Stoddart, J. F.; Heath, J. R. *Nature* **2007**, 445, 414-417.
- [3] Anelli, P. L.; Spencer, N.; Stoddart, J. F. *J. Am. Chem. Soc.* **1991**, 113, 5131-5133.
- [4] Bissell, R. A.; Cordova, E.; Kaifer, A. E.; Stoddart, J. F. *Nature* **1994**, 369, 133-137.
- [5] Asakawa, M.; Ashton, P. R.; Balzani, V.; Credi, A.; Hamers, C.; Mattersteig, G.; Montalti, M.; Shipway, A. N.; Spencer, N.; Stoddart, J. F.; Tolley, M. S.; Venturi, M.; White, A. J. P.; Williams, D. J. *Angew. Chem. Int. Ed.* **1998**, 37, 333-337.
- [6] Balzani, V.; Credi, A.; Mattersteig, G.; Matthews, O. A.; Raymo, F. M.; Stoddart, J. F.; Venturi, M.; White, A. J. P.; Williams, D. J. *J. Org. Chem.* **2000**, 65, 1924-1936.
- [7] Collier, C. P.; Mattersteig, G.; Wong, E. W.; Luo, Y.; Beverly, K.; Sampaio, J.; Raymo, F. M.; Stoddart, J. F.; Heath, J. R. *Science* **2000**, 289, 1172-1175.
- [8] Barboiu, M.; Lehn, J.-M. *Proc. Natl. Acad. Sci. U.S.A.* **2002**, 99, 5201-5206.
- [9] Hogg, L.; Leigh, D. A.; Lusby, P. J.; Morelli, A.; Parsons, S.; Wong, J. K. Y. *Angew. Chem., Int. Ed.* **2004**, 43, 1218-1221.
- [10] Zheng, X.; Mulcahy, M. E.; Horinek, D.; Galeotti, F.; Magnera, T. F.; Michl, J. *J. Am. Chem. Soc.* **2004**, 126, 4540-4542.
- [11] Hawthorne, M. F.; Zink, J. I.; Skelton, J. M.; Bayer, M. J.; Liu, C.; Livshits, E.; Baer, R.; Neuhauser, D. *Science* **2004**, 303, 1849-1851.
- [12] de Jong, J. J. D.; Lucas, L. N.; Kellogg, R. M.; van Esch, J. H.; Reringa, B. L. *Science* **2004**, 304, 278-281.

- [13] Turberfield, A. J.; Mitchell, J. C.; Yurke, B.; Mills, A. P.; Blakey, M. I.; Simmel, F. C. *Phys. Rev. Lett.* **2003**, 90, art. no.118102.
- [14] Liu, H. Q.; Schmidt, J. J.; Bachand, G. D.; Rizk, S. S.; Looger, L. L.; Hellinga, H. W.; Montemagno, C. D. *Nat. Mater.* **2002**, 1, 173-177.
- [15] Choi, J. W.; Flood, A.; Steuerman, D. W.; Nygaard, S.; Braunschweig, A.; Moonen, N.; Laursen, B.; Luo, Y.; DeItonno, E.; Peters, A. J.; Jeppesen, J. O.; Stoddart, J. F.; Heath, J. R. *Chem. Eur. J.* **2006**, 12, 261-279.
- [16] Collier, C. P.; Jeppesen, J. O.; Luo, Y.; Perkins, J.; Wong, E. W.; Heath, J. R.; Stoddart, J. F. *J. Am. Chem. Soc.* **2001**, 123, 12632-12641.
- [17] Diehl, M. R.; Steuerman, D. W.; Tseng, H. R.; Vignon, S. A.; Star, A.; Celestre, P. C.; Stoddart, J. F.; Heath, J. R. *ChemPhysChem* **2003**, 4, 1335-1339.
- [18] Credi, A.; Balzani, V.; Langford, S. J.; Stoddart, J. F. *J. Am. Chem. Soc.* **1997**, 119, 2679-2681.
- [19] Collier, C. P.; Wong, E. W.; Belohradsky, M.; Raymo, F. M.; Stoddart, J. F.; Kuekes, P. J.; Williams, R. S.; Heath, J. R. *Science* **1999**, 285, 391-394.
- [20] Elizarov, A. M.; Chiu, S. H.; Stoddart, J. F. *J. Org. Chem.* **2002**, 67, 9175-9181.
- [21] Carroll, R. L.; Gorman, C. B. *Angew. Chem. Int. Ed.* **2002**, 41, 4379-4400.
- [22] Yu, H. B.; Luo, Y.; Beverly, K.; Stoddart, J. F.; Tseng, H. R.; Heath, J. R. *Angew. Chem. Int. Ed.* **2003**, 42, 5706-5711.
- [23] Heath, J. R.; Ratner, M. A. *Phys. Today* **2003**, 56, 43-49.
- [24] Balzani, V.; Gomez-Lopez, M.; Stoddart, J. F. *Acc. Chem. Res.* **1998**, 31, 405-414.
- [25] Balzani, V.; Credi, A.; Raymo, F. M.; Stoddart, J. F. *Angew. Chem. Int. Ed.* **2000**, 39, 3349-3391.
- [26] Chia, S. Y.; Cao, J. G.; Stoddart, J. F.; Zink, J. I. *Angew. Chem. Int. Ed.* **2001**, 40, 2447-2451.
- [27] Belohradsky, M.; Elizarov, A. M.; Stoddart, J. F. *Collect. Czech. Chem. Commun.* **2002**, 67, 1719-1728.
- [28] Hernandez, R.; Tseng, H. R.; Wong, J. W.; Stoddart, J. F.; Zink, J. I. *J. Am. Chem. Soc.* **2004**, 126, 3370-3371.
- [29] Badjic, J. D.; Balzani, V.; Credi, A.; Silvi, S.; Stoddart, J. F. *Science* **2004**, 303, 1845-1849.
- [30] Tseng, H. R.; Vignon, S. A.; Stoddart, J. F. *Angew. Chem., Int. Ed.* **2003**, 42, 1491-1495.

- [31] Jeppesen, J. O.; Perkins, J.; Becher, J.; Stoddart, J. F. *Angew. Chem. Int. Ed.* **2001**, 40, 1216-1221.
- [32] Jeppesen, J. O.; Nielsen, K. A.; Perkins, J.; Vignon, S. A.; Di Fabio, A.; Ballardini, R.; Gandolfi, M. T.; Venturi, M.; Balzani, V.; Becher, J.; Stoddart, J. F. *Chem. Eur. J.* **2003**, 9, 2982-3007.
- [33] Yamamoto, T.; Tseng, H. R.; Stoddart, J. F.; Balzani, V.; Credi, A.; Marchioni, F.; Venturi, M. *Collect. Czech. Chem. Commun.* **2003**, 68, 1488-1514.
- [34] Tseng, H. R.; Vignon, S. A.; Celestre, P. C.; Perkins, J.; Jeppesen, J. O.; Di Fabio, A.; Ballardini, R.; Gandolfi, M. T.; Venturi, M.; Balzani, V.; Stoddart, J. F. *Chem. Eur. J.* **2004**, 10, 155-172.
- [35] Kang, S. S.; Vignon, S. A.; Tseng, H. R.; Stoddart, J. F. *Chem. Eur. J.* **2004**, 10, 2555-2564.
- [36] Livoreil, A.; Dietrichbuecker, C. O.; Sauvage, J. P. *J. Am. Chem. Soc.* **1994**, 116, 9399-9400.
- [37] Flood, A. H.; Peters, A. J.; Vignon, S. A.; Steurman, D. W.; Tseng, H.-R.; Kang, S.; Heath, J. R.; Stoddart, J. F. *Chem. Eur. J.* **2004**, 24, 6558-6561.
- [38] Steurman, D. W.; Tseng, H.-R.; Peters, A. J.; Flood, A. H.; Jeppesen, J. O.; Nielsen, K. A.; Stoddart, J. F.; Heath, J. R. *Angew. Chem. Int. Ed.* **2004**, 43, 6486-6491.
- [39] Lee, I. C.; Frank, C. W.; Yamamoto, T.; Tseng, H.-R.; Flood, A. H.; Stoddart, J. F.; Jeppesen, J. O. *Langmuir* **2004**, 20, 5809-5828.
- [40] Tseng, H. R.; Wu, D. M.; Fang, N. X. L.; Zhang, X.; Stoddart, J. F. *ChemPhysChem* **2004**, 5, 111-116.
- [41] Raehm, L.; Kern, J. M.; Sauvage, J. P.; Hamann, C.; Palacin, S.; Bourgoin, J. P. *Chem. Eur. J.* **2002**, 8, 2153-2162.
- [42] Jang, Y. H.; Kim, Y. H.; Jang, S. S.; Hwang, S. G.; Goddard, W. A., III *Abstr. Pap., Am. Chem. Soc.* **2004**, 227, U850-U850.
- [43] Jang, S. S.; Jang, Y. H.; Kim, Y.-H.; Goddard, W. A., III; Flood, A. H.; Laursen, B. W.; Tseng, H.-R.; Stoddart, J. F.; Jeppesen, J. O.; Choi, J. W.; Steurman, D. W.; DeIonno, E.; Heath, J. R. *J. Am. Chem. Soc.* **2005**, 127, 1563-1575.
- [44] Jang, S. S.; Jang, Y. H.; Kim, Y. H.; Goddard, W. A., III; Choi, J. W.; Heath, J. R.; Laursen, B. W.; Flood, A. H.; Stoddart, J. F.; Norgaard, K.; Bjornholm, T. *J. Am. Chem. Soc.* **2005**, 127, 14804-14816.
- [45] Jang, Y. H.; Jang, S. S.; Goddard, W. A., III *J. Am. Chem. Soc.* **2005**, 127, 4959-4964.

- [46] Jang, Y. H.; Goddard, W. A., III *J. Phys. Chem. B* **2006**, 110, 7660-7665.
- [47] Kim, Y.-H.; Goddard, W. A., III *J. Phys. Chem. C* **2007**, 111, 4831-4837.
- [48] Jeppesen, J. O.; Nygaard, S.; Vignon, S. A.; Stoddart, J. F. *Eur. J. Org. Chem.* **2004**, 196, 220.
- [49] Dichtel, W. R.; Heath, J. R.; Stoddart, J. F. *Philos. Trans. R. Soc. A, Math. Phys. Eng. Sci.* **2007**, 365, 1607-1625.
- [50] Carter, E. A.; Ciccotti, G.; Hynes, J. T.; Kapral, R. *Chem. Phys. Lett.* **1989**, 156, 472-477.
- [51] Sprik, M.; Ciccotti, G. *J. Chem. Phys.* **1998**, 109, 7737-7744.
- [52] Trzesniak, D.; Kunz, A. P. E.; van Gunsteren, W. F. *ChemPhysChem* **2007**, 8, 162-169.
- [53] *Jaguar*, V. 5.0 ed.; Schrödinger Inc.: Portland, 2003.
- [54] Evans, D. J.; Morriss, G. P. *Statistical Mechanics of Nonequilibrium Liquids*; Academic Press: London, 1990.
- [55] Fixman, M. *Proc. Natl. Acad. Sci. U.S.A.* **1974**, 71, 3050-3053.
- [56] Mayo, S. L.; Olafson, B. D.; Goddard, W. A., III *J. Phys. Chem.* **1990**, 94, 8897-8909.
- [57] Jang, S. S.; Molinero, V.; Cagin, T.; Goddard, W. A., III *J. Phys. Chem. B* **2004**, 108, 3149-3157.
- [58] Jang, S. S.; Lin, S.-T.; Cagin, T.; Molinero, V.; Goddard, W. A., III *J. Phys. Chem. B* **2005**, 109, 10154-10167.
- [59] Jang, S. S.; Goddard, W. A. *J. Phys. Chem. C* **2007**, 111, 2759-2769.
- [60] Jang, S. S.; Lin, S.-T.; Maiti, P. K.; Blanco, M.; Goddard, W. A., III; Shuler, P.; Tang, Y. *J. Phys. Chem. B* **2004**, 108, 12130-12140.
- [61] Jang, S. S.; Goddard, W. A. *J. Phys. Chem. B* **2006**, 110, 7992-8001.
- [62] Plimpton, S. J. *J. Comput. Phys.* **1995**, 117, 1-19.
- [63] Plimpton, S. J.; Pollock, R.; Stevens, M. *The Eighth SIAM Conference on Parallel Processing for Scientific Computing Minneapolis*; 1997.
- [64] Swope, W. C.; Andersen, H. C.; Berens, P. H.; Wilson, K. R. *J. Chem. Phys.* **1982**, 76, 637-649.
- [65] Castro, R.; Nixon, K. R.; Evanseck, J. D.; Kaifer, A. E. *J. Org. Chem.* **1996**, 61, 7298-7303.

- [66] Ashton, P. R.; Balzani, V.; Becher, J.; Credi, A.; Fyfe, M. C. T.; Mattersteig, G.; Menzer, S.; Nielsen, M. B.; Raymo, F. M.; Stoddart, J. F.; Venturi, M.; Williams, D. J. *J. Am. Chem. Soc.* **1999**, 121, 3951-3957.
- [67] Bryce, M. R.; Cooke, G.; Duclairoir, F. M. A.; Rotello, V. M. *Tetrahedron Lett.* **2001**, 42, 1143-1145.
- [68] Nielsen, M. B.; Jeppesen, J. O.; Lau, J.; Lomholt, C.; Damgaard, D.; Jacobsen, J. P.; Becher, J.; Stoddart, J. F. *J. Org. Chem.* **2001**, 66, 3559-3563.
- [69] Leigh, D. A.; Murphy, A.; Smart, J. P.; Deleuze, M. S.; Zerbetto, F. *J. Am. Chem. Soc.* **1998**, 120, 6458-6467.
- [70] Leigh, D. A.; Troisi, A.; Zerbetto, F. *Chem. Eur. J.* **2001**, 7, 1450-1454.
- [71] Deleuze, M. S.; Leigh, D. A.; Zerbetto, F. *J. Am. Chem. Soc.* **1999**, 121, 2364-2379.
- [72] Brough, B.; Northrop, B. H.; Schmidt, J. J.; Tseng, H. R.; Houk, K. N.; Stoddart, J. F.; Ho, C. M. *Proc. Natl. Acad. Sci. U.S.A.* **2006**, 103, 8583-8588.
- [73] Lin, S. T.; Blanco, M.; Goddard, W. A. *J. Chem. Phys.* **2003**, 119, 11792-11805.
- [74] Lin, S. T.; Jang, S. S.; Cagin, T.; Goddard, W. A. *J. Phys. Chem. B* **2004**, 108, 10041-10052.

Chapter 4

Sodium Diffusion through Aluminum-Doped Zeolite BEA System: Effect of Water Solvation

Reproduced with permission from Kim, H; Deng, W.-Q.; Goddard, W. A.; Jang S. S.; Davis M. E.; Yang Y. J. Phys. Chem. C 2009, 113, 819. Copyright 2009 American Chemical Society.

4.1 Abstract

To investigate the effect of hydration on the diffusion of sodium ions through the aluminum-doped zeolite BEA system ($\text{Si}/\text{Al} = 30$), we used the grand canonical Monte Carlo (GCMC) method to predict the water absorption into aluminosilicate zeolite structure under various conditions of vapor pressure and temperature, followed by molecular dynamics (MD) simulations to investigate how the sodium diffusion depends on the concentration of water molecules. The predicted absorption isotherm shows first-order-like transition, which is commonly observed in hydrophobic porous systems. The MD trajectories indicate that the sodium ions diffuse through zeolite porous structures via hopping mechanism, as previously discussed for similar solid electrolyte systems. These results show that above 15 wt % hydration (good solvation regime) the formation of the solvation cage dramatically increases sodium diffusion by reducing the hopping energy barrier by 25 % from the value of 3.8 kcal/mol observed in the poor solvation regime.

4.2 Introduction

Zeolites constitute a unique class of the porous materials widely used in ion exchange, selective catalysis, and molecular sieve applications [1, 2]. An important property for many of these applications is migration of the absorbed water molecules. It has been observed that water migration in such porous materials proceeds differently than in the bulk water phase under the same temperature and

chemical potential conditions [3, 4, 5, 6]; hence, we undertook a study of how nanoscale confinement in zeolites affects such of properties as structure, dynamics, and thermodynamics with absorbed molecules [7, 8, 9, 10, 11, 12, 13, 14, 15, 16, 17, 18].

In aluminosilicate zeolites the aluminum is generally incorporated in the three-dimensional framework in the form of AlO_4^- surrounded by neighboring SiO_4 while alkali metals such as Na^+ or K^+ are in the pores, interacting electrostatically with the zeolite framework. These positively charged and Movable cations in various zeolite systems have been studied intensively [7, 8, 19, 20, 21, 22, 23, 24, 25, 26, 27, 28, 29] since they impart many interesting properties to the zeolite systems. In particular, the ionic conductivity of zeolites can be controlled by the level of nonframework ions and their hydration (undoped zeolites are insulators with an electronic band gap of ~ 7 eV) [9]. The chemical nature, hydrophilicity, and selectivity for binding guest molecules in zeolites can be manipulated as appropriate for many practical applications [10, 11].

One recent interesting application of zeolites is as proton exchange membranes for fuel cells (PEMFC) [12, 13, 14, 15, 16, 17]. Here the molecular sieving capability and tunable acidity/hydrophilicity of zeolites can be incorporated to form a polyelectrolyte-based membrane that could improve the high temperature/low humidity performance of fuel cells [18].

We report here studies of the aluminosilicate zeolite BEA ($\text{Si}/\text{Al} = 30$). A distinct structural feature of interest for BEA is its three-dimensional channel structure which is characterized by ~ 1 nm diameter channels (Figure 4.1) in which water molecules may form a continuous phase, thereby facilitate ionic transport which makes membranes based on such materials useful as a replacement for polymer electrolyte membranes (PEM) for fuel cell applications. In PEM fuel cell membrane such as Nafion, the protons are transported through two mechanisms: vehicular diffusion of protonated waters and Grotthuss diffusion in which protons hop from water to water, with the relative contributions depending on the water content, counterions, porosity, temperature etc. Of course, diffusion of sodium or potassium cations occurs only through hopping. In this study, we determine how the nanometer scale confinement in the aluminosilicate zeolite BEA ($\text{Si}/\text{Al} = 30$) affects sodium diffusion.

First, we used grand canonical Monte Carlo (GCMC) simulations to predict the water absorption of aluminosilicate zeolite BEA system at various conditions, and then we applied the equilibrium molecular dynamics (MD) simulations on the diffusion starting with the hydrated systems obtained from the GCMC simulations. During such MD simulations, we sampled the time evolution of both the sodium diffusion and the water structure associated with the sodium ions.

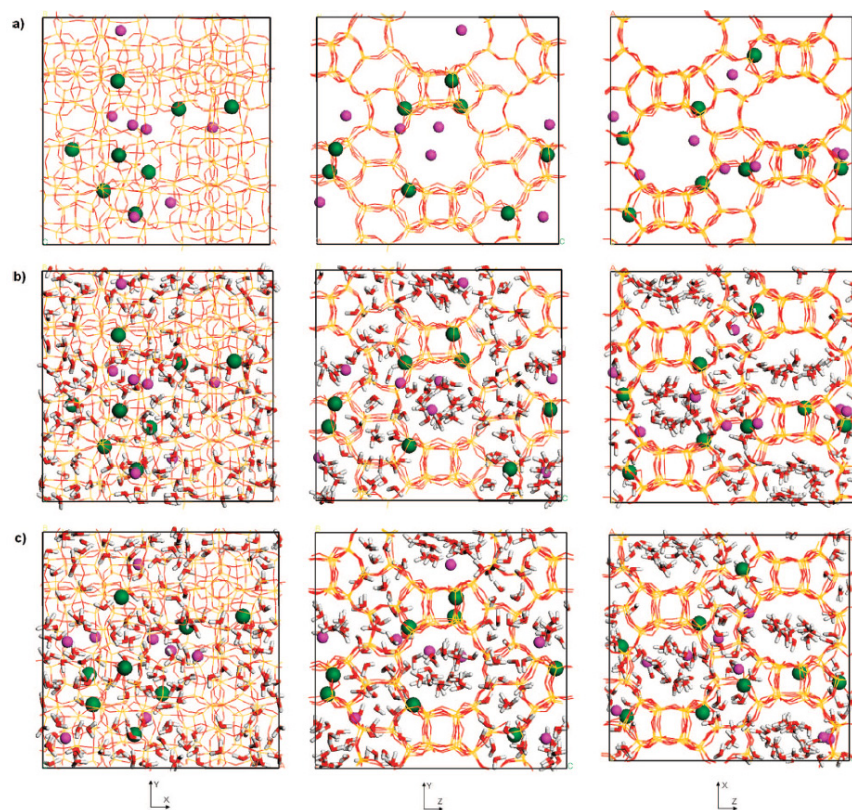


Figure 4.1: Atomistic structure for the primitive periodic cell with composition of $\text{Na}_8\text{Al}_8\text{Si}_{248}\text{O}_{512}$. This shows green balls are aluminum and magenta balls are sodium. (a) Minimized aluminosilicate zeolite BEA structures without H_2O , (b) snapshot of zeolite BEA structures after the GCMC simulation for 298.15 K and 101.3250 kPa, and (c) snapshot of zeolite BEA structures after 4 ns NPT MD simulation at 298.15 K and 101.3250 kPa.

4.3 Simulation Details

4.3.1 Force Field

To calculate the energy and geometry of the zeolite framework, we employed Burchart force field (FF) [19] developed to describe aluminosilicate structures and the van der Waals interactions with the Na. This FF uses the Lennard-Jones 12 – 6 form for the van der Waals interactions between all atoms of the framework. To describe the interactions between water molecules, we used the F3C water FF [20]. For the off-diagonal van der Waals interactions between different types of atoms, we used the geometric-mean combination rule. The Lennard-Jones interactions were terminated beyond 18.0 Å, using a cubic spline function starting at 15.0 Å.

The atomic charges of the individual atoms of the zeolite frame were determined using the charge equilibration (QEq) method [21]. Since our simulation cell contains eight AlO_4^- sites, the total charge of the framework is set by -8 . The eight sodium ions each were taken to have $+1$ charge, leading to charge neutrality of the simulation cell. The atomic charge of the water is from the F3C model [20]. The particle-particle particle-mesh (PPPM) method [22] was employed to compute the electrostatic using an accuracy criterion of 10^{-5} .

4.3.2 Grand Canonical Monte Carlo (GCMC) method and Molecular Dynamics (MD) Simulation

To predict the water absorption in aluminosilicate zeolite BEA framework as a function of partial pressure and temperature, we carried out grand canonical Monte Carlo (GCMC) simulations [23, 24] using the Sorption module of Cerius2 [25]. Since the chemical potential of the adsorbed phase equals the chemical potential of the bulk gas at equilibrium condition, the GCMC simulation makes multiple attempts to add one water molecule according to the probability

$$P_{add} = \min \left[1, \frac{V}{(N+1)\Lambda^3} \exp \left(-\frac{\Delta U}{k_B T} \right) \right], \quad (4.1)$$

or subtract one with the following probability

$$P_{sub} = \min \left[1, \frac{N\Lambda^3}{V} \exp \left(-\frac{\Delta U}{k_B T} \right) \right], \quad (4.2)$$

where V is the pore volume, N is the number of water molecules in the simulated system, Λ is the thermal de Broglie wavelength, and ΔU is the change in potential energy. For each GCMC simulation, we ran 2×10^8 Monte Carlo steps (MCS), during which the zeolite framework including sodium ions were fixed and water molecules were moved by the Metropolis sampling rule [26, 27]. Each Monte Carlo step is allowed four different types of operations—translation, rotation, creation,

and destructions of the water molecule with equal probabilities.

All molecular dynamics (MD) simulations were performed using the LAMMPS (large-scale atomic/molecular massively parallel simulator) MD code developed by Plimpton at Sandia [28, 29]. The velocity Verlet algorithm [30] was used to solve the equations of motion with a time step of 1.0 fs. The isobaric-isothermal ensembles (NPT) were generated using Nosé-Hoover thermostat with a temperature damping relaxation time of 0.1 ps and the Andersen-Hoover barostat with a dimensionless cell mass factor of 1.0. A series of MD simulations were conducted at constant temperature of 298.15 K with various pressure conditions from 0.1013 to 101.3250 kPa. To understand the effect of temperature, another set of simulations were performed at constant pressure of 101.3250 kPa with various temperature conditions from 298.15 to 453.15 K.

4.3.3 Construction of Models and Calculation of Properties

We used the $2 \times 2 \times 1$ superstructure of zeolite BEA (based on the X-ray crystallography database [31]) as the periodic simulation cell for the MD. Then, eight silicon atoms in the channels were randomly chosen and replaced with aluminum atoms to have the lowest energy using substitutional disorder option of Cerius2 [25]. This leads to a Si/Al ratio of 30, with a simulation cell consisting of 8 AlO_4^- and 248 SiO_4 tetrahedral sites with an overall composition of $\text{Na}_8\text{Al}_8\text{Si}_{248}\text{O}_{512}$.

The eight sodium ions were initially placed near the aluminum-doped sites, and the full structure of zeolite frame including the sodium ions were energy minimized. Then the water contents were determined from GCMC simulations at various pressure and temperature conditions.

Then we carried out 8 – 12 ns NPT MD simulations and evaluated such properties as density, pair correlation function, and diffusion coefficients using the full trajectory files.

4.4 Results and Discussion

4.4.1 Water Absorption

Using GCMC, the chemical potential of water in zeolite frame was equilibrated with that of the external reservoir at various vapor pressure conditions ranging from 0.1013 to 101.3250 kPa. The water absorption isotherm at 298.15 K and the temperature dependence of water adsorption at 101.3250 kPa are shown at Figures 4.2 and 4.3, respectively.

We were unable to locate published water adsorption isotherms for zeolite BEA with Si/Al of 30. Thus the data shown in Figures 4.2 and 4.3 are from simulation only. We observe a stepwise condensation at 3.5 kPa. The amount of water uptake increases abruptly and then shows fast saturation up to ~ 50 molecules per crystallographic unit cell, which can be regarded as a maximum loading number at 298.15 K. Previous studies discovered that a spontaneous condensation of water

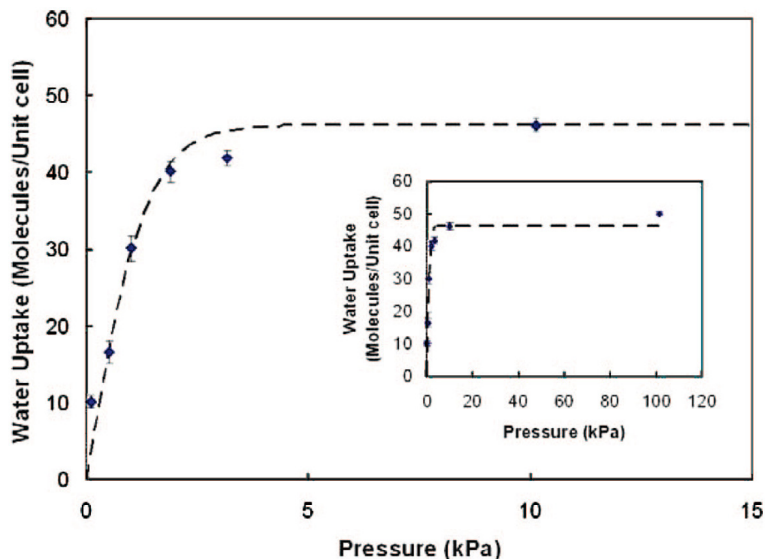


Figure 4.2: Dashed line is the least-squares fitted to $f(x) = a \tanh(bx)$, where $a = 46.19$ molecules/unit cell and $b = 0.753$ (1/kPa). We obtain a vapor pressure of 3.578 kPa for the point at which the water uptake reaches to 99 % of the maximum loading uptake.

occurs in hydrophobic porous materials such as sodium faujasites of NaY and NaX [32], silicate-1 zeolites [33, 34] and carbon nanotubes [35]. Here, the term “hydrophobic” is used because of the spontaneous condensation behavior: if the surface of the nanopore were hydrophilic, then water absorption would proceed gradually over wide range of pressure through wetting the surface of the nanopore instead of increasing abruptly at a certain narrow pressure range. We expect that the capillary condensation would follow a first-order-like transition since the nonwetting character of the pore prohibits the intrusion of liquid water until a certain hydraulic pressure. This suggests that the aluminosilicate BEA zeolite system may sustain some extent of hydrophobicity even after some of the hydrophobic SiO_4 sites are replaced by hydrophilic AlO_4^- sites.

The temperature dependence of water absorption is plotted at Figure 4.3 at 101.3250 kPa. As the temperature increases, the amount of water uptake in zeolite frame decreases. This type of temperature dependency of water uptake has been observed in the experiments on the zeolite-4A structure [36] and in other simulation studies [32]. Of particular interest is that at 423 K, this BEA aluminosilicate zeolite frame still holds 20 % of water absorbed at 300 K. We expect that this capability to retain significant amount of water at high temperature could make these materials useful as a replacement for performance of the PEM for fuel cell operation under high temperature/low humidity condition.

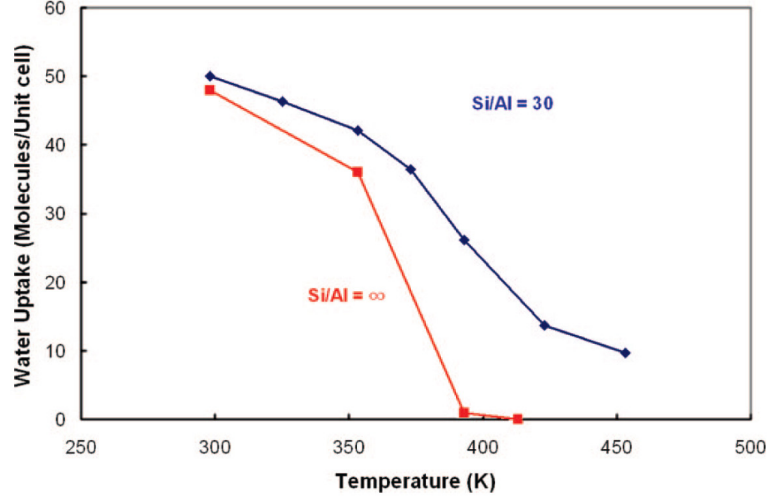


Figure 4.3: Predicted temperature-dependence of water uptake at 101.3250 kPa when the zeolite BEA has no aluminum doping (red curve) and Si/Al = 30 (blue curve). The presence of aluminum-doped sites as well as sodium ions enhance the water uptake amount especially in the high temperature.

4.4.2 Structure of Water in Zeolite

To characterize the water structure we calculated the density-normalized O(water)-O(water) pair correlation function, $4\pi r^2 \rho g_{O(water)-O(water)}$ where r is the distance and ρ is the number density of water. Figure 4.4a shows $4\pi r^2 \rho g_{O(water)-O(water)}$ plots for water absorbed in various vapor pressure conditions and compares to the values for bulk water. Integrating the first peak in Figure 4.4a leads to the coordination number CN. For bulk water we obtain CN = 4.59, in good agreement with CN = 4.5, from neutron diffraction experiment [37]. Figure 4.4b summarizes the change of the coordination numbers as a function of pressure, showing a behavior identical with the absorption isotherm in Figure 4.2. This provides clear evidence for the spontaneous condensation in which all the water molecules absorbed into the system participate in water clusters. Figure 4.4 shows that the structure of the water absorbed in the zeolite framework approaches to that of bulk phase water as the water uptake/pressure is increased to 101.3250 kPa. However, the saturated value of CN of the absorbed phase (~ 3.8) is smaller than the CN of the bulk phase (4.5). This is reasonable because of the huge surface area of 1362.99 m²/g of the nanopores of the zeolite (cf. activated carbon has 500 – 1500 m²/g). We observed similar behavior for water in Nafion and Dendrion polymer membranes [38, 39, 40].

In order to investigate the effect of the sodium ion on the water structure, we analyzed the density-normalized Na-O(water) pair correlation function, $4\pi r^2 \rho g_{Na-O(water)}$ and the water coordination number of sodium ion as shown in Figure 4.5, parts a and b, respectively. Similar to $4\pi r^2 \rho g_{O(water)-O(water)}$ in Figure 4.4 we see that $4\pi r^2 \rho g_{Na-O(water)}$ increases with increasing pressure with a first peak position that does not change with pressure. However, the increase of the

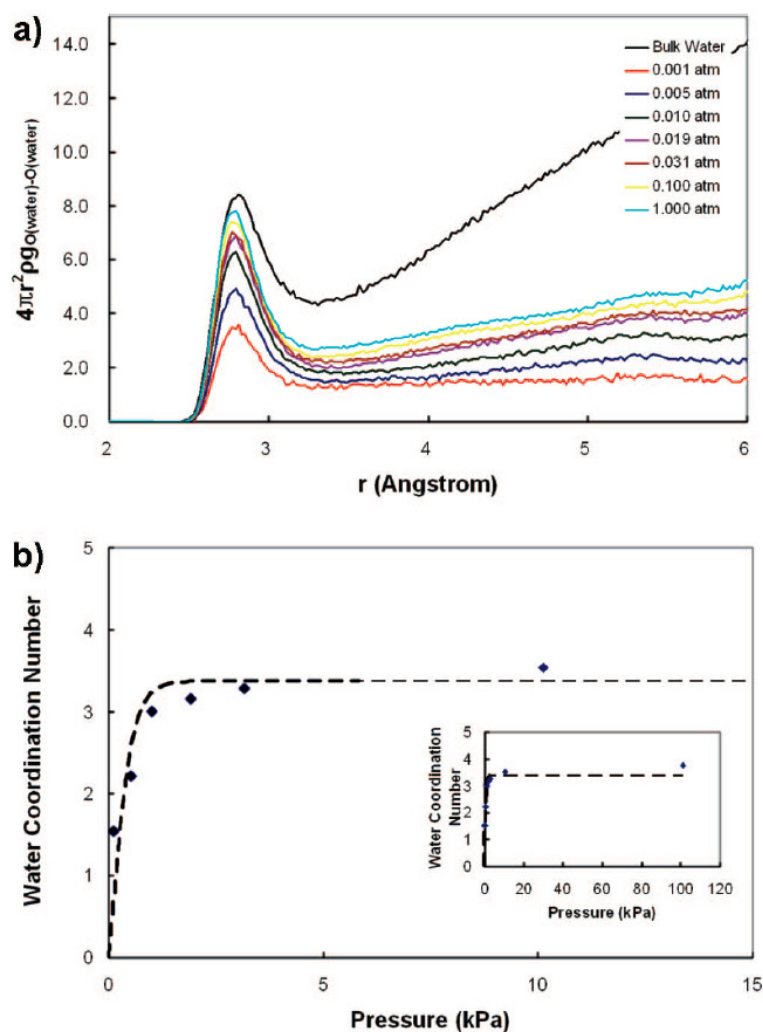


Figure 4.4: (a) Probability of finding additional water molecules at a specific distance from each water molecule. This is obtained as the product of pair correlation functions of water oxygens, $g_{O(water)-O(water)}$ with water density ρ and $4\pi r^2$. (b) Water coordination number (CN) of water molecule as a function of pressure. The CN of water molecule is obtained from the integration of curve a up to first minimum, which is at 3.7 Å. The saturated value of CN of the adsorbed phase (~ 3.8) is smaller than the CN of the bulk phase (4.5).

first peak intensity of $4\pi r^2 \rho g_{Na-O(water)}$ up to $\sim 3.5 \text{ \AA}$ was not significant compared to that of $4\pi r^2 \rho g_{O(water)-O(water)}$. This indicates that the first water solvation shell for the sodium ion saturates rapidly toward $CN = \sim 5.0$ (see Figure 5b inset), which is consistent with the previous indication that water molecules cluster with sodium rather than interact with the surface of the nanopore, (indicating a hydrophobic nature of the nanopore surface). We believe that this is because the strong interaction of the net charge in the sodium ion enhances the development of its solvation structure. This value shows excellent agreement with the experiment which finds 4.82 [41].

4.4.3 Effect of Water Contents on Sodium Diffusion

The diffusion coefficient of the sodium ion was calculated at pressures ranging from 0.1013 to 101.3250 kPa, as summarized at Table 4.1. To characterize the nature of the diffusion, Figure 4.6 shows the log-log plot of the mean square displacements (MSD) versus time. For times up to ~ 20 ps, the MSD increases as a function of $t^{1/2}$ indicating single file diffusion (SFD) behavior. For simulation times longer than 20 ps, the MSD shows a normal Fickian behavior ($MSD \propto t$). This transition of MSD from SFD to normal Fickian diffusion occurs when the pore confines the particles but still allows the particles to pass by each other [42]. In the long time Fickian regime, we obtained the diffusion coefficient D from the mean square displacements of the sodium ions using Equation 4.3,

$$D = \langle (r(t) - r(0))^2 \rangle / 6t. \quad (4.3)$$

In order to examine how the dynamics of sodium ion is influenced by its water solvation shell, we analyzed the diffusion coefficient of sodium ion versus water coordination number at 298.15 K. From Figure 4.7, we observed a dramatic jump at about $CN = 4.5$ that corresponds to the point of the water uptake saturation in the absorption isotherm (Figure 4.2). Indeed, Faux and his co-workers [43, 44, 45] reported theoretical studies that the diffusion coefficient of sodium in zeolite-4A system increases from $1 \times 10^{-7} \text{ cm}^2/\text{s}$ to $10 \times 10^{-7} \text{ cm}^2/\text{s}$ as the number of water molecules per unit cell increases from 0 to 224 in agreement with the trend and order of magnitude of the diffusion coefficient in our simulations. Furthermore, Faux *et al.* also observed a sudden jump of the sodium diffusion coefficient between 112 and 168 water molecules per unit cell, but did not explain the origin. We believe that this results directly from the degree of solvation. This spontaneous condensation of water (discussed in Section 4.4.1), leads to two regimes for the ionic diffusion in the presence of water. Detailed analysis of sodium ion trajectories allows us to enunciate why a threshold amount of water uptake is critical to enhance the diffusion of the ion from the microscopic point of view. The doped AlO_4^- sites are Brønsted acid sites [46] that bound the nonframework cations via strong Coulomb interaction. Parts a and b of Figure 4.8 show the time profile of the Al-Na distances for the good solvation regime (vapor pressure = 101.3250 kPa) and the poor solvation regime (vapor

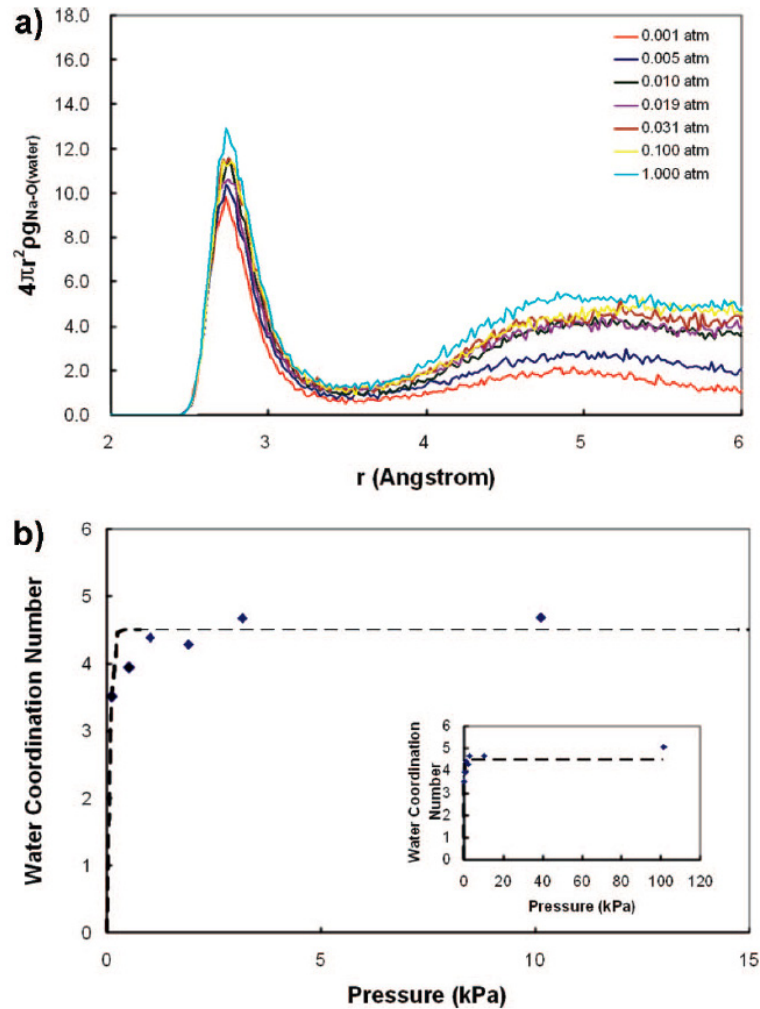


Figure 4.5: (a) Probability of finding sodium ions at a specific distance from each water molecule. This is obtained as the product of pair correlation functions of sodium atoms and water oxygen, $g_{Na-O}(water)$ with water density ρ and $4\pi r^2$. (b) Water coordination number (CN) of sodium ions as a function of pressure. The CN of water molecule is obtained from the integration of curve a up to first minimum, which is at 3.5 Å. The saturated value of CN of the absorbed phase (~ 5.0) is same to the CN of the bulk phase.

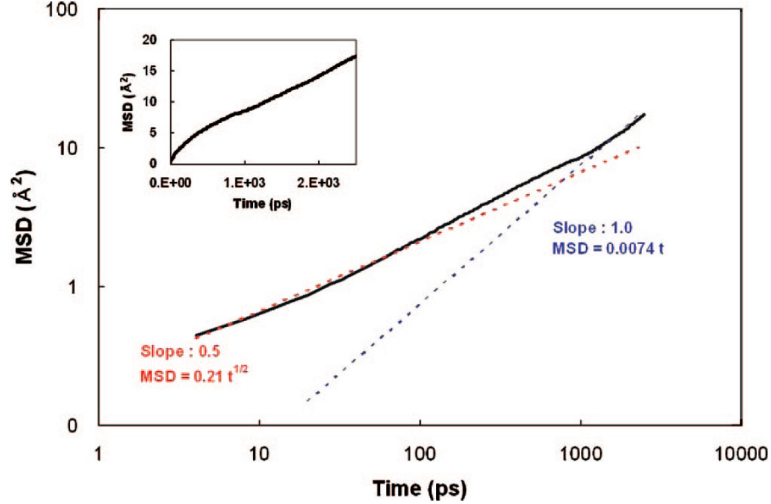


Figure 4.6: Log-log plot of mean square displacements (MSD) vs time at 298.15 K and 101.3250 kPa based on a trajectory of 12 ns. Initially the MSD shows $\text{MSD} \propto t^{1/2}$ up to $t \approx 20$ ps, but the times $> \sim 2$ ns, we see normal 3D Fickian behavior ($\text{MSD} \propto t$). The Fickian regime leads to a diffusion coefficient of $D = 1.233 \times 10^{-7} \text{ cm}^2/\text{s}$.

Table 4.1: Vapor Pressures, Water Uptake/Cell, Water Coordination Numbers of the Water Molecule (up to 3.7 Å Cutoff), Water Coordination Numbers of the Sodium Ion (up to 3.5 Å Cutoff), and Diffusion Coefficients from NPT MD at Temperature of 298.15 K

vapor pressure (kPa)	water uptake/cell	CN (water)	CN (sodium)	diffusion coefficient (cm^2/s)
0.1013	10.15	1.55	3.51	$(0.338 \pm 0.033) \times 10^{-7}$
0.5066	16.57	2.22	3.94	$(0.382 \pm 0.048) \times 10^{-7}$
1.0133	30.08	3.01	4.39	$(0.642 \pm 0.219) \times 10^{-7}$
1.9006	40.10	3.16	4.29	$(1.431 \pm 0.041) \times 10^{-7}$
3.1677	41.86	3.29	4.67	$(1.170 \pm 0.035) \times 10^{-7}$
10.1325	46.18	3.54	4.68	$(1.478 \pm 0.368) \times 10^{-7}$
101.3250	50.00	3.77	5.04	$(1.466 \pm 0.601) \times 10^{-7}$

pressure = 0.1013 kPa), respectively. This shows clearly that each sodium ion localizes within ~ 5 Å of one of the aluminum-doped sites and diffuses by hopping from one site to a nearest neighbor aluminum site. Thus, the diffusion of sodium ion occurs through the hopping mechanism between AlO_4^- sites (the Brönsted acid sites) with the energy barrier of 3.5 – 4.0 kcal/mol caused by the electrostatic interaction. Figure 4.8a indicates that the hopping events occur every 2 ns on average in the good solvation regime, whereas Figure 4.8b shows just 1 hop within 12 ns in the poor solvation regime. This explains why the diffusion coefficient of sodium ion is ~ 10 times larger in the good solvation regime than in the poor solvation regime as in Table 4.1. Sufficient numbers of water molecules are the most critical in creating solvation cage and helping the ionic hopping.

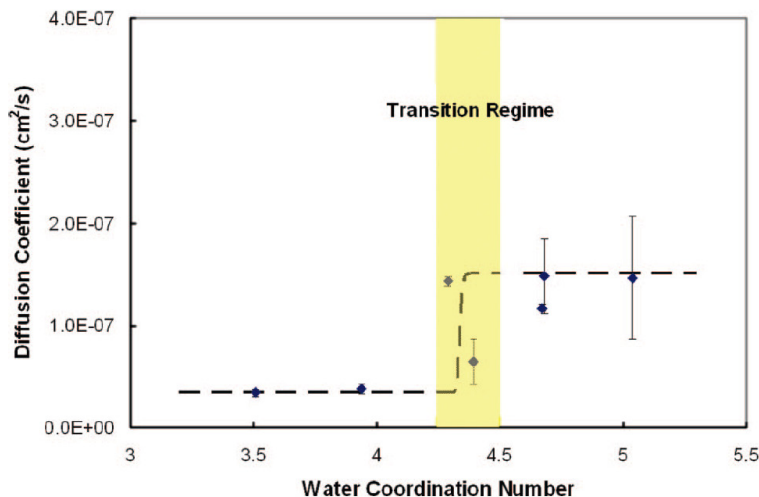


Figure 4.7: Dependence of diffusion coefficient of sodium ion on water coordination number (CN) of sodium ion. The diffusion coefficients were calculated from three partitioned trajectories of 12 ns NPT simulations (each partition has 4 ns length), and the error bars were evaluated from the diffusion coefficients obtained from the three partitioned trajectories. This represents pressures from 0.1013 to 101.3250 kPa at 298.15 K. At a pressure of ~ 2.0 kPa, we find an abrupt change in the water CN. When the sodium ion is solvated by > 4.5 water molecules, its diffusion coefficient increases abruptly by a factor of 3.5. The dashed line is to guide the eye.

4.4.4 Effect of Temperature on Sodium Diffusion

We calculated the diffusion coefficients of the sodium ions confined in the aluminosilicate zeolite BEA membrane are obtained for various temperatures ranging 298.15 K to 453.15 K. For each temperature, the amount of water uptake was determined using GCMC simulation (Figure 4.3). The temperature effect on the sodium diffusion was taken from MD simulations based on the hydrated zeolite. These diffusion coefficients are presented in Table 4.2 and Figure 4.9. Up to 373.15 K, the diffusion coefficient of sodium ion increases with increasing temperature, as expected for a normal activated process. However, we observe from Figure 4.9 that the diffusion coefficient decreases with increasing temperature from 373.15 K to 453.15 K. This anomaly is a consequence of the less hydration of the zeolite at high temperature as previously discussed in Section 4.4.2. Here, the insufficient water absorption results in a less developed solvation shell, which cannot facilitate the sodium ion hopping events. Thus, the diffusion coefficient decreases at high temperature range with less number of water molecules. Therefore, just as in the discussion about good solvation and poor solvation regimes that depend on the vapor pressure, we consider that the good solvation regime applies up to 373.15 K, while the poor solvation regime applies beyond 400 K (the 393.15 K point lies within the transition regime.)

Normally, the temperature dependence for diffusion coefficient is written in terms of a standard Arrhenius equation, Equation 4.4.

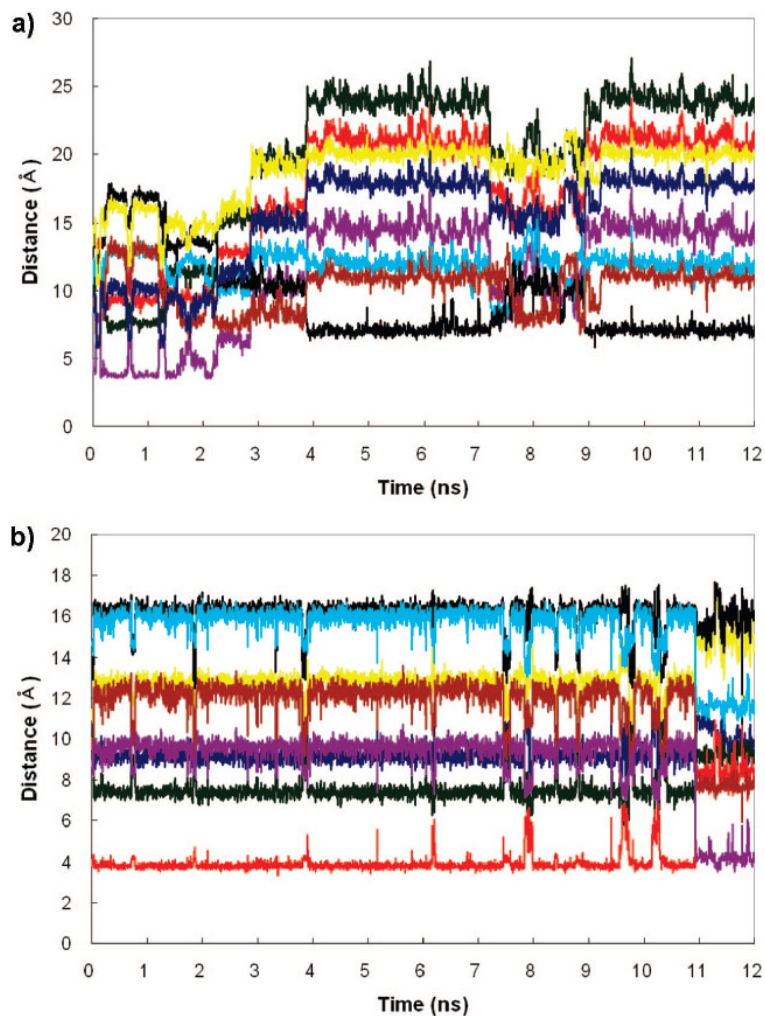


Figure 4.8: Time dependence of the distances of one sodium ion to all 8 aluminum atoms of the zeolite membrane. The distance to each aluminum atom is shown with a different color. (a) Vapor pressure is 101.3250 kPa (good solvation regime) at 298.15 K. This shows that it took 2 ns for the Na to hop from a position 4.8 Å from the purple Al to a position 7.5 Å from the black Al. Here a distance of 4.8 Å indicates one water shell between the Na and the Al, while 7.5 Å indicates separate water shells around each; (b) vapor pressure is 0.1013 kPa (poor solvation regime) at 298.15 K. In this case the Na remains at 4 Å from the Al which indicates that the Na remains coordinated to the O of the Al.

$$D = A_{diff} \exp\left(-\frac{\Delta E}{k_B T}\right), \quad (4.4)$$

where the ΔE implies the energy barrier for the hopping from one site to another site. $A_{diff} = L^2 k_B T / h \exp(ns/R)$ is the prefactor, a product of frequency factor (activation entropy term) with a hopping-related length (L). k_B is the Boltzmann constant and T is the absolute temperature. In order to include the solvation effect, we define the stabilization energy ΔE_{solv} due to the solvation. This leads to a modified Equation 4.4 where $A_{diff-solve}$ now includes a correction for solvation.

$$D = A_{diff-solve} \exp\left(-\frac{\Delta E - \Delta E_{solv}}{k_B T}\right). \quad (4.5)$$

We assume that the ΔE_{solv} is a step function which is zero for the poor solvation regime and nonzero for the good solvation regime, which implies that the incomplete solvation shell of sodium ion has no effect to stabilization. The Arrhenius plot for each regime is shown in Figure 4.10 and the curve for each regime is fitted with a linear equation using least-squares fitting method. From the slope of the fitted line, we estimate the $\Delta E = 3.810$ kcal/mol for the poor solvation regime and the $\Delta E - \Delta E_{solv} = 3.540$ kcal/mol for the good solvation regime. Thus, the stabilization energy by solvation (ΔE_{solv}) becomes 0.270 kcal/mol. The y -intercepts lead to $A_{diff} = -10.70$ cm²/s and $A_{diff-solve} = -9.76$ cm²/s. The nearly unit value for A suggests that the diffusion mechanism for both regimes is basically identical, supporting the Equation 4.5. Although no experimental data has been reported for the energy barrier of the diffusion of sodium ion, the energy barrier for the diffusion of sodium ion in the β alumina (known as a good ionic conductor) has been measured experimentally [47, 48]. Since the sodium ion in the β alumina is also believed to jump around aluminum oxide sites, these values should be comparable with ours. Kim *et al.* [47] reported that the barrier as 3.275 kcal/mol from the measurement of ionic conductivity and 3.897 kcal/mol from the measurement of sodium tracer diffusion. Also the values from Whittingham and Huggins [48] obtained values of 3.81 kcal/mol from the tracer diffusion measurement and 3.95 kcal/mol from the dielectric loss measurement. All these values are very comparable to our ΔE value of 3.540 kcal/mol, supporting the accuracy of our simulations. On the basis of these comparable values of the energy barrier, we expect that the stabilization energy for the hydrated system would also be reasonable although the effect of hydration in such aluminosilicate system has yet been reported.

4.5 Conclusions

Combining GCMC and MD simulations, we studied the effect of hydration on the sodium dynamics. From the absorption isotherm, we observed that the water absorption in BEA zeolites proceeds with a spontaneous condensation at a pressure of 3.5 kPa and a temperature of 298.15 K even though

Table 4.2: Temperature, Water Uptake/Cell, and Diffusion Coefficients at Constant Pressure Condition of 101.3250 kPa

temperature (K)	water uptake/cell	CN (water)	CN (sodium)	diffusion coefficient (cm ² /s)
298.15	50.00	3.77	5.04	$(1.466 \pm 0.601) \times 10^{-7}$
325.15	46.25	3.73	4.71	$(2.372 \pm 0.024) \times 10^{-7}$
353.15	42.12	3.72	4.24	$(3.762 \pm 0.822) \times 10^{-7}$
373.15	36.50	3.46	4.39	$(4.806 \pm 0.226) \times 10^{-7}$
393.15	26.17	3.27	4.08	$(3.725 \pm 0.188) \times 10^{-7}$
423.15	13.73	2.45	3.63	$(2.630 \pm 0.459) \times 10^{-7}$
453.15	9.75	1.74	3.42	$(3.042 \pm 0.301) \times 10^{-7}$

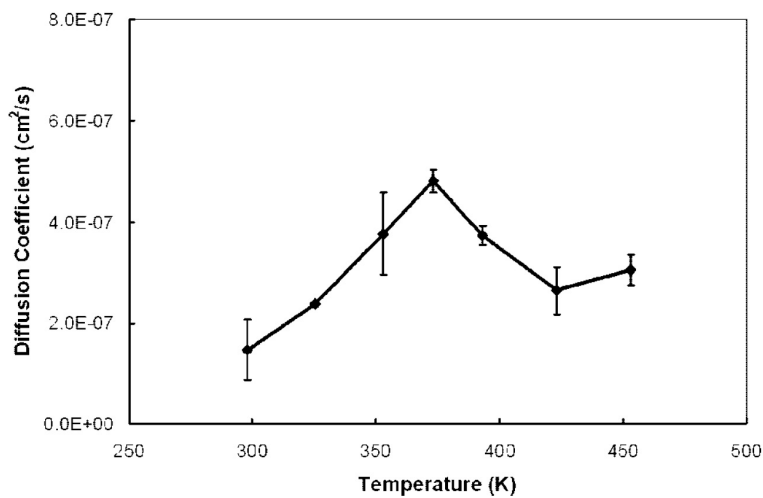


Figure 4.9: Dependence of the sodium diffusion coefficient on the temperature for a vapor pressure of 101.3250 kPa. The diffusion coefficients were calculated from three partitioned trajectories of 12 ns NPT simulations (each partition has 4 ns length), and the error bars were evaluated from the diffusion coefficients obtained from the three partitioned trajectories. Up to 373.15 K, the diffusion coefficient increases with increasing temperature, whereas it decreases beyond 373.15 K due to the depletion of the water solvation.

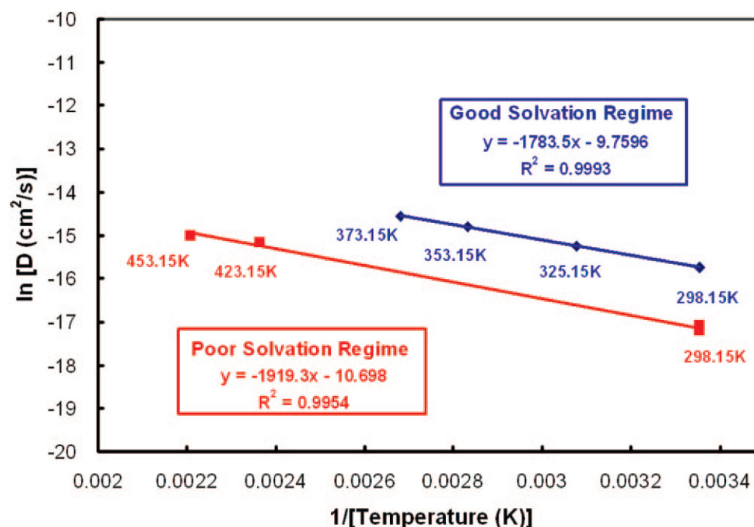


Figure 4.10: Arrhenius plots of diffusion coefficient from each solvation regime: the red squares are for the poor solvation regime and the blue diamond is for the good solvation regime. The solid black line is a linear fitting of each regime. This leads to $D_{300K} = 3.762 \times 10^{-8} \text{ cm}^2/\text{s}$ and $E_{act} = 3.810 \text{ kcal/mol}$ for the poor solvation regime and $D_{300K} = 1.512 \times 10^{-7} \text{ cm}^2/\text{s}$ and $E_{act} = 3.540 \text{ kcal/mol}$ for the good solvation regime, and the equation of each fitted line and R^2 value are inset in the figure.

the internal space of zeolite remains hydrophobic. Below the pressure of 101.3250 kPa, the water uptake of the zeolite decreases monotonically with increasing temperature. From the pair correlation functions, we found that the tetrahedral water solvation structure for water molecule is suppressed by the hydrophobic pore surfaces. In contrast, the water solvation structure surrounding the sodium ion remains ~ 5.0 . This difference is a direct consequence of the strong electrostatic interaction of the positively charged sodium ion with water molecules.

The MD trajectories indicate that the sodium ions are electrostatically bound to the aluminum-doped sites and the diffusion of the sodium ions proceeds via hopping mechanism among these aluminum-doped sites (Figure 4.8).

On the basis of the spontaneous water condensation process, we found the two regimes: a good solvation regime below 373.15 K and a poor solvation regime above 400 K. The Arrhenius plot of each regime leads to an energy barrier of 3.540 kcal/mol for the diffusion of sodium ion for the good solvation regime and of 3.810 kcal/mol for the poor solvation regime. This leads to an estimate of 0.270 kcal/mol for the stabilization energy due to the solvation of sodium ion.

This study of the sodium diffusion through BEA zeolite shows that the ionic diffusion in the confined geometry depends on the degree of solvation by water which distinguishes it from bulk diffusion. As a next step, we are planning to directly investigate the proton diffusion through the aluminum-doped zeolite BEA system based on results of the current study.

4.6 Acknowledgments

This research was supported in part by the Department of Energy (DE-FG02-05ER15716, William S. Millman). The facilities of the Materials and Process Simulation Center used for these studies were supported by DURIP-ARO, DURIP-ONR.

Bibliography

- [1] Zones, S. I.; Davis, M. E. *Curr. Opin. Solid State Mater. Sci.* **1996**, 1, 107-117.
- [2] Davis, M. E. *Nature* **2002**, 417, 813-821.
- [3] Truskett, T. M.; Debenedetti, P. G.; Torquato, S. *J. Chem. Phys.* **2001**, 114, 2401-2418.
- [4] Gallo, P.; Ricci, M. A.; Rovere, M. *J. Chem. Phys.* **2002**, 116, 342-346.
- [5] Giaya, A.; Thompson, R. W. *J. Chem. Phys.* **2002**, 117, 3464-3475.
- [6] Brovchenko, I.; Geiger, A.; Oleinikova, A. *J. Chem. Phys.* **2004**, 120, 1958-1972.
- [7] Maurin, G.; Bell, R. G.; Devautour, S.; Henn, F.; Giuntini, J. C. *J. Phys. Chem. B* **2004**, 108, 3739-3745.
- [8] Lee, Y.; Vogt, T.; Hriljac, J. A.; Parise, J. B.; Hanson, J. C.; Kim, S. J. *Nature* **2002**, 420, 485-489.
- [9] Demkov, A. A.; Sankey, O. F. *Chem. Mater.* **1996**, 8, 1793-1806.
- [10] Maurin, G.; Llewellyn, P.; Poyet, T.; Kuchta, B. *J. Phys. Chem. B* **2005**, 109, 125-129.
- [11] Calero, S.; Dubbeldam, D.; Krishna, R.; Smit, B.; Vlugt, T. J. H.; Denayer, J. F. M.; Martens, J. A.; Maesen, T. L. M. *J. Am. Chem. Soc.* **2004**, 126, 11377-11386.
- [12] Carrette, L.; Friedrich, K. A.; Stimming, U. *ChemPhysChem* **2000**, 1, 162-193.
- [13] Kreuer, K. D. *J. Membr. Sci.* **2001**, 185, 29-39.
- [14] Paddison, S. *J. Annu. Rev. Mater. Res.* **2003**, 33, 289-319.
- [15] Li, Q. F.; He, R. H.; Jensen, J. O.; Bjerrum, N. *J. Chem. Mater.* **2003**, 15, 4896-4915.
- [16] Mauritz, K. A.; Moore, R. B. *Chem. Rev.* **2004**, 104, 4535-4585.
- [17] Hickner, M. A.; Pivovar, B. S. *Fuel Cells* **2005**, 5, 213-229.

- [18] Holmberg, B. A.; Hwang, S. J.; Davis, M. E.; Yan, Y. S. *Microporous Mesoporous Mater.* **2005**, 80, 347-356.
- [19] Burchart, E. D.; Verheij, V. A.; Vanbekkum, H.; Vandegraaf, B. *Zeolites* **1992**, 12, 183-189.
- [20] Levitt, M.; Hirshberg, M.; Sharon, R.; Laidig, K. E.; Daggett, V. *J. Phys. Chem. B* **1997**, 101, 5051-5061.
- [21] Rappe, A. K.; Goddard, W. A. *J. Phys. Chem.* **1991**, 95, 3358-3363.
- [22] Hockney, R. W.; Eastwood, J. W. *Computer simulation using particles*; McGraw-Hill: New York, 1981.
- [23] Rasmus, D. M.; Hall, C. K. *AIChE J.* **1991**, 37, 769-779.
- [24] Goodbody, S. J.; Watanabe, K.; Macgowan, D.; Walton, J.; Quirke, N. *J. Chem. Soc., Faraday Trans.* **1991**, 87, 1951-1958.
- [25] Accelrys Inc.: San Diego, CA, 1999.
- [26] Allen, M. P.; Tildesley, D. J. *Computer Simulation of Liquids*; Oxford University Press: Oxford, U.K., 1987.
- [27] Frenkel, D.; Smit, B. *Understanding Molecular Simulations: From Algorithms to Applications*; Academic Press: London, 2002.
- [28] Plimpton, S. J. *Comput. Phys.* **1995**, 117, 1-19.
- [29] Plimpton, S. J.; Pollock, R.; Stevens, M. Minneapolis, MN, 1997.
- [30] Swope, W. C.; Andersen, H. C.; Berens, P. H.; Wilson, K. R. *J. Chem. Phys.* **1982**, 76, 637-649.
- [31] Baerlocher, C.; McCusker, L. B. Database of zeolite Structures: <http://www.iza-structure.org/databases/>.
- [32] Di Lella, A.; Desbiens, N.; Boutin, A.; Demachy, I.; Ungerer, P.; Bellat, J. P.; Fuchs, A. H. *Phys. Chem. Chem. Phys.* **2006**, 8, 5396-5406.
- [33] Desbiens, N.; Demachy, I.; Fuchs, A. H.; Kirsch-Rodeschini, H.; Soulard, M.; Patarin, J. *Angew. Chem., Int. Ed.* **2005**, 44, 5310-5313.
- [34] Desbiens, N.; Boutin, A.; Demachy, I. *J. Phys. Chem. B* **2005**, 109, 24071-24076.
- [35] Hummer, G.; Rasaiah, J. C.; Noworyta, J. P. *Nature* **2001**, 414, 188-190.
- [36] Gorbach, A.; Stegmaier, M.; Eigenberger, G. *Ads.-J. Int. Ads. Soc.* **2004**, 10, 29-46.

- [37] Soper, A. K.; Phillips, M. G. *Chem. Phys.* **1986**, 107, 47-60.
- [38] Jang, S. S.; Goddard, W. A., III *J. Phys. Chem. C* **2007**, 111, 2759-2769.
- [39] Jang, S. S.; Lin, S. T.; Cagin, T.; Molinero, V.; Goddard, W. A., III *J. Phys. Chem. B* **2005**, 109, 10154-10167.
- [40] Jang, S. S.; Molinero, V.; Cagin, T.; Goddard, W. A., III *J. Phys. Chem. B* **2004**, 108, 3149-3157.
- [41] Vaudry, F.; DiRenzo, F.; Espiau, P.; Fajula, F.; Schulz, P. *Zeolites* **1997**, 19, 253-258.
- [42] Keffer, D.; McCormick, A. V.; Davis, H. T. *Mol. Phys.* **1996**, 87, 367-387.
- [43] Faux, D. A.; Smith, W.; Forester, T. R. *J. Phys. Chem. B* **1997**, 101, 1762-1768.
- [44] Faux, D. A. *J. Phys. Chem. B* **1998**, 102, 10658-10662.
- [45] Faux, D. A. *J. Phys. Chem. B* **1999**, 103, 7803-7808.
- [46] Franke, M. E.; Simon, U. *Phys. Status Solidi B: Basic Res.* **2000**, 218, 287-290.
- [47] Kim, K. K.; Mundy, J. N.; Chen, W. K. *J. Phys. Chem. Solids* **1979**, 40, 743-755.
- [48] Whitting, Ms; Huggins, R. A. *J. Chem. Phys.* **1971**, 54, 414.

Chapter 5

Experimental and Theoretical Investigation into the Correlation between Mass and Ion Mobility for Choline and Other Ammonium Cations in N₂

Reproduced with permission from Kim, H.; Kim, H. I.; Johnson, P. V.; Beegle, L. W.; Beauchamp, J. L.; Goddard, W. A.; Kanik, I. Anal. Chem. 2008, 80, 1928. Copyright 2008 American Chemical Society.

5.1 Abstract

A number of tertiary amine and quaternary ammonium cations spanning a mass range of 60–146 amu (trimethylamine, tetramethylammonium, trimethylethylammonium, *N,N*-dimethylaminoethanol, choline, *N,N*-dimethylglycine, betaine, acetylcholine, (3-carboxypropyl)trimethylammonium) were investigated using electrospray ionization ion mobility spectrometry. Measured ion mobilities demonstrate a high correlation between mass and mobility in N₂. In addition, identical mobilities within experimental uncertainties are observed for structurally dissimilar ions with similar ion masses. For example, dimethylethylammonium (88 amu) cations and protonated *N,N*-dimethylaminoethanol cations (90 amu) show identical mobilities (1.93 cm² V⁻¹ s⁻¹) though *N,N*-dimethylaminoethanol contains a hydroxyl functional group while dimethylethylammonium only contains alkyl groups. Computational analysis was performed using the modified trajectory (TJ) method with nonspherical N₂ molecules as the drift gas. The sensitivity of the ammonium cation collision cross-sections to the details of the ion-neutral interactions was investigated and compared to other classes of organic molecules (carboxylic acids and abiotic amino acids). The specific charge distribution of the

molecular ions in the investigated mass range has an insignificant affect on the collision cross-section.

5.2 Introduction

The development of soft ionization methods such as electrospray ionization (ESI) [1] have expanded the application of ion mobility spectrometry (IMS) [2, 3] to structural investigations of nonvolatile biomolecules in the gas phase [4]. ESI allows soft sampling by transferring intact ions directly from the solution phase to the gas phase. Using this distinctive advantage of ESI, the shapes and sizes of various biomolecular ions from monomeric molecules to macrosized protein complexes have been investigated. The combination of ESI and IMS has facilitated conformational studies of macroions including clusters (oligomers) [5, 6, 7], peptides [8, 9], and proteins [10, 11, 12]. In addition, ion mobilities of organic molecules such as amino acids [13, 14], carboxylic acids [15], and dinucleotides [16], as well as other organic molecules [17, 18], have been reported.

To provide a firm foundation for studies of the shapes of complex organic molecular ions using IMS, many research groups have endeavored to develop theoretical models to predict ion mobilities and related cross-sections of gas-phase molecular ions. Griffin *et al.* [19] have shown that mass and mobility are only correlated on the order of 20 % within a collection of structurally unrelated compounds spanning a mass range of $\sim 70 - 500$ amu. The correlations are improved up to 2 % when only structurally related compounds are considered. Karpas and co-workers have established models to predict the mobility for a number of compound classifications including acetyls, aromatic amines, and aliphatic amines drifting in He, N₂, air, Ar, CO₂, and SF₆ [20, 21]. Our laboratory has applied a 12 - 4 potential model in studies of amino acids and carboxylic acids drifting in N₂ and CO₂ [14, 15]. Recently, Steiner *et al.* have reported predictions of mobilities for a series of different classes of amines (primary, secondary, tertiary) in various drift gases, such as He, Ne, Ar, N₂, and CO₂, using several theoretical models (rigid-sphere, polarization-limit, 12 - 6 - 4, and 12 - 4 potential model) [22].

Computational modeling related to interpretation of IMS data has been developed by several groups. Efforts toward theoretical ion mobility predictions using computational methods face difficulties associated with complicated collision integrals and the design of functions to accurately describe the ion-neutral interaction potential. Bowers and co-workers have proposed a project approximation method, which is based on a hard-sphere description of the interaction potential [23]. The trajectory (TJ) method, which has been proposed by Jarrold and co-workers, adopts more realistic soft-core interactions [24].

Ion mobility constants (K) can be derived from the collision cross-section using the equation [25]

$$K = \frac{(18\pi)^{1/2}}{16} \frac{1}{\mu^{1/2}} \frac{ze}{(k_B T)^{1/2}} \frac{1}{\Omega_D N}, \quad (5.1)$$

where μ is reduced mass, N is the number density of the neutral gas molecule, and z is the charge of the ion. The collision cross-section, Ω_D , is given by [24]

$$\Omega_D = \frac{1}{8\pi^2} \int_0^{2\pi} d\theta \int_0^\pi d\phi \int_0^{2\pi} d\gamma \frac{\pi}{8} \left(\frac{\mu}{k_B T} \right)^3 \int_0^\infty dg e^{-\mu/2k_B T} g^5 \int_0^\infty db 2b (1 - \cos \chi(\theta, \phi, \gamma, g, b)) \quad (5.2)$$

and θ , ϕ , and γ are the three-dimensional collision angles, g is the relative velocity, and b is the impact parameter. Because the scattering angle $\chi(\theta, \phi, \gamma, g, b)$ depends on the pairwise potential between the ion and neutral gas molecules, the accuracy of computed cross-section values is determined by the quality of the interaction potential model. The potential employed in the TJ method [24] for a He drift gas is given by

$$\Phi(\theta, \phi, \gamma, b, r) = 4\epsilon \sum_i^n \left[\left(\frac{\sigma}{r_i} \right)^{12} - \left(\frac{\sigma}{r_i} \right)^6 \right] - \frac{\alpha}{2} \left(\frac{ze}{n} \right)^2 \left[\left(\sum_i^n \frac{x_i}{r_i^3} \right)^2 + \left(\sum_i^n \frac{y_i}{r_i^3} \right)^2 + \left(\sum_i^n \frac{z_i}{r_i^3} \right)^2 \right]. \quad (5.3)$$

The first term is a sum over short-range van der Waals interactions, and the second term represents long-range ion-induced dipole interactions. In the expression, ϵ is the depth of the potential well, σ is the value of distance (r) between the centers of mass of the each atom in the ion and neutral gas molecule at the potential minimum, and R is the neutral polarizability. The coordinates, r_i , x_i , y_i , and z_i , are defined by the relative positions of the atoms with respect to the neutral. Utilizing the given ion-neutral interaction potential functions, the integrals in Equation 5.2 can be processed numerically. Monte Carlo integration schemes are used for the integration over θ , ϕ , γ , and b . The numerical integration over g is performed using a combination of the Runge-Kutta-Gill integration method and the Adams-Moulton predictor corrector integration method.

Choline is a precursor for phosphatidylcholine, sphingomyelin, and other important biological molecules [26]. Further, it is a component of cell membrane lipids in biological systems, and it plays an important role in their repair. Choline can be oxidized to betaine, which is readily demethylated to yield N , N -dimethylglycine [26]. Decomposition of choline yields trimethylamine and dimethylamine [27]. Searching for lipids and their components (i.e., choline) may be a valuable strategy in the search for evidence of extinct or extant life elsewhere in the cosmos. Under the high oxidizing conditions and significant ultraviolet flux found on the surface of Mars, one would expect decomposition products of lipids to include various alkylamines [28].

In the present study, mobilities have been measured for a number of quaternary and tertiary ammonium cations related to choline and its derivatives drifting in N_2 . Of particular interest was the possible dependence of mass-mobility correlations with the heavy atom (C, N, O) complements present in the molecular ion, comparing, for example, alkylated ammonium ions to abiotic amino acids (betaine and N , N -dimethylglycine). A modified TJ method for the ion-neutral interaction,

to account for the potential associated with the nonspherical drift gas N_2 , has been applied to predict cross-sections of these polyatomic ammonium cations and to test the sensitivity of collision cross-section to details of the ion-neutral interaction. Comparisons of the results from the ammonium cations to other classes of organic molecules (carboxylic acids and abiotic amino acids) are presented. The origin of the observed correlation between mass and mobility of ammonium cations is discussed.

5.3 Experimental Section

5.3.1 Chemicals and Reagents

All the compounds studied in this work were purchased from Sigma Aldrich (St. Louis, MO) and were used without further purification. All solvents (water, methanol, acetic acid) were HPLC grade and were purchased from EMD Chemicals Inc. (Gibbstown, NJ). Quaternary ammonium samples were prepared by dissolving known quantities of ammonium ions in a solvent consisting of 50 % water and 50 % methanol by volume to give sample concentrations in the range of 100 μ M. Tertiary amine samples were prepared as 300 μ M in a solvent of 50:50 water and methanol with 1 % acetic acid by volume.

5.3.2 Electrospray Ionization Ion Mobility Spectrometer

The ESI-IMS instrument and the data acquisition system used in this investigation were based on designs previously described by Hill and co-workers [17, 29] and have been described in detail by Johnson *et al.* [14]. The drift length of the ion mobility spectrometer was 13.65 cm and was operated in the positive mode. A drift voltage of 3988 V, corresponding to electric field strength of 292 V/cm, was employed. All measurements were made at local atmospheric pressure (\sim 730 Torr) while a counterflow of the preheated drift gas was introduced at the detection end of the drift region at a flow rate of \sim 800 mL/min. The sample solution was delivered by an Eldex Micropro liquid chromatography pump at a flow rate of 3 μ L/min into a stainless steel electrospray needle, which was held at a potential 3 – 4 kV above the entrance to the desolvation region of the spectrometer. The gap between the electrospray needle and the entrance electrode was \sim 2 cm.

Ions were introduced into the drift region through the ion gate in 0.2-ms pulses. Signals collected at the Faraday cup were amplified by a factor of 10^9 (Stanford Research Systems model SR570 low-noise current preamplifier) and recorded as a function of drift time in 0.02-ms-wide channels. Typically, 1000 individual 0 – 25-ms scans were averaged to produce the final spectra used in the analysis. Resolution of the instrument was found to be \sim 0.43 ms full width at half-maximum (FWHM) with drift times in the range 12 – 17 ms for the ions studied and the parameters employed in these experiments.

Throughout this work, it was assumed that ESI of the prepared samples resulted in singly charged ammonium cations. The assumption was confirmed by ESI mass spectrometric analysis using a Finnigan LCQ Deca XP ion trap mass spectrometer. The mass spectra of all nine samples in the present study show singly charged monomeric molecular cations as the major ionic species. Since the experiments were conducted with the drift cell at 473 K, it was further assumed that there was no significant water cluster formation based on previous IMS-MS studies [18, 30].

Reduced ion mobilities, K_0 , were determined from the recorded spectra and the experimental parameters according to the usual relation,

$$K_0 = \left(\frac{273 \text{ K}}{T} \right) \left(\frac{P}{760 \text{ Torr}} \right) \frac{D^2}{Vt}, \quad (5.4)$$

where V is the voltage drop across the drift region, D is the drift length, t is the drift time, P is the pressure, and T is the temperature. With the above parameters expressed in units of V, cm, s, Torr, and K, respectively, Equation 5.4 gave the reduced mobility in the typical units of $\text{cm}^2 \text{V}^{-1} \text{s}^{-1}$. The experimental uncertainties of the determined K_0 values are estimated to be $\sim 3\%$ based on the half width at half-maximum (HWHM) of each drift time peak in the averaged ion mobility spectra.

5.3.3 Computational Modeling

More than 500 possible molecular conformations were investigated through dihedral angles of -180° to 180° at the PM5 level using CAChe 6.1.12 (Fujitsu, Beaverton, OR). Then, the lowest-energy structures were determined using density functional theory (DFT) with a number of candidate low-energy structures from the previous PM5 calculations. DFT calculations were performed using Jaguar 6.0 (Schrödinger, Inc., Portland, OR) utilizing the Becke three-parameter functional (B3) [31] combined with the correlation functional of Lee, Yang, and Parr (LYP) [32], using the 6-31G** basis set [33]. The optimized structures of ammonium cations investigated in the present study are shown in Figure 5.2.

The TJ method [24], originally developed by Jarrold and coworkers, was modified to describe the interaction between ions and an N_2 drift gas and expand the applicability of the TJ method beyond cases of ions drifting in He. As shown in Equation 5.3, the potential used in the original TJ method consists of two terms representing van der Waals and ion-induced dipole interactions, which are characterized by the Lennard-Jones parameters (ϵ, σ) and the neutral polarizability (α), respectively. We set the polarizability of N_2 at the experimentally determined value [34] of $1.710 \times 10^{-24} \text{ cm}^3$ and took the Lennard-Jones parameters described in the universal force field [35], which is a general purpose force field optimized for all the elements in the periodic table. Due to the linear geometry of N_2 , two more consequences should be additionally taken into account; the ion-quadrupole interaction

and the orientation of the molecule. We mimic the quadrupole moment of N_2 , $(-4.65 \pm 0.08) \times 10^{-40}$ C cm² [36], by displacing charges by negative q ($0.4825e$) to each nitrogen atom and one positive $2q$ at the center of the nitrogen molecule. Hence, the ion-quadrupole potential can be expressed with simple summations of partial charges as follows:

$$\Phi_{IQ} = \sum_{j=1}^3 \sum_i^n \frac{z_i z_j e^2}{r_{ij}}, \quad (5.5)$$

where indexes i and j denote the atoms of the ion, three points of N_2 . $j = 1$ and 3 indicate the two nitrogen atoms, and $j = 2$ indicates the center of mass position of N_2 .

To consider the orientation of the nitrogen molecule rigorously, all possible trajectories with varying molecular orientations were taken into account. It has been widely accepted that the ion field does not exclusively quench the rotational angular momentum of the neutral molecule and only partial locking occurs during the collision process [37, 38]. Thus, we assumed that the interaction potential averaged over the rotational degree of freedom generates an appropriated average impact parameter [39]. The calculated rotation time of a N_2 molecule (~ 620 ns) implies that approximately three molecular rotations occur during a collision between an ion and N_2 taking place (~ 2 ps). The orientations of N_2 are sampled along with x , y , and z axes to represent all the three-dimensional rotational space. Then the orientation averaged interaction potential is evaluated using Boltzmann weighting. Using these different weights, the orientation averaged interaction potential is evaluated, and this potential is used to compute the collision cross-section.

For the calculations of collision cross-section of ions, it is assumed that the DFT optimized structures are rigid. To ensure that the assumption is valid for the ammonium cations investigated in the present study, the collision cross-sections of two extreme conformations for the largest two ionic molecules, acetylcholine and (3-carboxypropyl)trimethylammonium, are estimated. The DFT calculated electronic energies reveal that the extended structures of both acetylcholine and (3-carboxypropyl)trimethylammonium are unstable by 4.24 and 0.547 kcal/mol, respectively, compared to cyclic structures shown in Figure 5.2. The maximum difference between two conformations of (3-carboxypropyl)-trimethylammonium is calculated as $\sim 7 \text{ \AA}^2$, which we can set as a maximum error bound originating from the structural uncertainty.

5.4 Results

5.4.1 Mass-Mobility Correlation of Ammonium Cations

IMS spectra were obtained as described above. The drift times of the ammonium cations were determined from the location of the peak maximums. Figure 5.1 shows example spectra taken with pure

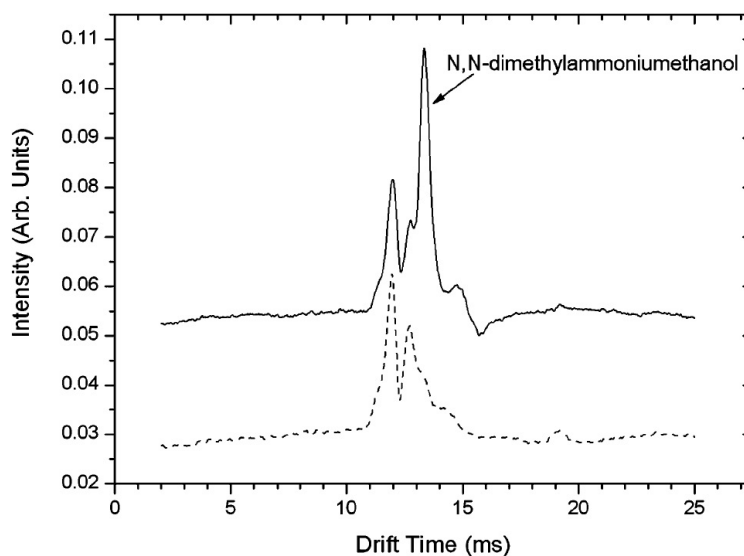


Figure 5.1: Examples of the ion mobility spectra taken in this study. Shown are two spectra taken in 730 Torr N_2 . The electric field strength and the temperature of the drift tube were 292 V/cm and 473 K, respectively. The dash curve is a spectrum taken with pure solvent being introduced to the electrospray needle while the solid curve is a spectrum of solvent and $300 \mu\text{M}$ *N,N*-dimethylammoniummethanol. The two spectra were smoothed (10 point adjacent averaging) and shifted in intensity by an additive constant to avoid overlap. The *N,N*-dimethylammoniummethanol feature is indicated in the figure. The unlabeled features correspond to ionized solvent (water, methanol, acetic acid) and atmospheric constituents ionized through proton transfer (due to the open nature of the ESI-IMS instrument).

solvent being introduced to the electrospray needle and with 300 μM *N,N*-dimethylammoniumethanol dissolved in the solvent. These spectra are characteristic of those considered in this work. Measured drift times, reduced ion mobilities (in N_2 drift gas), and determined Ω_D for the nine ammonium cations chosen for this study are listed in Table 5.1 along with their respective molecular weights. The 12–4 potential model, which has proven satisfactory to model experimental data [14, 15, 20, 21, 22] has been used for the analysis of the experimentally determined mobilities of ammonium cations. The potential is expressed as

$$\Phi(r) = \frac{\epsilon}{2} \left\{ \left(\frac{\sigma - a}{r - a} \right)^{12} - 3 \left(\frac{\sigma - a}{r - a} \right)^4 \right\}, \quad (5.6)$$

where ϵ , r , and σ are defined above and the parameter a is the location of center charge from the center of mass in the ion. Rearrangement of Equation 5.6, along with the substitution of the appropriate constants, yields

$$K_0^{-1} = (1.697 \times 10^{-4}) (\mu T)^{1/2} \sigma^2 \Omega^{(1,1)*}, \quad (5.7)$$

which gives the reduced ion mobility in terms units of $\text{cm}^2 \text{V}^{-1} \text{s}^{-1}$. $\Omega^{(1,1)*}$ is the dimensionless collision integral, where $\Omega_D = \pi \sigma^2 \Omega^{(1,1)*}$. Derivation of Equation 5.7 from Equation 5.6 is well described by Johnson *et al.* [14]. Equation 5.7 was fit to the data set of ammonium ion mobilities in N_2 using a nonlinear least-squares fitting procedure [14]. The plot of K_0^{-1} versus ion mass for ammonium cations drifting in N_2 is shown in Figure 5.2 along with the best fit to the data. As seen in Figure 5.2, all nine ammonium cations investigated in the present study exhibit a good correlation ($R^2 = 0.99$) between mass and mobility of ion. In particular, the two different classes of ammonium cations (tertiary and quaternary) investigated in this study exhibit a common mass-mobility correlation. Further, the heteroatomic complements of the molecular ions do not impact the mass-mobility correlation.

5.4.2 Tertiary and Quaternary Ammonium Cations with Similar Molecular Weights

Two sets of cations, which have similar molecular weights but different structures, were chosen to investigate the influence of the composition and structural details of the ion on the mobility. The molecular weights of trimethylethylammonium and *N,N*-dimethylammoniumethanol are 88 and 90 amu, respectively. There is a significant structural difference between these two ions in addition to variation in the degree of alkylation to the ammonium groups. Protonated *N,N*-dimethylammoniumethanol possesses a hydroxyl group at the ethyl group while trimethylethylammonium possesses only alkyl groups. The molecular weights of choline and *N,N*-dimethylglycine

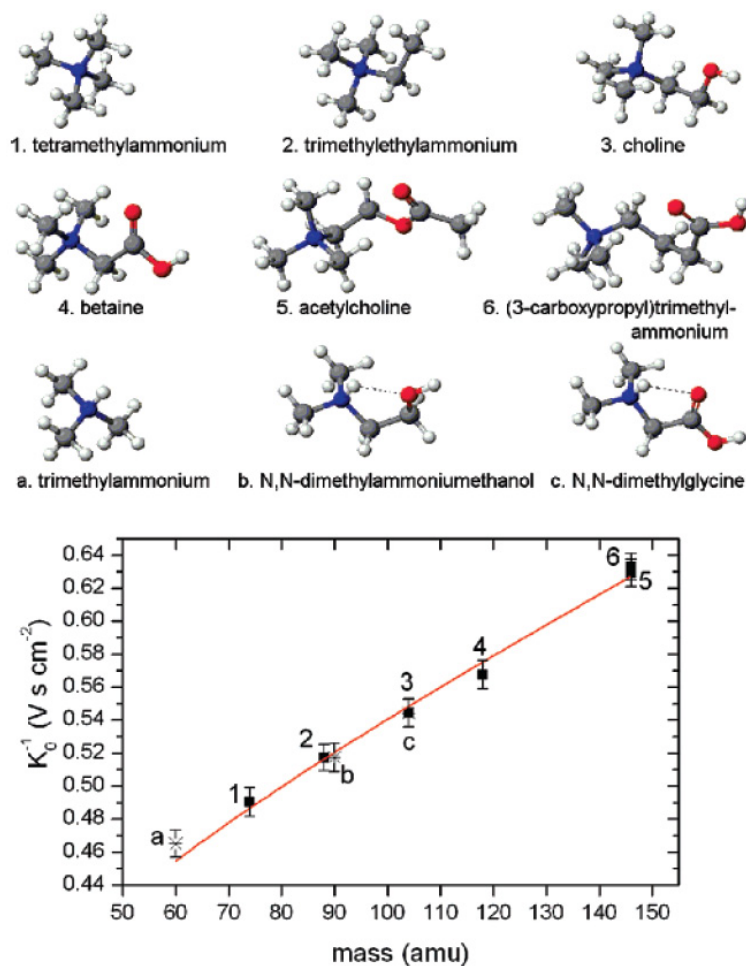


Figure 5.2: Plot of K_0^{-1} for 3° and 4° ammonium cations drifting in N₂ versus ion mass. Experimentally determined data for 3° ammonium and 4° ammonium cations are shown as asterisks and solid squares, respectively. The solid line is the fit of the 12 – 4 potential model to the ammonium cation data set. DFT optimized structure of each numerically or alphabetically labeled ion is shown above. Optimized geometries are obtained at B3LYP/6-31G** level. The hydrogen bonds are indicated with dashed lines.

Table 5.1: Drift Times, Reduced Mobilities, and Collision Cross-Sections of Ammonium Cations in N₂ Drift Gas

ammonium cation	^a MW	^b DT	^c K_0	^d Ω_D
trimethylammonium	60	12.1	2.15	91.2
tetramethylammonium	74	12.7	2.04	95.3
trimethylethylammonium	88	13.4	1.93	102.2
<i>N, N</i> -dimethylammoniumethanol	90	13.4	1.93	100.9
choline	104	14.1	1.84	104.5
<i>N, N</i> -dimethylglycine	104	14.1	1.84	102.3
betaine	118	14.7	1.76	105.3
acetylcholine	146	16.3	1.59	118.5
(3-carboxypropyl)trimethylammonium	146	16.4	1.58	115.9

^aMolecular weight (amu). ^bDrift time (ms). ^cReduced mobility (cm² V⁻¹ s⁻¹). ^dCollision cross-section (Å²).

cation are both 104 amu. Protonated *N, N*-dimethylglycine cations contain a carboxyl group while choline possesses a hydroxyl group. Experimentally determined mobility values of trimethylethylammonium and *N, N*-dimethylammoniumethanol are identical at 1.93 cm² V⁻¹ s⁻¹. Mobilities of both choline and *N, N*-dimethylglycine cation are measured as 1.84 cm² V⁻¹ s⁻¹. It is inferred that the contribution of the oxygen atom to the mobility (ion-neutral ion-neutral interaction) is not significantly different from that of a methylene group in the investigated ammonium cations.

5.4.3 Functional Group Isomers of Ammonium Cations

Two functional group isomers, acetylcholine and (3-carboxypropyl)-trimethylammonium cation, were examined to study the influence of the location of oxygen atoms on the molecular ion's mobility. As seen in Figure 5.2, acetylcholine and (3-carboxypropyl)trimethylammonium are not distinguishable based on their mobilities.

5.4.4 Collision Cross-Sections of Ions in N₂ via the Trajectory Method

Theoretical Ω_D of the ammonium cations investigated in this study were evaluated using the modified TJ method. Prior to application of the modified TJ method to the ammonium cations, we tested the model on previously published experimental data. Figure 5.3a shows the plot of experimentally determined Ω_D of carboxylic acid anions [15] and abiotic amino acid cations [14] in N₂ versus those determined theoretically using the modified TJ method following the procedure described in the Experimental Section. Theoretical Ω_D of both carboxylic acid anions and abiotic amino acid cations exhibit good agreement with experimental values. The agreement is within 5 % in the worst-case deviation with less than 2 % deviation on average. Figure 5.3b shows the plot of Ω_D of ammonium cations obtained experimentally versus theoretical collision cross-sections calculated

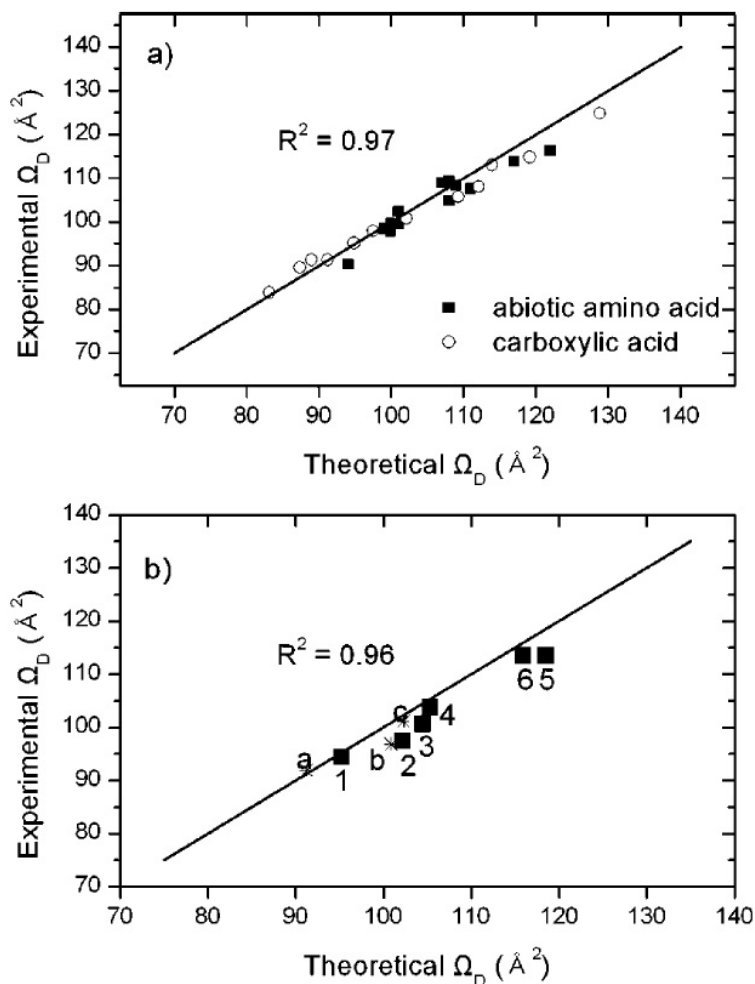


Figure 5.3: (a) Plot of experimentally determined collision cross-sections (Ω_D) of abiotic amino acid cations [14] and carboxylic acid anions [15] in N_2 versus theoretically determined Ω_D using the modified TJ method for N_2 drift gas. Abiotic amino acid cation data are shown as solid squares and carboxylic acid anion data are shown as empty circles. The solid line is $y = x$. (b) Plot of experimentally determined collision cross-sections (Ω_D) of 3° and 4° ammonium cations in N_2 versus theoretically determined Ω_D using the modified TJ method for N_2 drift gas. 3° ammonium cation data are shown as asterisks and 4° ammonium cation data are shown as solid squares. Each ion is labeled with the appropriate identifying number and alphabet shown in Figure 5.1. The solid line is $y = x$.

using the modified TJ method. The worst observed deviation of the model from the experimental cross-sections is 5 % with an average deviation of 2.5 %.

5.5 Discussion

5.5.1 Classical Ion-Neutral Collision Model

The cross-section includes the information regarding the ion-neutral interaction. An ion and a neutral interact through the long-range ion-induced dipole potential, which is given by

$$\Phi_{IID} = -\frac{(ze)^2\alpha}{2r^4}, \quad (5.8)$$

where z , R , and r are defined above. The effective potential, $\Phi_{eff}(r)$, is expressed as $\Phi_{IID} + L^2/2\mu r^2$, where L is angular momentum of the collision partners about the center of mass of the combined system. The critical impact parameter $b^* = (2\alpha e^2/\text{KE})^{1/4}$ is derived by setting KE equal to the maximum effective potential, $\Phi_{eff}^*(r)$, which is given by $1/2(\text{KE})^2 b^4/\alpha e^2$, where KE is the relative kinetic energy. Then the Langevin capture cross-section is

$$\Omega_L = \pi (b^*)^2 = \pi \sqrt{\frac{2\alpha e^2}{\text{KE}}}. \quad (5.9)$$

When the hard-sphere collision radius, R_c , is greater than b^* , the Langevin model is no longer appropriate and collisions are dominated by large angle deflections appropriate for a hard-sphere model. In this case, momentum transfer is no longer dominated by long-range interactions. In order to assess the ion-neutral collision under our experimental conditions, b^* and Ω_L are evaluated from the mean relative kinetic energies. The evaluated Ω_L and b^* are then compared to the experimental Ω_D and R_c (Table 5.2). The hard-sphere collision radius R_c is determined from the experimental Ω_D by equating it to πR_c^2 . Experimental mean relative kinetic energies can be determined from the Wannier energy formula,

$$\text{KE} = \frac{1}{2}\mu g^2 = \frac{3}{2}k_B T + \frac{1}{2}M v_d^2, \quad (5.10)$$

where M is mass of drift gas molecule and v_d is drift velocity of ion [40]. Under the current experimental conditions described in the Experimental Section, b^* is calculated on the order of 5 Å. Comparison with R_c shows that b^* in our system is on the same order, i.e., less than 1 Å smaller (Table 5.2). It is therefore inferred that the group of molecules studied here are on the borderline between being dominated by long-range versus short-range interactions, favoring some orbiting at lower collision energies, which would then determine the cross-section for momentum transfer and hence the mobility.

5.5.2 Computational Trajectory Method

Ammonium cations investigated in this study exhibit a correlation between mass and mobility (Figure 5.2). In order to understand and estimate the effect of the each component of the ion-neutral interaction potential in terms of the observed mass-mobility correlation in our experimental system, theoretical calculations were performed using the modified TJ method. The collision cross-sections (Ω_D) were evaluated using molecular ions with restricted interaction potentials and artificial charge distributions. Comparisons of the Ω_D of tertiary (3°) and quaternary (4°) ammonium cations, abiotic amino acid cations, and carboxylic acid anions, which are calculated with different interaction potentials, are shown in Figures 5.4 and 5.5.

5.5.3 Ion-Quadrupole Potential

In order to understand the role of the ion-quadrupole interaction in ion-neutral interactions, the Ω_D are computed without ion-quadrupole interactions. The presence of the quadrupole moment elevates the Ω_D by 2.8 % for the ammonium cations, 2.7 % for the abiotic amino acid cations, and 4.2 % for carboxylic acid anions (Figure 5.4a). Overall, it is observed that the addition of the ion-quadrupole potential to the model for ion- N_2 interaction improves the agreement between experimental and theoretical Ω_D values. Previously, Su and Bowers reported quadrupole effects for molecules with high quadrupole moments using the average quadrupole orientation theory [41]. They demonstrated the significance of quadrupole effects, especially in the case when the ionic charge and quadrupole moment have the same polarity [41]. In analogy, a larger quadrupole effect is observed in carboxylic acid anions versus ammonium and abiotic amino acid cations, since nitrogen has a negative quadrupole moment. During the collision process, therefore, the change of a favorable orientation induced by the total ionic charge influences the collision cross-sections via ion-quadrupole interaction. This causes the observed difference of the N_2 drift gas in ion-neutral interactions compared to spherical drift gas (i.e., He).

5.5.4 Ion-Induced Dipole Potential

In order to understand the effect of the long-range ion-induced dipole interactions between ions and neutral N_2 molecules, theoretical collision cross-section with the van der Waals and ion-induced dipole potential ($\Omega_{D,VDW+IID}$) of molecular ions are compared to collision cross-sections computed after assigning the total charge of the ionic molecule as neutral ($\Omega_{D,VDW}$). The calculated $\Omega_{D,VDW}$ with the van der Waals-only potential are $\sim 8-23$ % smaller than the calculated $\Omega_{D,VDW+IID}$. The observed difference is attributed mainly to the lack of long-range interactions. Figure 5.4b shows plots of theoretically determined $\Omega_{D,VDW}$ over the theoretical $\Omega_{D,VDW+IID}$ of 3° and 4° ammonium cations, abiotic amino acid cations, and carboxylic acid anions in N_2 versus ion mass. The agreement

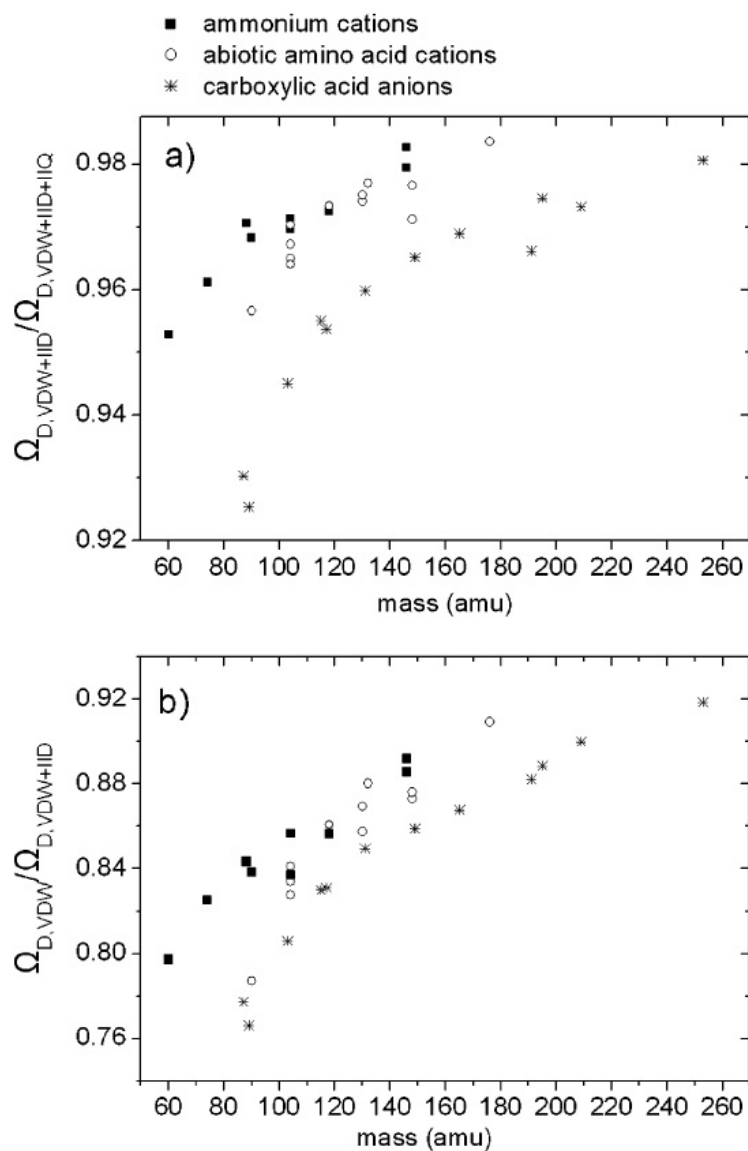


Figure 5.4: Plots of theoretically determined collision cross-sections (Ω_D) (a) with potential from van der Waals and ion-induced dipole ($VDW + IID$) interactions over the theoretical Ω_D with original pairwise potential, van der Waals + ion-induced dipole + ion-quadrupole ($VDW + IID + IQ$) interactions, and (b) with potential from van der Waals potential (VDW) over the theoretical Ω_D with potential from van der Waals and ion-induced dipole ($VDW + IID$) interactions of 3° and 4° ammonium cations, abiotic amino acid cations, and carboxylic acid anions in N_2 versus ion mass. The ammonium cation data, the abiotic amino acid cation, and carboxylic acid anion data are shown as solid squares, empty circles, and asterisks, respectively.

Table 5.2: Critical Impact Parameter, b^* , Langevin Capture Cross-Section, Ω_L , and Mean Relative Kinetic Energies, KE, during the Experiments with Experimentally Determined Hard-Sphere Collision Radius, R_c for Each Ammonium Cation

ammonium cation	KE (kcal/mol)	b^* (Å)	Ω_L (Å ²)	R_c (Å)
trimethylammonium	1.70	5.08	81.0	5.41
tetramethylammonium	1.69	5.09	81.3	5.48
trimethylethylammonium	1.67	5.10	81.7	5.57
<i>N,N</i> -dimethylammoniummethanol	1.67	5.10	81.7	5.55
choline	1.65	5.11	82.1	5.66
<i>N,N</i> -dimethylglycine	1.65	5.11	82.1	5.67
betaine	1.64	5.12	82.5	5.75
acetylcholine	1.60	5.15	83.4	6.01
(3-carboxypropyl)trimethylammonium	1.60	5.15	83.5	6.01

between the $\Omega_{D,VDW}$ of ions and the $\Omega_{D,VDW+IID}$ increases from 75 to 92 % along with the mass of the molecular ion increases (Figure 5.4b). This is easy to rationalize since the contribution of the van der Waals interaction increases as the size (i.e., number of atoms) of the molecular ion increases. As a result, it can be concluded that the contribution of long-range ion-induced dipole interaction is important for the Ω_D of small size molecular ions, while the van der Waals interaction prominently affects to the Ω_D in large size molecular ions in this study.

5.5.5 Van der Waals Potential

The plots of the Ω_D of 3° and 4° ammonium cations, abiotic amino acid cations, and carboxylic acid anions determined only with the van der Waals potential versus ion mass are shown in Figure 5.5, providing the comparison with the corresponding Ω_D from original pairwise potential, which is the combined potential of van der Waals, ion-induced dipole, and ion-quadrupole interactions. It is notable that the characteristic relative $\Omega_{D,VDW}$ show high similarity to the relative Ω_D from the original theoretical calculations. It is inferred that the distinction between the Ω_D for each ion is largely due to the short-range van der Waals interaction between ion and neutral N₂ molecule. The molecular weight and specific geometry of the ions is considered to dominate the short-range van der Waals interaction, which affect the collision cross-section of the ion.

5.5.6 Mass-Mobility Correlation

It has been suggested from the classical ion-neutral collision calculation that our ion-neutral collision occurs at the borderline between systems dominated by either long-range or short-range interactions. This is well supported from the theoretical investigation using the TJ method. The contribution of long-range interaction to the Ω_D of ammonium cations is large (~ 30 %) for small ions and decreases

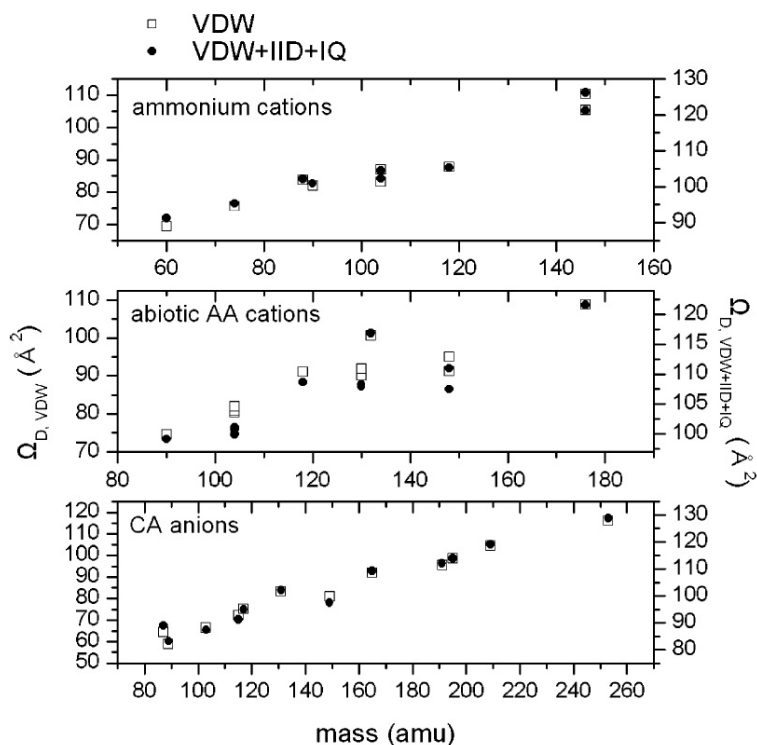


Figure 5.5: Plots of theoretically determined collision cross-sections (Ω_D) of 3° and 4° ammonium cations, abiotic amino acid cations, and carboxylic acid anions in N_2 versus ion mass. The calculated Ω_D of the molecular ions only with van der Waals (VDW) interaction with N_2 are shown as empty squares (left y -axis). The calculated Ω_D of the molecular ions with original pairwise potential, van der Waals + ion-induced dipole + ion-quadrupole ($VDW + IID + IQ$) interactions, with N_2 are shown as solid circles (right y -axis).

Table 5.3: Theoretically Determined Collision Cross-Sections of 3° and 4° Ammonium Cations

ammonium cation	${}^a\Omega_D$ (${}^bVDW+$ ${}^cIID+{}^dIQ$)	${}^a\Omega_D$ (${}^bVDW+$ cIID)	${}^a\Omega_D$ (bVDW)	${}^a\Omega_D$ (e center charge)
trimethylammonium	91.2	86.9	69.3	91.3
tetramethylammonium	95.3	91.6	75.6	95.1
trimethylethylammonium	102.2	99.2	83.7	101.0
<i>N,N</i> -dimethylammoniummethanol	100.9	97.7	81.9	100
choline	104.5	101.5	87.0	104
<i>N,N</i> -dimethylglycine	102.3	99.2	83.0	101.7
betaine	105.3	102.4	87.7	105.3
acetylcholine	126.3	123.7	110.3	120.2
(3-carboxypropyl)trimethylammonium	121.1	119.0	105.4	117.8

a Collision cross-section (\AA^2). b Van der Waals potential. c Ion-induced dipole interaction. d Ion-quadrupole interaction. e Ionic charge at center of mass.

to less than 10 % as the size of the ion increases.

Previous studies have suggested that charge localization on certain functional groups and the specific structure of the ion play major roles in the interaction between ions and neutral gas molecules in IMS [7, 8, 9]. In order to assess the effect of specific charge distribution in the molecular ion on Ω_D , the ionic Ω_D were evaluated after assigning the charge of the molecular ion at the center of mass. In general, Ω_D of ions, in which a total charge +1 has been assigned at the center of mass in the molecule exhibit insignificant deviations from the Ω_D of the ions determined with DFT calculated Mulliken charge distributions. The Ω_D of the ammonium cations with the charge at the center of mass show an average deviation of 0.7 % from the Ω_D of ions with Mulliken charge distributions (Table 5.3). The Ω_D of the carboxylic acid anions and abiotic amino acid cations exhibit 0.64 and 2.7 % deviations, respectively, between the two models. This implies that the influence of the ion charge distribution on Ω_D is minimal. The distance of the center of charge from the center of mass was calculated to investigate the specific charge distribution of the molecular ion in the present study. The average distance between the centers of charge from the centers of mass in the molecular ions is 0.7 Å for ammonium cations, and 0.9 Å for abiotic amino acid cations and carboxylic acid anions. It is inferred that the sizes of the molecular ions investigated in this study are too small to expect localization of the charge to a specific site.

In the previous section, we discussed that all potential terms, ion-quadrupole, ion-induced dipole, and van der Waals potential, are important considerations in determining the collision cross-section of the ions. Especially 75–95 % of collision cross-section is contributed by van der Waals interactions, which implies that strong mass-mobility correlations are highly affected by the geometries of the ions. This can explain the correlation observed in previous studies such as carboxylic acids and amino acids in terms of their structural similarity [14, 15]. However, it is not able to explain the strong correlation among the ammonium cations. Localization of the charge in molecular ions induces specific gas-phase intramolecular cyclic structures of deprotonated carboxylate anions [15, 42] and protonated abiotic amino acid cations [14]. However, DFT optimized structures of highly alkylated ammonium cations show no significant influence of the localization of the charge on the structures (Figure 5.2).

To evaluate the pure geometrical effect on the Ω_D , we calculated the molecular volume and surface area of ions in N_2 , which are also known as solvent-excluded volume and area [43], using the Maximal Speed Molecular Surface (MSMS) program [44]. The volume and surface area of ion are traced by the inward-facing part of the probe sphere as it rolls over the ion [43]. The radius of the probe sphere is set to be the hard-sphere diameter of N_2 molecule, 3.70 Å. A distinct mass-volume correlation among the ammonium cations with different numbers of oxygen atoms is found. However, the surface area demonstrates a higher correlation with ion mass for the overall mass range. For example, the volume increases 7.6 and 5.6 % from trimethylethylammonium (88 amu) to choline

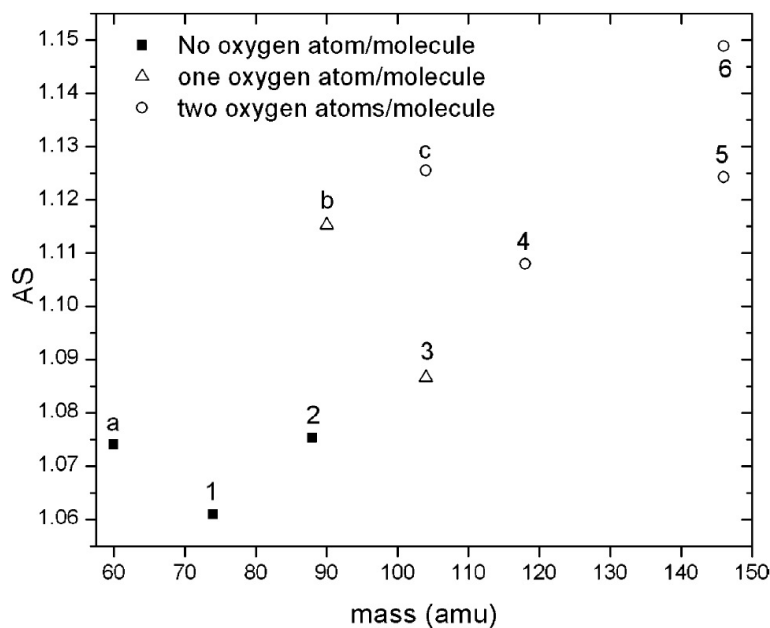


Figure 5.6: Plot of the total shape asymmetry (AS) of the ammonium cations versus ion mass. The ammonium cations with no oxygen atom are shown as solid squares. The ions containing one oxygen atom and two oxygen atoms are shown as empty triangles and empty circles, respectively. The DFT optimized structure of each numerically or alphabetically labeled ion is shown in Figure 5.2.

(104 amu) and betaine (118 amu) while the surface area increases 6.1 and 6.8 %, respectively. Using the obtained molecular volume and surface area, the molecular ion's asymmetry of the total shape is determined (Figure 5.6). The asymmetry of the total shape (AS) is expressed as

$$AS = \left(\frac{S}{4\pi} \right) \left(\frac{3V}{4\pi} \right)^{-2/3} = \frac{1}{4.836} \left(\frac{S}{V^{2/3}} \right), \quad (5.11)$$

where S and V are molecular surface area and volume, respectively. When the molecular ion is symmetrical (i.e., spherical) AS becomes unity, with AS increasing from unity as the asymmetry in shape increases. As seen in Figure 5.6, higher asymmetry is observed as the number of oxygen atoms and the size of the ion increase. Although the larger content of oxygen atom makes for smaller molecular volumes, it increases the asymmetry of the total shape, which increases the surface area of the ion. It is therefore inferred that our observed strong mass-mobility correlation is largely due to geometrical factors. This allows us to comprehend the observed mass-mobility correlation among two different classes of ammonium cations with the heteroatom complements in the present study.

5.6 Conclusions

A high correlation between mass and mobility in N_2 is observed from a number of tertiary and quaternary ammonium cations. The classical ion-neutral collision calculation implies that the group

of molecules studied here are on the borderline between being dominated by long-range versus short-range interactions, favoring some orbiting at lower collision energies, which would then determine the cross-section. Theoretical investigation using a modified trajectory (TJ) method also indicates that all potential terms, ion-quadrupole, ion-induced dipole, and van der Waals potential, are important considerations in determining the collision cross-section of the ions. For the smaller molecular ions, the importance of long-range interaction is emphasized, while short-range interactions dominate the collision cross-sections of the larger molecular ions. The evaluated volume and surface area suggest that shape asymmetry of the ammonium cations plays a small but significant role in determining the observed correlation between mass and mobility. The increase of the asymmetry in the shape of an ion compensates the reduction of the ion's volume, which finally yields similar mobilities of the ammonium cations with similar molecular weight investigated in this study, independent of their heteroatom complement.

5.7 Acknowledgments

This research was carried out at the Jet Propulsion Laboratory, California Institute of Technology, under a contract with the National Aeronautics and Space Administration (NASA), the Noyes Laboratory of Chemical Physics, California Institute of Technology, and the Material and Process Simulation Center, Beckman Institute, California Institute of Technology. Financial support through NASA's Astrobiology Science and Technology Instrument Development, Planetary Instrument Definition and Development, and Mars Instrument Development programs is gratefully acknowledged. We appreciate the support provided by the Mass Spectrometry Resource Center in the Beckman Institute. The authors greatly appreciate Prof. Martin Jarrold at Indiana University Bloomington for generously allowing us to use and modify the Mobcal program. Hyungjun Kim and Hugh I. Kim contributed equally to this work.

Bibliography

- [1] Fenn, J. B.; Mann, M.; Meng, C. K.; Wong, S. F.; Whitehouse, C. M. *Science* **1989**, 246, 64-71.
- [2] Shumate, C. B.; Hill, H. H. *Anal. Chem.* **1989**, 61, 601-606.
- [3] Wittmer, D.; Luckenbill, B. K.; Hill, H. H.; Chen, Y. H. *Anal. Chem.* **1994**, 66, 2348-2355.
- [4] Creaser, C. S.; Griffiths, J. R.; Bramwell, C. J.; Noreen, S.; Hill, C. A.; Thomas, C. L. P. *Analyst* **2004**, 129, 984-994.
- [5] Gidden, J.; Ferzoco, A.; Baker, E. S.; Bowers, M. T. *J. Am. Chem. Soc.* **2004**, 126, 15132-15140.
- [6] Julian, R. R.; Hodyss, R.; Kinnear, B.; Jarrold, M. F.; Beauchamp, J. L. *J. Phys. Chem. B* **2002**, 106, 1219-1228.
- [7] Counterman, A. E.; Clemmer, D. E. *J. Phys. Chem. B* **2001**, 105, 8092-8096.
- [8] Kaleta, D. T.; Jarrold, M. F. *J. Phys. Chem. A* **2002**, 106, 9655-9664.
- [9] Wu, C.; Siems, W. F.; Klasmeier, J.; Hill, H. H. *Anal. Chem.* **2000**, 72, 391-395.
- [10] Shelimov, K. B.; Clemmer, D. E.; Hudgins, R. R.; Jarrold, M. F. *J. Am. Chem. Soc.* **1997**, 119, 2240-2248.
- [11] Hudgins, R. R.; Woenckhaus, J.; Jarrold, M. F. *Int. J. Mass Spectrom.* **1997**, 165, 497-507.
- [12] Clemmer, D. E.; Jarrold, M. F. *J. Mass Spectrom.* **1997**, 32, 577-592.
- [13] Beegle, L. W.; Kanik, I.; Matz, L.; Hill, H. H. *Anal. Chem.* **2001**, 73, 3028-3034.
- [14] Johnson, P. V.; Kim, H. I.; Beegle, L. W.; Kanik, I. *J. Phys. Chem. A* **2004**, 108, 5785-5792.
- [15] Kim, H. I.; Johnson, P. V.; Beegle, L. W.; Beauchamp, J. L.; Kanik, I. *J. Phys. Chem. A* **2005**, 109, 7888-7895.
- [16] Gidden, J.; Bowers, M. T. *Eur. Phys. J. D.* **2002**, 20, 409-419.
- [17] Asbury, G. R.; Klasmeier, J.; Hill, H. H. *Talanta* **2000**, 50, 1291-1298.

- [18] Asbury, G. R.; Wu, C.; Siems, W. F.; Hill, H. H. *Anal. Chim. Acta* **2000**, 404, 273-283.
- [19] Griffin, G. W.; Dzidic, I.; Carroll, D. I.; Stillwel, R. N.; Horning, E. C. *Anal. Chem.* **1973**, 45, 1204-1209.
- [20] Berant, Z.; Karpas, Z. *J. Am. Chem. Soc.* **1989**, 111, 3819-3824.
- [21] Karpas, Z.; Berant, Z. *J. Phys. Chem.* **1989**, 93, 3021-3025.
- [22] Steiner, W. E.; English, W. A.; Hill, H. H. *J. Phys. Chem. A* **2006**, 110, 1836-1844.
- [23] Vonhelden, G.; Hsu, M. T.; Kemper, P. R.; Bowers, M. T. *J. Chem. Phys.* **1991**, 95, 3835-3837.
- [24] Mesleh, M. F.; Hunter, J. M.; Shvartsburg, A. A.; Schatz, G. C.; Jarrold, M. F. *J. Phys. Chem.* **1996**, 100, 16082-16086.
- [25] Mason, E. A.; O'hara, H.; Smith, F. J. *J. Phys. B* **1972**, 5, 169-176.
- [26] Blusztajn, J. K. *Science* **1998**, 281, 794-795.
- [27] Zeisel, S. H.; Dacosta, K. A.; Youssef, M.; Hensey, S. *J. Nutr.* **1989**, 119, 800-804.
- [28] McHowat, J.; Jones, J. H.; Creer, M. H. *J. Lipid Res.* **1996**, 37, 2450-2460.
- [29] Wu, C.; Siems, W. F.; Asbury, G. R.; Hill, H. H. *Anal. Chem.* **1998**, 70, 4929-4938.
- [30] Asbury, G. R.; Hill, H. H. *Anal. Chem.* **2000**, 72, 580-584.
- [31] Becke, A. D. *J. Chem. Phys.* **1993**, 98, 5648-5652.
- [32] Lee, C. T.; Yang, W. T.; Parr, R. G. *Phys. Rev. B* **1988**, 37, 785-789.
- [33] Harihara, P. C.; Pople, J. A. *Chem. Phys. Lett.* **1972**, 16, 217-219.
- [34] Olney, T. N.; Cann, N. M.; Cooper, G.; Brion, C. E. *Chem. Phys.* **1997**, 223, 59-98.
- [35] Rappe, A. K.; Casewit, C. J.; Colwell, K. S.; Goddard, W. A.; Skiff, W. M. *J. Am. Chem. Soc.* **1992**, 114, 10024-10035.
- [36] Graham, C.; Imrie, D. A.; Raab, R. E. *Mol. Phys.* **1998**, 93, 49-56.
- [37] Dugan, J. V.; Palmer, R. W. *Chem. Phys. Lett.* **1972**, 13, 144-149.
- [38] Dugan, J. V.; Magee, J. L. *J. Chem. Phys.* **1967**, 47, 3103-3112.
- [39] Bowers, M. T. *Gas Phase Ion Chemistry*; Academic Press: New York, 1979; Vol. 1.
- [40] Wannier, G. H. *Bell Syst. Tech. J.* **1953**, 32, 170-254.

- [41] Su, T.; Bowers, M. T. *Int. J. Mass Spectrom. Ion Processes* **1975**, 17, 309-319.
- [42] Woo, H. K.; Wang, X. B.; Lau, K. C.; Wang, L. S. *J. Phys. Chem. A* **2006**, 110, 7801-7805.
- [43] Connolly, M. L. *J. Am. Chem. Soc.* **1985**, 107, 1118-1124.
- [44] Sanner, M. F.; Olson, A. J.; Spohner, J. C. *Biopolymers* **1996**, 38, 305-320.

Chapter 6

Structural Characterization of Unsaturated Phospholipids Using Traveling Wave Ion Mobility Spectrometry

6.1 Abstract

A number of phosphatidylcholine (PC) cations spanning a mass range of 400 to 1000 Da are investigated using electrospray ionization mass spectrometry coupled with traveling wave ion mobility spectrometry (TWIMS). A high correlation between mass and mobility is demonstrated with saturated phosphatidylcholine cations in N_2 . A significant deviation from this mass-mobility correlation line is observed for the unsaturated PC cation. We found that the double bond in the acyl chain causes a 5 % reduction in drift time. The drift time is reduced at a rate of ~ 1 % for each additional double bond. Theoretical collision cross-sections of PC cations exhibit good agreement with experimentally evaluated values. Collision cross-sections are determined using the recently derived relationship between mobility and drift time in TWIMS stacked ring ion guide (SRIG) and compared to estimate collision cross-sections using empiric calibration method. Computational analysis was performed using the modified trajectory (TJ) method with nonspherical N_2 molecules as the drift gas. The difference between estimated collision cross-sections and theoretical collision cross-sections of PC cations is related to the sensitivity of the PC cation collision cross-sections to the details of the ion-neutral interactions. The origin of the observed correlation and deviation between mass and mobility of PC cations is discussed in terms of the structural rigidity of these molecules using molecular dynamics simulations.

6.2 Introduction

Lipids are essential biological components and have critical roles for cell structure, energy storage, and metabolic control [1]. Characterizing their structures is an essential part of lipid analysis. In addition, searching for lipid molecules is a valuable strategy for finding traces of extinct or extant life elsewhere in outer space. Lipids and biomembranes can be preserved for a long period; thus, detailed characterization of these biomarker compositions allows for the assessment of major contributing species [2]. Lipids offer records of modern and ancient life, environmental conditions, and changes in history. However, the variety and *in situ* alteration of lipids also increases complexity, making them difficult to characterize fully [3].

The separation and characterization of phospholipids using tandem ion mobility mass spectrometry (IM-MS) has been investigated by several research groups [4, 5, 6, 7]. Utilizing matrix-assisted laser desorption ionization (MALDI) with IM-MS, phospholipid ions have been separated from other biomolecule ions [4, 8]. Separation can be achieved based on the correlation between mass and ion mobility. Phospholipids in tissue samples have been directly analyzed using MALDI-IM-MS [4, 5]. These studies have reported that phospholipid ions have slower mobility than peptide, carbohydrate, and nucleotide ions with similar masses [4, 7, 8, 9]. In general, peptides, nucleotides, and carbohydrates form globular conformations in the gas phase due to intramolecular Coulombic interactions [10, 11, 12]. However, such interactions are difficult to achieve for phospholipid molecules because their major components are aliphatic acyl chains. Recently, Jackson *et al.* reported the effects of various head and tail groups of phospholipids on mass-mobility correlations using MALDI-IM-MS [6]. They report a slight increase in the mobility of phospholipids as the degree of unsaturation on the acyl chain increases.

The correlation between the mass and mobility of molecular ions has been used to separate and characterize ions related to the mobility of gas phase ion molecules. In the early 1970s, Griffin *et al.* [13] showed that mass and mobility are strongly correlated for structurally related compounds. In the late 1980s, Karpas and Berant demonstrated distinct mass-mobility correlations of acetyls, aromatic amines, and aliphatic amines drifting in various drift gases including He, N₂, CO₂, and air [14, 15]. Clemmer and co-workers have demonstrated distinct mass-mobility correlations for peptides with molecular weights of 500 to 2500 Da [16]. Recently, Thalassinos *et al.* characterized phosphorylated peptides as having higher mobilities than their non-phosphorylated counterparts [17].

Our laboratory has investigated the distinct mass-mobility correlations of amino acids and carboxylic acids drifting in N₂ and CO₂ [18, 19]. Recently, we experimentally observed a high correlation between mass and mobility of tertiary and quaternary ammonium cations in N₂ [20]. This observed correlation was investigated using classical ion-neutral collision dynamic theories and computational

calculation using a modified trajectory (TJ) method. From these theoretical investigations, the ammonium cations in the mass range from 60 Da to 150 Da are on the borderline between being dominated by long range versus short range interactions with N_2 . In addition, all potential terms, ion-quadrupole, ion-induced dipole, and van der Waals potential are important considerations for determining the collision cross-sections of the ions in N_2 .

In this paper, we measure drift times for a number of phosphatidylcholines (PC) spanning a mass range of 400 to 1000 Da in N_2 using a commercial traveling wave ion mobility spectrometry (TWIMS) coupled with orthogonal acceleration time-of-flight (oa-TOF) mass spectrometry (Waters Synapt HDMS). Of particular interest is the possible dependence of mass-mobility correlations on the symmetry, length, and degree of saturation of the acyl chains. Despite a wide range of TWIMS applications in various chemistry fields [17, 21, 22, 23, 24, 25], studies have only begun to understand the principal physics behind the TWIMS drift time and ion mobility. A number of studies have employed the empiric calibration method to estimate mobilities and collision cross-sections of analyte ions from the drift times in TWIMS [17, 21, 22, 25, 26]. Recently, Shvartsburg and Smith quantitatively revealed the relationship between drift time and ion mobility in TWIMS [27].

Jarrold and co-workers have proposed a TJ method based on a soft-core ion-neutral interaction potential to interpret collision cross-sections of ion molecules [28]. A modified TJ method for the ion-neutral interaction to account for the potential associated with the non-spherical drift gas N_2 has been applied to predict collision cross-sections of PC cations and to test the sensitivity of these cross-sections in order to detail the structural rigidity of these molecules [20]. Results from the estimated collision-cross sections using empiric calibration are compared with the evaluated relationship between TWIMS drift time and mobility by Shvartsburg and Smith [27]. The origin of the observed correlation and deviation between PC mass and mobility is discussed.

6.3 Experimental Section

6.3.1 Chemicals and Reagents

All phosphatidylcholines studied in this work were purchased from Avanti Polar Lipids (Alabaster, AL) and were used without further purification. All solvents (water, methanol, and formic acid) were HPLC grade and were purchased from EMD Chemicals Inc. (Gibbstown, NJ). Calibrant peptides (GGGGGG and AAAAAA), cytochrome C, and trypsin from porcine pancreas were purchased from Sigma-Aldrich (St. Louis, MO). Samples were prepared by dissolving known quantities of molecules in a solvent consisting of 1 : 1 water and methanol with 0.1 % formic acid by volume to yield sample concentrations in the range of 50 μ M. Trypsin digest of cytochrome C was prepared by incubating 200 μ M of cytochrome C with 6 μ g of trypsin from porcine pancreas in 1 mL of water containing 25 mM ammonium bicarbonate (NH_4HCO_3) at 37°C for 4 hours. The trypsin was then removed

using a Millipore Microcon centrifugal filter fitted with an Ultracel YM-10 membrane. The sample solution was diluted to an appropriate concentration for ESI with 1:1 water/methanol and 0.1 % formic acid by volume. Phospholipid and peptide ions examined in this study are listed in Table 6.1 along with their respective molecular weights.

Phosphatidylcholines examined in this study are named by their acyl chain length and number of double bonds. For example, 1-steroyl-2-oleoyl-*sn*-phosphatidylcholine (SOPC), which comprises two 18 carbon acyl chains and one double bond, is referred to as 18:0-18:1 PC.

6.3.2 Electrospray Ionization Traveling Wave Ion Mobility Mass Spectrometer

Experiments were performed on a Synapt HDMS traveling wave ion mobility orthogonal acceleration time-of-flight (TW-IM-*oa*-TOF, Waters, Manchester, U.K.) in positive ion mode. The details of the instrument have been described elsewhere [29, 30]. Source temperature of 100°C, capillary voltage of 3 kV, desolvation temperature of 250°C, and cone voltage of 30 V were set as parameters for ESI. Other parameters of the instrument were optimized to achieve the best separation of phospholipids without the roll-over effect [29]. Nitrogen drift gas was introduced to the TWIMS stacked ring ion guide (SRIG) at a 25 mL/min flow rate, which corresponds to 0.39 Torr. The traveling wave (T-wave) height and velocity were optimized as 8 V and 300 m/s, respectively. For each sample, 150 spectra were obtained and averaged for analysis. The drift times of the singly charged phospholipid cations and peptides were determined from the location of the ion mobility peak maxima extracted manually using MassLynx (v 4.1) software (Waters corp. Milford, MA). Resolution of the instrument was found to be ~ 0.8 ms in full width at half maximum (FWHM) with drift times for the ions studied and the parameters employed in this study.

6.3.3 Collision Cross-Section Calibration

Previously published collision cross-sections of singly charged peptide hexaglycine, hexaalanine, and tryptic digest of cytochrome C in helium drift gas were used to create a calibration curve [16]. Recently published PC collision cross-sections determined in helium drift gas were also used for the calibration [9]. The calibration procedure was adopted from Thalassinos *et al.* [17]. The effective drift time (t_d'') of the calibrant was corrected for mass independent and mass dependent time. The published collision cross-section of the calibrant was scaled by reduced mass in N₂. The effected drift time was plotted against the corrected published collision cross-section (Ω_D'). The plot was used to fit a linear and power trend. The equation from the fitting result was used to estimate collision cross-sections of phospholipids with reduced mass.

Table 6.1: Mass, Drift time, and Corrected Drift Time of Ion Molecule Used in This Study

Name	cationization	^c mass	t_d (ms)	^d t'_d (ms)
^a 5:0-5:0 PC	H ⁺	426	3.58	3.39
	Na ⁺	448	3.97	3.77
^a 8:0-8:0 PC	H ⁺	510	4.99	4.78
	Na ⁺	532	5.50	5.29
^a 11:0-11:0 PC	H ⁺	595	6.40	6.18
	Na ⁺	617	6.85	6.62
^a 14:0-16:0 PC	H ⁺	707	8.06	7.82
	Na ⁺	729	8.32	8.07
^a 16:0-16:0 PC	H ⁺	735	8.64	8.39
	Na ⁺	757	8.77	8.51
^a 18:0-14:0 PC	H ⁺	735	8.58	8.33
	Na ⁺	757	8.77	8.51
^{a,b} 16:0-18:2 PC	H ⁺	759	8.51	8.26
^a 18:0-16:0 PC	H ⁺	763	8.96	8.71
	Na ⁺	785	9.15	8.89
^a 16:0-20:4 PC	H ⁺	783	8.58	8.32
^{a,b} 18:0-18:2 PC	H ⁺	787	8.90	8.64
^a 18:0-18:1 PC	H ⁺	789	8.96	8.70
^a 18:0-18:0 PC	H ⁺	791	9.41	9.15
^a 16:0-22:6 PC	H ⁺	807	8.83	8.57
^a 24:0-24:0 PC	H ⁺	959	12.2	11.9
^b KK (cytC)	H ⁺	275	1.86	1.70
^b HK (cytC)	H ⁺	284	1.86	1.70
^b GKK (cytC)	H ⁺	332	2.37	2.20
^b GGGGGG	H ⁺	362	2.18	2.00
^b ATNE (cytC)	H ⁺	434	3.20	3.01
^b AAAAAA	H ⁺	446	3.14	2.94
^b KATNE (cytC)	H ⁺	563	4.29	4.07
^b Ac-GDVEK (cytC)	H ⁺	590	4.80	4.58
^b GITWK (cytC)	H ⁺	605	5.12	4.89
^b IFVQK (cytC)	H ⁺	635	5.70	5.46
^b YIPGTK (cytC)	H ⁺	679	6.02	5.78
^b MIFAGIK (cytC)	H ⁺	780	7.36	7.10
^b Bradykinin	H ⁺	1061	10.2	9.94
^b TGPNLHGLFGR (cytC)	H ⁺	1169	11.8	11.5

^aMolecules examined in this study. ^bMolecules used as calibrant. ^cAll ions are singly charged. ^dMass dependent corrected drift time.

6.3.4 Computational Modeling

Collision cross-sections of ions were calculated using the modified TJ method [20], which consists of two potential terms representing van der Waals and ion-induced dipole interactions characterized by Lennard-Jones parameters and neutral polarizability, respectively [28]. The modified TJ method describes the interaction between ions and an N₂ drift gas that expands applicability beyond cases of ions drifting in He (details of this modification can be found elsewhere) [20]. In brief, we set the polarizability of neutral gas for N₂ (1.710×10^{-24} cm²). Due to the linear geometry of N₂, two more consequences were taken into account: ion-quadrupole interaction and molecule orientation. The ion-quadrupole interaction is expressed in simple summations of partial charges of negative q ($0.4825e$) to each nitrogen atom and one positive $2q$ at the center of the nitrogen molecule. The orientations of N₂ are sampled along the x -, y -, and z -axis; the averaged interaction potential is evaluated using Boltzmann weighting.

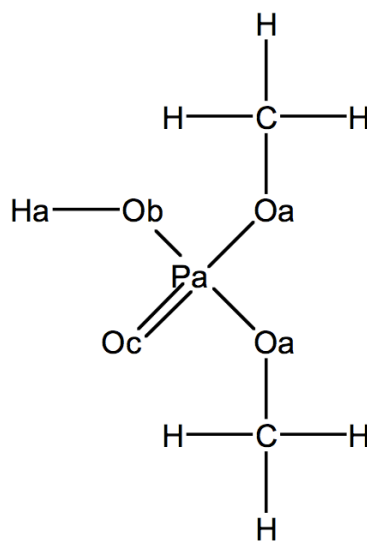
In order to consider the effect of structural fluctuation on the collision cross-section at room temperature, we performed NVT molecular dynamics (MD) simulations using a Nosé-Hoover thermostat at 300 K. The inter-atom interactions are described with the all-atom CHARMM PARAM27 force field [31] using the LAMMPS (large-scale atomic/molecular massively parallel simulator) code [32]. We adopted the “sp₂ C-sp₃ C-sp₂ C” angle parameter and the “sp₂ C-sp₂ C-sp₃ C-sp₂ C” dihedral parameters from reference [33], which were optimized using 1,4-pentadiene. The partial charge distribution of protonated phosphate (O₃P-O-H) was optimized using Mulliken charge distributions from density functional theory (DFT) calculations (Table 6.2), since the common CHARMM force field only has a partial charge distribution of negatively charged phosphate (O₃P-O⁻). The systems are pre-equilibrated for 100 ps, and the conformations are sampled every one ps from the 200 ps simulations. We note that such a procedure allows for canonical sampling of the conformations at 300 K. We analyzed the collision cross-sections and potential energies of all sampled conformations of PC.

6.4 Results

6.4.1 Saturated Phosphatidylcholine Cations

The drift times, t_d , of the PC cations were determined as described above. The drift times were then corrected with the mass dependent flight time, defined as the time that an ion spent in the TOF [17, 26]. Measured and corrected drift times for the PC cations chosen for this study are found in Table 6.1. The corrected drift time from TWIMS was plotted against the mass to charge (m/z) of the ion, and the plot was used to fit a linear trend. The plot of drift time versus mass for singly protonated PC cations is shown in Figure 6.1 along with the linear fit to the data. As seen

Table 6.2: Optimized Partial Charge Distribution of Protonated Phosphate from the DFT Calculation of Protonated Dimethyl Phosphate (The Partial Charges with Atom Types for CHARMM Force Field are Tabulated.)



	^a Mulliken Charge	Force Field Charge	Force Field Type
Pa	1.16	1.50	PL
Oa	-0.51	-0.49	OSL
Ob	-0.54	-0.52	OHL
Oc	-0.57	-0.56	O2L
Ha	0.35	0.36	HOL

^aComputed from density functional theory (DFT) calculation using Jaguar 6.0 of Schrödinger company with B3LYP functional and 6-31G** basis set.

in Figure 6.1a, all saturated PC cations investigated in this study (400 – 1000 Da) exhibit a good correlation ($R^2 > 0.999$) between mass and drift time (i.e., ion mobility). In particular, symmetry of the two acyl chains in the phospholipid does not affect the common mass-mobility correlation of a saturated PC cation.

6.4.2 Unsaturated Phosphatidylcholine Cations

The usual acyl chain length of membrane phospholipids vary from 18 to 20 carbon atoms [34]. Most unsaturated phospholipids contain one acyl chain with one or more *cis*-double bonds and a saturated one as a second acyl chain [34]. We have selected unsaturated PC cations with these characteristics to investigate the dependence of mass-mobility correlations on the presence of double bonds in the acyl chains of membrane phospholipids (Table 6.1).

Figure 6.1b shows a plot of corrected drift time versus mass for PC cations from 700 Da to 810 Da along with the linear fit to the data. A good correlation ($R^2 = 0.984$) is still observed for the saturated PC cations within the mass range. However, a poor correlation between mass and mobility from unsaturated and saturated PC cations is also observed ($R^2 = 0.487$). Unsaturated PC cations show higher mobilities (i.e., faster drift time) compared to saturated PC cations. Corrected drift times of 16:0-18:2 PC (MW 759) and 16:0-20:4 PC (MW 783) are measured as 8.26 ms and 8.32 ms, respectively. They traveled in the SRIG faster than smaller saturated PC cations such as 16:0-16:0 and 18:0-14:0 (MW 735), which have 8.39 ms and 8.33 ms drift times, respectively. The corrected drift time of 16:0-22:6 PC (MW 807) is measured as 8.57 ms. Compared to the 8.71 ms and 9.15 ms, which are corrected drift times of two smaller saturated PC cations, 18:0-16:0 PC (MW 763) and 18:0-18:0 PC (MW 791), respectively, 16:0-22:6 PC travels across the SRIG faster.

The presence of a *cis*-double bond causes the acyl chain to bend. In addition, a double bond causes a relatively rigid acyl chain structure compared to that of the saturated acyl chain. It is inferred that these two factors cause smaller collision cross-sections and thus faster mobility than unsaturated PC cations.

6.4.3 Sodiated Phosphatidylcholine Cations

Figure 6.1c shows the plot of drift time versus mass for protonated and sodiated PC cations. The sodiated PC cations investigated in this study exhibit a good mass-mobility correlation ($R^2 = 0.996$) with protonated PC ions. A recent investigation by Kim *et al.* reported that short range interactions are most important for the collision cross-sections of molecular ions larger than 150 Da [20]. The PC cations (400 – 1000 Da) investigated in this study are larger than ions that Kim *et al.* [20] investigated (60 – 250 Da). Thus, the importance of short range interactions is emphasized for collision cross-sections of PC cations. In numerous cases, metal cations have been shown to cause

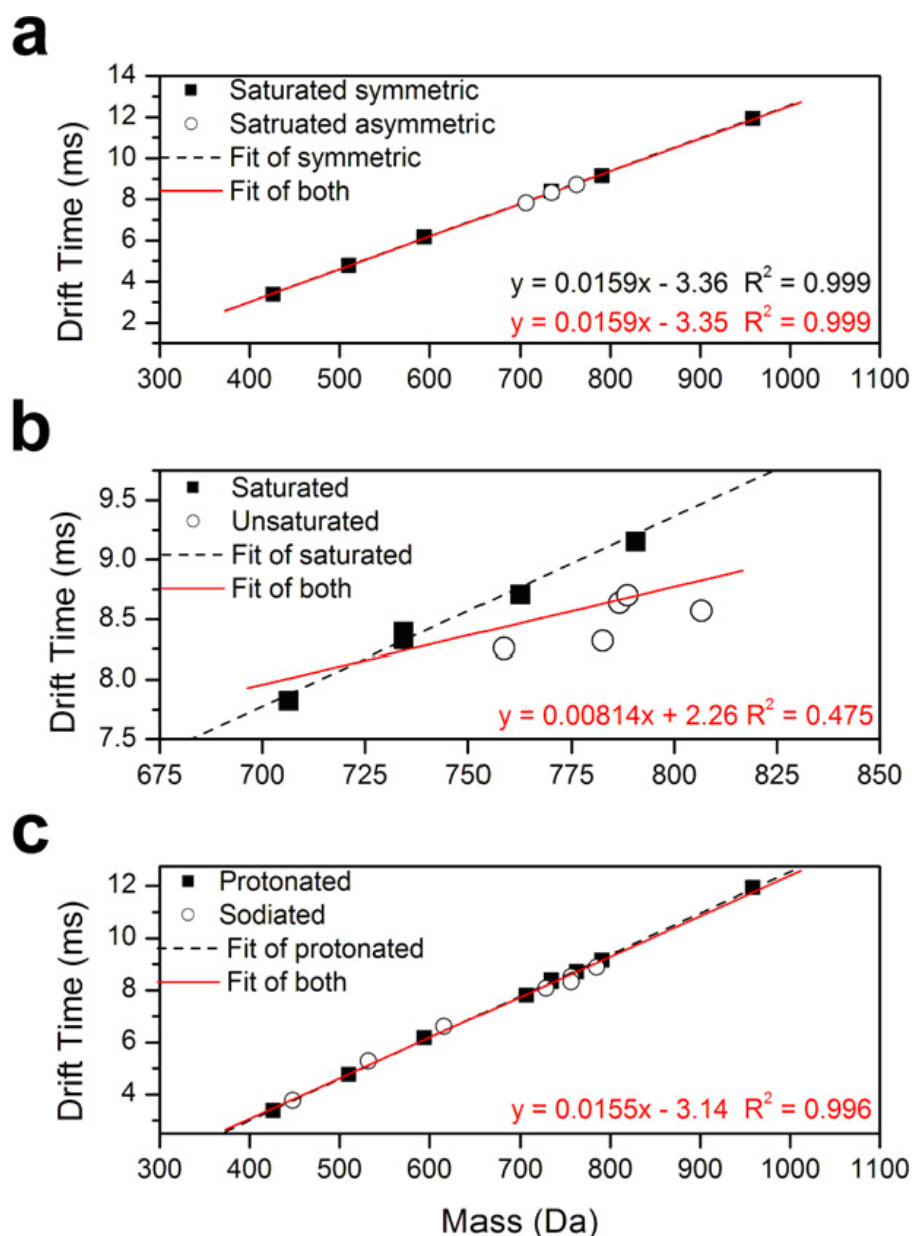


Figure 6.1: (a) Plot of drift time of saturated phosphatidylcholine (PC) cations in traveling wave ion mobility spectrometer versus ion mass. Experimentally determined data for symmetric PC and asymmetric PC cations are shown as solid squares and empty circles, respectively. The black dash and red solid lines are the linear fit to the symmetric PC cation data set and to both symmetric and asymmetric PC cation data set, respectively. (b) Plot of drift time of PC cations spanning mass range 700 – 800 Da in traveling wave ion mobility spectrometer versus ion mass. Experimentally determined data for saturated PC and unsaturated PC cations are shown as solid squares and empty circles, respectively. The black dash and red solid lines are the linear fit to the saturated PC cation data set and to both saturated and unsaturated PC cation data set, respectively. (c) Plot of drift time of protonated and sodiated PC cations in traveling wave ion mobility spectrometer versus ion mass. Experimentally determined data for protonated PC and sodiated PC cations are shown as solid squares and empty circles, respectively. The black dash and red solid lines are the linear fit to the protonated PC cation data set and to both protonated and sodiated PC cation data set, respectively.

Table 6.3: Collision Cross-Sections of Phosphatidylcholine Cations in N₂ Drift Gas Estimated and Evaluated using Empiric Calibration Method and Equations from Shavartsburg and Smith [27], respectively. Theoretically Determined Collision Cross-Sections in N₂ and He are also Listed.

PC	mass	Ω_D (Å ²)				
		Estimated (linear fit)	Estimated (power fit)	Evaluated	^a Theoretical (in N ₂)	^a Theoretical (in He)
5:0-5:0	426	143.4	136.1	244.8	255.3	162.5
8:0-8:0	510	171.0	159.5	289.2	301.3	197.3
11:0-11:0	594	193.1	183.0	327.3	335.0	223.8
14:0-16:0	706	214.9	210.7	367.0	361.1	248.2
16:0-16:0	734	221.9	220.4	379.9	400.7	277.1
18:0-14:0	734	221.1	219.3	378.4	363.7	254.4
16:0-18:2	758	220.1	218.0	376.7	388.2	265.8
18:0-16:0	762	225.5	225.7	386.7	364.1	254.2
16:0-20:4	782	220.7	218.9	377.8	357.0	250.6
18:0-18:2	786	224.5	224.4	385.0	387.1	270.3
18:0-18:1	788	225.3	225.5	386.4	396.2	274.4
18:0-18:0	790	230.5	233.2	396.2	395.3	275.3
16:0-22:6	806	223.6	223.2	383.3	366.8	258.0
24:0-24:0	958	258.7	280.4	451.2	423.4	305.1

^aAveraged over 200 conformations.

specific peptide structures in the gas phase through Columbic interactions with backbone amide, carboxyl, amine, and functional groups [35, 36]. In contrast, PC is composed of two esterified acyl chains and one phosphorylcholine attached to glycerol [1]. In the sodiated PC cations, sodium cation interacts solely with the phosphate group without inducing a noticeable conformation change of PC. Thus, a good correlation between mass and mobility is observed from PC cations regardless of whether they are protonated or sodiated.

6.4.4 Estimated Collision Cross-Sections of Ions Using T-Wave Calibration

A number of studies have employed empiric calibration methods to estimate collision cross-sections of ions using a set of calibrant ions [17, 21, 22, 25, 26]. To understand the structural characteristics related to collision cross-sections of PC cations, the calibration method was applied to estimate collision cross-sections. Figure 6.2a shows the calibration plots of Ω'_D versus t''_d for 14 singly charged peptides and 6 PC cations (Table 6.1). Due to the different natures of peptide and PC ions in the gas phase, we fit only the peptide calibrants first. Then we compared the fit of peptide calibrants to the fit result from the combined peptide and PC calibrants. Both linear fit and power fit to the calibrants were performed, and both fittings exhibit a high correlation coefficient ($R^2 = 0.98$ and 0.99 , respectively). Thalassinos *et al.* reported that linear fit is appropriate for calibration with

small peptides. However, a slightly higher correlation was observed for power fitting in the present study. Nearly identical calibration curves were obtained from both fits for peptide and combined peptide and PC calibrants. The nature of ions in the gas phase influenced the different mass-mobility correlations. However, the empiric calibration considered only the relationship between Ω'_D and t'_d . Thus, utilizing appropriate Ω_D for calibration is more important than the chemical category of the calibrant. Figure 6.2b summarizes the estimated collision cross-sections of protonated PC cations. The estimated collision cross-section values of PC cations are found in Table 6.3.

6.4.5 Determination of Collision Cross-Sections of Ions

Shavartsburg and Smith derived equations to describe the quantitative relationship between drift time and ion mobility in TWIMS [27]. Under the condition that $KE_{\max} < s$, where K is ion mobility, E_{\max} is maximum electric field (E), and s is wave velocity, the mobility of an ion is related to the average ion velocity in TWIMS as [27]

$$\bar{v} = \frac{K^2}{bs} \int_0^b E^2(x) ds, \quad (6.1)$$

where $E(x)$ is a half-sinusoidal traveling wave function and b is the waveform baseline width. Note that the equation ignores the focusing field and restricts the dynamics to axial coordinates of the SRIG. The rearrangement of Equation 6.1 with drift length L and the corrected drift time t'_d yields

$$K = \sqrt{\frac{Lbs}{t'_d \int_0^b E^2(x) dx}}. \quad (6.2)$$

Once K is determined, the reduced mobility K_0 can be determined according to

$$K_0 = \left(\frac{273 \text{ K}}{T}\right) \left(\frac{P}{760 \text{ Torr}}\right) K, \quad (6.3)$$

where P and T are the experimental pressure and temperature, respectively. Finally, the collision cross-section of an ion is evaluated by the relation [37, 38]

$$\Omega_D = \frac{3q}{16N_0} \left(\frac{2\pi}{\mu_{N_2} k_B T}\right)^{1/2} \frac{1}{K_0}, \quad (6.4)$$

where N_0 is the number density at standard state (273 K and 760 Torr), q is the charge on the ion, μ is the reduced mass of ion and N_2 , k_B is the Boltzmann constant, T is the temperature in the drift region, and Ω_D is the collision cross-section. The evaluated collision cross-sections of the examined PC cations are listed in Table 6.3. Note that a significant difference is found between the estimated Ω_D and the evaluated Ω_D . The evaluated Ω_D values are on average $\sim 42\%$ larger than the estimated Ω_D values from both power and linear fit. It is of note that the collision cross-sections of calibrants

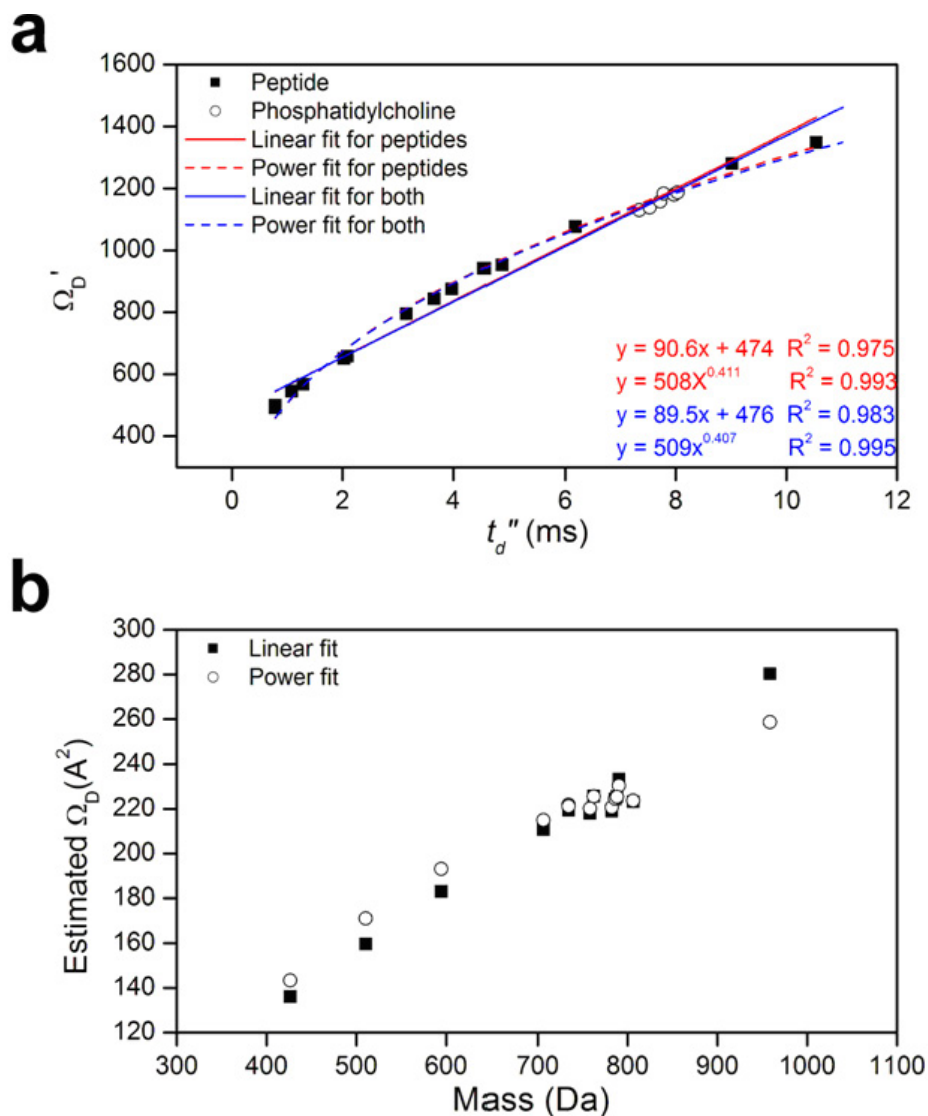


Figure 6.2: (a) Plot of corrected empiric cross-sections versus effective drift times for 14 peptides and 4 phosphatidylcholines (PC). For each peptide and PC the singly charged cation is used. Linear trend and power trend lines are shown as solid and dash lines, respectively. (b) A plot of the estimated cross-sections versus the ion mass for PC cations investigated in this study. The estimated collision cross-sections from linear trend and power trend are shown as solid squares and empty circles, respectively.

are determined in He [9, 16] while the drift gas used in TWIMS is N_2 . A strong contribution of short range interaction between ion and neutral is expected for Ω_D of an ion at the mass range of PC [20]. Yet, a considerable contribution is still considered from long range interactions of ion-neutral, linear shape, and larger mass in N_2 for the determination of Ω_D of an ion. It is inferred that the observed difference of Ω_D values are caused by lack of these terms in the calibration procedure.

6.4.6 Calculated Collision Cross-Sections of Ions Using the Trajectory Method

The Ω_D of the PC cations investigated in this study were calculated using the TJ method in N_2 [20] and He (Table 6.3) [28]. The MD simulation trajectories of the PC cation for 200 ps reveal that the two acyl chains undergo large structural fluctuation due to the thermal energy at 300 K. Figure 6.3a shows the time profile of the C-C distance between the carbon atoms at the end of each chain of the 18:0-18:0 PC during 200 ps of dynamics. The distance between two carbon atoms fluctuates in the range of 5 to 25 Å within a 5 to 20 ps time period. In order to account for the sufficient amount of conformational change required for Ω_D calculation, we need to sample the conformations at every 1 ps. Then, the average Ω_D can be determined using the TJ method in N_2 and He for the 200 structures on the MD simulation trajectories [20, 28].

Figure 6.3b shows the plot of Ω_D for PC cations evaluated using the Shavartsburg and Smith [27] equations versus the theoretical Ω_D in N_2 calculated using the modified TJ method. The theoretical Ω_D values of PC cations exhibit good agreement with the experimentally evaluated values. The agreement is within 6.2 % in the worst-case deviation with 3.2 % deviation on average. This shows that the experimental collision cross-sections of analyte ions can be determined using Synapt HDMS and the relationship between SRIG drift time and mobility derived by Shavartsburg and Smith [27]. In contrast, poor agreement was observed from the estimated Ω_D of PC cations from the linear fit and power fit calibration curves with deviations of 71.2 % and 73 % on average, respectively.

6.5 Discussion

6.5.1 Effect of Drift Gas on Ion Mobility

The difference between the estimated Ω_D of the PC cation using empiric calibration and the evaluated Ω_D using Equations 6.2 to 6.4 can be explained by the different polarizabilities, sizes, and shapes of He and N_2 molecules. In drift tube ion mobility spectrometry (DTIMS), the drift time, which corresponds to the effective drift time in TWIMS, t_d'' , is inversely proportional to the ion mobility, K :

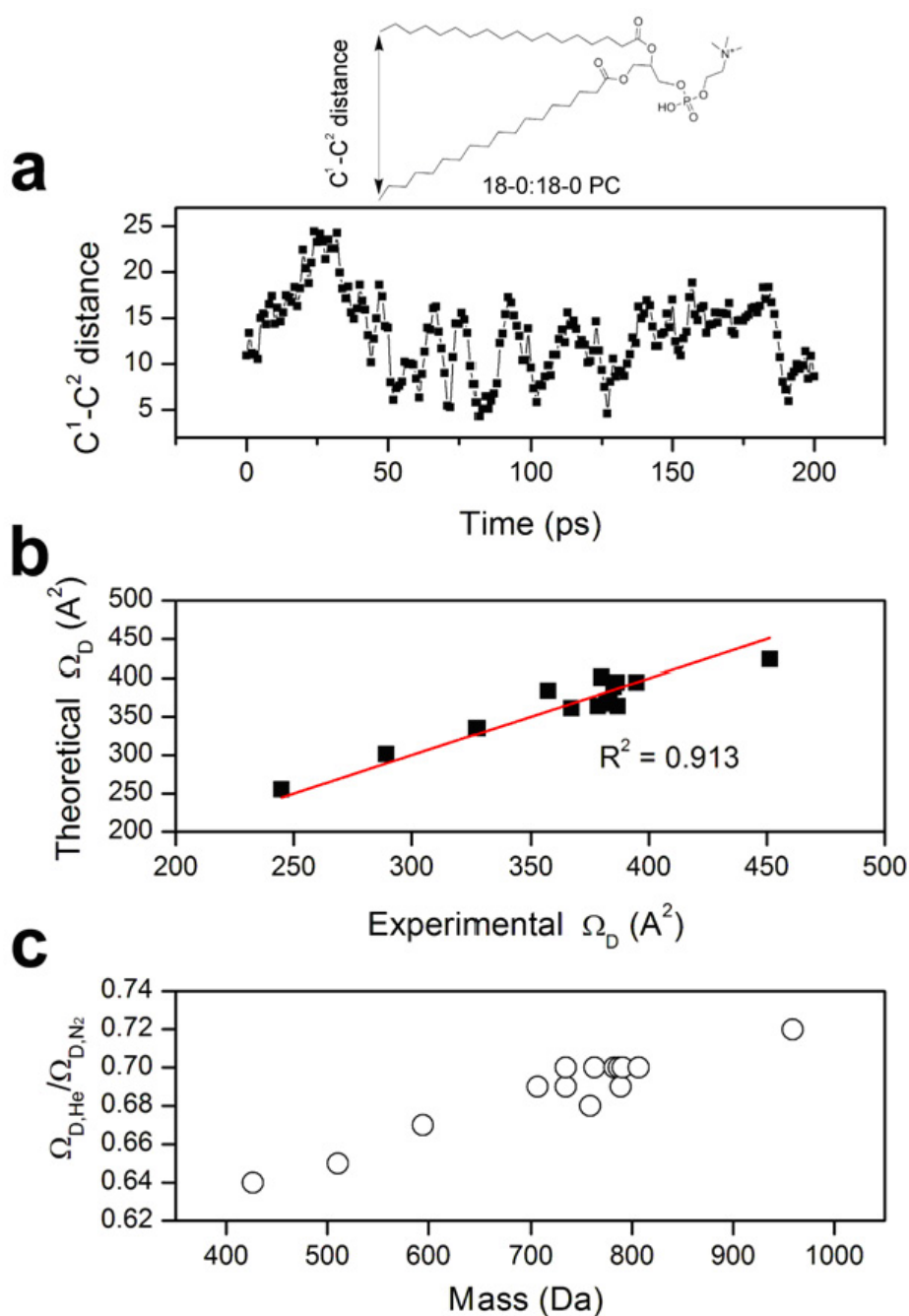


Figure 6.3: (a) Time profile of the distance between the carbon atoms at the end of each acyl chain of 18:0-18:0 phosphatidylcholine during 200 ps of the molecular dynamics simulation. The fluctuation is ranging from ~ 5 Å to ~ 25 Å with the time period of 5 – 20 ps. Approximately 17 times of fluctuation is observed from this trajectory. (b) Plot of experimentally determined collision cross-sections (Ω_D) of phosphatidylcholine (PC) cations in N_2 against theoretically determined Ω_D using the modified TJ method for N_2 drift gas. The theoretical Ω_D is obtained by averaging Ω_D for 200 structures from MD simulations. The solid line is $y = x$. (c) Plot of theoretical Ω_D in He over theoretical Ω_D in N_2 versus mass of PC cations.

$$K = L^2/Vt_d'', \quad (6.5)$$

where V is voltage across the drift tube. The relationship between K and Ω_D is described as [39]

$$K = \frac{3q}{16N} \left(\frac{2\pi}{\mu k_B T} \right)^{1/2} \frac{1}{\Omega_D}. \quad (6.6)$$

The corrected collision cross-section, Ω'_D , for the empiric calibration is defined as [17, 26]

$$\Omega'_D = \frac{\Omega_D \mu^{1/2}}{q}. \quad (6.7)$$

From Equations 6.5 through 6.7, we obtain the proportional relationship between t_d'' and Ω'_D . As discussed earlier, the default drift gas of TWIMS of Synapt HDMS is N_2 [17, 30, 40]. Calibration methods commonly employ the empirical Ω_D determined in He [16]. Thus, the corrected collision cross-section, Ω'_{D,N_2} , using the reduced mass in N_2 , μ_{N_2} , is related to the Ω_D in He as

$$\Omega'_{D,N_2} = \frac{\Omega_{D,N_2} \mu_{N_2}^{1/2}}{q} = \frac{\Omega_{D,He} \mu_{N_2}^{1/2}}{q}. \quad (6.8)$$

This relationship works if $\Omega_{D,He} \approx \Omega_{D,N_2}$. Hill and co-workers have demonstrated the high dependence of Ω_D of ions on drift gas [41, 42]. Beegle *et al.* demonstrated the different polarizability effects of the drift gas molecule on the Ω_D of the ion molecule using a series of homologous Gly peptides [41]. As the size of the Gly peptide increases, the difference between Ω_D in N_2 and in He decreases. The short range interaction for Ω_D becomes more important as the ion size increases [20]. Thus, the pre-assumption for the empiric calibration is valid when the size of the ion is very large; geometric factors of neutral and long range ion-neutral interactions are completely negligible for the determination of Ω_D [26]. Theoretically calculated Ω_D in N_2 and He further support this argument. Figure 6.3c shows the plot of the theoretical Ω_D in He divided by Ω_D in N_2 versus the mass of PC cations. As the size of the cation increases from 426 Da to 959 Da, the agreement between the two theoretical Ω_D values increases from 64 % to 72 %. As a result, for the mass range of the PC cations (400 – 1000 Da), estimating Ω_D using the empiric calibration method is not valid.

6.5.2 Geometrical Effect on the Collision Cross-Sections of Phosphatidylcholine Cations

Figure 6.4a shows the plot of theoretical characteristic Ω_D of PC cations versus ion mass compared with the corresponding surface area of PC cations in N_2 at 300 K using the Maximal Speed Molecular Surface (MSMS) program [43, 44]. Note that high similarity is observed from the characteristics of relative Ω_D from theoretical calculation and the relative surface areas of PC cations. This implies

that the Ω_D for each PC cation is largely influenced by the short range van der Waals interaction between the ion and the neutral N_2 molecule. The molecular weight and specific geometry of the ions dominate the short range van der Waals interaction, which affects the collision cross-section of the ion [20].

The mobility of ion K becomes field-dependent at a high electric field [45]. The field dependence of K depends on the nature properties of ion-neutral interactions. In general, high field behavior of an ion is observed when the ion acquires enough energy from E to change the nature of the ion-neutral collisions [45]. The total average energy of the ions can be determined from the Wannier energy formula as follows:

$$\frac{3}{2}k_B T_{eff} = \frac{3}{2}k_B T + \frac{1}{2}Mv_d^2, \quad (6.9)$$

where T_{eff} is an effective temperature of ion, M is the mass of a drift gas molecule, and v_d is the drift velocity of an ion [46]. The thermal kinetic energy is $3/2k_B T$, and the field energy is $1/2Mv_d^2$. The low field behavior of an ion is achieved when

$$\frac{3}{2}k_B T \gg \frac{1}{2}Mv_d^2. \quad (6.10)$$

Ion mobility spectrometers typically operate at low electric fields. The typical E/N range for the low field is a few Townsend ($\text{Td} = 10^{-17} \text{ Vcm}^2$) [18, 45]. Although the applied voltage in the TWIMS is as low as 8 V in this study, due to the low pressure of the SRIG (0.39 Torr in this study), the average E/N is ~ 80 Td. This is an order of magnitude larger than common IMS operating field. In addition, E/N increases to as much as ~ 230 Td at E_{\max} of traveling wave.

The primary effect of a high electric field is to heat the ions [45], which increases their internal energy through ion-neutral collisions. This collisional activation can result in conformation changes of the ions. Figure 6.4b shows the plots of the Ω_D of PC cations evaluated using the Shavartsburg and Smith [27] equations versus ion mass compared with the corresponding surface area of PC cations in N_2 at 300 K and 400 K. Greater similarity is observed from the characteristic relative Ω_D and the relative surface areas of PC cations at 400 K compared to the relative surface areas at 300 K. Although the experiment was performed at ~ 300 K, field heating induced a shift in ion conformation distribution to slightly higher energy state. This results in a greater similarity of the characteristic between relative Ω_D at 300 K and relative surface area at higher temperature, 400 K.

6.5.3 Mass-Mobility Correlations of Phosphatidylcholine Cations

Saturated PC cations investigated in this study exhibit a good correlation between mass and mobility (Figure 6.1a). However, deviations from the correlation are observed in unsaturated PC cations (Figure 6.1b). In the previous study, we discussed the importance of van der Waals potential for

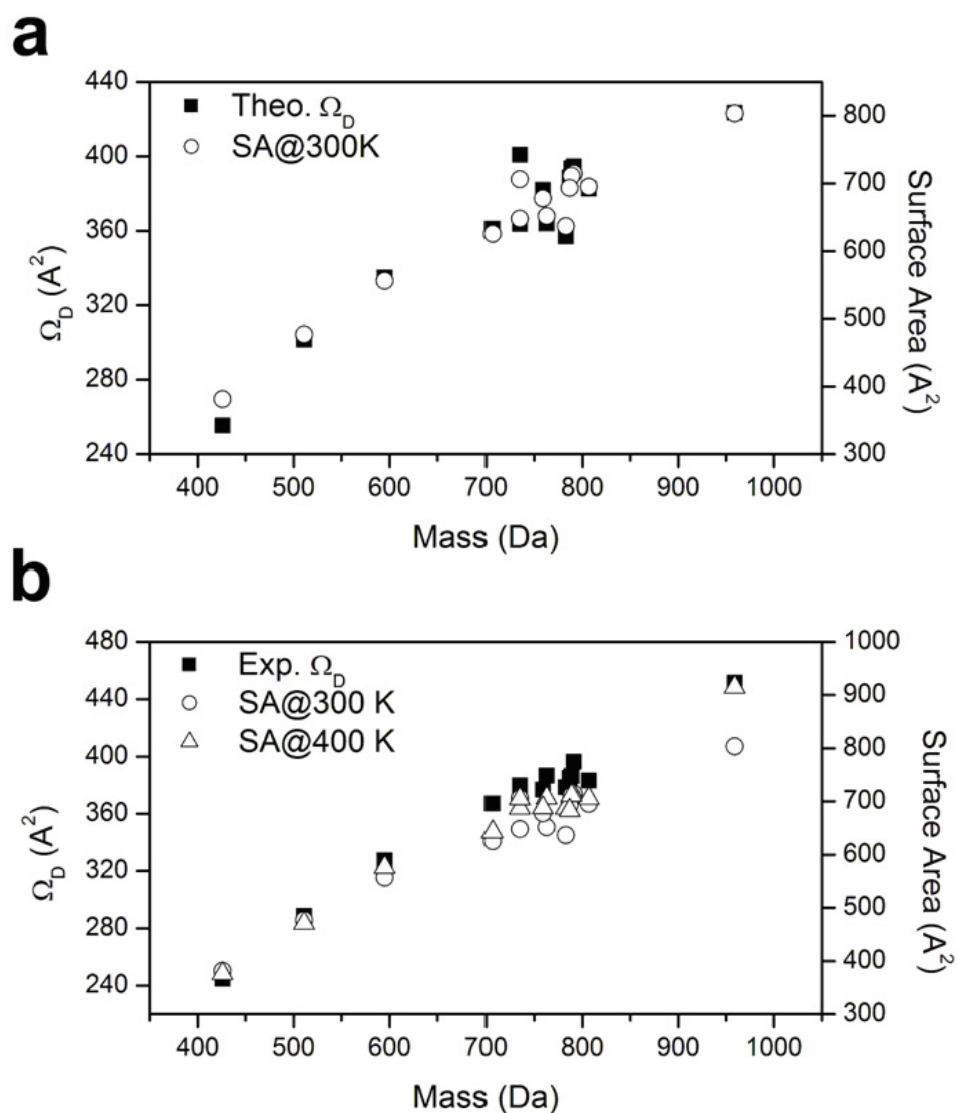


Figure 6.4: (a) Plots of theoretically determined collision cross-sections (Ω_D) and surface areas of phosphatidylcholine (PC) cations in N₂ versus ion mass. The calculated average Ω_D of the 200 ion conformations are shown as solid squares (left y -axis). The calculated surface areas of PC cations in N₂ at 300 K are shown as empty circles (right y -axis). (b) Plots of experimentally evaluated Ω_D and surface areas of phosphatidylcholine (PC) cations in N₂ versus ion mass. The Ω_D of PC cations are shown as solid squares (left y -axis). The calculated surface areas of PC cations in N₂ at 300 K and 400 K are shown as empty circles and empty triangle, respectively (right y -axis).

determining the collision cross-section of an ion as the ion size increases [20]. This implies that strong mass-mobility correlation is highly affected by the geometry of the ion. In order to understand the mass-mobility correlation of saturated PC cations and deviations of unsaturated PC cations from the correlation plot, we investigate structures of PC cations with corresponding Ω_D .

The minimum energy (E_0) structures of some of the saturated PC cations examined in this study are shown in Figure 6.5a. The structures with the closest Ω_D to the experimental values are also shown along with their corresponding relative energy values (E^*). The plot of Ω_D for the PC cations experimentally evaluated using the Shavartsburg and Smith [27] equations versus the theoretical Ω_D values of E_0 and E^* is shown in Figure 6.5b. Slightly larger Ω_D values are observed from PC cations with longer acyl chains (≥ 18 carbon) compared to the Ω_D values calculated from minimum energy structures. In contrast, smaller Ω_D values are observed from PC cations with short acyl chains (≤ 16 carbon). Note that PC cations with an acyl chain longer than 16 carbons form globular structures that are energetically favored. It is inferred that intramolecular van der Waals interactions of acyl chains drives the globular conformation to be preferred for large PC cations. However, extended structures are energetically favored for those with a shorter acyl chain (fewer than 16 carbons), whose steric effects prevent them from forming globular conformations in the gas phase. In contrast to peptide or protein ions, PC cations do not have strong intramolecular interactions to stabilize certain conformations. The energy difference between the E_0 structure and the E^* structure is only 19 kcal/mol on average. Thus, the conformations of these ions may fluctuate while traveling in the SRIG. As discussed earlier, the internal energy of an ion increases with collisional activations from the traveling wave electric field, which results in continual excitation of the ion [27]. The shift in ion conformations occurs toward slightly excited (E^*) state. Especially for larger molecules (18 or more carbon acyl chains), a significant increase in Ω_D occurs, since the increase in internal energy of these large molecules increases the importance of the entropy. As a result, the structural similarity of the saturated PC cations is maintained with moderately extended structures regardless of the length and symmetry of the PC acyl chains (Figure 6.5a); this promotes a good correlation between mass and mobility.

6.5.4 Characterizing Unsaturated Phosphatidylcholines from Mass-Mobility Correlation

Unsaturated PC cations exhibit significantly deviated mobility values from the mass-mobility correlation plot of saturated PC cations (Figure 6.1b). The drift time is reduced by $\sim 5\%$ for the unsaturated PC cation with one double bond; the drift time reduces further at a rate of $\sim 1\%$ for the additional double bond. Jackson *et al.* recently reported a $\sim 0.5\%$ reduction in drift time for each additional double bond of phospholipids in DTIMS. In the present study, the larger difference in

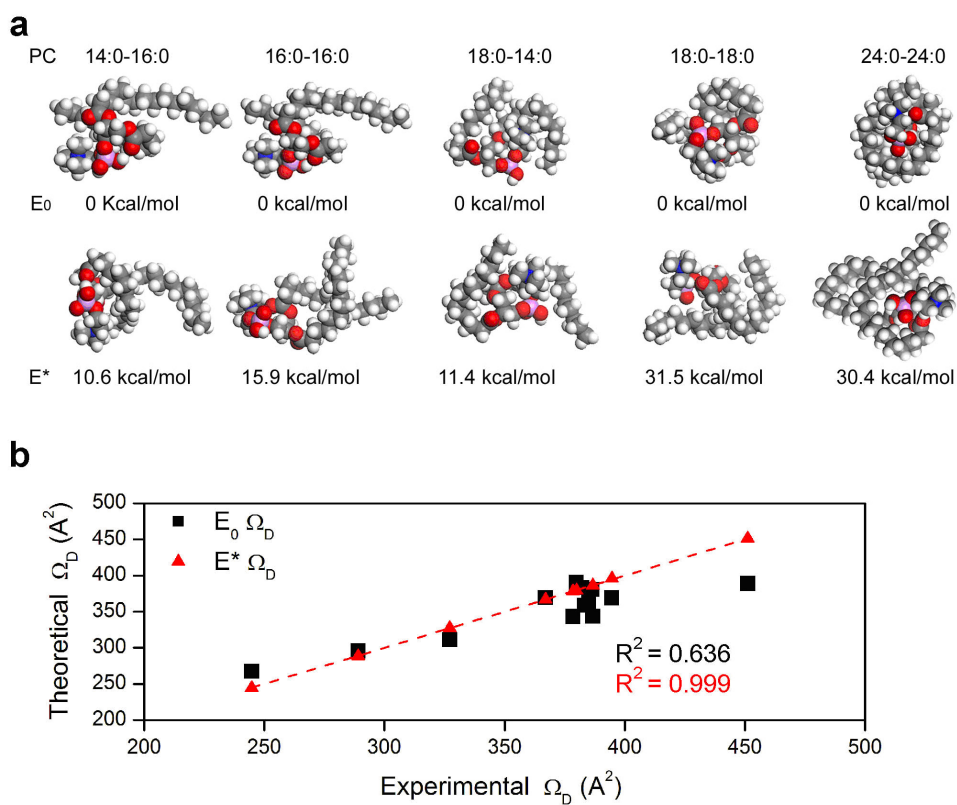


Figure 6.5: (a) MD simulated structures of saturated phosphatidylcholine cations at minimum energy state (E_0) are shown. The structures of the closest Ω_D to the experimental values are also shown along with corresponding relative energy values (E^*). (b) Plot of experimentally determined collision cross-sections (Ω_D) of phosphatidylcholine (PC) cations in N_2 against theoretically determined Ω_D at E_0 and E^* using the modified TJ method for N_2 drift gas. The solid line is $y = x$.

Table 6.4: Theoretically Determined Collision Cross-Sections (Ω_D) of Phosphatidylcholine Cations at Minimum Energy State (E_0). The Differences of Ω_D ($\Delta\Omega_D$) and Potential Energy (ΔE) from the PC Structure at E_0 to Experimentally Determined Ω_D .

PC	Ω_{D,E_0} (\AA^2)	$\Delta\Omega_D$ (%)	ΔE (kcal/mol)
5:0-5:0	267.08	9.1	15.2
8:0-8:0	295.44	2.1	10.6
11:0-11:0	311.24	-4.9	34.7
14:0-16:0	369.21	0.6	10.3
16:0-16:0	390.55	2.8	15.9
18:0-14:0	343.25	-9.3	11.4
16:0-18:2	382.85	1.6	10.4
18:0-16:0	343.38	-11.2	28.7
16:0-20:4	333.7	-11.7	26.8
18:0-18:2	362.37	-5.9	10.6
18:0-18:1	380.32	-1.6	2.21
18:0-18:0	368.93	-6.9	31.5
16:0-22:6	358.53	-6.5	30.2
24:0-24:0	388.94	-13.8	30.4

the mobility of unsaturated PC cations compared to saturated PC cations results from the different rate of conformation changes in TWIMS. Figure 6.6 shows structures of selected unsaturated PC cations at E_0 along with the conformations at E^* . For unsaturated PC cations, a smaller shift in Ω_D is observed from the Ω_D of the most stable conformation compared to saturated PCs of similar mass. For those PC cations with more than 16 carbon acyl chains, saturated PC cations exhibit a ~ 10 % difference in Ω_D on average, while unsaturated PC cations show only ~ 5 % difference on average (Table 6.4). As observed in Figure 6.6, the major change in conformation occurs at the saturated acyl chain, while the conformation of the unsaturated acyl chain (yellow) maintains a bent structure. The presence of *cis*-double bonds in an acyl chain prevents the unsaturated acyl chain from extending by activation. As a result, less fluctuation in the ion structure occurred among unsaturated PC cations in the TWIMS. Unsaturated PC cations show smaller Ω_D values than saturated PC cations, which can form more extended conformations. This is logical given that globular structures of unsaturated PC cations are more compact and therefore have smaller collision cross-sections. This allows us to characterize unsaturated PC cations based on their mobility, and thus collision cross-sections, using TWIMS.

6.6 Conclusions

A high correlation between mass and mobility in N_2 is observed from a number of saturated PC cations in TWIMS. A significant deviation from this mass-mobility correlation is observed with unsaturated PC cations. Theoretical investigation using a modified TJ method indicates that the

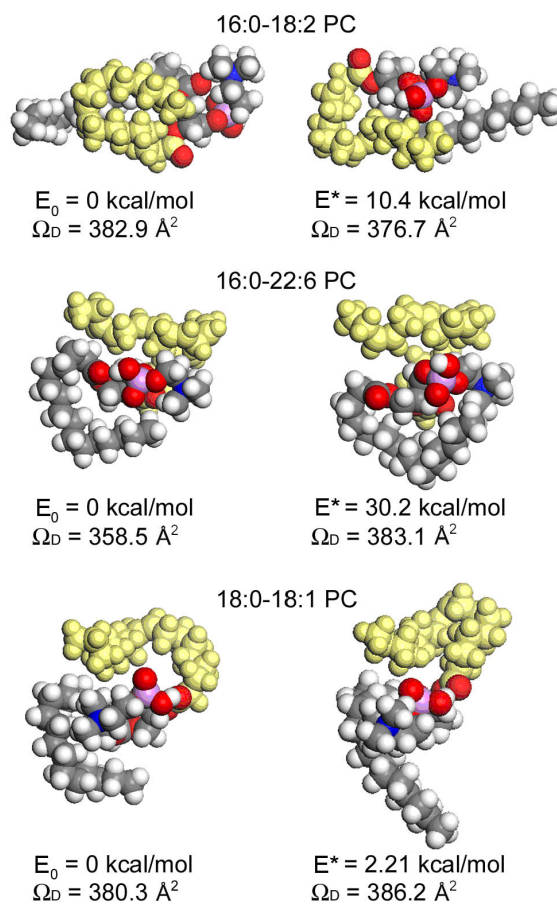


Figure 6.6: MD simulated structures of unsaturated phosphatidylcholine cations at minimum energy state (E_0) are shown. The structures of the closest Ω_D to the experimental values are also shown along with corresponding relative energy values (E^*). Unsaturated acyl chain is colored in yellow.

empiric calibration method is not suitable to estimate collision cross-sections for PC cations. Instead, we evaluate collision cross-sections using a quantitative relationship between drift time and mobility derived by Shavartsburg and Smith [27]. In addition to the lack of intramolecular interactions among PC cations, collisional excitation of the ions in the SRIG induces a shift in ion conformational distribution. The unsaturated acyl chain remains bent, while the saturated acyl chain extends under the electric field, which causes larger collision cross-sections for saturated PCs and smaller ones for unsaturated PCs. The initial double bond in the acyl chain yields an approximately 5 % reduction in drift time, with further drift time reduction at the rate of ~ 1 % for each additional double bond. As a result, greater separation and characterization of unsaturated PC cations can be achieved using TWIMS.

6.7 Acknowledgments

This research was carried out at the Jet Propulsion Laboratory, California Institute of Technology, under a contract with the National Aeronautics and Space Administration (NASA), the University of California Los Angeles Mass Spectrometry and Proteomics Technology Center, and the Material and Process Simulation Center, Beckman Institute, California Institute of Technology. Financial support through NASA's Astrobiology Science and Technology Instrument Development, Planetary Instrument Definition and Development, and Mars Instrument Development programs is gratefully acknowledged. JAL acknowledges support from the NIH (RR20004).

Bibliography

- [1] Gurr, M. I.; Hardwood, J. L. *Lipid Biochemistry*; 4th ed.; Chapman and Hall: New York, 1991.
- [2] Simoneit, B. R. T.; Summons, R. E.; Jahnke, L. L. *Orig. Life Evol. Biosph.* **1998**, 28, 475-483.
- [3] Mossoba, M. M.; Kramer, J. K. G.; Brenna, J. T.; McDonald, R. E. *Lipid Analysis and Lipidomics* AOCS Publishing 2006.
- [4] Woods, A. S.; Ugarov, M.; Egan, T.; Koomen, J.; Gillig, K. J.; Fuhrer, K.; Gonin, M.; Schultz, J. A. *Anal. Chem.* **2004**, 76, 2187-2195.
- [5] Jackson, S. N.; Ugarov, M.; Egan, T.; Post, J. D.; Langlais, D.; Schultz, J. A.; Woods, A. S. *J. Mass Spectrom.* **2007**, 42, 1093-1098.
- [6] Jackson, S. N.; Ugarov, M.; Post, J. D.; Egan, T.; Langlais, D.; Schultz, J. A.; Woods, A. S. *J. Am. Soc. Mass Spectrom.* **2008**, 19, 1655-1662.
- [7] McLean, J. A.; Ridenour, W. B.; Caprioli, R. M. *J. Mass Spectrom.* **2007**, 42, 1099-1105.
- [8] Fenn, L. S.; McLean, J. A.; Springer Heidelberg: 2008, p 905-909.
- [9] Fenn, L. S.; Kliman, M.; Mahsut, A.; Zhao, S. R.; McLean, J. A. **2009**, *In Press*.
- [10] Gidden, J.; Bowers, M. T. *J. Am. Soc. Mass Spectrom.* **2003**, 14, 161-170.
- [11] Fenn, L. S.; McLean, J. A. *Chem. Commun.* **2008**, 5505-5507.
- [12] Jarrold, M. F. *Annu. Rev. Phys. Chem.* **2000**, 51, 179-207.
- [13] Griffin, G. W.; Dzidic, I.; Carroll, D. I.; Stillwel, R. N.; Horning, E. C. *Anal. Chem.* **1973**, 45, 1204-1209.
- [14] Berant, Z.; Karpas, Z. *J. Am. Chem. Soc.* **1989**, 111, 3819-3824.
- [15] Karpas, Z.; Berant, Z. *J. Phys. Chem.* **1989**, 93, 3021-3025.
- [16] Valentine, S. J.; Counterman, A. E.; Clemmer, D. E. *J. Am. Soc. Mass Spectrom.* **1999**, 10, 1188-1211.

- [17] Thalassinou, K.; Grabenauer, M.; Slade, S. E.; Hilton, G. R.; Bowers, M. T.; Scrivens, J. H. *Anal. Chem.* **2009**, 81, 248-254.
- [18] Johnson, P. V.; Kim, H. I.; Beegle, L. W.; Kanik, I. *J. Phys. Chem. A* **2004**, 108, 5785-5792.
- [19] Kim, H. I.; Johnson, P. V.; Beegle, L. W.; Beauchamp, J. L.; Kanik, I. *J. Phys. Chem. A* **2005**, 109, 7888-7895.
- [20] Kim, H.; Kim, H. I.; Johnson, P. V.; Beegle, L. W.; Beauchamp, J. L.; Goddard, W. A.; Kanik, I. *Anal. Chem.* **2008**, 80, 1928-1936.
- [21] Ruotolo, B. T.; Giles, K.; Campuzano, I.; Sandercock, A. M.; Bateman, R. H.; Robinson, C. V. *Science* **2005**, 310, 1658-1661.
- [22] Ruotolo, B. T.; Hyung, S. J.; Robinson, P. M.; Giles, K.; Bateman, R. H.; Robinson, C. V. *Angew. Chem.-Int. Edit.* **2007**, 46, 8001-8004.
- [23] Smith, D. P.; Giles, K.; Bateman, R. H.; Radford, S. E.; Ashcroft, A. E. *J. Am. Soc. Mass Spectrom.* **2007**, 18, 2180-2190.
- [24] Bagal, D.; Zhang, H.; Schnier, P. D. *Anal. Chem.* **2008**, 80, 2408-2418.
- [25] Williams, J. P.; Scrivens, J. H. *Rapid Commun. Mass Spectrom.* **2008**, 22, 187-196.
- [26] Ruotolo, B. T.; Benesch, J. L. P.; Sandercock, A. M.; Hyung, S. J.; Robinson, C. V. *Nat. Protoc.* **2008**, 3, 1139-1152.
- [27] Shvartsburg, A. A.; Smith, R. D. *Anal. Chem.* **2008**, 80, 9689-9699.
- [28] Mesleh, M. F.; Hunter, J. M.; Shvartsburg, A. A.; Schatz, G. C.; Jarrold, M. F. *J. Phys. Chem.* **1996**, 100, 16082-16086.
- [29] Giles, K.; Pringle, S. D.; Worthington, K. R.; Little, D.; Wildgoose, J. L.; Bateman, R. H. *Rapid Commun. Mass Spectrom.* **2004**, 18, 2401-2414.
- [30] Pringle, S. D.; Giles, K.; Wildgoose, J. L.; Williams, J. P.; Slade, S. E.; Thalassinou, K.; Bateman, R. H.; Bowers, M. T.; Scrivens, J. H. *Int. J. Mass Spectrom.* **2007**, 261, 1-12.
- [31] MacKerell, A. D.; Bashford, D.; Bellott, M.; Dunbrack, R. L.; Evanseck, J. D.; Field, M. J.; Fischer, S.; Gao, J.; Guo, H.; Ha, S.; Joseph-McCarthy, D.; Kuchmir, L.; Kuczera, K.; Lau, F. T. K.; Mattos, C.; Michnick, S.; Ngo, T.; Nguyen, D. T.; Prodhom, B.; Reiher, W. E.; Roux, B.; Schlenkrich, M.; Smith, J. C.; Stote, R.; Straub, J.; Watanabe, M.; Wiorkiewicz-Kuczera, J.; Yin, D.; Karplus, M. *J. Phys. Chem. B* **1998**, 102, 3586-3616.
- [32] Plimpton, S. *J. Comput. Phys.* **1995**, 117, 1-19.

- [33] Feller, S. E.; Gawrisch, K.; MacKerell, A. D. *J. Am. Chem. Soc.* **2002**, 124, 318-326.
- [34] Alberts, B.; Bray, D.; Hopkin, K.; Johnson, A.; Lewis, J.; Raff, M.; Roberts, K.; Walter, P. *Essential Cell Biology*; Second ed.; Garland Science: New York, 2004.
- [35] Kohtani, M.; Kinnear, B. S.; Jarrold, M. F. *J. Am. Chem. Soc.* **2000**, 122, 12377-12378.
- [36] Wyttenbach, T.; Liu, D. F.; Bowers, M. T. *J. Am. Chem. Soc.* **2008**, 130, 5993-6000.
- [37] Revercomb, H. E.; Mason, E. A. *Anal. Chem.* **1975**, 47, 970-983.
- [38] Eiceman, G. A.; Karpas, Z. *Ion Mobility Spectrometry*; CRC Press: Boca Raton, FL, 1994.
- [39] Mason, E. A.; O'hara, H.; Smith, F. J. *J. Phys. B* **1972**, 5, 169-176.
- [40] Scarff, C. A.; Thalassinos, K.; Hilton, G. R.; Scrivens, J. H. *Rapid Commun. Mass Spectrom.* **2008**, 22, 3297-3304.
- [41] Beegle, L. W.; Kanik, I.; Matz, L.; Hill, H. H. *Int. J. Mass Spectrom.* **2002**, 216, 257-268.
- [42] Matz, L. M.; Hill, H. H.; Beegle, L. W.; Kanik, I. *J. Am. Soc. Mass Spectrom.* **2002**, 13, 300-307.
- [43] Connolly, M. L. *J. Am. Chem. Soc.* **1985**, 107, 1118-1124.
- [44] Sanner, M. F.; Olson, A. J.; Spohner, J. C. *Biopolymers* **1996**, 38, 305-320.
- [45] Carr, T. W.; Baim, M. A.; Cohen, M. J.; Dam, R. J.; Hagen, D. F.; Hill, H. H.; Mason, E. A.; Siegel, M. W.; Spangler, G. E.; Wernlund, R. F. *Plasma Chromatography*; Plenum Press: New York, 1984.
- [46] Wannier, G. H. *Bell Syst. Tech. J.* **1953**, 32, 170-254.

Chapter 7

Interfacial Reactions of Ozone with Lipids and Proteins in a Model Lung Surfactant System

7.1 Abstract

Oxidative stresses from irritants such as hydrogen peroxide and ozone (O_3) can cause dysfunction of the pulmonary surfactant (PS) in the human lung, resulting in chronic diseases of the respiratory tract. For identification of structural changes of major components of PS due to the heterogeneous reaction with O_3 , field induced droplet ionization (FIDI) mass spectrometry is utilized to probe the surfactant layer system. FIDI is a soft ionization method in which ions are extracted from the surface of micro liter volume droplets. We report the structurally specific oxidative changes of SP-B₁₋₂₅ (a shortened version of human surfactant protein B) and 1-palmitoyl-2-oleoyl-*sn*-phosphatidylglycerol (POPG) due to reaction with O_3 at the air-liquid interface. We also present studies of the interfacial oxidation of SP-B₁₋₂₅ in a non-ionizable 1-palmitoyl-2-oleoyl-*sn*-glycerol monolayer as a model lung surfactant system, where the competitive oxidation of the two components is observed. Our results indicate that the heterogeneous reaction at the interface is different from that in the bulk phase. For example, we observe the hydroxyhydroperoxide and the secondary ozonide as major products of the heterogeneous ozonolysis of POPG. These products are metastable and difficult to observe in the bulk-phase. In addition, compared to the nearly complete homogeneous oxidation of SP-B₁₋₂₅, only a subset of the amino acids known to react with ozone is oxidized in the hydrophobic interfacial environment. Combining these experimental observations with the results of molecular dynamics simulations provides an improved understanding of the interfacial structure and chemistry of a model lung surfactant system when subject to oxidative stress.

7.2 Introduction

The human lung is constantly exposed to airborne environmental insults. Long-term and immediate exposure of lungs to pathogens, air pollutants, and other irritants can be a major cause of acute and chronic injuries such as cardiopulmonary mortality and lung cancer [1, 2, 3]. Lung disease is the third leading cause of death in the United States and ~\$154 billion is spent for direct and indirect lung disease-related health care every year [3]. Lung disease death rates are still increasing and more efforts to understand the chemical as well as the physical characteristics of lung system are required.

Pulmonary surfactant (PS) is a complex mixture of lipids and proteins [4] found in the lungs that reduces the surface tension of the alveolar sacs during the breath cycle. Phospholipids form oriented monolayers at the air-liquid interface. The principal phospholipid component of the layer, 1,2-dipalmitoyl-*sn*-phosphatidylcholine (DPPC), can achieve a very low surface tension (~ 0 mN/m) [5, 6] while the higher fluidity of unsaturated phospholipids such as 1-palmitoyl-2-oleoyl-*sn*-phosphatidylglycerol (POPG) improves the adsorption and spreading properties of surfactant at the air-liquid interface [6]. Surfactant protein B (SP-B) enhances phospholipid adsorption and spreading from the sub-phase to the interface [7], and inherited deficiencies in SP-B are lethal at birth [8]. Despite its vital importance, little is known about the interactions of the protein with phospholipids to form final lipid-protein complexes in the PS [9] as well as the manner in which this complex environment modifies the interaction of reactive oxygen species (ROS) with individual components.

A number of studies have reported the chemical changes of major components of PS under various oxidative stresses [10, 11, 12], as well as changes in physical properties, which cause acute lung injury and respiratory failure [1, 13, 14]. For example, Uppu *et al.* used human red-blood cell membranes as a model lung system and demonstrated their oxidation via a bulk-phase O_3 application [11]. The alteration of structure and physical properties of SP-B by ROS has been reported by Possmayer and co-workers [12, 14]. Yet, understanding detailed mechanisms of chemical and physical changes in the complex PS system is still an active and challenging field of research. In particular, the oxidative change of major PS components by a heterogeneous air-liquid reaction with an external oxidative source (i.e. O_3) has not been studied thoroughly at the molecular level. An increasing number of studies have focused on the heterogeneous chemistry of small molecules at the air-liquid interface, mainly using mass spectrometric [15] and spectroscopic [16] techniques, as well as theoretical methods [17]. Fewer studies have considered the air-liquid interfacial chemistry of biologically relevant systems. Exemplifying the latter, Colussi and co-workers recently reported heterogeneous reactions with O_3 of ascorbic acid [18] and uric acid [19], which are components of the pulmonary epithelial lining fluid, using mass spectrometry.

Field induced droplet ionization mass spectrometry (FIDI-MS) comprises a soft ionization method to sample ions from the surface of microliter droplets [15, 20, 21]. It is ideally suited to monitor time

dependent heterogeneous reactions at the air-liquid interface. A pulsed electric field stretches neutral droplets until they develop dual Taylor cones, emitting streams of positively and negatively charged submicron droplets in opposite directions. In practice, a quiescent hanging droplet is formed on the end of a capillary and then exposed to gas-phase reactants for a variable period of time, followed by FIDI-MS sampling of molecular species present in the interfacial layer (Figure 7.1).

In this study, we utilize FIDI-MS for probing air-liquid interfacial oxidation of POPG, representative of the major unsaturated anionic lipids in lung surfactant, and SP-B₁₋₂₅ (FPIPLPY-CWLCRALIKRIQAMIPKG) by O₃. Synthetic α -helical SP-B₁₋₂₅ is reported to produce the same effect as the entire 79 amino acid SP-B [22, 23, 24]. Sampling droplets with an interfacial layer of POPG or SP-B₁₋₂₅ exposed to O₃ gas over a range of reaction times reveals distinct air-liquid interfacial chemistry. In addition, we examine the heterogeneous reaction of a model PS system comprising SP-B₁₋₂₅ and 1-palmitoyl-2-oleoyl-*sn*-glycerol (POG) with O₃. POG is non-ionizable lipid with properties at the air-liquid interface similar to POPG. It is employed to avoid undesired competition of ionization with SP-B₁₋₂₅ at the surface of the droplet during the FIDI experiment. For comparison to the observed heterogeneous chemistry, we also report homogeneous reactions of SP-B₁₋₂₅ with dissolved ozone. Structures of POPG, POG, and SP-B₁₋₂₅ are shown in Figure 7.2. The observed interfacial reactions are correlated with positioning of SP-B₁₋₂₅ in a lipid monolayer as determined by means of molecular dynamic (MD) simulations.

7.3 Methods

7.3.1 Chemicals and Reagents

Sodium salts of POPG and POG were purchased from Avanti Polar Lipid (Alabaster, AL). SP-B₁₋₂₅ was purchased from Biomer Technology (Hayward, CA). All solvents were purchased from EMD Chemicals Inc. (Gibbstown, NJ).

7.3.2 Online FIDI-MS Technique and Heterogeneous Oxidation by O₃

The FIDI-MS instrument used in this investigation were based on designs previously described by Grimm *et al.* [15]. A ~ 2 mm o.d. droplet of analyte solution is suspended from the end of a 28-gauge stainless steel capillary (Small Parts Inc.). The droplet is located on center in the region between the plate electrode and the MS inlet; the plate and inlet were separated by 6 mm. A high-voltage pulse ($\pm 7 \times 10^5$ V m⁻¹, 20 ms) is applied on the parallel plate electrode and sampling capillary to achieve FIDI. Ozonolysis reactions occur between 0 and 30 s after a quiescent droplet is achieved ($\sim 1 - 2$ s). A pencil-style UV calibration lamp (model 6035, Oriol) generates ~ 20 ppm O₃. 100 μ M POPG, 50 μ M SP-B₁₋₂₅, or mixtures of 100 μ M POG and 50 μ M SP-B₁₋₂₅ in 1:1

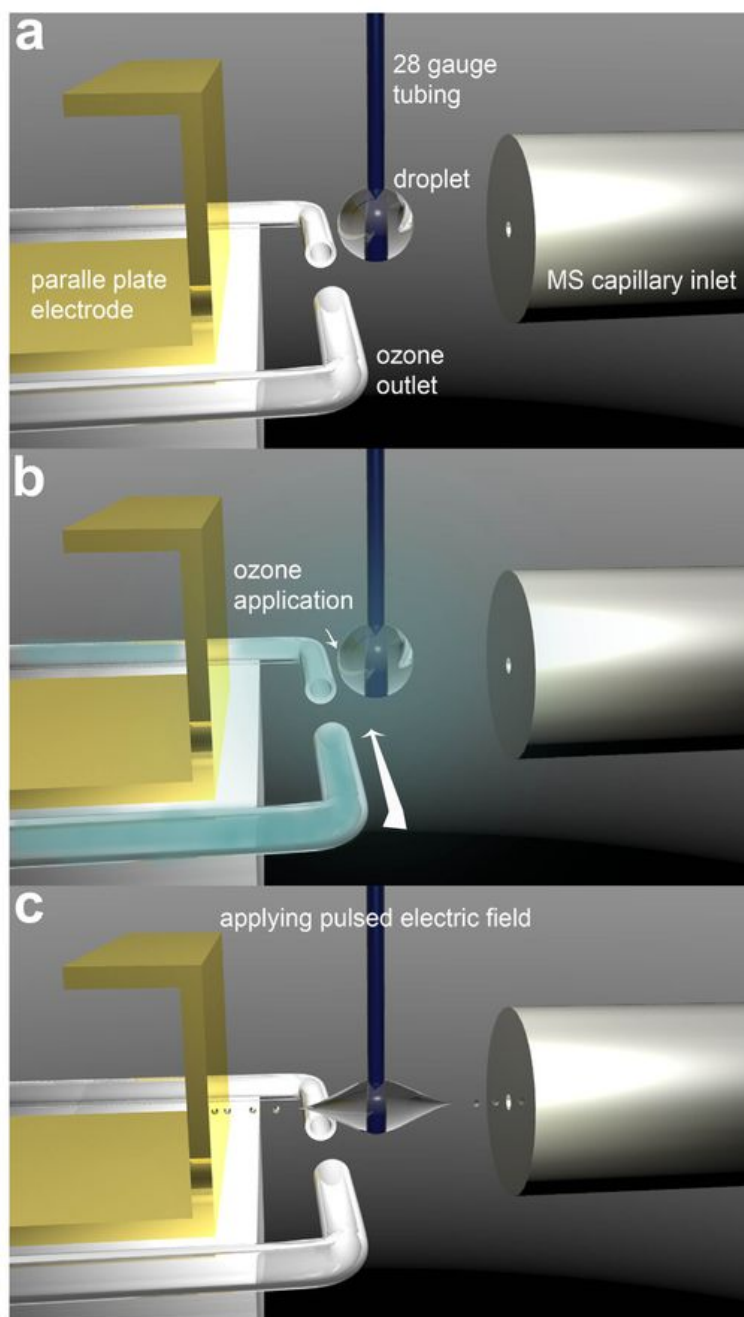


Figure 7.1: Illustration of FIDI-MS methodology for studies of interfacial reactions. (a) A quiescent hanging droplet of analyte-containing solution is formed on the end of a capillary. All electrical components remain at ground as the droplet is formed and reacts in a field-free environment. (b) The droplet is exposed to gas-phase reactants for a variable period of time to allow for heterogeneous reactions between gas-phase and solution-phase species. (c) After a reaction period, a pulsed electric field stretches the neutral droplet until it emits a stream of positively and negatively charged submicron droplets in opposite directions. Ionized reactants and products from heterogeneous reactions enter the capillary inlet of the mass analyzer. Either positive or negative ions can be sampled.

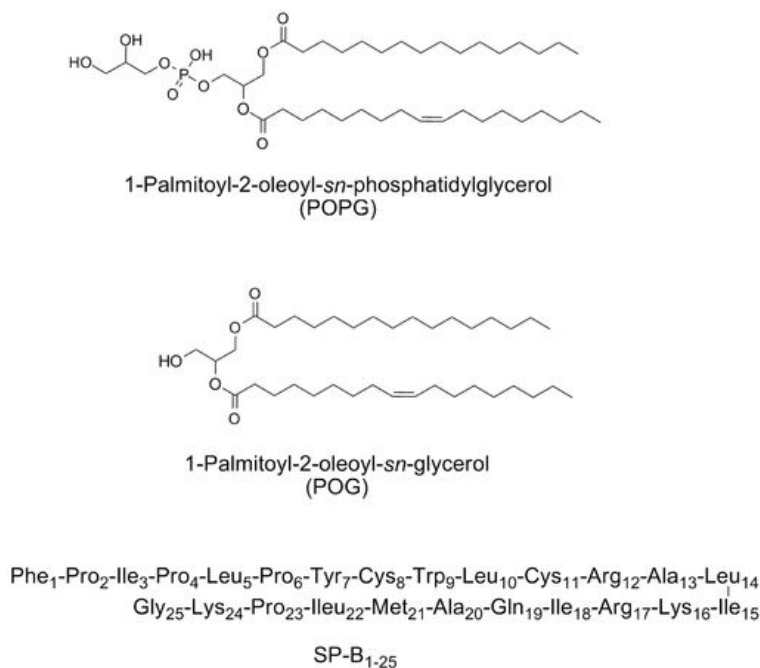


Figure 7.2: Structures of POPG, POG, and SP-B₁₋₂₅ investigated in this study.

(by volume) water and methanol feed the droplet source. The FIDI-MS spectra reported in this study were obtained by averaging five to ten individually acquired spectra from separately prepared droplets. The m/z of each ion was determined from the locations of the peak maxima identified in the mass spectra. The experimental details for the bulk-phase O₃ application and the Fenton reaction of SP-B₁₋₂₅ are described in Appendix H.

7.3.3 Molecular Dynamic Simulations

The MD simulations were performed with the all-atom CHARMM PARAM27 [25] force field using the LAMMPS (large-scale atomic/molecular massively parallel simulator) code [26]. To describe the water, we used a flexible TIP3P potential, which needs additional Hooke's constants, K of 900 kcal/mol/Å² for OH bond and K of 110 kcal/mol/rad² for HOH angle to the 3-site-rigid TIP3P model [25]. The initial conformation of SP-B₁₋₂₅ was taken from the Protein Data Bank structure (1DFW). The particle-particle particle-mesh (PPPM) method [27] was employed to compute the electrostatic using an accuracy criterion of 10⁻⁵.

The initial structures for the lipid monolayer-water systems were prepared with 48 hexagonally-packed lipids on the 3168, 3264, 3744, and 4464 water molecules for the 55, 60, 65, and 70 Å²/lipid surface densities, respectively. A pure-repulsive wall potential, $E = \epsilon \left[2/15 (\sigma/r)^9 - (\sigma/r)^3 \right]$, where $\epsilon = 0.1521$ kcal/mol and $\sigma = 3.1538$ Å with cut-off distance of 2.7071 Å, was applied at $z = 0$ to

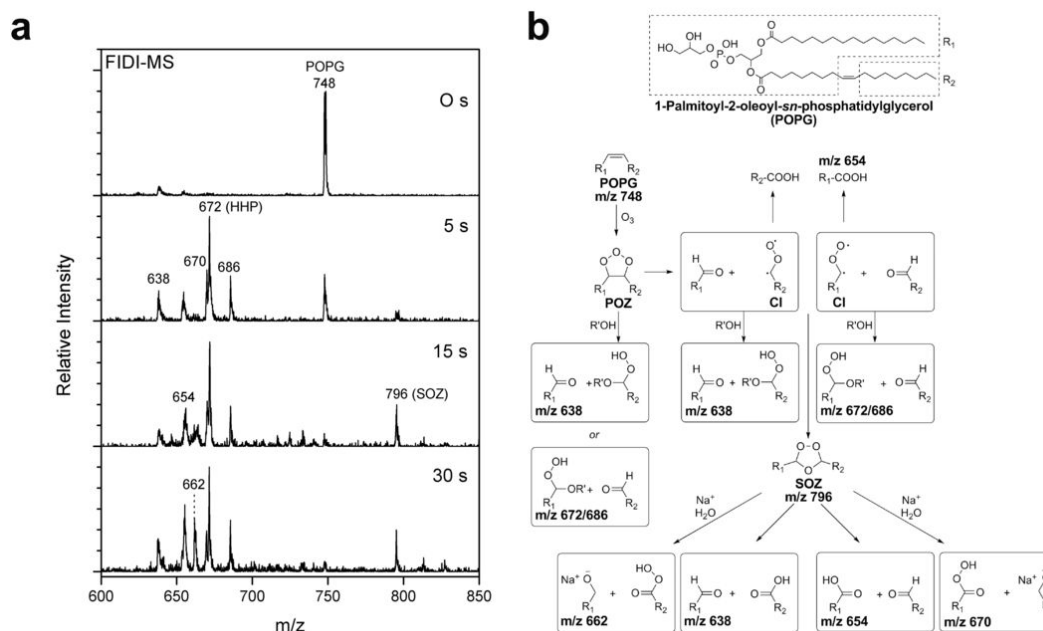


Figure 7.3: (a) Heterogeneous reaction of POPG with O_3 as a function of time. In the absence of ozone, the negative ion FIDI-MS spectrum of POPG is dominated by the singly deprotonated POPG peak at m/z 748. POPG is depleted after 15 s of the exposure and oxidation products are dominated by deprotonated hydroxyhydroperoxide (HHP) at m/z 672. The aldehyde, carboxylic acid, and methoxyhydroperoxide products are observed at m/z 638, m/z 654, and m/z 686, respectively. The secondary ozonide (SOZ) and sodiated alcohol products show up in the spectra at m/z 796 and m/z 662, respectively. (b) Summary of heterogeneous oxidation of POPG with O_3 at the air-liquid interface. R' is H for water and CH_3 for methanol.

prevent the water from diffusing in the negative z -direction. The dimensions of the simulation cells used were ($55.21 \text{ \AA} \times 47.82 \text{ \AA} \times 200.0 \text{ \AA}$) for the $55 \text{ \AA}^2/\text{lipid}$, ($57.67 \text{ \AA} \times 49.94 \text{ \AA} \times 200.0 \text{ \AA}$) for the $60 \text{ \AA}^2/\text{lipid}$, ($60.02 \text{ \AA} \times 51.98 \text{ \AA} \times 200.0 \text{ \AA}$), for the $65 \text{ \AA}^2/\text{lipid}$, and ($62.28 \text{ \AA} \times 53.94 \text{ \AA} \times 200.0 \text{ \AA}$) for the $70 \text{ \AA}^2/\text{lipid}$ surface densities. The systems were equilibrated for 0.5 ns using 300 K NVT MD simulations by applying Nosé-Hoover thermostat with a temperature damping relaxation time of 0.1 ps. Then, 2.0 ns NVT MD simulations were performed, and these trajectories are employed for the analysis of the atomic profiles.

The initial structure for the SP- B_{1-25} in the POG or POPG monolayer was constructed using the final structure after the simulation of the lipid monolayer-water system with the surface density of 60 \AA^2 . After removing six neighboring lipids, the SP- B_{1-25} is inserted into the resultant cavity with an α -helical axis orientation angle of 34° to the interfacial plane. Then the dimensions of the simulation cells were slightly adjusted to ($57.88 \text{ \AA} \times 50.12 \text{ \AA} \times 200.0 \text{ \AA}$). Similar to the lipid monolayer simulations, 0.5 ns equilibration followed by 2.0 ns NVT MD simulation was performed at 300 K. To analyze the trajectories, we averaged the population over the last 0.5 ns of the 2.0 ns trajectories.

7.4 Results and Discussion

7.4.1 Interfacial Reaction of POPG with O₃

The *cis*-double bond of an unsaturated phospholipid reacts with O₃ yielding aldehyde and carboxylic acid products directly from primary ozonide (POZ) or through energetic Criegee intermediates (CI), while saturated phospholipids such as DPPC remain intact. In this study we have investigated the heterogeneous reaction of O₃ with POPG as a representative unsaturated phospholipid in PS system. The negative ion FIDI-MS spectra for ozonolysis of POPG in a water/methanol (1:1 by volume) droplet are shown in Figure 7.3a along with the proposed reaction mechanisms (Figure 7.3b). Singly deprotonated POPG, observed at m/z 748, is seen as a dominant species in the FIDI-MS spectrum before O₃ application (Figure 7.3a). Products resulting from ozonolysis of POPG appear at least as early as 5 s after exposing the droplet to O₃. The relative abundance of the reactant POPG decreases dramatically after 15 s of exposure, and then the FIDI-MS spectrum is dominated by ozonolysis products after 30 s. The time for consuming 90 – 99 % of POPG to form the primary ozonide (POZ) at the air-liquid interface is calculated to be $\sim 10 - 20$ s (see Appendix G). This agrees well with the experimental observation of this study.

It is noteworthy that hydroxyhydroperoxide (HHP), methoxyhydroperoxide (MHP), and the SOZ, which are known to be metastable species in the bulk-phase, are observed as major products of POPG ozonolysis in the FIDI-MS spectra (Figure 7.3a) [28]. In order to yield HHP, a Criegee intermediate (CI) or a POZ is required to react with a water molecule [28, 29]. Rapid decomposition of HHP through proton transfers from water molecules yields ROS [29], which makes it difficult to observe HHP directly in the bulk-phase. The water density at the air-liquid interfacial region is significantly lower than in the bulk-phase [30]. In addition, water molecules in a lipid monolayer are observed to be localized within the lipid head group region due to the strong interactions with polar head groups [31]. These conditions allow HHP to be abundant in the lipid monolayer at the air-liquid interface, which is a characteristic of the heterogeneous reaction of POPG compared to the homogeneous reaction [29]. The observed MHP originates from the reaction of a CI or POZ with a methanol molecule in the droplet.

A significant abundance of SOZ is observed in the FIDI-MS spectra after exposing the droplet to O₃ for 15 s. The structure of SOZ (m/z 796) is confirmed by low energy collision induced dissociation (CID), which yields the aldehyde (m/z 638) and carboxylic acid (m/z 654) fragments. The peak corresponding to SOZ continues to build up in the spectrum as the POPG lipid is depleted. We infer that the observed SOZ is not formed by direct rearrangement of POZ but rather by recombination of the CI with aldehydes (Figure 7.3b) [28, 32]. In the bulk-phase, however, faster reaction with water molecules prevents the CI from reacting with aldehyde to form SOZ [33]. A significant amount of the sodiated alcohol product (m/z 662) is observed after exposing the droplet to O₃ for 30 s. This

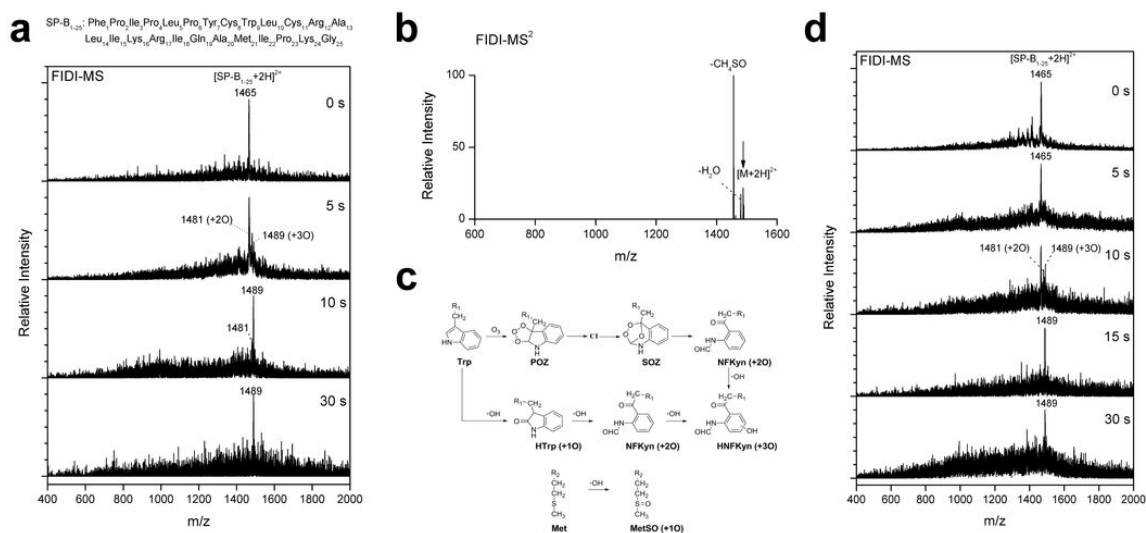


Figure 7.4: (a) Air-liquid interfacial oxidation of SP-B₁₋₂₅ by O₃ as a function of time. In the absence of ozone, the positive ion FIDI-MS spectrum of SP-B₁₋₂₅ is dominated by the doubly protonated SP-B₁₋₂₅ peak at m/z 1465. The products at m/z 1481 and m/z 1489 correspond to doubly protonated SP-B₁₋₂₅ with two oxygen atoms and with three oxygen atoms, respectively, appear after the droplet is exposed to O₃ for 5 s. The triply oxygenated product at m/z 1489 dominates the FIDI-MS spectrum after exposing the droplet to O₃ for 10 s. No further oxidation of the peptide is observed up to 30 s of exposure. (b) FIDI-MS² of doubly charged triply oxygenated SP-B₁₋₂₅ product from heterogeneous oxidation yields an exclusive fragment at m/z 1457 resulting from the elimination of hydrosulfinylmethane (CH₄SO). (c) The oxidation mechanisms of Trp by ozonolysis and hydrolysis with hydrolysis mechanism of Met in peptide. (d) Air-liquid interfacial oxidation of SP-B₁₋₂₅ by O₃ in the POG monolayer as a function of time. Doubly protonated SP-B₁₋₂₅ products with two oxygen atoms and with three oxygen atoms appear after the droplet is exposed to O₃ for 10 s. The triply oxygenated product dominates the FIDI-MS spectrum after exposing the droplet to O₃ for 15 s and no further oxidation of the peptide is observed up to 30 s of exposure.

product is due to the dissociation of SOZ followed by the association with sodium cation. This suggests that after SOZ is produced under an anhydrous environment, the newly formed hydrophilic molecule interacts with sodium cation in the liquid-phase to yield the sodiated alcohol product. These SOZ and sodiated alcohol products are characteristic of specific air-liquid interface chemistry during POPG ozonolysis.

7.4.2 Interfacial Oxidation of SP-B₁₋₂₅

The positive ion FIDI-MS spectra for the oxidation of SP-B₁₋₂₅ by O₃ are shown in Figure 7.4a. The doubly protonated SP-B₁₋₂₅ is observed as the dominant species in the FIDI-MS spectrum before O₃ application. Products resulting from the oxidation of SP-B₁₋₂₅ by O₃ appear after the droplet is exposed to O₃ for 5 s. The products at m/z 1481 and m/z 1489 correspond to doubly protonated SP-B₁₋₂₅ with two oxygen atoms and with three oxygen atoms, respectively. The FIDI-MS spectrum of the droplet with SP-B₁₋₂₅ is dominated by the triply oxygenated product at m/z

1489 after exposing the droplet to O_3 for 10 s. No further oxidation of the peptide is observed up to 30 s of exposure. The FIDI-MS spectra show that the doubly oxygenated product immediately undergoes further oxidation to form the stable product with three oxygen atoms.

The FIDI collision induced dissociation (CID) spectrum (FIDI-MS²) of the product at m/z 1489 is shown in Figure 7.4b. The CID of triply oxygenated SP-B_{1–25} from heterogeneous oxidation yields an exclusive fragment at m/z 1457 resulting from the elimination of hydrosulfinylmethane (CH_4SO), which is the characteristic CID fragment of methionine sulfoxide (MetSO) [34]. This indicates that the oxidation of the methionine residue (Met₂₁) in SP-B_{1–25} results from the heterogeneous ozonolysis. The other two oxygen atoms are added to the tryptophan residue (Trp₉) forming N-formylkynrenine (NFKyn) (see Appendix H).

In order to investigate the difference between the interfacial and bulk-phase reactions of O_3 with SP-B_{1–25}, O_3 was bubbled into a solution containing SP-B_{1–25}. Oxidation using the Fenton reaction is also performed to compare the bulk-phase ozonolysis to bulk-phase oxidation by OH radical (see Appendix H for detailed analysis). The Fenton reaction yields a series of oxidized SP-B_{1–25} products with up to 10 oxygen atoms while the bulk-phase O_3 reaction yields dominating products of 3- and 9-oxygenated SP-B_{1–25}. For the comparison to heterogeneous ozonolysis of SP-B_{1–25}, the products with three additional oxygen atoms from both reactions are analyzed. Bulk-phase O_3 application yields two triply oxygenated SP-B_{1–25} products, one with NFKyn (+ 2O) and MetSO (+ 1O), and the other with hydroxy-N-formylkynrenine (HNFKyn, + 3O). The Fenton reaction yields only the product with HNFKyn.

Ozone has limited solubility in water. For a gas-phase concentration of 20 ppm O_3 , the equilibrium concentration of O_3 dissolved in aqueous solution is calculated as 22.6 nM by Henry's law [35]. In addition, O_3 is unstable in water, and rapidly forms secondary oxidants [36]. The major secondary oxidant formed by O_3 in water is OH radical [37]. This implies that two major O_3 oxidation pathways, ozonolysis and hydroxylation, can be observed at the air-liquid interface. The triply oxygenated SP-B_{1–25} is formed concomitantly with the formation of the doubly oxygenated SP-B_{1–25} after exposing the droplet to O_3 for 5 – 10 s (Figure 7.4a). The oxidation mechanisms of Trp and Met in peptide are shown in Figure 7.4c. The NFKyn can be formed via direct ozonolysis of Trp [38] or hydrolysis of hydroxytryptophan (HTrp) [12]. However, the formation of MetSO from Met occurs primarily by secondary oxidants [39]. The NFKyn of the heterogeneous reaction results from the direct ozonolysis of Trp₉, which is located at the hydrophobic N-terminal side of SP-B_{1–25}. Met₂₁, which likely forms MetSO, is located at the hydrophilic C-terminal site. Intact Cys₈ and Cys₁₁ support this observed O_3 oxidation of SP-B_{1–25}. The rate constant for reaction of Cys with ozone is three orders of magnitude larger than that of Trp and Met [40]. However, the oxidation of Cys to yield sulfonic acid occurs primarily by reactions with secondary oxidants [41], which are not present in significant concentration in the vicinity of the hydrophobic segment of the peptide where

Cys₈ and Cys₁₁ are located. The formation of HNFKyn requires at least one secondary oxidation step (Figure 7.4c). After NFKyn is formed by either direct ozonolysis or reaction with secondary oxidants, the Met and NFKyn undergo competitive oxidation to yield MetSO ($k = 1.4 \times 10^{-11} \text{ cm}^3 \text{ molecule}^{-1} \text{ s}^{-1}$) and HNFKyn ($k = 1.3 \times 10^{-11} \text{ cm}^3 \text{ molecule}^{-1} \text{ s}^{-1}$) by ROS in the bulk-phase [42]. The heterogeneous ozonolysis of Trp₉ induces a change in peptide orientation at the interface. This results in Cys₈ and Cys₁₁ being exposed to ROS for oxidation in the bulk phase, which yields total 9-oxygenated SP-B₁₋₂₅.

7.4.3 Oxidation of SP-B₁₋₂₅ in POG Monolayer by O₃

The interfacial reaction of SP-B₁₋₂₅ with ozone was also examined in a monolayer of the non-ionizable lipid POG. Almost identical FIDI-MS spectra are observed compared to the spectra obtained for ozonolysis of SP-B₁₋₂₅ without POG except for an ~ 5 s time delay for initiation of the reaction (Figure 7.4d). The FIDI-MS spectrum of the SP-B₁₋₂₅/POG droplet is dominated by the triply oxygenated product after 15 s of exposure. No further oxidation of the peptide is observed up to 30 s exposure.

The observed time delay of the reaction provides a critical clue regarding the location of SP-B₁₋₂₅ in the monolayer. From the FIDI-MS spectra, it takes $\sim 10 - 20$ s for POPG at the air-liquid interface to be consumed by O₃ (Figure 7.3a). Both POG and POPG possess a palmitic acid chain and an oleic acid chain, the latter of which reacts with O₃. Under the assumption that the reactivity of POG is similar to that of POPG, the initiation of the SP-B₁₋₂₅ ozonolysis is expected after the droplet is exposed to O₃ for 10 – 20 s, if the peptide is completely shielded by lipid acyl chains. However, the observed short time delay of the initiation of SP-B₁₋₂₅ ozonolysis suggests that the peptide competes directly with POG for reaction with O₃. This is consistent with a picture in which the peptide is collocated at the air-liquid interface with POG at the surface of the droplet.

7.4.4 Interactions of SP-B₁₋₂₅ in a Lipid Monolayer

We carried out MD simulations for the POPG monolayer and POG monolayer in a water box for 2.0 ns with four different surface densities (55, 60, 65, and 70 Å²/lipid), which are reported as a proper density range for pulmonary surfactant function from previous theoretical studies [43, 44, 45]. Figure 7.5 shows the atomic density profiles of oxygen atoms of water molecules, saturated carbon atoms, and unsaturated carbon atoms of lipid acyl chains along $\pm\Delta z$, which is z -direction relative to the averaged phosphorous atom of POPG or hydroxyl hydrogen of POG. The POPG monolayer and POG monolayer exhibit almost identical atomic density profiles. Slightly stronger interaction between POPG and water is observed from their larger area of overlapping density (~ 1.6 times). This is due to the strong ion-dipole interactions between POPG phosphate group

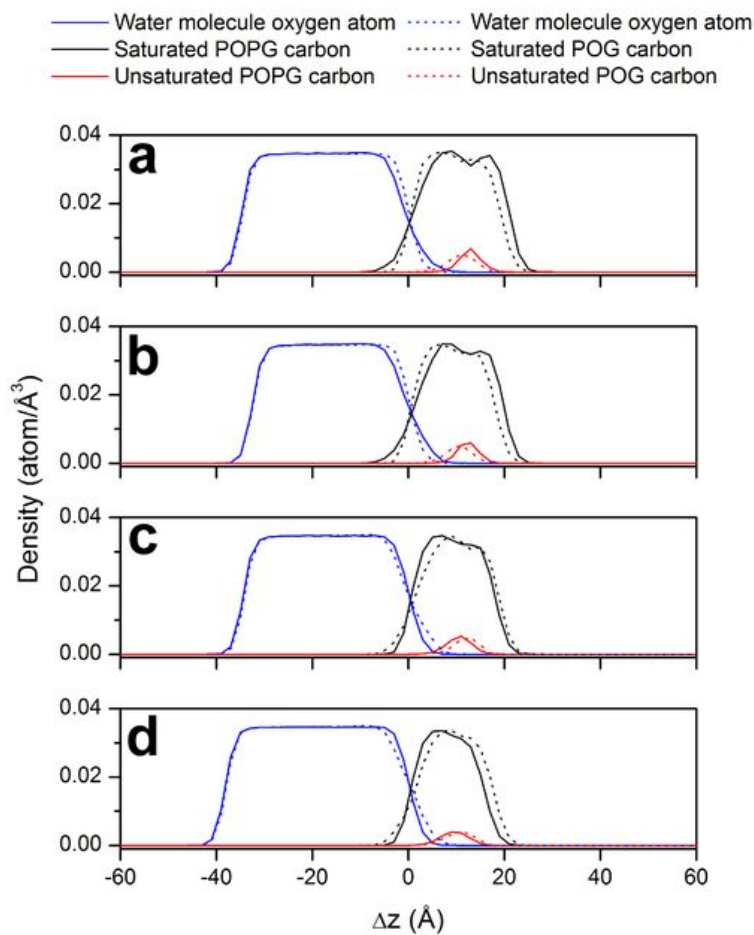


Figure 7.5: Atomic density profiles of POPG monolayer systems (solid lines) and POG monolayer systems (dotted lines) as a function of Δz , where the air/liquid interface is 0, and proceeding left to right from the water to the lipid layer. The lipid surface densities are (a) 55 Å²/lipid, (b) 60 Å²/lipid, (c) 65 Å²/lipid, and (d) 70 Å²/lipid. Blue lines denote the density profiles of oxygen atoms of water molecules, black lines denote that of saturated carbons of lipid acyl chains, and red lines denote that of unsaturated carbons of lipid acyl chains.

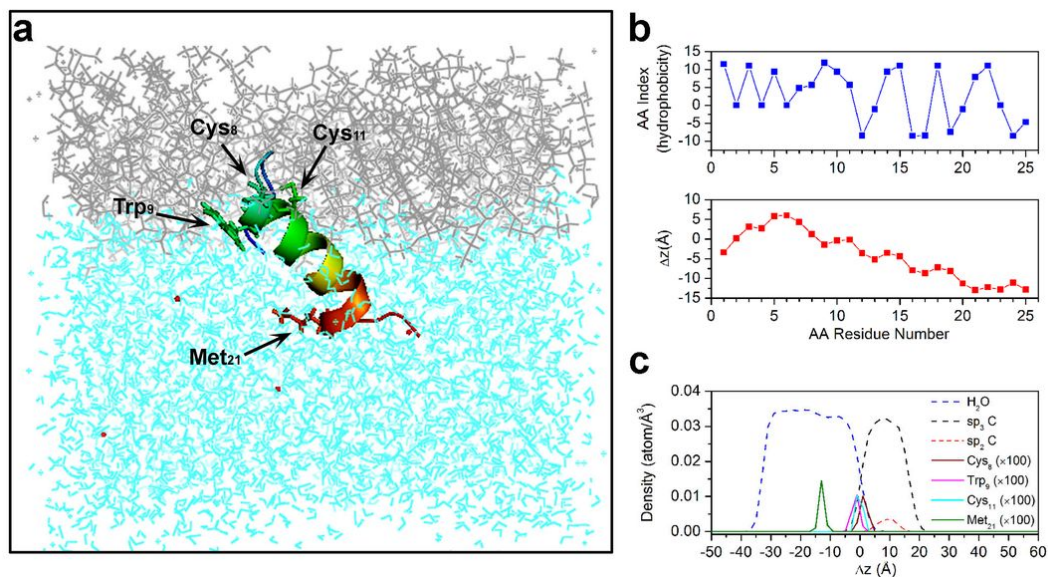


Figure 7.6: (a) Final snapshot after 2.0 ns of MD simulation of SP-B₁₋₂₅ in a POG monolayer at 60 Å²/lipid. The peptide is shown in rainbow color (C-terminal: red, N-terminal: blue). Lipids, water molecules, and chloride are shown in purple, cyan, and red, respectively. (b) AA hydrophobicities [46] (top) and Δz of C $_{\alpha}$ of each residue averaged during the last 0.5 ns of a 2.0 ns duration MD simulation (bottom) are plotted as a function of amino acid residue number. The air/water interface is located near $\Delta z = 0$. (c) Atomic density profiles of SP-B₁₋₂₅ in POG monolayer at 60 Å²/lipid as a function of Δz during the last 0.5 ns of the 2.0 ns MD simulation. Blue dash line denotes the density profiles of oxygen atoms of water molecules. Black and red dash lines denote those of separately summed saturated and unsaturated carbons of lipid acyl chains, respectively. Wine, magenta, cyan, and olive solid lines denote the 100 times scaled density profiles of the C $_{\alpha}$ carbon of Cys₈, Trp₉, Cys₁₁, Met₂₁ residues, respectively.

and water molecules, which is absent from the POG monolayer. The water density at the double bond of POPG (5 – 20 Å) is ~ 0.0005 atom/Å³, which is ~ 70 times less dense than in the bulk-phase (~ 0.035 atom/Å³). The low water concentrations around the double bond explains the experimental observation of the intermediates and metastable products from heterogeneous ozonolysis, including SOZ, HHP, and MHP (Figure 7.3a), which are difficult to observe in water-rich environments [28, 29, 33].

We performed 2.0 ns duration MD simulations of the POG/SP-B₁₋₂₅/water monolayer with 60 Å²/lipid surface density as a representative case. The final snapshot in Figure 7.6a shows that the SP-B₁₋₂₅ is located at the air-liquid interface. The hydrophobicity index of each amino acid (AA) residue in the peptide is shown in Figure 7.6b (top) [46]. Relatively strong hydrophobicity is found for the N-terminal side of the peptide with Leu, Ile, and Pro residues. In contrast, hydrophilicity is expected from C-terminal side due to Arg, Lys, and Gln residues. The MD simulated Δz of C $_{\alpha}$ of each residue exhibits a good correlation with the hydrophobicity index. The hydrophobic N-terminal side of the peptide is located above the air-liquid interface, while the hydrophilic C-terminal side is

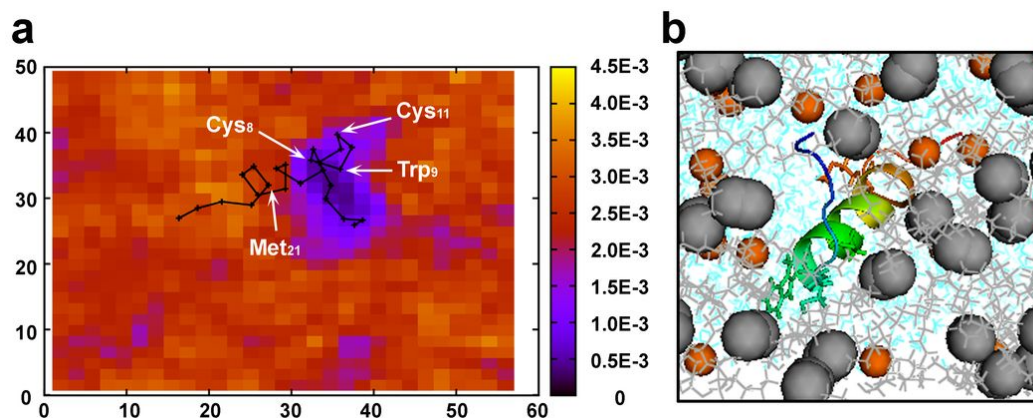


Figure 7.7: (a) The xy -projected density profiles of saturated carbon atoms of lipid acyl chains from MD simulations is shown with colors and the averaged positions of C_{α} carbons of SP-B₁₋₂₅ in the POG monolayer is shown with a black line (each residue is shown with cross). (b) Top view of final snapshot after 2.0 ns of MD simulation of SP-B₁₋₂₅ in a POG monolayer at $60 \text{ \AA}^2/\text{lipid}$. The peptide is shown in rainbow color (C-terminal: red, N-terminal: blue). Lipids and water molecules are shown in gray and cyan, respectively. Black spheres denote unsaturated carbon atoms of lipid acyl chains, and orange spheres denote hydroxyl oxygen atoms.

located under the interface (Figure 7.6b bottom). Figure 7.6c shows the atomic density profiles of oxygen atoms of water molecules as well as saturated and unsaturated carbon atoms of POG acyl chains along Δz . The 100 times scaled atomic density profiles of the C_{α} carbon of Cys₈, Trp₉, Cys₁₁, and Met₂₁ residues are also shown in Figure 7.6c. The density profiles show a good agreement with the hydrophobicity index. In practice, a low water density is found around Trp₉, which leads to the formation of NFKyn via direct ozonolysis. The water density around Met₂₁ is observed to be sufficiently high to expect ROS formation and subsequent reaction to yield MetSO. In contrast, the low water density near Cys₈ and Cys₁₁ inhibits their oxidation by ROS.

Based on the competitive reactivity of POG and SP-B₁₋₂₅ with O_3 we suggest above that they are collocated at the interface. The MD simulations of SP-B₁₋₂₅ in a lipid monolayer support our interpretation. Trp₉ and Met₂₁ of SP-B₁₋₂₅ lie below (in the z -direction) the location of the lipid double bonds (Figure 7.6c). Figure 7.7a shows the xy -projected density profiles of saturated carbon atoms of lipid acyl chains with the averaged positions of C_{α} of AA residues of SP-B₁₋₂₅. It is noteworthy that lipid acyl chains do not shelter the peptide at the air-liquid interface. The top view of the MD simulation final snapshot in Figure 7.7b illustrates that SP-B₁₋₂₅ is not shielded by unsaturated carbons (black spheres) of lipids. The strong amphiphilic characteristic and the large surface area of SP-B₁₋₂₅ cause the peptide to position itself at the air-liquid interface where it displaces lipids. As a result, SP-B₁₋₂₅ forms an island in a lipid monolayer that causes the hydrophobic portion of the peptide to be exposed to O_3 despite its location below the position of lipid double bonds. We also simulated SP-B₁₋₂₅ in the POPG monolayer. The peptide penetrates

deeper into the POPG monolayer due to the strong electrostatic interaction between the cationic AA residues (Arg₁₂, Arg₁₇, and Lys₁₆) and the anionic phosphate group of POPG (Figures 7.8a and 7.8b), which agrees with previous simulations in anionic lipid monolayers [43, 47]. SP-B₁₋₂₅ forms an island in the POPG monolayer and the anhydrous environments in the lipid monolayer may lead SP-B₁₋₂₅ to be more susceptible to direct ozonolysis than to modification by ROS (Figures 7.8c and 7.9).

7.5 Conclusions

Summarizing, to understand the unique chemistry at a model lung surfactant/air interface under O₃ exposure, we utilized the FIDI-MS technique to analyze chemical reactions at this interface. In the FIDI-MS spectra, oxidized products distinct from those formed in the bulk-phase were observed from SP-B₁₋₂₅ alone and imbedded in the POG monolayer. We also carried out MD simulations that provide additional insights into the interactions between lipids, SP-B₁₋₂₅, and water molecules in the interfacial region. In these simulations the location of SP-B₁₋₂₅ relative to the lipids provides a rationalization for the experimental observation that the peptides compete with the lipids for reaction with O₃.

The oxidation of PS causes surface dysfunction in adsorption, respreading, and reduction of surface tension [14, 48]. Once the O₃ traverses the air-liquid interface, it decays rapidly concomitant with the formation of ROS in regions with high water densities [36]. However, due to the high reactivity with PS at the interface, it has been thought that little or none of the O₃ can penetrate the PS monolayer to attack the epithelium cells below [49]. Instead of direct attack by O₃ and its ROS derivatives, secondary oxidized products of PS, such as HHP, have been expected to yield cellular damage [49]. We have found that more than 60 % of the heterogeneous oxidation products of POPG by O₃ are peroxides. These products, which are more water soluble than others, eventually dissolve into the water droplet. Then, rapid decomposition of products yields reactive oxygen species (ROS) [29] which causes cellular damage below the monolayer.

Possible protection of SP-B from homogeneous oxidation by PS lipids has been suggested in an earlier study [12]. However, we have shown that SP-B₁₋₂₅ is oxidized directly by heterogeneous reaction with O₃ since it is located at the air-liquid interface with significant exposure to O₃. The homogeneous oxidation of SP-B by ROS is known to reduce its surface activity and function [12, 14]. We have observed fast formation of NFKyn from the direct ozonolysis of Trp₉ at the hydrophobic N-terminal side of SP-B₁₋₂₅. The oxidized residue reduces the hydrophobicity of the N-terminal side of the peptide. This induces a change in peptide orientation in the monolayer that results in NFKyn, Cys₈, and Cys₁₁ being exposed to ROS for further oxidation. As a result, further oxidation of SP-B₁₋₂₅ by a heterogeneous reaction with O₃ produces effects similar to those seen in homogeneous

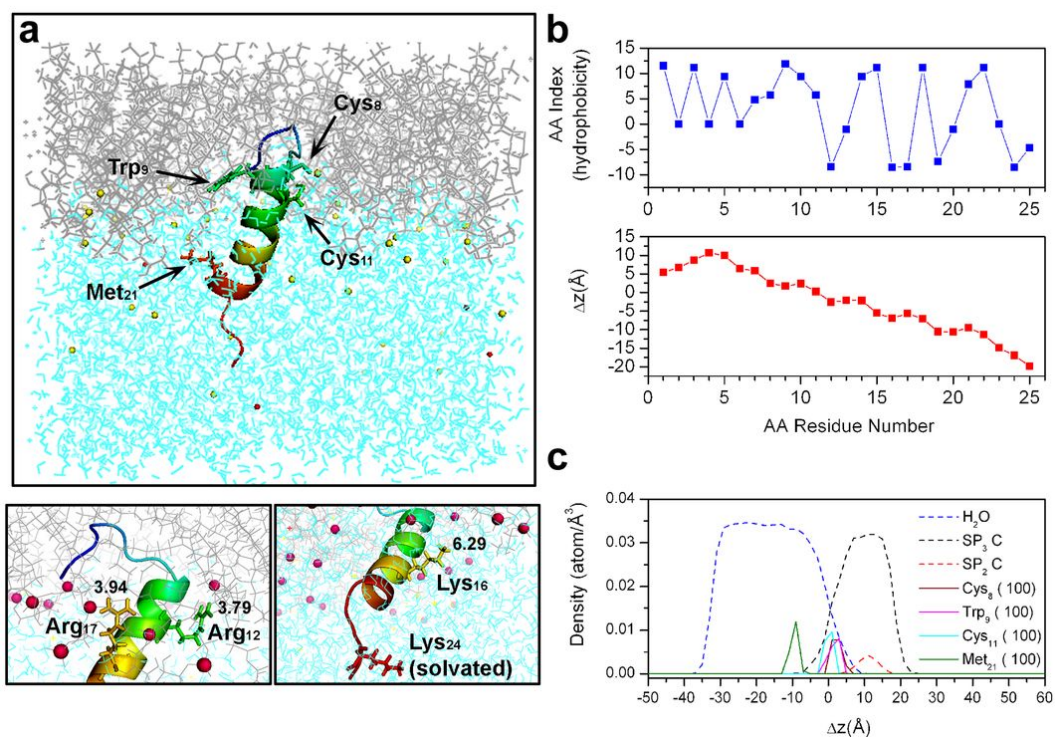


Figure 7.8: (a) Final snapshot after 2.0 ns MD simulation of SP-B₁₋₂₅ in POPG monolayer at 60 Å²/lipid is shown at top panel. The peptide is shown in rainbow color (C-terminal: red, N-terminal: blue), lipids in gray, water molecules in cyan, and chloride ions in red. Lower left and right show that Arg residues and Lys residues (displayed with sticks) are interacting with phosphate groups of lipids, respectively. (Phosphorous atoms are in magenta.) (b) AA index for hydrophobicity scale [46] (top) and Δz of C_α of each residue averaged during the last 0.5 ns trajectory of 2.0 ns duration MD simulations (bottom) are plotted as a function of amino acid residue number. The air/water interface is located near Δz = 0. (c) Atomic density profiles of SP-B₁₋₂₅ in POG monolayer at 60 Å²/lipid as a function of Δz during the last 0.5 ns of the 2.0 ns MD simulation. Blue dash line denotes the density profiles of oxygen atoms of water molecules. Black and red dash lines denote those of saturated and unsaturated carbons of lipid acyl chains, respectively. Wine, magenta, cyan, and olive solid lines denote the 100 times scaled density profiles of the C_α carbon of Cys₈, Trp₉, Cys₁₁, and Met₂₁ residues, respectively.

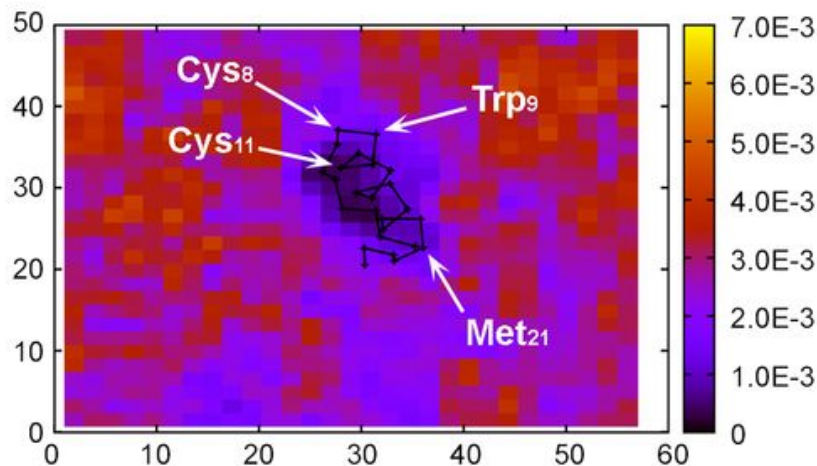


Figure 7.9: The xy -projected density profiles of saturated carbon atoms of lipid acyl chains is shown with colors and the averaged positions of C_{α} carbons of SP-B₁₋₂₅ in the POPG monolayer is shown with a black line (each residue is shown with cross).

oxidation.

Our findings present a detailed explanation for the mechanisms of the possible damage to the pulmonary system by ROS or direct ozone exposure. Further studies with a more elaborate model system comprising SP-B, SP-C, and various lipids could further clarify the effect of other environmental exposures, such as smoking and airborne particles, on the lung surfactant system.

7.6 Acknowledgments

The research described in this paper was carried out at the Beckman Institute and the Noyes Laboratory of Chemical Physics at the California Institute of Technology, the Computational NanoBioTechnology Laboratory at Georgia Institute of Technology and Jet Propulsion Laboratory under a contract with the National Aeronautics and Space Administration and funded through the Director's Research and Development Fund. We appreciate the support provided by the Beckman Institute Mass Spectrometry Resource Center. Partial support was also provided by the National Science Foundation (NSF) under grant No. CHE-0416381 (JLB, PI) and the National Cancer Institute under grant No. 5U54 CA119347 (JRH, PI).

Bibliography

- [1] Anseth, J.; Goffin, A.; Fuller, G.; Ghio, A.; Kao, P. *Am. J. Respir. Cell Mol. Biol.* **2005**, *33*, 161-168.
- [2] Halliwell, B.; Gutteridge, J. *Biochem. J.* **1984**, *219*, 1-14.
- [3] Stansfield, A.; Jump, Z.; Sodlosky, S.; Rappaport, S.; Edelman, N.; Haldorsen, J.; Javed, T.; Martin, C.; Margulies, E. *ed. Maple, D*; American Lung Association National Headquarters: New York, 2008.
- [4] Vangolde, L.; Batenburg, J.; Robertson, B. *Physiol. Rev.* **1988**, *68*, 374-455.
- [5] Schram, V.; Hall, S. *Biophys. J.* **2004**, *86*, 3734-3743.
- [6] Hawco, M.; Davis, P.; Keough, K. *J. Appl. Physiol.* **1981**, *51*, 509-515.
- [7] Perez-Gil J.; Keough K. *Biochim. Biophys. Acta-Mol. Basis Dis.* **1998**, *1408*, 203-217.
- [8] Clark J.; Wert S.; Bachurski C.; Stahlman M.; Stripp B.; Weaver T.; Whitsett J. *Proc. Natl. Acad. Sci. U. S. A.* **1995**, *92*, 7794-7798.
- [9] Perez-Gil, J. *Biophys. J.* **2008**, *94*, 1542-1543.
- [10] Pryor, W.; Das, B.; Church, D. *Chem. Res. Toxicol.* **1991**, *4*, 341-348.
- [11] Uppu, R. M.; Cueto, R.; Squadrito, G. L.; Pryor, W. A. *Arch. Biochem. Biophys.* **1995**, *319*, 257-266.
- [12] Manzanares, D.; Rodriguez-Capote, K.; Liu, S. Y.; Haines, T.; Ramos, Y.; Zhao, L.; Doherty-Kirby, A.; Lajoie, G.; Possmayer, F. *Biochemistry* **2007**, *46*, 5604-5615.
- [13] Andersson, S.; Kheiter, A.; Merritt, T. A. *Lung* **1999**, *177*, 179-189.
- [14] Rodriguez-Capote, K.; Manzanares, D.; Haines, T.; Possmayer, F. *Biophys. J.* **2006**, *90*, 2808-2821.
- [15] Grimm, R. L.; Hodyss, R.; Beauchamp, J. L. *Anal. Chem.* **2006**, *78*, 3800-3806.

- [16] Voss, L. F.; Hadad, C. M.; Allen, H. C. *J. Phys. Chem. B* **2006**, 110, 19487-19490.
- [17] Mundy, C. J.; Kuo, I. F. W. *Chem. Rev.* **2006**, 106, 1282-1304.
- [18] Enami, S.; Hoffmann, M. R.; Colussi, A. J. *Proc. Natl. Acad. Sci. U. S. A.* **2008**, 105, 7365-7369.
- [19] Enami, S.; Hoffmann, M. R.; Colussi, A. J. *J. Phys. Chem. B* **2008**, 112, 4153-4156.
- [20] Grimm, R. L.; Beauchamp, J. L. *J. Phys. Chem. B* **2003**, 107, 14161-14163.
- [21] Grimm, R. L.; Beauchamp, J. L. *J. Phys. Chem. B* **2005**, 109, 8244-8250.
- [22] Takamoto, D. Y.; Lipp, M. M.; von Nahmen, A.; Lee, K. Y. C.; Waring, A. J.; Zasadzinski, J. A. *Biophys. J.* **2001**, 81, 153-169.
- [23] Bruni, R.; Tausch, H. W.; Waring, A. J. *Proc. Natl. Acad. Sci. U. S. A.* **1991**, 88, 7451-7455.
- [24] Longo, M. L.; Bisagno, A. M.; Zasadzinski, J. A. N.; Bruni, R.; Waring, A. J. *Science* **1993**, 261, 453-456.
- [25] MacKerell, A.D.; Bashford, D.; Bellott, M.; Dunbrack, R. L.; Evanseck, J. D.; Field, M. J.; Fischer, S.; Gao, J.; Guo, H.; Ha, S.; Joseph-McCarthy, D.; Kuchnir, L.; Kuczera, K.; Lau, F. T. K.; Mattos, C.; Michnick, S.; Ngo, T.; Nguyen, D. T.; Prodhom, B.; Reiher, W. E.; Roux, B.; Schlenkrich, M.; Smith, J. C.; Stote, R.; Straub, J.; Watanabe, M.; Wiorkiewicz-Kuczera, J.; Yin, D.; Karplus, M. *J. Phys. Chem. B* **1998**, 102, 3586-3616.
- [26] Plimpton, S. *J. Comput. Phys.* **1995**, 117, 1-19.
- [27] Hockney, R. W.; Eastwood, J. W. *Computer simulation using particles*; McGraw-Hill: New York, 1981.
- [28] Karagulian, F.; Lea, A. S.; Dilbeck, C. W.; Finlayson-Pitts, B. J. *Phys. Chem. Chem. Phys.* **2008**, 10, 528-541.
- [29] Santrock, J.; Gorski, R. A.; Ogara, J. F. *Chem. Res. Toxicol.* **1992**, 5, 134-141.
- [30] Rivera, J. L.; Starr, F. W.; Paricaud, P.; Cummings, P. T. *J. Chem. Phys.* **2006**, 125, 8.
- [31] Ghosh, A.; Smits, M.; Bredenbeck, J.; Bonn, M. *J. Am. Chem. Soc.* **2007**, 129, 9608.
- [32] Lai, C. C.; Yang, S. H.; Finlayson-Pitts, B. J. *Langmuir* **1994**, 10, 4637-4644.
- [33] Pryor, W. A. *Am. J. Clin. Nutr.* **1991**, 53, 702-722.
- [34] Clauser, K. R.; Hall, S. C.; Smith, D. M.; Webb, J. W.; Andrews, L. E.; Tran, H. M.; Epstein, L. B.; Burlingame, A. L. *Proc. Natl. Acad. Sci. U. S. A.* **1995**, 92, 5072-5076.

- [35] Seinfeld, J. H.; Pandis, S. N. *Atmospheric chemistry and physics: From air pollution to climate change*; John Wiley & Sons: New York, 1998.
- [36] von Gunten, U. *Water Res.* **2003**, *37*, 1443-1467.
- [37] Pryor, W. A. *Free Radic. Biol. Med.* **1994**, *17*, 451-465.
- [38] Pryor, W. A.; Uppu, R. M. *J. Biol. Chem.* **1993**, *268*, 3120-3126.
- [39] Schoneich, C. *BBA-Proteins Proteomics* **2005**, *1703*, 111-119.
- [40] Pryor, W. A.; Giamalva, D. H.; Church, D. F. *J. Am. Chem. Soc.* **1984**, *106*, 7094-7100.
- [41] Berlett, B. S.; Stadtman, E. R. *J. Biol. Chem.* **1997**, *272*, 20313-20316.
- [42] Buxton, G. V.; Greenstock, C. L.; Helman, W. P.; Ross, A. B. *J. Phys. Chem. Ref. Data* **1988**, *17*, 513-886.
- [43] Kaznessis, Y. N.; Kim, S.; Larson, R. G. *J. Mol. Biol.* **2002**, *322*, 569-582.
- [44] Baoukina, S.; Monticelli, L.; Risselada, H. J.; Marrink, S. J.; Tieleman, D. P. *Proc. Natl. Acad. Sci. U. S. A.* **2008**, *105*, 10803-10808.
- [45] Kaznessis, Y. N.; Kim, S. T.; Larson, R. G. *Biophys. J.* **2002**, *82*, 1731-1742.
- [46] Kawashima, S.; Ogata, H.; Kanehisa, M. *Nucleic Acids Research* **1999**, *27*, 368-369.
- [47] Freites, J. A.; Choi, Y.; Tobias, D. J. *Biophys. J.* **2003**, *84*, 2169-2180.
- [48] Gilliard, N.; Heldt, G. P.; Lored, J.; Gasser, H.; Redl, H.; Merritt, T. A.; Spragg, R. G. *J. Clin. Invest.* **1994**, *93*, 2608-2615.
- [49] Pryor, W. A. *Free Radic. Biol. Med.* **1992**, *12*, 83-88.

Appendix A

Discussions on Coarse-Graining of Time- and Length-Scale in Monte Carlo Simulations for AN-OPE SAM

In order to connect from the atomistic quantum level to macroscopic level, it is necessary to coarse grain the system. We discuss below some of the consequences of the coarse graining on time- and length-scale.

A.1 Time-Scale

From the NN model, the energies required to initiate the P-to-T transition under $1.2 \text{ V}/\text{\AA}$ and T-to-P transition without external field are $\Delta E^\ddagger = 11.58 \text{ kcal/mol}$ and $\Delta E^\ddagger = 12.52 \text{ kcal/mol}$, respectively. Assuming $\Delta S^\ddagger = k_B \ln(2500)$, from Eyring equation, $k = k_B T/h \exp(\Delta S^\ddagger/k_B) \exp(-\Delta E^\ddagger/k_B T)$, we obtain $\tau_0 = 1/k = 1.9 \times 10^{-8} \text{ s}$ and $\tau_0 = 9.3 \times 10^{-8} \text{ s}$ for P-to-T case and T-to-P case, respectively. By comparing these values with MC results of $\tau_0 = 274, 193 \text{ MCS}$ and $\tau_0 = 357, 135 \text{ MCS}$, we can estimate 1 MCS as an order of $\sim 10^{-13} \text{ s}$. Thus, in actual unit, the sweep rates of $1 \times 10^{-8} \text{ V/MCS}$, $4 \times 10^{-8} \text{ V/MCS}$, and $2 \times 10^{-7} \text{ V/MCS}$ are around $1 \times 10^5 \text{ V/s}$, $4 \times 10^5 \text{ V/s}$, and $2 \times 10^6 \text{ V/s}$, which are $\sim 10^6$ times faster than the experimental conditions.

A.2 Length-Scale

We found that in our simulations, the total time taken for the complete P-to-T transition under the constant external field of F , $t_{\text{P-to-T}}(F)$ is highly overestimated when F is near F_c due to the periodic boundary condition. It is a well known fact that the finite-size effect in simulations becomes serious near the critical point of phase transition [1]. This artifact makes the transition occur at once after

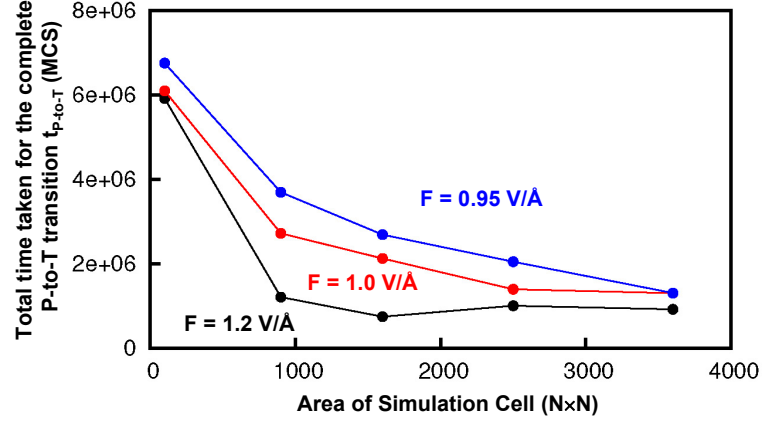


Figure A.1: Total time taken for the complete P-to-T transition, $t_{\text{P-to-T}}$ by varying the area of the periodic simulation cell as $10 \times 10 = 100$, $30 \times 30 = 900$, $40 \times 40 = 1600$, $50 \times 50 = 2500$, and $60 \times 60 = 3600$. Black line denotes the change of $t_{\text{P-to-T}}$ under the external field of $F = 1.2 \text{ V/\AA}$, red line denotes the change of $t_{\text{P-to-T}}$ scaled by 10 under the external field of $F = 1.0 \text{ V/\AA}$, and blue line denotes the change of $t_{\text{P-to-T}}$ scaled by 15 under the external field of $F = 0.95 \text{ V/\AA}$. The $t_{\text{P-to-T}}$ value is converged at the area of 900–1600 and 2500–3600 when $F = 1.2 \text{ V/\AA}$ and 1.0 V/\AA , respectively. When $F = 0.95 \text{ V/\AA}$, the $t_{\text{P-to-T}}$ value is not converged until the area of 3600. This infers that we need much larger simulation cell to get the right converged value of $t_{\text{P-to-T}}$ as the F approaches to the critical field, $F_c = 0.56 \text{ V/\AA}$. Otherwise, we will get the overestimated value of $t_{\text{P-to-T}}$ near F_c .

the bias voltage is increased sufficiently, and finally yields a narrower range of NDR (Figure A.1).

Appendix B

Effect of Molecular Fluctuations on the Electrical Conductivity of AN-OPE SAM

Electrical conductivity through the AN-OPE is estimated using the fitting equation of Figure 2.8 based on the twisting angles, χ_1 and χ_2 , from MD simulations with (10×10) unit cell. We mimicked two sets of voltage sweep cycle by following MD procedures:

- (a) QM optimized P structure is employed for the initial structure, then, annealed in the absence of external field. The conformations are almost co-planar as predicted from QM calculation with a well-developed HB network. Estimated conductivity is large with the averaged value of 0.035.
- (b) External field of 1.2 V/\AA is turned on to the final structure of (a). The SAM structure is partially disordered and χ_1 has largest probability at 90° . Estimated conductivity 3.21 times decreases to 0.011.
- (c) QM optimized T structure is employed for the initial structure, then, annealed under the external field of 1.2 V/\AA . Structural fluctuation allows AN-OPEs to have $\sim 90^\circ$ twisted conformations, resulting the loss of HB network. SAM is well-ordered. Estimated conductivity remains same to (b) with the value of 0.011.
- (d) External field is turned down from the final structure of (a). SAM forms a pretty disordered structure and χ_1 has no strongly preferring angle. Estimated conductivity 1.23 times increases to 0.013.
- (e) The final structure from step (d) is annealed in the absence of external field. SAM still has disordered structure, however, probability at $\chi_1 = 90^\circ$ slightly decreases. Estimated conductivity is slightly increased to 0.014.

- (f) External field of 1.2 V/\AA is re-turned on to the final structure of (e). Structure and twisting angle is similar to (b), however, it is a bit more disordered. Thus, estimated conductivity is a bit smaller than (b) with the value of 0.010.
- (g) The final structure from step (d) is annealed under the external field of 1.2 V/\AA , and the SAM has still similar structure to (f). Estimated conductivity remains same to (f) with the value of 0.010.
- (h) External field is re-turned down from the final structure of (g). SAM forms a more disordered structure to (d). Thus, estimated conductivity is smaller than (d) with the value of 0.012.
- (i) The final structure from step (h) is annealed in the absence of external field. SAM still has a disordered structure, however, probability at $\chi_1 = 90^\circ$ slightly decreases. Estimated conductivity is 1.05 times increased to 0.013.

The conductivities during the second cycle (f,g,h,i) shows $\sim 6 \%$ smaller values compared to the conductivities during the first cycle (b,c,d,e). These results are shown at Figure B.1.

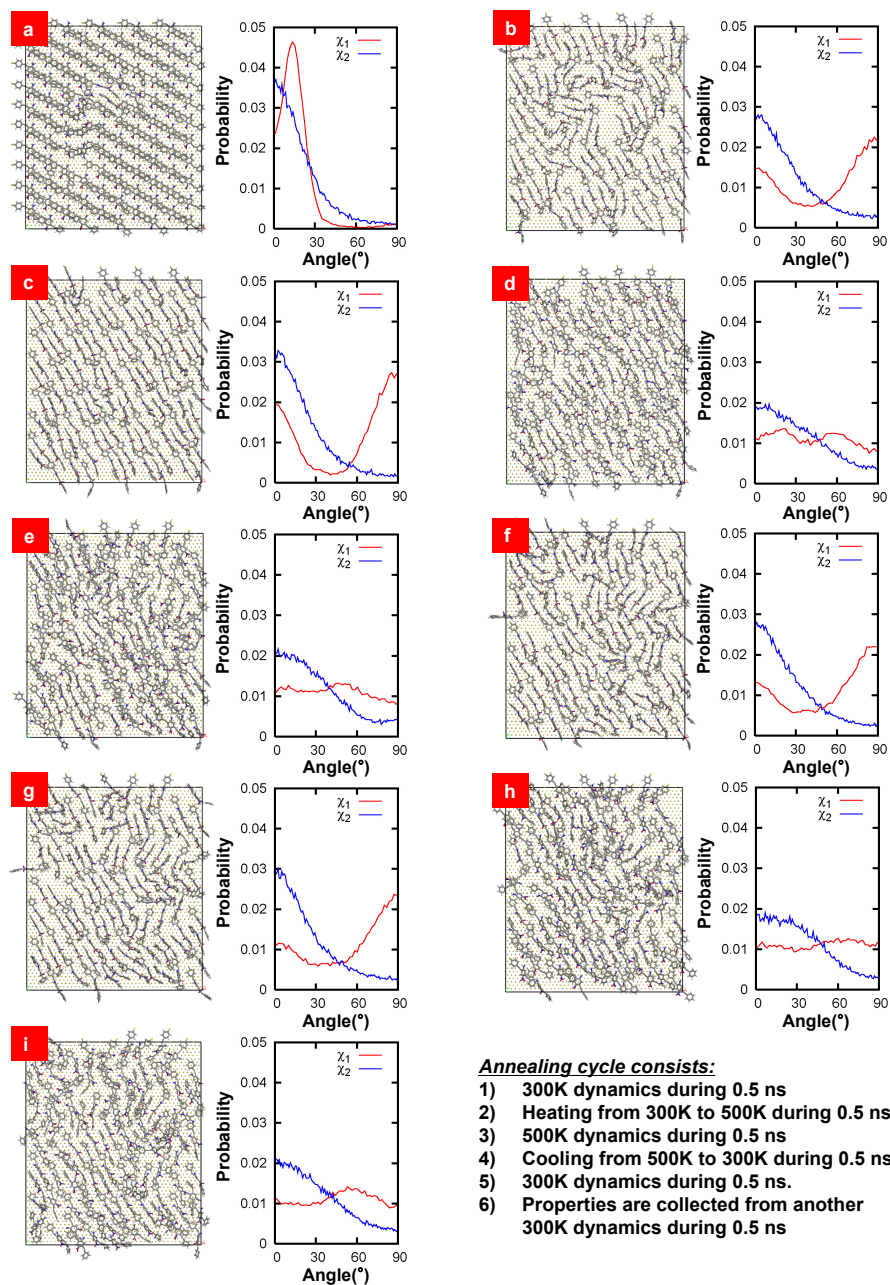
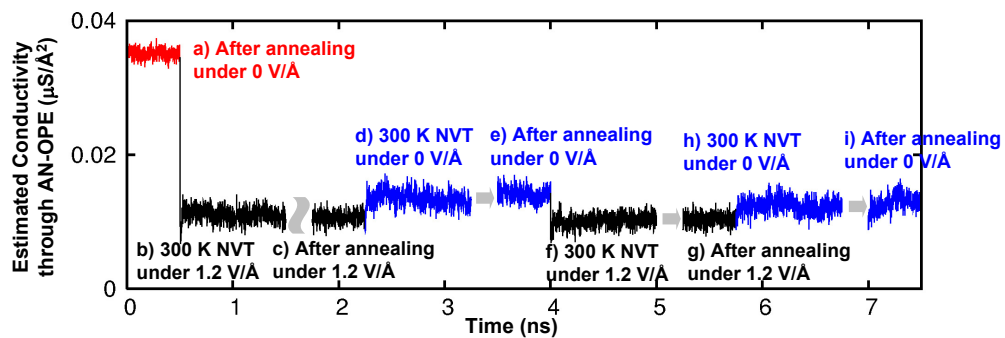


Figure B.1: (top panel) Electrical conductivity through the AN-OPE is estimated based on the twisting angles from MD simulations with (10×10) unit cell. (bottom panels) The final snapshot after each step is shown with the populations of χ_1 and χ_2 , which are averaged during the last 0.5 ns dynamics.

Appendix C

NDR in Other OPE-derivative Systems

We investigated that how our mechanism predicts the possibility of NDR in other systems containing other OPE derivatives.

C.1 Bare OPE

For bare OPE (B-OPE) with no functional groups our mechanism would suggest that there is no NDR effect, since the lack of functional groups leads to only a small molecular dipole moment to interact with the external field and there is no mechanism for the increased applied field to convert from the high conductance P phase to the low conductance T phase. Reference [2] shows the experimental data on B-OPE, which shows no NDR effect.

C.2 Nitro OPE

We calculated that the SAM of 5-nitro monosubstituted OPE system (N-OPE) on Au (111) surface. We figured out that N-OPE also can have two conformations of P and T on the SAM by forming weak HB networks along $[11\bar{2}0]$ direction and $[10\bar{1}0]$ direction, respectively. The lack of amino group makes NO_2 form a weak HB with the positive aromatic H atoms of the adjacent molecules (Figure C.1).

The twist angles are $\chi = 4^\circ$ and $\chi = 163^\circ$ and the heights of the terminal ring are 8.73 Å and 7.63 Å for P and T, respectively. These are almost identical to the values in AN-OPE case. Therefore, we expect the conductance ratio for N-OPE to be very similar to AN-OPE.

From PBE DFT calculations, P is more stable than T by 6.57 kcal/mol when no external field is applied. The dipole moment components in the $[0001]$ direction are 3.83 (2.01) debye for P and 6.61 (3.86) debye for T from the analysis of Mulliken charges, while the parenthetical values are

from quantum mechanical wave-function. Thus, the favorable state is changed from P to T as the external field is applied (Figure C.2). This suggests that the N-OPE also undergoes conformational change from P to T as the bias voltage increases. The critical field F_c is calculated as 0.49 V/\AA and 0.74 V/\AA when using dipole moments from Mulliken charge and QM wave-function, respectively. Since these are in the range of the F_c in AN-OPE system (0.56 V/\AA), the critical bias voltage where NDR occurs is similar to the critical bias voltage of AN-OPE system of $\sim 0.6 \text{ V}$. Reference [2] also shows the experimental data on N-OPE, which shows a well-defined hysteretic NDR at $\sim 0.6 \text{ V}$ as predicted from our calculations.

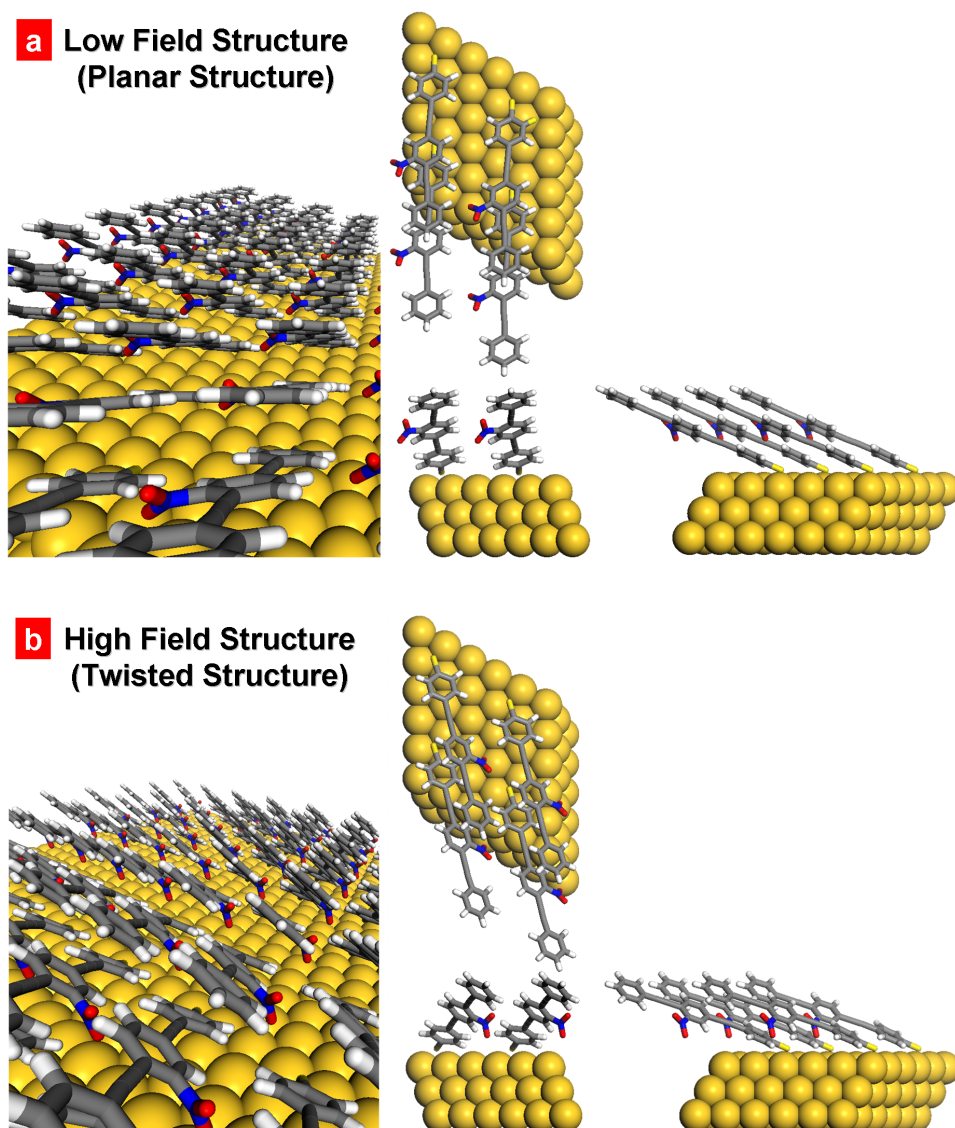


Figure C.1: (a) Optimized geometry for the low field structure (P) of N-OPE SAM. Here $[0001]$ is the surface normal and the views are along z -axis (upper middle), y -axis (lower middle), and x -axis (lower right). The left picture is a perspective along the axis of one plane of molecules. The weak hydrogen bonding network is aligned along the $[11\bar{2}0]$ direction. (b) Optimized geometry for the high field structure (T) of N-OPE SAM. Here $[0001]$ is the surface normal and the views are along z -axis (upper middle), y -axis (lower middle), and x -axis (lower right). The left picture is a perspective along the axis of one plane of molecules. The weak hydrogen bonding network is aligned along the $[10\bar{1}0]$ direction.

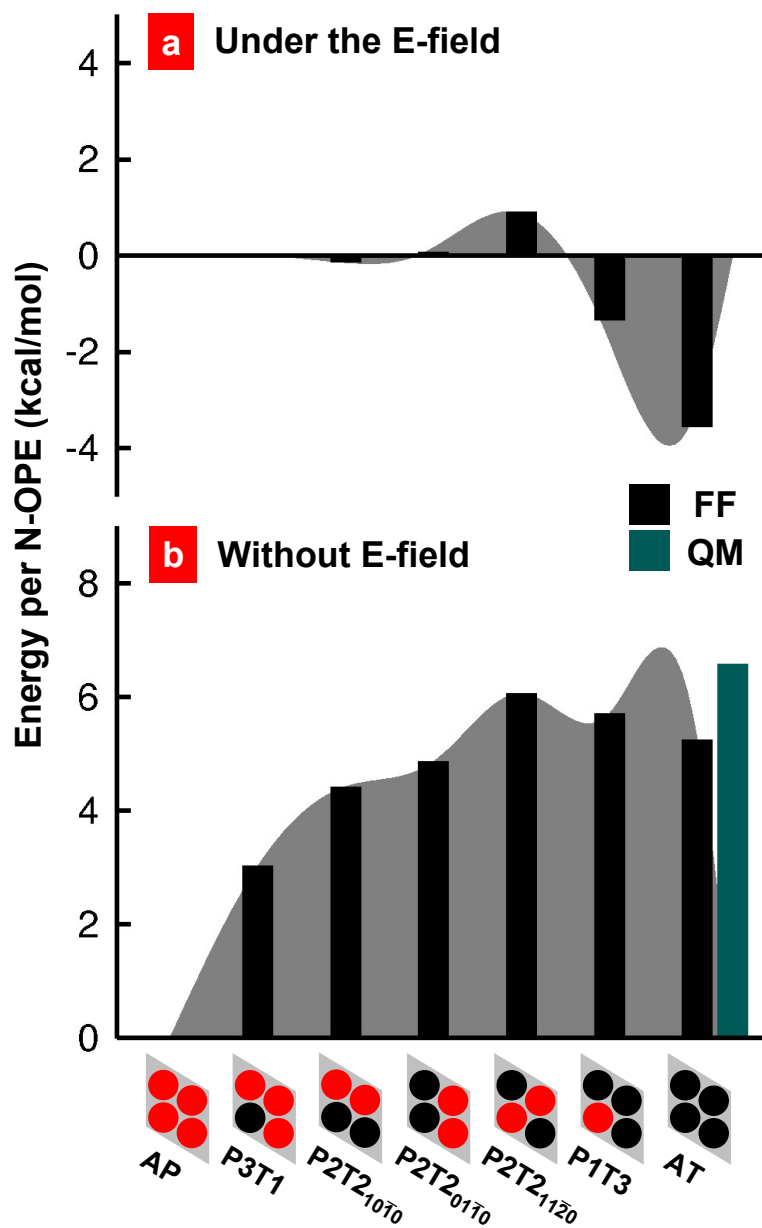


Figure C.2: (a) Energies of various conformations of N-OPE relative to the AP conformation computed with a 0.6 V/\AA external field from FF calculations (black histograms). (b) Energies of various conformations of N-OPE relative to the AP conformation computed with no external field from FF calculations (black histograms), and QM calculations (green histograms).

Appendix D

Conversion Factor between External Electric Field and Bias Voltage

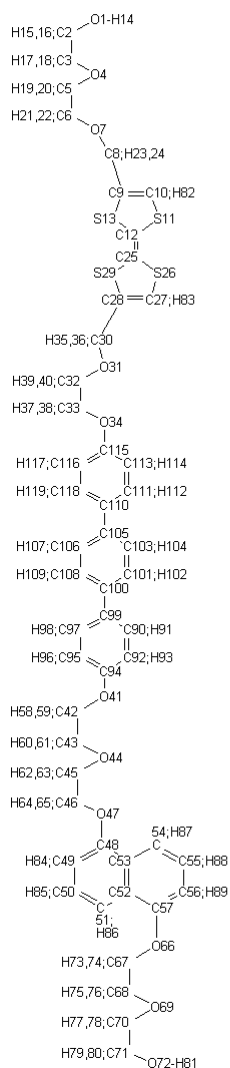
To connect the NEGF results and MC simulations, we need to convert the magnitude of external field, F , into the bias voltage, V . Since the critical bias voltage V_c is observed as ~ 0.6 V from the experiment and the critical field F_c is 0.56 V/Å in our NN model, we set the linear coefficient c as 0.93 Å⁻¹, which is defined by F/V .

Appendix E

Mulliken Charge Distributions of Bistable [2]Rotaxane Molecular Switch Depending on CBPQT⁴⁺ Ring's Position

The shuttling motion of charge accepting cyclobis-(paraquat-*p*-phenylene) (CBPQT⁴⁺) between the charge donating stations such as tetrathiafulvalene (TTF) and 1,5-dioxynaphthalene (DNP) moieties is governed by the charge transfer amount between the ring and the backbone. Since the potential energy surface that the CBPQT⁴⁺ ring suffers while traveling along the backbone has a large dependency on the local charge distribution of the rotaxane molecule, we performed DFT calculations for 9 different rings' positions by varying the oxidation states, 0, +1, and +2. Computed Mulliken charge distributions are tabulated in this section.

a) Backbone



b) CBPQT⁴⁺ ring

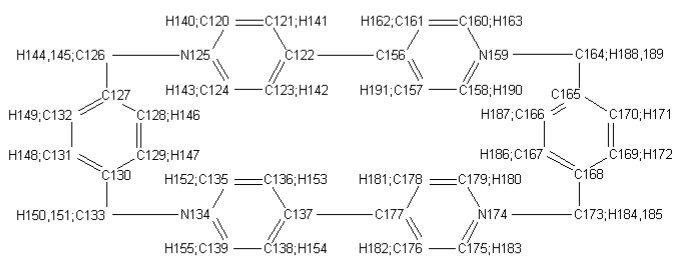


Figure E.1: Structures of a) backbone part and b) CBPQT⁴⁺ ring part with numbered atoms. The assigned numbers on the atoms are associated with the partial charge distribution data shown in Tables E.1, E.2, and E.3.

Table E.1: Partial Charge Distribution of Neutral Rotaxane when the Center of Mass of the CBPQT⁴⁺ Ring Moves from $z = 10.92 \text{ \AA}$ (TTF side) to $z = 44.83 \text{ \AA}$ (DNP side)

$z = 10.92 \text{ \AA}$															
01	-0.5382	C25	-0.3287	C49	-0.1555	H73	0.1454	C97	-0.1001	C121	-0.1305	H145	0.1753	C169	-0.0964
C2	0.0386	S26	0.2392	C50	-0.0636	H74	0.1450	H98	0.1234	C122	0.1089	H146	0.1392	C170	-0.0997
C3	0.0644	C27	-0.2631	C51	-0.0545	H75	0.1133	C99	0.0338	C123	-0.1530	H147	0.1390	H171	0.1167
C4	-0.5061	C28	-0.1531	C52	-0.0662	H76	0.1136	C100	0.0458	C124	0.1503	H148	0.1206	H172	0.1187
05	0.0809	S29	0.2279	C53	-0.0660	H77	0.1135	C101	-0.1075	H125	-0.4090	H149	0.1203	C173	-0.1699
C6	0.0400	C30	0.0921	C54	-0.0541	H78	0.1132	H102	0.1251	C126	-0.1694	H150	0.1758	H174	-0.4127
07	-0.5162	031	-0.5111	C55	-0.0641	H79	0.1038	C103	-0.1094	C127	0.0979	H151	0.1747	C175	0.1642
C8	0.0910	C32	0.0469	C56	-0.1512	H80	0.1037	H104	0.1219	C128	-0.1228	H152	0.1676	C176	-0.1350
C9	-0.1521	C33	0.0546	C57	0.4161	H81	0.3257	C105	0.0442	C129	-0.1221	H153	0.1396	C177	0.1107
C10	-0.2770	034	-0.5323	H58	0.1162	H82	0.1725	C106	-0.1097	C130	0.0930	H154	0.1467	C178	-0.1538
S11	0.2519	H35	0.1195	H59	0.1165	H83	0.1838	H107	0.1160	C131	-0.1025	H155	0.1713	C179	0.1485
C12	-0.3314	H36	0.0993	H60	0.1121	H84	0.1514	C108	-0.1073	C132	-0.0962	C156	0.1030	H180	0.1752
S13	0.2401	H37	0.1066	H61	0.1123	H85	0.1541	H109	0.1246	C133	-0.1670	C157	-0.1264	H181	0.1518
H14	0.3251	H38	0.1120	H62	0.1132	H86	0.1684	C110	0.0278	H134	-0.4094	C158	0.1579	H182	0.1386
H15	0.0985	H39	0.1190	H63	0.1133	H87	0.1615	C111	-0.1017	C135	0.1581	H159	-0.4091	H183	0.1589
H16	0.1002	H40	0.1108	H64	0.1406	H88	0.1557	H112	0.1217	C136	-0.1275	C160	0.1412	H184	0.1691
H17	0.1048	041	-0.5246	H65	0.1408	H89	0.1626	C113	-0.1234	C137	0.1055	C161	-0.1499	H185	0.1802
H18	0.1024	C42	0.0409	066	-0.4800	C90	-0.1002	H114	0.1130	C138	-0.1411	H162	0.1514	H186	0.1291
H19	0.0961	C43	0.0594	067	0.0066	H91	0.1229	C115	0.3105	C139	0.1509	H163	0.1743	H187	0.1321
H20	0.0861	044	-0.5104	068	0.0661	C92	-0.1185	C116	-0.1241	H140	0.1670	C164	-0.1660	H188	0.1761
H21	0.1065	C45	0.0615	069	-0.4963	H93	0.1330	H117	0.1181	H141	0.1414	C165	0.0905	H189	0.1751
H22	0.1183	C46	0.0157	C70	0.0609	C94	0.3278	C118	-0.1012	H142	0.1502	C166	-0.1151	H190	0.1627
H23	0.0908	047	-0.4889	C71	0.0341	C95	-0.1183	H119	0.1243	H143	0.1742	C167	-0.1154	H191	0.1373
H24	0.1188	C48	0.4122	072	-0.5288	H96	0.1323	C120	0.1554	H144	0.1770	C168	0.0977	Total	4.0000
$z = 15.66 \text{ \AA}$															
01	-0.5354	C25	-0.3661	C49	-0.1546	H73	0.1468	C97	-0.1017	C121	-0.1304	H145	0.1792	C169	-0.1051
C2	0.0359	S26	0.2715	C50	-0.0629	H74	0.1463	H98	0.1198	C122	0.0989	H146	0.1450	C170	-0.1064
C3	0.0682	C27	-0.2746	C51	-0.0530	H75	0.1147	C99	0.0329	C123	-0.1558	H147	0.1434	H171	0.1284
04	-0.5076	C28	-0.1462	C52	-0.0660	H76	0.1150	C100	0.0439	C124	0.1486	H148	0.1146	H172	0.1268
C5	0.0749	S29	0.2325	C53	-0.0659	H77	0.1150	C101	-0.1090	H125	-0.4095	H149	0.1142	C173	-0.1644
C6	0.0423	C30	0.0856	C54	-0.0525	H78	0.1147	H102	0.1232	C126	-0.1559	H150	0.1758	H174	-0.4130
07	-0.5133	031	-0.5186	C55	-0.0634	H79	0.1052	C103	-0.1117	C127	0.0860	H151	0.1745	C175	0.1411
C8	0.0915	C32	0.0514	C56	-0.1501	H80	0.1052	H104	0.1156	C128	-0.1116	H152	0.1764	C176	-0.1341
C9	-0.1370	C33	0.0644	C57	0.4175	H81	0.3271	C105	0.0401	C129	-0.1133	H153	0.1486	C177	0.1040
C10	-0.2477	034	-0.5377	H58	0.1154	H82	0.1991	C106	-0.1119	C130	0.0935	H154	0.1513	C178	-0.1543
S11	0.2436	H35	0.0999	H59	0.1155	H83	0.1581	H107	0.1071	C131	-0.1146	H155	0.1754	C179	0.1551
C12	-0.3058	H36	0.1066	H60	0.1123	H84	0.1531	C108	-0.1087	C132	-0.1144	C156	0.0879	H180	0.1804
S13	0.2640	H37	0.1000	H61	0.1123	H85	0.1562	H109	0.1218	C133	-0.1607	C157	-0.1168	H181	0.1553
H14	0.3230	H38	0.1023	H62	0.1136	H86	0.1702	C110	0.0280	H134	-0.4175	C158	0.1067	H182	0.1365
H15	0.0995	H39	0.0950	H63	0.1137	H87	0.1636	C111	-0.1035	C135	0.1631	H159	-0.4037	H183	0.1650
H16	0.0994	H40	0.0979	H64	0.1415	H88	0.1582	H112	0.1217	C136	-0.1311	C160	0.1531	H184	0.1748
H17	0.1030	041	-0.5256	H65	0.1416	H89	0.1648	C113	-0.1255	C137	0.0930	C161	-0.1407	H185	0.1796
H18	0.1033	C42	0.0421	066	-0.4785	C90	-0.1019	H114	0.0988	C138	-0.1571	H162	0.1581	H186	0.1417
H19	0.0962	C43	0.0589	067	0.0052	H91	0.1192	C115	0.3010	C139	0.1475	H163	0.1819	H187	0.1407
H20	0.0964	044	-0.5101	068	0.0654	C92	-0.1191	C116	-0.1266	H140	0.1764	C164	-0.1597	H188	0.1802
H21	0.1134	C45	0.0616	069	-0.4937	H93	0.1309	H117	0.1045	H141	0.1533	C165	0.0778	H189	0.1741
H22	0.1142	C46	0.0145	C70	0.0596	C94	0.3255	C118	-0.1029	H142	0.1507	C166	-0.1225	H190	0.1709
H23	0.1231	047	-0.4874	C71	0.0336	C95	-0.1190	H119	0.1247	H143	0.1779	C167	-0.1207	H191	0.1437
H24	0.1247	C48	0.4136	072	-0.5257	H96	0.1302	C120	0.1602	H144	0.1764	C168	0.0821	Total	4.0000
$z = 18.75 \text{ \AA}$															
01	-0.5336	C25	-0.3276	C49	-0.1537	H73	0.1479	C97	-0.1044	C121	-0.1257	H145	0.1794	C169	-0.1082
C2	0.0349	S26	0.2626	C50	-0.0622	H74	0.1474	H98	0.1124	C122	0.0874	H146	0.1468	C170	-0.1069
C3	0.0686	C27	-0.2950	C51	-0.0510	H75	0.1102	C99	0.0293	C123	-0.1464	H147	0.1486	H171	0.1133
04	-0.5057	C28	-0.1555	C52	-0.0662	H76	0.1105	C100	0.0429	C124	0.1496	H148	0.1172	H172	0.1131
C5	0.0723	S29	0.2815	C53	-0.0659	H77	0.1105	C101	-0.1114	H125	-0.4116	H149	0.1170	C173	-0.1727
C6	0.0434	C30	0.0756	C54	-0.0507	H78	0.1103	H102	0.1216	C126	-0.1591	H150	0.1800	H174	-0.4059
07	-0.5136	031	-0.5159	C55	-0.0625	H79	0.1001	C103	-0.1140	C127	0.0627	H151	0.1800	C175	0.1519
C8	0.0891	C32	0.0604	C56	-0.1484	H80	0.1000	H104	0.1048	C128	-0.1156	H152	0.1734	C176	-0.1312
C9	-0.1367	C33	0.0561	C57	0.4201	H81	0.3230	C105	0.0307	C129	-0.1181	H153	0.1379	C177	0.0871
C10	-0.2433	034	-0.5499	H58	0.1132	H82	0.2039	C106	-0.1140	C130	0.0637	H154	0.1528	C178	-0.1492
S11	0.2179	H35	0.1088	H59	0.1134	H83	0.1603	H107	0.0939	C131	-0.1034	H155	0.1830	C179	0.1455
C12	-0.2990	H36	0.1023	H60	0.1121	H84	0.1541	C108	-0.1110	C132	-0.1026	C156	0.0841	H180	0.1841
S13	0.3122	H37	0.0927	H61	0.1120	H85	0.1579	H109	0.1198	C133	-0.1607	C157	-0.1294	H181	0.1566
H14	0.3227	H38	0.0929	H62	0.1138	H86	0.1736	C110	0.0338	H134	-0.4152	C158	0.1561	H182	0.1349
H15	0.0999	H39	0.0951	H63	0.1138	H87	0.1652	C111	-0.1041	C135	0.1586	H159	-0.4072	H183	0.1777
H16	0.1000	H40	0.0956	H64	0.1418	H88	0.1605	H112	0.1252	C136	-0.1229	C160	0.1460	H184	0.1778
H17	0.1039	041	-0.5280	H65	0.1421	H89	0.1631	C113	-0.1390	C137	0.0931	C161	-0.1474	H185	0.1812
H18	0.1041	C42	0.0441	066	-0.4753	C90	-0.1047	H114	0.0777	C138	-0.1515	H162	0.1563	H186	0.1399
H19	0.0987	C43	0.0584	067	0.0019	H91	0.1124	C115	0.3001	C139	0.1520	H163	0.1841	H187	0.1401
H20	0.0989	044	-0.5104	068	0.0699	C92	-0.1206	C116	-0.1395	H140	0.1781	C164	-0.1716	H188	0.1838
H21	0.1137	C45	0.0619	069	-0.5035	H93	0.1272	H117	0.0780	H141	0.1399	C165	0.0753	H189	0.1774
H22	0.1146	C46	0.0136	C70	0.0620	C94	0.3214	C118	-0.1031	H142	0.1530	C166	-0.1068	H190	0.1782
H23	0.1281	047	-0.4860	C71	0.0369	C95	-0.1206	H119	0.1263	H143	0.1822	C167	-0.1067	H191	0.1354
H24	0.1291	C48	0.4151	072	-0.5375	H96	0.1261	C120	0.1532	H144	0.1819	C168	0.0784	Total	4.0000
$z = 23.27 \text{ \AA}$															
01	-0.5279	C25	-0.3086	C49	-0.1582	H73	0.1443	C97	-0.1072	C121	-0.1336	H145	0.1741	C169	-0.1167
C2	0.0329	S26	0.3543	C50	-0.0650	H74	0.1439	H98	0.1019	C122	0.0917	H146	0.1418	C170	-0.1121
C3	0.0686	C27	-0.2483	C51	-0.0574	H75	0.1106	C99	0.0222	C123	-0.1462	H147	0.1403	H171	0.1147
04	-0.5049	C28	-0.1425	C52	-0.0664	H76	0.1108	C100	0.0446	C124	0.1463	H148	0.1170	H172	0.1171
C5	0.0712	S29	0.3447	C53	-0.0660	H77	0.1112	C101	-0.1131	H125	-0.4239	H149	0.1248	C173	-0.1604
C6	0.0422	C30	0.0685	C54	-0.0571	H78	0.1109	C103	-0.1231	C126	-0.1481	H150	0.1767	H174	-0.4187
07	-0.5141	031	-0.5163	C55	-0.0652	H79	0.1008	H102	-0.1230	C127	0.0648	H151	0.1780	C175	

z = 28.17 Å															
C1	-0.5279	C25	-0.3052	C49	-0.1814	H73	0.1186	C97	-0.1307	C121	-0.1208	H145	0.1859	C169	-0.1017
C2	0.0336	S26	0.4090	C50	-0.0854	H74	0.1186	H98	0.0822	C122	0.1032	H146	0.1403	C170	-0.1042
C3	0.0642	C27	-0.2440	C51	-0.0911	H75	0.0976	C99	0.0113	C123	-0.1394	H147	0.1347	H171	0.1225
C4	-0.4978	C28	-0.1406	C52	-0.0708	H76	0.0977	C100	0.0256	C124	0.1505	H148	0.1268	H172	0.1199
C5	0.0698	S29	0.4042	C53	-0.0635	H77	0.0989	C101	-0.1375	N125	-0.4077	H149	0.1277	C173	-0.1670
C6	0.0369	C30	0.0737	C54	-0.1008	H78	0.0985	H102	0.1047	C126	-0.1678	H150	0.1751	N174	-0.4116
C7	-0.5149	O31	-0.5186	C55	-0.0796	H79	0.0953	C103	-0.1342	C127	0.0696	H151	0.1877	C175	0.1652
C8	0.0870	C32	0.0555	C56	-0.1795	H80	0.0923	H104	0.1000	C128	-0.1174	H152	0.1696	C176	-0.1240
C9	-0.1346	C33	0.0403	C57	0.3787	H81	0.1363	C105	0.0210	C129	-0.1136	H153	0.1413	C177	0.1034
C10	-0.2362	O34	-0.5223	H58	0.1055	H82	0.2260	C106	-0.1352	C130	0.0801	H154	0.1621	C178	-0.1446
S11	0.4294	H35	0.1448	H59	0.1010	H83	0.1894	H107	0.1008	C131	-0.1037	H155	0.1885	C179	0.1510
C12	-0.5105	H36	0.1428	H60	0.1089	H84	0.0799	C108	-0.1374	C132	-0.1027	H156	0.0998	H180	0.1850
S13	0.4158	H37	0.1076	H61	0.1103	H85	0.0904	H109	0.1023	C133	-0.1756	C157	-0.1168	H181	0.1518
H14	0.3259	H38	0.1057	H62	0.1115	H86	0.1230	C110	0.0149	N134	-0.4041	C158	0.1546	H182	0.1500
H15	0.1039	H39	0.1262	H63	0.1122	H87	0.0956	C111	-0.1266	C135	0.1486	N159	-0.4006	H183	0.1732
H16	0.1038	H40	0.1250	H64	0.1088	H88	0.0966	H112	0.0905	C136	-0.1203	C160	0.1550	H184	0.1879
H17	0.1086	O41	-0.5175	H65	0.1074	H89	0.1142	C113	-0.1250	C137	0.0971	C161	-0.1441	H185	0.1819
H18	0.1090	C42	0.0313	O66	-0.5197	C90	-0.1319	H114	0.1350	C138	-0.1463	H162	0.1600	H186	0.1463
H19	0.1038	C43	0.0775	C67	0.0387	H91	0.0784	C115	0.3213	C139	0.1520	H163	0.1897	H187	0.1459
H20	0.1045	O44	-0.5162	O68	0.0682	C92	-0.1264	C116	-0.1267	H140	0.1695	C164	-0.1759	H188	0.1892
H21	0.1215	C45	0.0451	O69	-0.5108	H93	0.1392	H117	0.1326	H141	0.1472	C165	0.0742	H189	0.1865
H22	0.1221	C46	0.0596	C70	0.0763	C94	0.3322	C118	-0.1282	H142	0.1656	C166	-0.1125	H190	0.1828
H23	0.1439	O47	-0.5225	C71	0.0350	C95	-0.1244	H119	0.0858	H143	0.1915	C167	-0.1173	H191	0.1540
H24	0.1448	C48	0.3625	O72	-0.5416	H96	0.1421	C120	0.1648	H144	0.1884	C168	0.0697	Total	4.0000
z = 32.22 Å															
O1	-0.5161	C25	-0.3055	C49	-0.1725	H73	0.1357	C97	-0.1262	C121	-0.1251	H145	0.1745	C169	-0.1091
C2	0.0282	S26	0.4047	C50	-0.0767	H74	0.1350	H98	0.0980	C122	0.0894	H146	0.1440	C170	-0.1080
C3	0.0666	C27	-0.2433	C51	-0.0753	H75	0.1040	C99	0.0160	C123	-0.1407	H147	0.1420	H171	0.1173
C4	-0.4995	C28	-0.1396	C52	-0.0682	H76	0.1045	C100	0.0354	C124	0.1447	H148	0.1305	H172	0.1207
O5	0.0678	S29	0.3949	C53	-0.0640	H77	0.1053	C101	-0.1447	N125	-0.4183	H149	0.1399	C173	-0.1633
O6	0.0406	C30	0.0786	C54	-0.0816	H78	0.1053	H102	0.0451	C126	-0.1515	H150	0.1733	N174	-0.4158
O7	-0.5148	O31	-0.5159	C55	-0.0736	H79	0.0980	C103	-0.1122	C127	0.0801	H151	0.1778	C175	0.1536
O8	0.0862	C32	0.0525	C56	-0.1652	H80	0.0978	H104	0.1207	C128	-0.1184	H152	0.1813	C176	-0.1322
O9	-0.1360	C33	0.0441	C57	0.3991	H81	0.1320	C105	0.0461	C129	-0.1211	H153	0.1505	C177	0.0938
C10	-0.2385	O34	-0.5289	H58	0.0984	H82	0.2178	C106	-0.1156	C130	0.0788	H154	0.1502	C178	-0.1458
S11	0.4169	H35	0.1408	H59	0.0976	H83	0.1936	C107	0.1196	C131	-0.1258	H155	0.1780	C179	0.1469
C12	-0.3088	H36	0.1388	H60	0.1013	H84	0.1093	C108	-0.1253	C132	-0.1260	C156	0.0906	H180	0.1777
S13	0.4024	H37	0.1120	H61	0.0996	H85	0.1272	H109	0.0851	C133	-0.1541	C157	-0.1265	H181	0.1549
H14	0.3290	H38	0.1120	H62	0.1145	H86	0.1252	C110	0.0170	N134	-0.4439	C158	-0.1447	H182	0.1367
H15	0.1095	H39	0.1213	H63	0.1132	H87	0.1252	C111	-0.1064	C135	0.1598	N159	-0.4128	H183	0.1681
H16	0.1093	H40	0.1201	H64	0.1103	H88	0.1211	H112	0.1043	C136	-0.1196	C160	0.1442	H184	0.1750
H17	0.1086	O41	-0.51425	H65	0.1215	H89	0.1473	C113	-0.1209	C137	0.0815	C161	-0.1504	H185	0.1762
H18	0.1090	C42	0.0439	O66	-0.4866	C90	-0.1211	H114	0.1273	C138	-0.1548	H162	0.1499	H186	0.1408
H19	0.1043	C43	0.0756	C67	0.0159	H91	0.0996	C115	0.3169	C139	0.1430	H163	0.1747	H187	0.1407
H20	0.1049	O44	-0.5151	O68	0.0707	C92	-0.0891	C116	-0.1220	H140	0.1665	C164	-0.1609	H188	0.1777
H21	0.1192	C45	0.0478	O69	-0.5089	H93	0.0664	H117	0.1270	H141	0.1388	C165	0.0777	H189	0.1741
H22	0.1198	C46	0.0446	C70	0.0674	C94	0.2924	C118	-0.1066	H142	0.1528	C166	-0.1205	H190	0.1665
H23	0.1404	O47	-0.5135	C71	0.0366	C95	-0.1345	H119	0.0998	H143	0.1788	C167	-0.1185	H191	0.1461
H24	0.1412	C48	0.3821	O72	-0.5391	H96	0.0991	C120	0.1553	H144	0.1788	C168	0.0792	Total	4.0000
z = 36.84 Å															
O1	-0.5259	C25	-0.3059	C49	-0.1820	H73	0.1240	C97	-0.1144	C121	-0.1372	H145	0.1807	C169	-0.1108
C2	0.0323	S26	0.4327	C50	-0.0869	H74	0.1231	H98	0.1205	C122	0.0815	H146	0.1424	C170	-0.1091
C3	0.0659	C27	-0.2407	C51	-0.0839	H75	0.0996	C99	0.0365	C123	-0.1454	H147	0.1427	H171	0.1262
O4	-0.5007	C28	-0.1385	C52	-0.0727	H76	0.1003	C100	0.0308	C124	0.1515	H148	0.1253	H172	0.1276
O5	0.0700	S29	0.4198	C53	-0.0569	H77	0.1025	C101	-0.1142	N125	-0.4075	H149	0.1276	C173	-0.1593
O6	0.0375	C30	0.0813	C54	-0.1058	H78	0.1025	H102	0.0814	C126	-0.1642	H150	0.1799	N174	-0.4069
O7	-0.5148	O31	-0.5156	C55	-0.0757	H79	0.0962	C103	-0.1122	C127	0.0767	H151	0.1839	C175	0.1585
O8	0.0867	C32	0.0474	C56	-0.1772	H80	0.0960	C105	0.0176	C128	-0.1154	H152	0.1779	C176	-0.1230
O9	-0.1354	C33	0.0490	C57	0.3883	H81	0.1397	C106	0.0409	C129	-0.1149	H153	0.1526	C177	0.0831
C10	-0.2366	O34	-0.5321	H58	0.0928	H82	0.2261	C107	-0.1129	C130	0.0801	H154	0.1653	C178	-0.1460
S11	0.4426	H35	0.1446	H59	0.0914	H83	0.2102	H107	0.1191	C131	-0.1101	H155	0.1893	C179	0.1575
C12	-0.3096	H36	0.1414	H60	0.0863	H84	0.0709	C108	-0.1163	C132	-0.1092	C156	0.0815	H180	0.1815
S13	0.4262	H37	0.1114	H61	0.0882	H85	0.1056	H109	0.1021	C133	-0.1681	C157	-0.1198	H181	0.1602
H14	0.3257	H38	0.1115	H62	0.0897	H86	0.1420	C110	0.0234	N134	-0.4067	C158	-0.1592	H182	0.1481
H15	0.1046	H39	0.1225	H63	0.0874	H87	0.0611	C111	-0.1060	C135	0.1594	N159	-0.4103	H183	0.1745
H16	0.1044	H40	0.1210	H64	0.0967	H88	0.0977	H112	0.1081	C136	-0.1348	C160	0.1436	H184	0.1823
H17	0.1074	O41	-0.51477	H65	0.1013	H89	0.1290	C113	-0.1234	C137	0.0778	C161	-0.1467	H185	0.1749
H18	0.1079	C42	0.0541	O66	-0.5145	C90	-0.1145	H114	0.1189	C138	-0.1459	H162	0.1589	H186	0.1428
H19	0.1030	C43	0.0649	C67	0.0296	H91	0.1232	C115	0.3113	C139	0.1519	H163	0.1838	H187	0.1428
H20	0.1037	O44	-0.5206	O68	0.0709	C92	-0.1426	C116	-0.1241	H140	0.1765	C164	-0.1576	H188	0.1767
H21	0.1210	C45	0.0525	O69	-0.5108	H93	0.0764	H117	0.1201	H141	0.1508	C165	0.0704	H189	0.1818
H22	0.1216	C46	0.0640	C70	0.0707	C94	0.3055	C118	-0.1059	H142	0.1658	C166	-0.1177	H190	0.1738
H23	0.1443	O47	-0.5284	C71	0.0368	C95	-0.1391	H119	0.1077	H143	0.1912	C167	-0.1177	H191	0.1484
H24	0.1451	C48	0.3469	O72	-0.5395	H96	0.0788	C120	0.1592	H144	0.1839	C168	0.0713	Total	4.0000
z = 40.99 Å															
O1	-0.5159	C25	-0.3067	C49	-0.2057	H73	0.1285	C97	-0.1074	C121	-0.1407	H145	0.1784	C169	-0.1095
C2	0.0293	S26	0.4372	C50	-0.1201	H74	0.1299	H98	0.1154	C122	0.1034	H146	0.1440	C170	-0.1101
C3	0.0656	C27	-0.2398	C51	-0.0974	H75	0.0984	C99	0.0306	C123	-0.1451	H147	0.1421	H171	0.1204
C4	-0.4982	C28	-0.1378	C52	-0.0737	H76	0.0972	C100	0.0343	C124	0.1507	H148	0.1211	H172	0.1186
O5	0.0681	S29	0.4222	C53	-0.0859	H77	0.1048	C101	-0.1161	N125	-0.4068	H149	0.1236	C173	-0.1667
O6	0.0382	C30	0.0830	C54	-0.1223	H78	0.1039	H102	0.0952	C126	-0.1588	H150	0.1776	N174	-0.4123
O7	-0.5149	O31	-0.5150	C55	-0.0841	H79	0.0958	C103	-0.1145	C127	0.0678	H151	0.1795	C175	0.1620
O8	0.0862	C32	0.0448	C56	-0.1764	H80	0.0988	H104	0.1093	C128	-0.1213	H152	0.1755	C176	-0.1338
O9	-0.1359														

Table E.2: Partial Charge Distribution of +1 Oxidized Rotaxane when the Center of Mass of the CBPQT⁴⁺ Ring Moves from $z = 10.92 \text{ \AA}$ (TTF side) to $z = 44.83 \text{ \AA}$ (DNP side)

$z = 10.92 \text{ \AA}$															
01	-0.5374	C25	-0.3310	C49	-0.1512	H73	0.1519	C97	-0.0909	C121	-0.1317	H145	0.1823	C169	-0.0971
C2	0.0394	S26	0.2497	C50	-0.0588	H74	0.1514	H98	0.1431	C122	0.1110	H146	0.1469	C170	-0.1002
C3	0.0616	C27	-0.2626	C51	-0.0466	H75	0.1168	C99	0.0421	C123	-0.1532	H147	0.1452	H171	0.1218
C4	-0.5052	C28	-0.1540	C52	-0.0661	H76	0.1171	C100	0.0541	C124	0.1519	H148	0.1186	H172	0.1212
05	0.0829	S29	0.2401	C53	-0.0671	H77	0.1193	C101	-0.0975	H125	-0.4077	H149	0.1218	C173	-0.1747
C6	0.0353	C30	0.0903	C54	-0.0439	H78	0.1191	H102	0.1466	C126	-0.1712	H150	0.1853	N174	-0.4084
07	-0.5164	031	-0.5120	C55	-0.0603	H79	0.1230	C103	-0.1017	C127	0.0969	H151	0.1816	C175	0.1784
C8	0.0927	C32	0.0465	C56	-0.1435	H80	0.1230	H104	0.1446	C128	-0.1219	H152	0.1803	C176	-0.1317
C9	-0.1515	C33	0.0470	C57	0.4246	H81	0.3399	C105	0.0567	C129	-0.1218	H153	0.1503	C177	0.1167
C10	-0.2775	034	-0.5247	H58	0.1252	H82	0.1811	C106	-0.1020	C130	0.0899	H154	0.1542	C178	-0.1522
S11	0.2587	H35	0.1257	H59	0.1257	H83	0.1865	H107	0.1386	C131	-0.1031	H155	0.1818	C179	0.1564
C12	-0.3311	H36	0.1027	H60	0.1181	H84	0.1578	C108	-0.0873	C132	-0.0964	C156	0.1058	H180	0.1891
S13	0.2507	H37	0.1114	H61	0.1182	H85	0.1651	H109	0.1461	C133	-0.1727	C157	-0.1276	H181	0.1639
H14	0.3272	H38	0.1184	H62	0.1180	H86	0.1778	C110	0.0290	H134	-0.4048	C158	0.1595	H182	0.1434
H15	0.0995	H39	0.1252	H63	0.1182	H87	0.1695	C111	-0.0947	C135	0.1653	H159	-0.4078	H183	0.1669
H16	0.1011	H40	0.1155	H64	0.1440	H88	0.1680	H112	0.1344	C136	-0.1252	C160	0.1422	H184	0.1751
H17	0.1060	041	-0.5109	H65	0.1442	H89	0.1741	C113	-0.1187	C137	0.1114	C161	-0.1505	H185	0.1891
H18	0.1040	C42	0.0286	066	-0.4718	C90	-0.0908	H114	0.1312	C138	-0.1392	H162	0.1584	H186	0.1308
H19	0.0955	C43	0.0606	C67	-0.0012	H91	0.1425	C115	0.3246	C139	0.1589	H163	0.1816	H187	0.1362
H20	0.0862	044	-0.5109	C68	0.0653	C92	-0.1101	C116	-0.1194	H140	0.1723	C164	-0.1681	H188	0.1831
H21	0.1097	C45	0.0575	069	-0.4994	H93	0.1579	H117	0.1370	H141	0.1453	C165	0.0897	H189	0.1804
H22	0.1212	C46	0.0132	C70	0.0593	C94	0.3479	C118	-0.0939	H142	0.1544	C166	-0.1148	H190	0.1638
H23	0.0940	047	-0.4878	C71	0.0207	C95	-0.1098	H119	0.1375	H143	0.1790	C167	-0.1156	H191	0.1374
H24	0.1214	C48	0.4187	072	-0.4878	H96	0.1573	C120	0.1569	H144	0.1823	C168	0.0949	Total	5.0000
$z = 15.66 \text{ \AA}$															
01	-0.4907	C25	-0.3683	C49	-0.1507	H73	0.1522	C97	-0.0941	C121	-0.1283	H145	0.1870	C169	-0.1049
C2	0.0201	S26	0.2822	C50	-0.0585	H74	0.1517	H98	0.1382	C122	0.1036	H146	0.1508	C170	-0.1067
C3	0.0653	C27	-0.2754	C51	-0.0459	H75	0.1175	C99	0.0413	C123	-0.1539	H147	0.1494	H171	0.1294
04	-0.5034	C28	-0.1483	C52	-0.0663	H76	0.1178	C100	0.0483	C124	0.1542	H148	0.1144	H172	0.1288
C5	0.0709	S29	0.2428	C53	-0.0669	H77	0.1199	C101	-0.1009	H125	-0.4064	H149	0.1135	C173	-0.1673
C6	0.0396	C30	0.0855	C54	-0.0433	H78	0.1197	H102	0.1407	C126	-0.1591	H150	0.1828	N174	-0.4099
07	-0.5136	031	-0.5192	C55	-0.0598	H79	0.1253	C103	-0.1071	C127	0.0841	H151	0.1801	C175	0.1459
C8	0.0912	C32	0.0505	C56	-0.1434	H80	0.1253	H104	0.1346	C128	-0.1115	H152	0.1802	C176	-0.1335
C9	-0.1368	C33	0.0603	C57	0.4247	H81	0.3417	C105	0.0505	C129	-0.1132	H153	0.1510	C177	0.1083
C10	-0.2459	034	-0.5334	H58	0.1238	H82	0.2073	C106	-0.1073	C130	0.0919	H154	0.1561	C178	-0.1531
S11	0.2609	H35	0.0995	H59	0.1242	H83	0.1612	H107	0.1255	C131	-0.1145	H155	0.1812	C179	0.1590
C12	-0.3060	H36	0.1100	H60	0.1177	H84	0.1585	C108	-0.1007	C132	-0.1147	C156	0.0940	H180	0.1886
S13	0.2820	H37	0.1037	H61	0.1177	H85	0.1657	H109	0.1392	C133	-0.1630	C157	-0.1150	H181	0.1625
H14	0.3395	H38	0.1057	H62	0.1179	H86	0.1732	C110	0.0259	H134	-0.4148	C158	0.1129	H182	0.1374
H15	0.1215	H39	0.0978	H63	0.1180	H87	0.1702	C111	-0.0989	C135	0.1671	H159	-0.3998	H183	0.1679
H16	0.1214	H40	0.1019	H64	0.1443	H88	0.1687	H112	0.1306	C136	-0.1308	C160	0.1590	H184	0.1808
H17	0.1113	041	-0.5132	H65	0.1445	H89	0.1746	C113	-0.1230	C137	0.0977	C161	-0.1393	H185	0.1869
H18	0.1115	C42	0.0305	066	-0.4718	C90	-0.0941	H114	0.1114	C138	-0.1556	H162	0.1668	H186	0.1457
H19	0.1018	C43	0.0601	C67	-0.0012	H91	0.1377	C115	0.3097	C139	0.1516	H163	0.1925	H187	0.1445
H20	0.1019	044	-0.5107	C68	0.0647	C92	-0.1118	C116	-0.1240	H140	0.1826	C164	-0.1637	H188	0.1881
H21	0.1178	C45	0.0579	069	-0.4978	H93	0.1539	H117	0.1170	H141	0.1572	C165	0.0764	H189	0.1810
H22	0.1187	C46	0.0125	C70	0.0592	C94	0.3429	C118	-0.0981	H142	0.1576	C166	-0.1223	H190	0.1766
H23	0.1280	047	-0.4862	C71	0.0194	C95	-0.1116	H119	0.1337	H143	0.1865	C167	-0.1204	H191	0.1470
H24	0.1299	C48	0.4194	072	-0.4806	H96	0.1531	C120	0.1656	H144	0.1827	C168	0.0817	Total	5.0000
$z = 18.75 \text{ \AA}$															
01	-0.4694	C25	-0.3207	C49	-0.1498	H73	0.1538	C97	-0.1005	C121	-0.1249	H145	0.1867	C169	-0.1077
C2	0.0185	S26	0.2837	C50	-0.0585	H74	0.1532	H98	0.1221	C122	0.0927	H146	0.1506	C170	-0.1063
C3	0.0589	C27	-0.2968	C51	-0.0453	H75	0.1222	C99	0.0352	C123	-0.1435	H147	0.1515	H171	0.1130
04	-0.4810	C28	-0.1570	C52	-0.0660	H76	0.1226	C100	0.0440	C124	0.1561	H148	0.1190	H172	0.1126
C5	0.0593	S29	0.3045	C53	-0.0671	H77	0.1233	C101	-0.1071	H125	-0.4085	H149	0.1185	C173	-0.1774
C6	0.0403	C30	0.0754	C54	-0.0426	H78	0.1230	H102	0.1302	C126	-0.1631	H150	0.1864	N174	-0.4027
07	-0.5144	031	-0.5167	C55	-0.0597	H79	0.1121	C103	-0.1124	C127	0.0607	H151	0.1878	C175	0.1594
C8	0.0864	C32	0.0590	C56	-0.1431	H80	0.1119	H104	0.1125	C128	-0.1159	H152	0.1739	C176	-0.1306
C9	-0.1356	C33	0.0573	C57	0.4253	H81	0.3337	C105	0.0350	C129	-0.1188	H153	0.1381	C177	0.0921
C10	-0.2392	034	-0.5496	H58	0.1178	H82	0.2145	C106	-0.1123	C130	0.0630	H154	0.1610	C178	-0.1481
S11	0.2563	H35	0.1119	H59	0.1184	H83	0.1659	H107	0.1002	C131	-0.1028	H155	0.1920	C179	0.1515
C12	-0.3035	H36	0.1059	H60	0.1156	H84	0.1603	C108	-0.1067	C132	-0.1020	C156	0.0886	H180	0.1924
S13	0.3465	H37	0.0924	H61	0.1155	H85	0.1664	H109	0.1279	C133	-0.1647	C157	-0.1274	H181	0.1622
H14	0.3463	H38	0.0924	H62	0.1167	H86	0.1787	C110	0.0336	H134	-0.4124	C158	0.1640	H182	0.1392
H15	0.1300	H39	0.0947	H63	0.1167	H87	0.1724	C111	-0.1020	C135	0.1654	H159	-0.4032	H183	0.1845
H16	0.1301	H40	0.0963	H64	0.1445	H88	0.1705	H112	0.1303	C136	-0.1209	C160	0.1527	H184	0.1863
H17	0.1213	041	-0.5207	H65	0.1448	H89	0.1753	C113	-0.1364	C137	0.0977	C161	-0.1458	H185	0.1893
H18	0.1214	C42	0.0381	066	-0.4717	C90	-0.1007	H114	0.0788	C138	-0.1494	H162	0.1632	H186	0.1456
H19	0.1155	C43	0.0585	C67	-0.0020	H91	0.1223	C115	0.3010	C139	0.1568	H163	0.1936	H187	0.1454
H20	0.1156	044	-0.5109	C68	0.0616	C92	-0.1159	C116	-0.1392	H140	0.1808	C164	-0.1765	H188	0.1917
H21	0.1220	C45	0.0602	069	-0.4809	H93	0.1399	H117	0.0782	H141	0.1413	C165	0.0740	H189	0.1860
H22	0.1230	C46	0.0108	C70	0.0526	C94	0.3315	C118	-0.1010	H142	0.1621	C166	-0.1055	H190	0.1858
H23	0.1376	047	-0.4847	C71	0.0312	C95	-0.1158	H119	0.1314	H143	0.1920	C167	-0.1056	H191	0.1405
H24	0.1388	C48	0.4206	072	-0.5125	H96	0.1387	C120	0.1613	H144	0.1899	C168	0.0767	Total	5.0000
$z = 23.27 \text{ \AA}$															
01	-0.4773	C25	-0.3072	C49	-0.1512	H73	0.1523	C97	-0.1066	C121	-0.1309	H145	0.1785	C169	-0.1157
C2	0.0184	S26	0.3874	C50	-0.0596	H74	0.1519	H98	0.1029	C122	0.1013	H146	0.1449	C170	-0.1109
C3	0.0622	C27	-0.2490	C51	-0.0474	H75	0.1178	C99	0.0216	C123	-0.1426	H147	0.1437	H171	0.1128
04	-0.4917	C28	-0.1455	C52	-0.0662	H76	0.1181	C100	0.0461	C124	0.1529	H148	0.1178	H172	0.1159
C5	0.0641	S29	0.3775	C53	-0.0674	H77	0.1215	C101	-0.1123	H125	-0.4153	H149	0.1264	C173	-0.1641
C6	0.0371	C30	0.0695	C54	-0.0444	H78	0.1212	H102	0.1261	C126	-0.1504	H150	0.1829	N174	-0.4101
07	-0.5149	031	-0.5174	C55	-0.0605	H79	0.1327	C103	-0.1229	C127	0.0644	H151	0.1841	C175	

$z = 28.17 \text{ \AA}$															
C1	-0.4928	C25	-0.3046	C49	-0.1541	H73	0.1543	C97	-0.1288	C121	-0.1220	H145	0.1850	C169	-0.1009
C2	0.0234	S26	0.4139	C50	-0.0587	H74	0.1539	H98	0.0887	C122	0.1014	H146	0.1400	C170	-0.1037
C3	0.0599	C27	-0.2438	C51	-0.0484	H75	0.1127	C99	0.0142	C123	-0.1415	H147	0.1348	H171	0.1237
O4	-0.4841	C28	-0.1407	C52	-0.0655	H76	0.1129	C100	0.0258	C124	0.1478	H148	0.1240	H172	0.1212
O5	0.0624	S29	0.4096	C53	-0.0675	H77	0.1139	C101	-0.1343	N125	-0.4094	H149	0.1230	C173	-0.1658
O6	0.0370	C30	0.0736	C54	-0.0430	H78	0.1136	H102	0.1045	C126	-0.1666	H150	0.1750	N174	-0.4128
O7	-0.5153	O31	-0.5188	C55	-0.1610	H79	0.1016	H103	-0.1331	C127	0.0705	H151	0.1866	C175	0.1636
O8	0.0854	C32	0.0549	C56	-0.1402	H80	0.1015	H104	0.1012	C128	-0.1168	H152	0.1679	C176	-0.1239
O9	-0.1351	C33	0.0401	C57	0.4263	H81	0.3260	C105	0.0236	C129	-0.1133	H153	0.1395	C177	0.1022
C10	-0.2356	O34	-0.5219	H58	0.1073	H82	0.2266	H106	-0.1334	C130	0.0849	H154	0.1579	C178	-0.1448
S11	0.4361	H35	0.1461	H59	0.1030	H83	0.1871	H107	0.1035	C131	-0.1032	H155	0.1848	C179	0.1438
C12	-0.3111	H36	0.1439	H60	0.1173	H84	0.1474	C108	-0.1352	C132	-0.1022	C156	0.0961	H180	0.1858
S13	0.4220	H37	0.1078	H61	0.1186	H85	0.1624	H109	0.1016	C133	-0.1749	C157	-0.1184	H181	0.1511
H14	0.3384	H38	0.1059	H62	0.1194	H86	0.1809	C110	0.0147	N134	-0.4049	C158	0.1498	H182	0.1447
H15	0.1202	H39	0.1271	H63	0.1201	H87	0.1669	C111	-0.1260	C135	0.1483	N159	-0.4024	H183	0.1668
H16	0.1200	H40	0.1257	H64	0.1384	H88	0.1700	H112	0.0908	C136	-0.1216	C160	0.1512	H184	0.1852
H17	0.1174	O41	-0.5212	H65	0.1373	H89	0.1804	C113	-0.1250	C137	0.0953	C161	-0.1455	H185	0.1821
H18	0.1179	C42	0.0389	O66	-0.4639	C90	-0.1297	H114	0.1357	C138	-0.1466	H162	0.1578	H186	0.1414
H19	0.1128	C43	0.0634	C67	-0.0075	H91	0.0843	C115	0.3218	C139	0.1509	H163	0.1864	H187	0.1374
H20	0.1134	O44	-0.5154	C68	0.0711	C92	-0.1272	C116	-0.1265	H140	0.1669	C164	-0.1733	H188	0.1880
H21	0.1246	C45	0.0541	O69	-0.4999	H93	0.1343	H117	0.1336	H141	0.1448	C165	0.0757	H189	0.1782
H22	0.1252	C46	0.0205	C70	0.0572	C94	0.3257	C118	-0.1270	H142	0.1545	C166	-0.1127	H190	0.1710
H23	0.1465	O47	-0.4931	C71	0.0379	C95	-0.1257	H119	0.0866	H143	0.1841	C167	-0.1171	H191	0.1443
H24	0.1473	C48	0.4154	O72	-0.5359	H96	0.1366	C120	0.1617	H144	0.1849	C168	0.0705	Total	5.0000
$z = 32.22 \text{ \AA}$															
O1	-0.4888	C25	-0.3055	C49	-0.1591	H73	0.1520	C97	-0.1275	C121	-0.1238	H145	0.1815	C169	-0.1070
C2	0.0209	S26	0.4325	C50	-0.0615	H74	0.1511	H98	0.0994	C122	0.0918	H146	0.1477	C170	-0.1063
C3	0.0612	C27	-0.2413	C51	-0.0541	H75	0.1187	C99	0.0162	C123	-0.1400	H147	0.1457	H171	0.1174
O4	-0.4864	C28	-0.1392	C52	-0.0651	H76	0.1194	C100	0.0346	C124	0.1501	H148	0.1262	H172	0.1212
O5	0.0626	S29	0.4228	C53	-0.0661	H77	0.1210	C101	-0.1438	N125	-0.4156	H149	0.1336	C173	-0.1661
O6	0.0371	C30	0.0786	C54	-0.0505	H78	0.1210	H102	0.0426	C126	-0.1551	H150	0.1796	N174	-0.4137
O7	-0.5154	O31	-0.5166	C55	-0.1636	H79	0.1235	C103	-0.1115	C127	0.0779	H151	0.1805	C175	0.1586
O8	0.0853	C32	0.0495	C56	-0.1444	H80	0.1232	H104	0.1242	C128	-0.1164	H152	0.1832	C176	-0.1316
C9	-0.1355	C33	0.0437	C57	0.4206	H81	0.3422	C105	0.0484	C129	-0.1181	H153	0.1505	C177	0.0963
C10	-0.2355	O34	-0.5276	H58	0.0989	H82	0.2275	C106	-0.1146	C130	0.0784	H154	0.1504	C178	-0.1443
S11	0.4472	H35	0.1464	H59	0.0988	H83	0.2056	C108	0.1251	C131	-0.1234	H155	0.1791	H179	0.1514
C12	-0.3107	H36	0.1442	H60	0.1052	H84	0.1360	C109	-0.1252	C132	-0.1205	C156	0.0930	H180	0.1823
H14	0.4314	H37	0.1131	H61	0.1028	H85	0.1570	H109	0.0837	C133	-0.1566	C157	-0.1251	H181	0.1597
H15	0.3394	H38	0.1130	H62	0.1188	H86	0.1749	C110	0.0170	N134	-0.4416	C158	0.1505	H182	0.1343
H16	0.1225	H39	0.1248	H63	0.1174	H87	0.1543	C111	-0.1060	C135	0.1615	N159	-0.4109	H183	0.1673
H17	0.1223	H40	0.1234	H64	0.1322	H88	0.1622	H112	0.1050	C136	-0.1168	C160	0.1486	H184	0.1720
H18	0.1169	O41	-0.5431	H65	0.1335	H89	0.1736	C113	-0.1203	C137	0.0869	C161	-0.1488	H185	0.1821
H19	0.1173	C42	0.0453	O66	-0.4710	C90	-0.1240	H114	0.1299	C138	-0.1544	H162	0.1559	H186	0.1412
H20	0.1123	C43	0.0711	C67	-0.0009	H91	0.1012	C115	0.3175	C139	0.1468	H163	0.1816	H187	0.1412
H21	0.1129	O44	-0.5149	C68	0.0642	C92	-0.0937	C116	-0.1215	H140	0.1717	C164	-0.1648	H188	0.1839
H22	0.1246	C45	0.0499	O69	-0.4920	H93	0.0693	H117	0.1298	H141	0.1432	C165	0.0763	H189	0.1797
H23	0.1252	C46	0.0298	C70	0.0569	C94	0.2897	C118	-0.1063	H142	0.1565	C166	-0.1187	H190	0.1686
H24	0.1473	O47	-0.5010	C71	0.0213	C95	-0.1365	H119	0.1007	H143	0.1827	C167	-0.1169	H191	0.1470
H24	0.1481	C48	0.4068	O72	-0.4864	H96	0.0984	C120	0.1604	H144	0.1832	C168	0.0781	Total	5.0000
$z = 36.84 \text{ \AA}$															
O1	-0.4780	C25	-0.3059	C49	-0.1708	H73	0.1457	C97	-0.1141	C121	-0.1377	H145	0.1861	C169	-0.1115
C2	0.0175	S26	0.4552	C50	-0.0703	H74	0.1447	H98	0.1227	C122	0.0804	H146	0.1496	C170	-0.1092
C3	0.0589	C27	-0.2386	C51	-0.0652	H75	0.1199	C99	0.0371	C123	-0.1468	H147	0.1497	H171	0.1291
O4	-0.4819	C28	-0.1377	C52	-0.0665	H76	0.1207	C100	0.0304	C124	0.1499	H148	0.1126	H172	0.1299
O5	0.0596	S29	0.4418	C53	-0.0610	H77	0.1233	C101	-0.1140	N125	-0.4076	H149	0.1137	C173	-0.1610
O6	0.0362	C30	0.0814	C54	-0.0741	H78	0.1233	H102	0.0808	C126	-0.1646	H150	0.1855	N174	-0.4067
O7	-0.5155	O31	-0.5159	C55	-0.1691	H79	0.1265	C103	-0.1116	C127	0.0770	H151	0.1835	C175	0.1615
O8	0.0846	C32	0.0445	C56	-0.1540	H80	0.1262	H104	0.1197	C128	-0.1148	H152	0.1824	C176	-0.1219
C9	-0.1353	C33	0.0490	C57	0.4100	H81	0.3451	C105	0.0416	C129	-0.1141	H153	0.1570	C177	0.0846
C10	-0.2343	O34	-0.5312	H58	0.0939	H82	0.2313	C106	-0.1124	C130	0.0804	H154	0.1618	C178	-0.1451
S11	0.4658	H35	0.1491	H59	0.0920	H83	0.2194	C108	0.1214	C131	-0.1094	H155	0.1857	C179	0.1526
C12	-0.3100	H36	0.1467	H60	0.0901	H84	0.1478	C109	-0.1160	C132	-0.1090	C156	0.0831	H180	0.1874
H14	0.4476	H37	0.1121	H61	0.0930	H85	0.1078	H109	0.0527	C133	-0.1689	C157	-0.1190	H181	0.1657
H15	0.3433	H38	0.1122	H62	0.0941	H86	0.1674	C110	0.0234	N134	-0.4066	C158	0.1610	H182	0.1364
H16	0.1279	H39	0.1253	H63	0.0937	H87	0.1083	C111	-0.1057	C135	0.1597	N159	-0.4106	H183	0.1700
H17	0.1276	H40	0.1237	H64	0.1124	H88	0.1394	C112	0.1041	C136	-0.1349	C160	0.1547	H184	0.1841
H18	0.1205	O41	-0.5481	H65	0.1158	H89	0.1627	C113	-0.1230	C137	0.0777	C161	-0.1469	H185	0.1794
H19	0.1210	C42	0.0559	O66	-0.4831	C90	-0.1141	H114	0.1205	C138	-0.1475	H162	0.1640	H186	0.1426
H20	0.1160	C43	0.0590	C67	0.0074	H91	0.1261	C115	0.3116	C139	0.1513	H163	0.1891	H187	0.1423
H21	0.1167	O44	-0.5199	C68	0.0615	C92	-0.1430	C116	-0.1237	H140	0.1805	C164	-0.1589	H188	0.1812
H22	0.1267	C45	0.0565	O69	-0.4869	H93	0.0746	H117	0.1218	H141	0.1545	C165	0.0704	H189	0.1830
H23	0.1272	C46	0.0451	C70	0.0559	C94	0.3033	C118	-0.1055	H142	0.1606	C166	-0.1188	H190	0.1685
H24	0.1502	O47	-0.5189	C71	0.0194	C95	-0.1395	H119	0.1087	H143	0.1857	C167	-0.1193	H191	0.1350
H24	0.1511	C48	0.3783	O72	-0.4767	H96	0.0770	C120	0.1590	H144	0.1823	C168	0.0710	Total	5.0000
$z = 40.99 \text{ \AA}$															
O1	-0.4992	C25	-0.3052	C49	-0.2062	H73	0.1302	C97	-0.0937	C121	-0.1396	H145	0.1771	C169	-0.1085
C2	0.0230	S26	0.4336	C50	-0.1216	H74	0.1316	H98	0.1388	C122	0.1037	H146	0.1400	C170	-0.1091
C3	0.0623	C27	-0.2415	C51	-0.0954	H75	0.0984	C99	0.0306	C123	-0.1447	H147	0.1386	H171	0.1123
O4	-0.4923	C28	-0.1401	C52	-0.0744	H76	0.0972	C100	0.0635	C124	0.1508	H148	0.1248	H172	0.1116
O5	0.0644	S29	0.4192	C53	-0.0847	H77	0.1055	C101	-0.1005	N125	-0.4065	H149	0.1268	C173	-0.1672
O6	0.0370	C30	0.0748	C54	-0.1236	H78	0.1047	H102	0.1441	C126	-0.1595	H150	0.1769	N174	-0.4123
O7	-0.5151	O31	-0.5161	C55	-0.1631	H79	0.0989	C103	-0.0929	C127	0.0680	H151	0.1839	C175	0.1629
O8	0.0858	C32	0.0531	C56	-0.1755	H80	0.0991	H104	0.1535	C128	-0.1229	H152	0.1668	C176	-0.1334
C															

Table E.3: Partial Charge Distribution of +2 Oxidized Rotaxane when the Center of Mass of the CBPQT⁴⁺ Ring Moves from $z = 10.92 \text{ \AA}$ (TTF side) to $z = 44.83 \text{ \AA}$ (DNP side)

$z = 10.92 \text{ \AA}$															
C1	-0.4596	C25	-0.3297	C49	-0.1448	H73	0.1605	C97	-0.0890	C121	-0.1310	H145	0.1870	C169	-0.0978
C2	0.0112	S26	0.2671	C50	-0.0570	H74	0.1600	H98	0.1477	C122	0.1127	H146	0.1497	C170	-0.1009
C3	0.0601	C27	-0.2613	C51	-0.0393	H75	0.1526	C99	0.0436	C123	-0.1525	H147	-0.1491	H171	0.1214
C4	-0.5032	C28	-0.1534	C52	-0.0648	H76	0.1532	C100	0.0567	C124	0.1549	H148	0.1198	H172	0.1226
C5	0.0762	S29	0.2547	C53	-0.0642	H77	0.1534	C101	-0.0954	H125	-0.4061	H149	-0.1228	C173	-0.1764
C6	0.0345	C30	0.0905	C54	-0.0415	H78	0.1531	H102	0.1515	C126	-0.1737	H150	0.1899	N174	-0.4069
C7	-0.5166	O31	-0.5123	C55	-0.0562	H79	0.1677	C103	-0.0997	C127	0.0954	H151	0.1862	C175	0.1722
C8	0.0915	C32	0.0442	C56	-0.1448	H80	0.1678	H104	0.1501	C128	-0.1221	H152	0.1827	C176	-0.1327
C9	-0.1514	C33	0.0456	C57	0.4249	H81	0.3747	C105	0.0591	C129	-0.1217	H153	0.1514	C177	0.1176
C10	-0.2763	O34	-0.5221	H58	0.1289	H82	0.1856	C106	-0.1000	C130	0.0888	H154	0.1580	C178	-0.1521
S11	0.2751	H35	0.1293	H59	0.1286	H83	0.1931	H107	0.1437	C131	-0.1042	H155	0.1862	C179	0.1577
C12	-0.3321	H36	0.1063	H60	0.1244	H84	0.1679	C108	-0.0952	C132	-0.0977	C156	0.1078	H180	0.1938
S13	0.2665	H37	0.1132	H61	0.1245	H85	0.1747	H109	0.1514	C133	-0.1743	C157	-0.1274	H181	0.1680
H14	0.3545	H38	0.1204	H62	0.1238	H86	0.1779	C110	0.0305	H134	-0.4037	C158	0.1523	H182	0.1435
H15	0.1376	H39	0.1284	H63	0.1239	H87	0.1767	C111	-0.0926	C135	0.1664	H159	-0.4063	H183	0.1691
H16	0.1391	H40	0.1186	H64	0.1506	H88	0.1773	H112	0.1390	C136	-0.1257	C160	0.1454	H184	0.1794
H17	0.1185	O41	-0.5087	H65	0.1508	H89	0.1737	C113	-0.1172	C137	0.1125	C161	-0.1501	H185	0.1940
H18	0.1161	C42	0.0274	O66	-0.4813	C90	-0.0889	H114	0.1361	C138	-0.1401	H162	0.1623	H186	0.1345
H19	0.1033	C43	0.0556	C67	0.0039	H91	0.1472	C115	0.3280	C139	0.1597	H163	0.1873	H187	0.1400
H20	0.0933	O44	-0.5029	O68	0.0341	C92	-0.1068	C116	-0.1179	H140	0.1757	C164	-0.1709	H188	0.1880
H21	0.1135	C45	0.0554	O69	-0.4294	H93	0.1625	H117	0.1421	H141	0.1460	C165	0.0882	H189	0.1862
H22	0.1258	C46	0.0061	C70	0.0396	C94	0.3505	C118	-0.0918	H142	0.1607	C166	-0.1152	H190	0.1690
H23	0.0969	O47	-0.4769	C71	-0.0059	C95	-0.1083	H119	0.1421	H143	0.1861	C167	-0.1159	H191	0.1410
H24	0.1266	C48	0.4245	O72	-0.3868	H96	0.1617	C120	0.1602	H144	0.1879	C168	0.0939	Total	6.0000
$z = 15.66 \text{ \AA}$															
C1	-0.4118	C25	-0.3665	C49	-0.1464	H73	0.1600	C97	-0.0898	C121	-0.1283	H145	0.1896	C169	-0.1049
C2	-0.0008	S26	0.2876	C50	-0.0571	H74	0.1594	H98	0.1472	C122	0.1048	H146	0.1525	C170	-0.1068
C3	0.0505	C27	-0.2751	C51	-0.0409	H75	0.1521	C99	0.0460	C123	-0.1534	H147	0.1511	H171	0.1288
O4	-0.4609	C28	-0.1483	C52	-0.0654	H76	0.1527	C100	0.0523	C124	0.1553	H148	0.1144	H172	0.1285
C5	0.0477	S29	0.2488	C53	-0.0652	H77	0.1523	C101	-0.0960	H125	-0.4058	H149	0.1136	C173	-0.1689
C6	0.0412	C30	0.0854	C54	-0.0423	H78	0.1520	H102	0.1493	C126	-0.1604	H150	0.1854	N174	-0.4098
C7	-0.5142	O31	-0.5195	C55	-0.0564	H79	0.1701	C103	-0.1033	C127	0.0836	H151	0.1830	C175	0.1471
C8	0.0866	C32	0.0501	C56	-0.1465	H80	0.1703	H104	0.1443	C128	-0.1117	H152	0.1806	C176	-0.1336
C9	-0.1374	C33	0.0576	C57	0.4244	H81	0.3757	C105	0.0568	C129	-0.1134	H153	0.1505	C177	0.1091
C10	-0.2447	O34	-0.5305	H58	0.1278	H82	0.2056	C106	-0.1036	C130	0.0914	H154	0.1585	C178	-0.1533
S11	0.2712	H35	0.1005	H59	0.1285	H83	0.1630	H107	0.1350	C131	-0.1145	H155	0.1841	C179	0.1599
C12	-0.3073	H36	0.1114	H60	0.1213	H84	0.1655	C108	-0.0957	C132	-0.1148	C156	0.0951	H180	0.1917
S13	0.2908	H37	0.1058	H61	0.1214	H85	0.1726	H109	0.1481	C133	-0.1643	C157	-0.1149	H181	0.1645
H14	0.3657	H38	0.1080	H62	0.1211	H86	0.1752	C110	0.0275	H134	-0.4148	C158	0.1542	H182	0.1376
H15	0.1570	H39	0.0998	H63	0.1211	H87	0.1755	C111	-0.0957	C135	0.1679	H159	-0.3991	H183	0.1691
H16	0.1568	H40	0.1040	H64	0.1485	H88	0.1758	H112	0.1360	C136	-0.1310	C160	0.1602	H184	0.1837
H17	0.1359	O41	-0.5065	H65	0.1487	H89	0.1723	C113	-0.1210	C137	0.0987	C161	-0.1393	H185	0.1901
H18	0.1362	C42	0.0258	O66	-0.4837	C90	-0.0896	H114	0.1188	C138	-0.1556	H162	0.1687	H186	0.1478
H19	0.1282	C43	0.0591	C67	0.0046	H91	0.1468	C115	0.3156	C139	0.1524	H163	0.1956	H187	0.1465
H20	0.1282	O44	-0.5105	O68	0.0344	C92	-0.1073	C116	-0.1221	H140	0.1830	C164	-0.1654	H188	0.1913
H21	0.1259	C45	0.0568	O69	-0.4322	H93	0.1643	H117	0.1245	H141	0.1564	C165	0.0761	H189	0.1841
H22	0.1269	C46	0.0079	C70	0.0408	C94	0.3521	C118	-0.0948	H142	0.1604	C166	-0.1223	H190	0.1783
H23	0.1331	O47	-0.4802	C71	-0.0071	C95	-0.1071	H119	0.1392	H143	0.1900	C167	-0.1204	H191	0.1474
H24	0.1350	C48	0.4241	O72	-0.3773	H96	0.1634	C120	0.1670	H144	0.1857	C168	0.0815	Total	6.0000
$z = 18.75 \text{ \AA}$															
C1	-0.4309	C25	-0.3153	C49	-0.1456	H73	0.1594	C97	-0.0949	C121	-0.1244	H145	0.1908	C169	-0.1077
C2	0.0058	S26	0.3018	C50	-0.0552	H74	0.1588	H98	0.1370	C122	0.0941	H146	0.1534	C170	-0.1065
C3	0.0513	C27	-0.2962	C51	-0.0406	H75	0.1402	C99	0.0473	C123	-0.1429	H147	0.1535	H171	0.1134
O4	-0.4589	C28	-0.1575	C52	-0.0649	H76	0.1407	C100	0.0461	C124	0.1581	H148	0.1180	H172	0.1124
C5	0.0506	S29	0.3241	C53	-0.0661	H77	0.1424	C101	-0.1007	H125	-0.4080	H149	0.1177	C173	-0.1802
C6	0.0371	C30	0.0752	C54	-0.0381	H78	0.1422	H102	0.1408	C126	-0.1649	H150	0.1901	N174	-0.4006
C7	-0.5151	O31	-0.5172	C55	-0.0555	H79	0.1626	C103	-0.1100	C127	0.0604	H151	0.1918	C175	0.1628
C8	0.0845	C32	0.0582	C56	-0.1422	H80	0.1627	H104	0.1252	C128	-0.1167	H152	0.1735	C176	-0.1304
C9	-0.1335	C33	0.0553	C57	0.4293	H81	0.3718	C105	0.0445	C129	-0.1200	H153	0.1370	C177	0.0951
C10	-0.2348	O34	-0.5475	H58	0.1247	H82	0.2233	C106	-0.1099	C130	0.0627	H154	0.1643	C178	-0.1477
S11	0.3872	H35	0.1154	H59	0.1254	H83	0.1706	H107	0.1126	C131	-0.1025	H155	0.1960	C179	0.1541
C12	-0.3088	H36	0.1090	H60	0.1207	H84	0.1671	C108	-0.1003	C132	-0.1017	C156	0.0902	H180	0.1976
S13	0.3748	H37	0.0939	H61	0.1205	H85	0.1748	H109	0.1387	C133	-0.1670	C157	-0.1275	H181	0.1655
H14	0.3590	H38	0.0943	H62	0.1210	H86	0.1816	C110	0.0331	H134	-0.4107	C158	0.1669	H182	0.1384
H15	0.1468	H39	0.0970	H63	0.1210	H87	0.1781	C111	-0.0991	C135	0.1678	H159	-0.4024	H183	0.1861
H16	0.1467	H40	0.0981	H64	0.1488	H88	0.1786	H112	0.1350	C136	-0.1199	C160	0.1551	H184	0.1941
H17	0.1322	O41	-0.5092	H65	0.1491	H89	0.1776	C113	-0.1372	C137	0.0987	C161	-0.1454	H185	0.1941
H18	0.1324	C42	0.0293	O66	-0.4767	C90	-0.0947	H114	0.0855	C138	-0.1486	H162	0.1670	H186	0.1479
H19	0.1263	C43	0.0583	C67	0.0002	H91	0.1373	C115	0.3056	C139	0.1590	H163	0.1988	H187	0.1479
H20	0.1265	O44	-0.5105	O68	0.0462	C92	-0.1090	C116	-0.1382	H140	0.1806	C164	-0.1788	H188	0.1967
H21	0.1281	C45	0.0577	O69	-0.4574	H93	0.1569	H117	0.0853	H141	0.1409	C165	0.0735	H189	0.1900
H22	0.1291	C46	0.0079	C70	0.0473	C94	0.3490	C118	-0.0981	H142	0.1652	C166	-0.1056	H190	0.1873
H23	0.1449	O47	-0.4814	C71	-0.0048	C95	-0.1087	H119	0.1362	H143	0.1956	C167	-0.1057	H191	0.1394
H24	0.1462	C48	0.4242	O72	-0.4108	H96	0.1557	C120	0.1636	H144	0.1937	C168	0.0762	Total	6.0000
$z = 23.27 \text{ \AA}$															
C1	-0.3942	C25	-0.2988	C49	-0.1472	H73	0.1583	C97	-0.1063	C121	-0.1317	H145	0.1846	C169	-0.1150
C2	-0.0049	S26	0.4117	C50	-0.0578	H74	0.1578	H98	0.1039	C122	0.0991	H146	0.1496	C170	-0.1103
C3	0.0461	C27	-0.2473	C51	-0.0423	H75	0.1454	C99	0.0221	C123	-0.1428	H147	0.1485	H171	0.1129
O4	-0.4478	C28	-0.1435	C52	-0.0655	H76	0.1459	C100	0.0462	C124	0.1552	H148	0.1189	H172	0.1161
C5	0.0405	S29	0.4010	C53	-0.0660	H77	0.1460	C101	-0.1114	H125	-0.4192	H149	0.1281	C173	-0.1685
C6	0.0378	C30	0.0685	C54	-0.0428	H78	0.1457	H102	0.1301	C126	-0.1540	H150	0.1900	N174	-0.4119
C7	-0.5154	O31	-0.5181	C55	-0.0571	H79	0.1687	C103	-0.1229	C127	0.0630	H151	0.1912	C175	0.1672
C8	0.0821	C3													

$z = 28.17 \text{ \AA}$															
C1	-0.4143	C25	-0.3044	C49	-0.1518	H73	0.1575	C97	-0.1302	C121	-0.1201	H145	0.1926	C169	-0.1004
C2	0.0009	S26	-0.4414	C50	-0.0575	H74	0.1571	H98	0.0862	C122	-0.1070	H146	0.1443	C170	-0.1035
C3	0.0491	C27	-0.2417	C51	-0.0451	H75	0.1261	C99	0.0133	C123	-0.1386	H147	0.1380	H171	0.1256
O4	-0.4490	C28	-0.1402	C52	-0.0653	H76	0.1264	C100	0.0237	C124	-0.1549	H148	0.1268	H172	0.1230
O5	0.0454	S29	0.4370	C53	-0.0666	H77	0.1297	C101	-0.1385	N125	-0.4059	H149	0.1255	C173	-0.1701
O6	0.0360	C30	0.0735	C54	-0.0417	H78	0.1294	H102	0.1047	C126	-0.1714	H150	0.1803	N174	-0.4100
O7	-0.5160	O31	-0.5197	C55	-0.0586	H79	0.1474	C103	-0.1353	C127	-0.0690	H151	0.1934	C175	0.1696
O8	0.0823	C32	0.0521	C56	-0.1415	H80	0.1475	H104	0.1035	C128	-0.1161	H152	0.1734	C176	-0.1230
O9	-0.1353	C33	0.0394	C57	0.4276	H81	0.3590	C105	0.0215	C129	-0.1124	H153	0.1438	C177	0.1065
C10	-0.2332	O34	-0.5200	H58	0.1076	H82	0.2323	C106	-0.1371	C130	0.0794	H154	0.1658	C178	-0.1430
S11	0.4651	H35	0.1519	H59	0.1033	H83	0.1567	H107	0.1037	C131	-0.1027	H155	0.1936	C179	0.1548
C12	-0.3124	H36	0.1495	H60	0.1195	H84	0.1579	C107	-0.1379	C132	-0.1020	C156	0.1012	H180	0.1919
S13	0.4493	H37	0.1083	H61	0.1209	H85	0.1667	H109	0.1040	C133	-0.1788	C157	-0.1158	H181	0.1572
H14	0.3650	H38	0.1065	H62	0.1216	H86	0.1810	C110	0.0145	N134	-0.4020	C158	0.1575	H182	0.1502
H15	0.1556	H39	0.1310	H63	0.1223	H87	0.1700	C111	-0.1267	C135	0.1539	N159	-0.3987	H183	0.1737
H16	0.1553	H40	0.1296	H64	0.1403	H88	0.1748	H112	0.0899	C136	-0.1202	C160	0.1581	H184	0.1925
H17	0.1383	O41	-0.5186	H65	0.1392	H89	0.1798	C113	-0.1243	C137	0.0995	C161	-0.1429	H185	0.1883
H18	0.1388	C42	0.0370	O66	-0.4704	C90	-0.1309	H114	0.1392	C138	-0.1449	H162	0.1663	H186	0.1464
H19	0.1337	C43	0.0631	C67	-0.0041	H91	0.0828	C115	0.3226	C139	0.1559	H163	0.1963	H187	0.1418
H20	0.1342	O44	-0.5159	C68	0.0583	C92	-0.1266	C116	-0.1260	H140	0.1745	C164	-0.1780	H188	0.1953
H21	0.1329	C45	0.0530	O69	-0.4865	H93	0.1388	H117	0.1371	H141	0.1511	C165	0.0743	H189	0.1833
H22	0.1335	C46	0.0183	C70	0.0546	C94	0.3277	C118	-0.1278	H142	0.1630	C166	-0.1119	H190	0.1792
H23	0.1543	O47	-0.4897	C71	0.0055	C95	-0.1249	H119	0.0851	H143	0.1940	C167	-0.1162	H191	0.1508
H24	0.1552	C48	0.4184	O72	-0.4303	H96	0.1410	C120	0.1697	H144	0.1921	C168	0.0696	Total	6.0000
$z = 32.22 \text{ \AA}$															
O1	-0.3980	C25	-0.3054	C49	-0.1606	H73	0.1530	C97	-0.1312	C121	-0.1218	H145	0.1901	C169	-0.1064
C2	-0.0036	S26	0.4775	C50	-0.0619	H74	0.1520	H98	0.1004	C122	0.0983	H146	0.1535	C170	-0.1059
C3	0.0410	C27	-0.2371	C51	-0.0552	H75	0.1212	C99	0.0139	C123	-0.1366	H147	0.1514	H171	0.1181
O4	-0.4305	C28	-0.1378	C52	-0.0648	H76	0.1219	C100	0.0341	C124	-0.1581	H148	0.1289	H172	0.1219
O5	0.0350	S29	0.4663	C53	-0.0656	H77	0.1241	C101	-0.1447	N125	-0.4110	H149	0.1364	C173	-0.1715
O6	0.0356	C30	0.0791	C54	-0.0516	H78	0.1241	H102	0.0384	C126	-0.1602	H150	0.1881	N174	-0.4089
O7	-0.5164	O31	-0.5174	C55	-0.0640	H79	0.1294	C103	-0.1106	C127	0.0760	H151	0.1895	C175	0.1675
O8	0.0801	C32	0.0438	C56	-0.1442	H80	0.1282	H104	0.1281	C128	-0.1153	H152	0.1923	C176	-0.1300
C9	-0.1355	C33	0.0444	C57	0.4200	H81	0.3463	C105	0.0490	C129	-0.1167	H153	0.1559	C177	0.1035
C10	-0.2316	O34	-0.5262	H58	0.0979	H82	0.2354	C106	-0.1136	C130	0.0770	H154	0.1626	C178	-0.1468
S11	0.4917	H35	0.1553	H59	0.0982	H83	0.2215	H107	0.1265	C131	-0.1227	H155	0.1924	H180	0.1594
C12	-0.3105	H36	0.1530	H60	0.1059	H84	0.1306	C108	-0.1254	C132	-0.1196	C156	0.1003	H181	0.1931
S13	0.4727	H37	0.1141	H61	0.1026	H85	0.1558	H109	0.0825	C133	-0.1619	C157	-0.1232	H182	0.1689
H14	0.3719	H38	0.1141	H62	0.1208	H86	0.1749	C110	0.0169	N134	-0.4368	C158	0.1587	H183	0.1447
H15	0.1645	H39	0.1303	H63	0.1190	H87	0.1749	C111	-0.1056	C135	0.1749	N159	-0.4061	H184	0.1795
H16	0.1642	H40	0.1289	H64	0.1301	H88	0.1619	H112	0.1069	C136	-0.1145	C160	0.1576	H185	0.1890
H17	0.1486	O41	-0.5426	H65	0.1317	H89	0.1745	C113	-0.1195	C137	0.0939	C161	-0.1458	H186	0.1885
H18	0.1491	C42	0.0426	O66	-0.4707	C90	-0.1296	H114	0.1325	C138	-0.1511	H162	0.1655	H187	0.1489
H19	0.1453	C43	0.0742	C67	-0.0012	H91	0.1028	C115	0.3176	C139	0.1545	H163	0.1926	H187	0.1488
H20	0.1458	O44	-0.5155	C68	0.0523	C92	-0.0977	C116	-0.1208	H140	0.1808	C164	-0.1701	H188	0.1918
H21	0.1375	C45	0.0462	O69	-0.4876	H93	0.0721	H117	0.1326	H141	0.1502	C165	0.0743	H189	0.1895
H22	0.1380	C46	0.0337	C70	0.0546	C94	0.2893	C118	-0.1058	H142	0.1686	C166	-0.1174	H190	0.1805
H23	0.1590	O47	-0.5037	C71	0.0188	C95	-0.1412	H119	0.1023	H143	0.1962	C167	-0.1156	H191	0.1571
H24	0.1599	C48	0.4038	O72	-0.4743	H96	0.1001	C120	0.1697	H144	0.1924	C168	0.0763	Total	6.0000
$z = 36.84 \text{ \AA}$															
O1	-0.4047	C25	-0.3037	C49	-0.1695	H73	0.1516	C97	-0.1109	C121	-0.1370	H145	0.1938	C169	-0.1116
C2	-0.0006	S26	0.4528	C50	-0.0675	H74	0.1506	H98	0.1291	C122	0.0856	H146	0.1561	C170	-0.1090
C3	0.0421	C27	-0.2397	C51	-0.0619	H75	0.1285	C99	0.0365	C123	-0.1449	H147	0.1557	H171	0.1261
O4	-0.4281	C28	-0.1384	C52	-0.0653	H76	0.1293	C100	0.0373	C124	-0.1550	H148	0.1126	H172	0.1255
O5	0.0343	S29	0.4388	C53	-0.0607	H77	0.1327	C101	-0.1113	N125	-0.4040	H149	0.1147	C173	-0.1650
O6	0.0397	C30	0.0780	C54	-0.0691	H78	0.1327	H102	0.0946	C126	-0.1681	H150	0.1941	N174	-0.4031
O7	-0.5154	O31	-0.5165	C55	-0.0678	H79	0.1427	C103	-0.1048	C127	0.0758	H151	0.1913	C175	0.1686
O8	0.0802	C32	0.0481	C56	-0.1493	H80	0.1425	H104	0.1333	C128	-0.1140	H152	0.1914	C176	-0.1202
C9	-0.1366	C33	0.0367	C57	0.4137	H81	0.3579	C105	0.0420	C129	-0.1134	H153	0.1610	C177	0.0892
C10	-0.2361	O34	-0.5186	H58	0.0956	H82	0.2245	C106	-0.1055	C130	0.0789	H154	0.1716	C178	-0.1430
S11	0.4640	H35	0.1505	H59	0.0906	H83	0.2121	H107	0.1354	C131	-0.1089	H155	0.1987	C179	0.1644
C12	-0.3073	H36	0.1480	H60	0.0977	H84	0.1096	C110	-0.1132	C132	-0.1098	C156	0.0873	H180	0.1945
S13	0.4451	H37	0.1205	H61	0.0942	H85	0.1531	H109	0.1178	C133	-0.1739	C157	-0.1181	H181	0.1742
H14	0.3682	H38	0.1213	H62	0.0939	H86	0.1731	C110	0.0320	N134	-0.4028	C158	0.1658	H182	0.1433
H15	0.1602	H39	0.1294	H63	0.0952	H87	0.1109	C111	-0.0991	C135	0.1685	N159	-0.4073	H183	0.1785
H16	0.1598	H40	0.1274	H64	0.1139	H88	0.1475	C112	-0.1231	C136	-0.1334	C160	0.1582	H184	0.1932
H17	0.1473	O41	-0.5463	H65	0.1162	H89	0.1705	C113	-0.1149	C137	0.0839	C161	-0.1453	H185	0.1840
H18	0.1478	C42	0.0549	O66	-0.4767	C90	-0.1108	H114	0.1444	C138	-0.1450	H162	0.1708	H186	0.1498
H19	0.1441	C43	0.0603	C67	0.0026	H91	0.1321	C115	0.3285	C139	0.1584	H163	0.1946	H187	0.1500
H20	0.1445	O44	-0.5202	C68	0.0563	C92	-0.1414	C116	-0.1156	H140	0.1869	C164	-0.1616	H188	0.1854
H21	0.1339	C45	0.0546	O69	-0.4753	H93	0.0782	H117	0.1458	H141	0.1565	C165	0.0695	H189	0.1910
H22	0.1344	C46	0.0456	C70	0.0502	C94	0.3086	C118	-0.0989	H142	0.1682	C166	-0.1181	H190	0.1744
H23	0.1523	O47	-0.5189	C71	0.0096	C95	-0.1378	H119	0.1280	H143	0.1943	C167	-0.1187	H191	0.1395
H24	0.1531	C48	0.3799	O72	-0.4415	H96	0.0834	C120	0.1653	H144	0.1891	C168	0.0696	Total	6.0000
$z = 40.99 \text{ \AA}$															
O1	-0.4191	C25	-0.3040	C49	-0.2109	H73	0.1354	C97	-0.0927	C121	-0.1382	H145	0.1877	C169	-0.1084
C2	0.0021	S26	0.4539	C50	-0.1242	H74	0.1369	H98	0.1407	C122	0.1099	H146	0.1482	C170	-0.1090
C3	0.0476	C27	-0.2403	C51	-0.0933	H75	0.1091	C99	0.0312	C123	-0.1412	H147	0.1466	H171	0.1156
O4	-0.4442	C28	-0.1400	C52	-0.0743	H76	0.1078	C100	0.0630	C124	-0.1589	H148	0.1245	H172	0.1148
O5	0.0424	S29	0.4385	C53	-0.0846	H77	0.1187	C101	-0.1008	N125	-0.4022	H149	0.1267	C173	-0.1729
O6	0.0379	C30	0.0753	C54	-0.1240	H78	0.1179	H102	0.1437	C126	-0.1650	H150	0.1871	N174	-0.4085
O7	-0.5156	O31	-0.5165	C55	-0.0823	H79	0.1301	C103	-0.0926	C127	0.0661	H151	0.1921	C175	0.1725
O8	0.0817	C32	0.0505	C56	-0.1732	H80	0.1305	H104	0.1551	C128	-0.1213	H152	0.1783	C176	-0.1312
C															

Appendix F

Consideration of Metric Effect on the Bistable [2]Rotaxane Molecule during the Constant MD Simulations using Fixman's Theorem

When we consider a system with N generalized coordinates q_i , associated conjugated momenta p_i , and masses m_i , the Hamiltonian of this system H is given by

$$H(p, q) = \frac{1}{2} \mathbf{p}^T \mathbf{M}^{-1} \mathbf{p} + V(\mathbf{q}), \quad (\text{F.1})$$

where \mathbf{M} is the “symmetric metric tensor” or “mass-metric tensor” that is defined as

$$M_{kl} = \sum_i^N m_i \frac{\partial \mathbf{r}_i}{\partial q_k} \cdot \frac{\partial \mathbf{r}_i}{\partial q_l}. \quad (\text{F.2})$$

Among N generalized coordinates, we consider that ν generalized coordinates q_i'' are constrained, and rests of them q_i' are not. Then, according to the Fixman's theorem [3], the ratio of the original partition function Q and the partition function from the constraint dynamics Q_c is

$$\frac{Q}{Q_c} = (\det \mathbf{Z})^{-1/2}, \quad (\text{F.3})$$

where

$$Z_{kl} = \sum_i^\nu \frac{1}{m_i} \frac{\partial q_k''}{\partial \mathbf{r}_i} \cdot \frac{\partial q_l''}{\partial \mathbf{r}_i}. \quad (\text{F.4})$$

In our simulation, the $(\det \mathbf{Z})$ is determined as the inverse of the CBPQT⁴⁺ ring's mass, $1/M_{\text{ring}}$. From Equation F.3, the difference between the original free energy $F = -k_B T \ln Q$ and the free

energy from the constraint dynamics $F_c = -k_B T \ln Q$ is determined by

$$F - F_c = -k_B T \ln (\det \mathbf{Z})^{-1/2} = -\frac{1}{2} k_B T \ln M_{\text{ring}} = \text{const.} \quad (\text{F.5})$$

Therefore, the metric effect only adds a constant scalar value to the absolute free energy values, which has no influence on the relative energetics.

Appendix G

Time for Consumption of POPG

The formation of primary ozonide (POZ), which is the first step in the ozonolysis of 1-palmitoyl-2-oleoyl-*sn*-phosphatidylglycerol (POPG) at the air-liquid interface, is described as



The ozone concentration is assumed to be constant during the reaction, which allows calculating the reaction rate using the pseudo-first order rate constant $k_2 = k_1 [\text{O}_3]$, where $k_1 = 4.5 \times 10^{-16} \text{ cm}^3 \text{ molecule}^{-1} \text{ s}^{-1}$ adopted from the OPPC ozonolysis on NaCl [4]. The ozone concentration, measured spectrophotometrically using an absorption cell with 10 cm path length, is determined to be $\sim 5 \times 10^{14} \text{ molecule cm}^{-3}$ (20 ppm). The reaction rate is expressed as

$$-\frac{d[\text{POPG}]_{surf}}{dt} = k_2 [\text{POPG}]_{surf,0}. \quad (\text{G.2})$$

Solving Equation G.2 gives

$$\frac{[\text{POPG}]_{surf}}{[\text{POPG}]_{surf,0}} = e^{-k_2 t}. \quad (\text{G.3})$$

For 90 % and 99 % depletion of POPG at the air-liquid interface, it takes $\sim 10 \text{ s}$ and $\sim 20 \text{ s}$, respectively.

Appendix H

Bulk-phase Ozonolysis

H.1 Methods

H.1.1 Chemicals and Reagents

Ammonium bicarbonate (NH_4HCO_3), iron (II) dichloride (FeCl_2), sodium ethylenediaminetetraacetic acid (EDTA), trypsin from porcine pancreas were purchased from Sigma-Aldrich (St. Louis, MO). SP-B₁₋₂₅ was purchased from Biomer Technology (Hayward, CA).

H.1.2 Bulk-phase O₃ Reaction

A continuous flow of ~ 20 ppm O₃ in air was applied to the 100 μM SP-B₁₋₂₅ solution in 1:1 (by volume) water and methanol solvent for 30 s, 1, 1.5, 2, 3, 4, and 5 min. The SP-B₁₋₂₅ solution was diluted to 50 μM for ESI with 1:1 water/methanol and 1 % acetic acid by volume. Trypsin digests of SP-B₁₋₂₅ and O₃ treated SP-B₁₋₂₅ were prepared by incubating 200 μM of SP-B₁₋₂₅ with 6 μg of trypsin from porcine pancreas in 1 mL of water containing 25 mM ammonium bicarbonate (NH_4HCO_3) at 37°C for 4 hours. The trypsin was then removed using a Millipore Microcon centrifugal filter fitted with an Ultracel YM-10 membrane. The sample solution was diluted to an appropriate concentration for ESI with 1:1 water/methanol and 1 % acetic acid by volume. Product analysis was performed on a Thermo Finnigan LCQ Deca XP ion trap mass spectrometer (ITMS) in positive and negative modes. The nomenclature proposed by Roepstorff and Fohlman [5] was used for the parent and fragment ions.

H.1.3 Fenton Reaction

SP-B₁₋₂₅ (500 μM) was incubated with 600 μM FeCl₂, 600 μM sodium EDTA, and 30 mM H₂O₂ in 1 mL water at 37°C for 12, 18, and 24 h. The peptide was purified using a Varian C18 OMIX 100 μL pipette tip. The sample solution was diluted to an appropriate concentration with 1:1

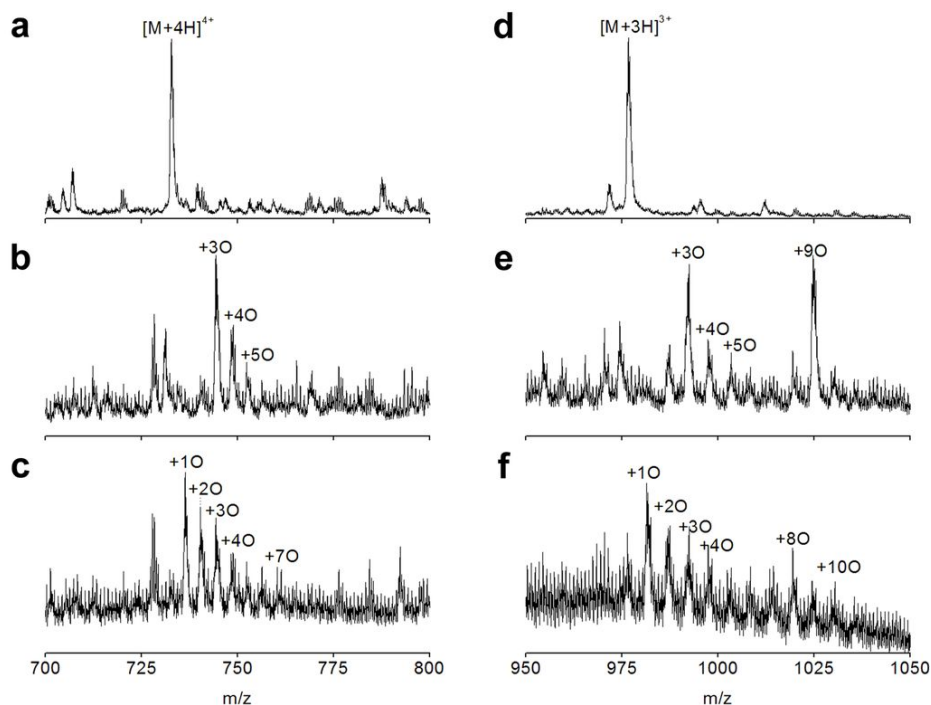


Figure H.1: (a) Quadruply charged SP-B_{1–25} and oxidized products from (b) the bulk-phase O₃ reaction and (c) the Fenton reaction with intact SP-B_{1–25}. (d) Triply charged SP-B_{1–25} and oxidized products from (e) the bulk-phase O₃ reaction and (f) the Fenton reaction are also shown.

water/methanol and 1 % acetic acid by volume. Product analysis was performed on a Micromass QToF2 quadrupole time of flight mass spectrometer in the positive ion mode.

H.2 Results and Discussion

Triply and quadruply protonated SP-B_{1–25} are observed as dominating ions in the ESI-MS spectrum with a small amount of doubly protonated peptides (Figures H.1a and H.1d). Figure H.1 shows oxidized products of triply and quadruply charged SP-B_{1–25} from the bulk-phase O₃ reaction and the Fenton reaction with intact SP-B_{1–25}. As seen in Figures H.1b and H.1e, incorporation of three and nine oxygens in SP-B_{1–25} are observed as major products from the bulk-phase O₃ reaction with the peptide. Other oxygenated peptides (+ 4O and + 5O) are also observed as minor products in the spectrum. The Fenton reaction yields a series of oxidized SP-B_{1–25} products with up to 10 oxygen atoms (Figures H.1c and H.1f). It is notable that the bulk-phase O₃ reaction yields dominating products of 3- and 9-oxygenated SP-B_{1–25}. This suggests the high stability of SP-B_{1–25} incorporating 3 and 9 oxygen atoms. In order to determine structures of the oxidized SP-B_{1–25} by the bulk-phase O₃ reaction, trypsin digest was performed after applying O₃ for 3 min to the SP-B_{1–25} solution.

SP-B₁₋₂₅: F₁P₂I₃P₄L₅P₆Y₇C₈W₉L₁₀C₁₁R₁₂A₁₃L₁₄I₁₅K₁₆R₁₇I₁₈Q₁₉A₂₀M₂₁I₂₂P₂₃K₂₄G₂₅

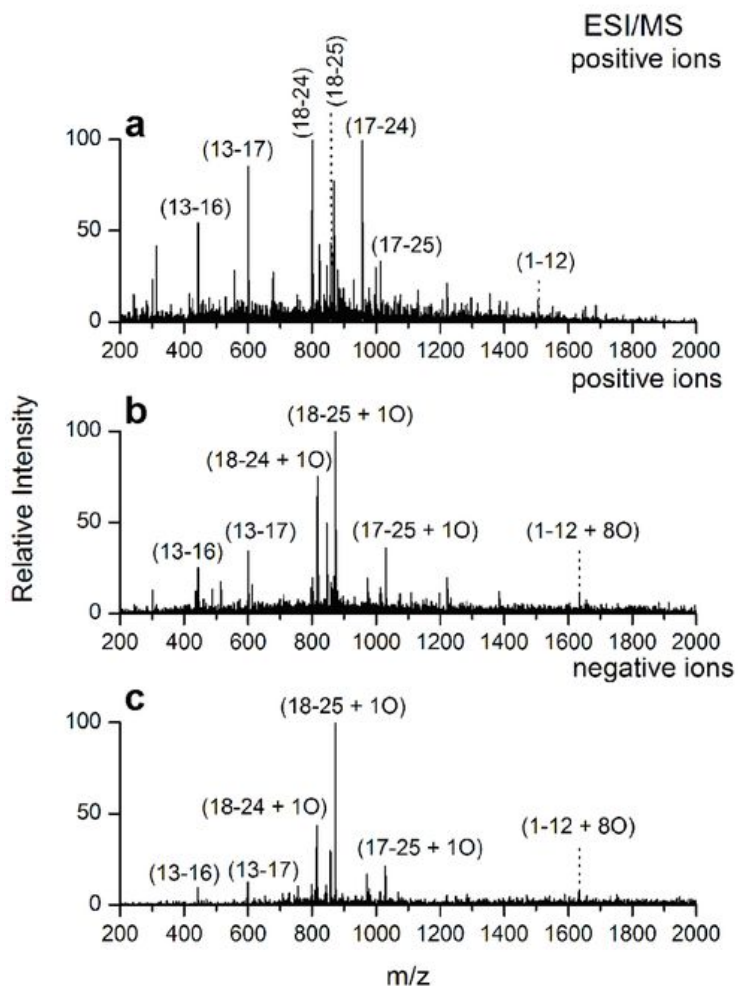


Figure H.2: (a) The ESI mass spectrum of the tryptic digests of SP-B₁₋₂₅ in positive mode. (b) The ESI mass spectrum of the tryptic digests of the oxidized SP-B₁₋₂₅ from the bulk-phase O₃ reaction in positive mode. (c) The negative mode ESI mass spectrum of the tryptic digests of the oxidized SP-B₁₋₂₅ from the bulk-phase O₃ reaction.

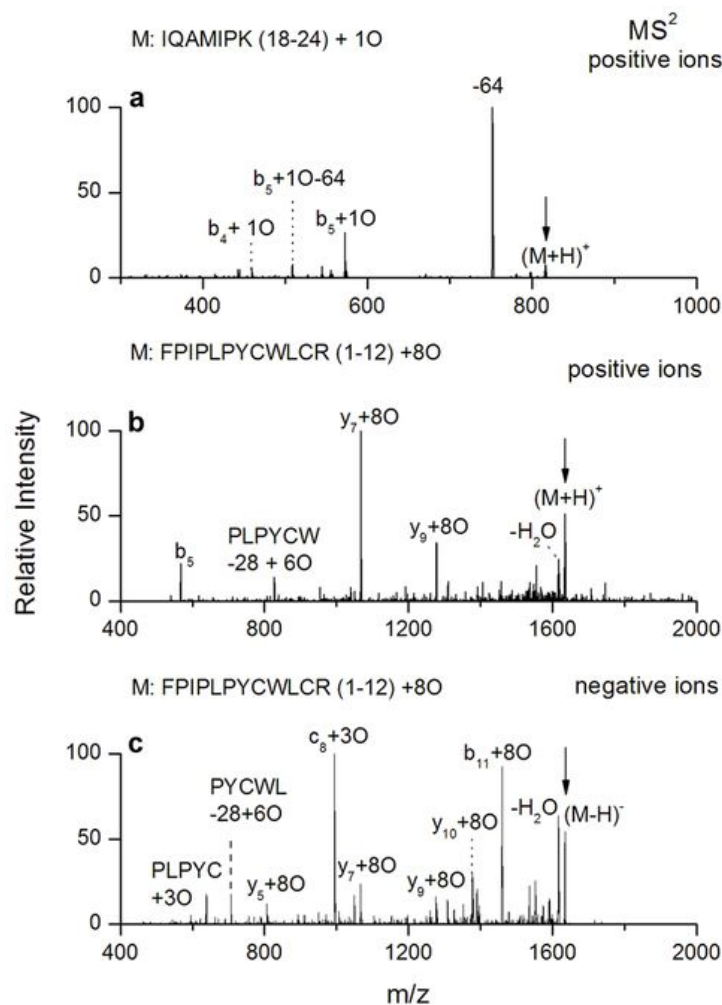


Figure H.3: (a) The CID spectrum of cationic IQAMIPK + 3O at m/z 817 from the tryptic digest of the oxidized SP-B₁₋₂₅. (b) The CID of cationic FPIPLPYCWLCR + 8O at m/z 1636 from the tryptic digest of the oxidized SP-B₁₋₂₅. (c) The CID of anionic FPIPLPYCWLCR + 8O at m/z 1634 from the tryptic digest of the oxidized SP-B₁₋₂₅.

The ESI mass spectrum of a trypsin digest of SP-B₁₋₂₅ exhibits 7 major ion peaks. The masses and segments of the observed tryptic digest ions of SP-B₁₋₂₅ are indicated in Figure H.2a. The ESI mass spectrum of a trypsin digest of SP-B₁₋₂₅ oxidized by reaction with bulk-phase O₃ exhibits segments with MetSO (m/z 817, m/z 874, and m/z 1030) and the less abundant N-terminal segment of FPIPLPYCWLCR + 8O at m/z 1636 in positive ion mode (Figure H.2b). The negative ion mode ESI mass spectrum also exhibits corresponding deprotonated segment ion peaks (Figure H.2c).

The structures of segments are confirmed by CID spectra. As seen in Figure H.3a, the CID of the ion at m/z 817 exhibits the elimination of hydrosulfinylmethane (CH₄SO, 64 mass unit), which is the characteristic dissociation pathway of methionine sulfoxide (MetSO) [6, 7]. The structure of the segment FPIPLPYCWLCR + 8O is also investigated using CID. Fragments from the CID of

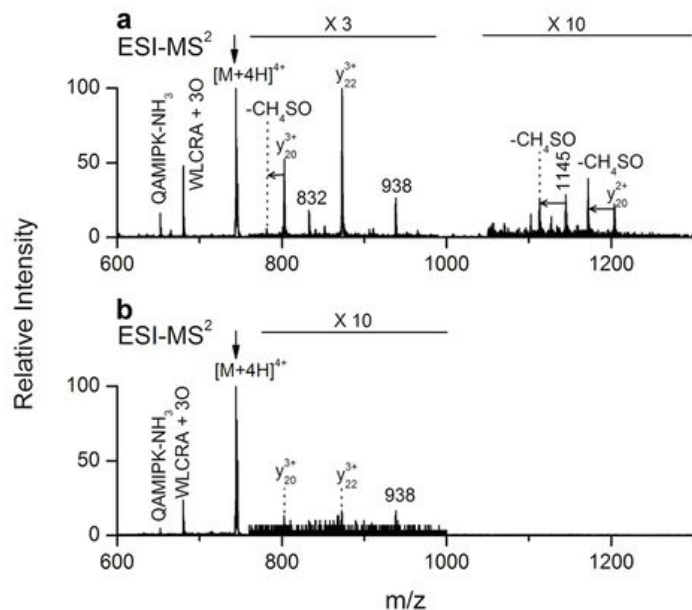


Figure H.4: ESI-MS² of triply oxygenated products of quadruply protonated SP-B_{1–25} from (a) bulk-phase O₃ application, and from (b) the Fenton reaction. M denotes a parent ion, which is triply oxygenated SP-B_{1–25}.

the cationic FPIPLPYCWLCR + 8O at m/z 1636 yields y -type fragments (y_7 and y_9) with all eight oxygen atoms as dominant products (Figure H.3b). The fragment PLPYCW with six oxygen atoms indicates that Cys₈ and Trp₉ are oxidized to sulfonic acid (+ 3O) and hydroxy-Nformylkynurenine (HNFKyn, + 3O), respectively. Thus, we can assume that Cys₁₁ is oxidized to sulfenic acid (+ 2O). The structures are further confirmed by the fragments of $c_8 + 3O$ and PLPYC + 3O resulting from the CID of FPIPLPYCWLCR + 8O in negative ion mode (Figure H.3c). It is notable that Cys₈ and Cys₁₁ are located next to each other in the helical structure [8]. Asymmetric oxidation of closely located Cys residues is caused by the possible formation of sulfonic anhydride (R₁-O₂SOSO₂-R₂). No segment peak is observed from the triply oxygenated SP-B_{1–25} after tryptic digest of the products from the bulk-phase O₃ reaction.

The observed high abundance of SP-B_{1–25} where 3 and 9 oxygen atoms have been added can be explained by the distinct oxidation mechanisms of O₃ in aqueous solution. Cys easily undergoes oxidation by O₃ to form sulfonic acid in aqueous solution primarily by reactions with secondary oxidants [9]. Cys₈ and Cys₁₁, which are located near the hydrophobic N-terminal site in SP-B_{1–25}, are hardly oxidized by reactive oxygen species (ROS) at the air-liquid interface. Trp₉ and Met₂₁ are oxidized to form NFKyn and MetSO by ozonolysis and ROS, respectively, by interfacial reactions. This induces a change in peptide orientation in the interface that results in NFKyn, Cys₈, and Cys₁₁ being exposed to ROS for further oxidation. As a result, NFKyn occurs to form HNFKyn and, simultaneously, Cys₈ and Cys₁₁ are also oxidized by ROS to form sulfonic anhydride.

The SP-B₁₋₂₅ products with three additional oxygen atoms from both reactions are analyzed using CID. Figure H.4 shows CID spectra (ESI-MS²) of triply oxygenated products of quadruply protonated SP-B₁₋₂₅ from bulk-phase O₃ application and from the Fenton reaction. The ESI-MS² spectrum of the triply oxygenated SP-B₁₋₂₅ by bulk-phase O₃ application implies the presence of two products, one with NFKyn (+ 2O) and MetSO (+ 1O), and the other with HNFKyn (+ 3O). Evidence of the MetSO in the oxidized SP-B₁₋₂₅ is found from the CID experiment involving the quadruply charged SP-B₁₋₂₅ product from the bulk-phase O₃ reaction (Figure H.4a). For example, the paired fragments of *y*₂₀-CH₄SO and *y*₂₀ fragments, which are observed at *m/z* 782 and *m/z* 803 (triply charged) and at *m/z* 1172 and *m/z* 1204 (doubly charged), confirm the presence of MetSO (Figure H.4a). Interesting CID fragments are also observed in the ESI-MS² spectrum. The singly charged fragment at *m/z* 680, *m/z* 832, and *m/z* 938 are WLCRA + 3O, LPYCWLCRALIKR + 3O and PLPYCWLCRALIKRI + 3O, respectively. These fragments are evidence of the formation of HNFKyn through the oxidation of Trp₉ from the bulk-phase O₃ reaction. This is further supported by the singly charged fragment at *m/z* 652, QAMIPK-NH₃, which indicates that no oxidation has occurred at Met₂₁. The ESI-MS² spectrum of the triply oxygenated SP-B₁₋₂₅ by bulk-phase O₃ reaction implies the presence of two products, one with NFKyn (+ 2O) and MetSO (+ 1O), and the other with HNFKyn (+ 3O). The CID fragment abundance implies that the bulk-phase O₃ reaction with SP-B₁₋₂₅ yields more product peptides with HNFKyn compared to product peptides with NFKyn and MetSO. The ESI-MS² spectrum of SP-B₁₋₂₅ product from the Fenton reaction is shown in Figure H.4b. The CID of the Fenton product exhibits the presence of HNFKyn at *m/z* 652, *m/z* 680, and *m/z* 938, which corresponds to the singly charged fragments QAMIPK-NH₃, WLCRA + 3O, and PLPYCWLCRALIKRI + 3O, respectively. However, evidence for the formation of the product with NFKyn and MetSO is not found in the spectrum.

Bibliography

- [1] Binder, K. *Rep. Prog. Phys.* **1997**, 60, 487-559.
- [2] Candra, P. M.S. Dissertation, University of Minnesota, 2006.
- [3] Fixman, M. *Proc. Natl. Acad. Sci. U.S.A.* **1974**, 71, 3050-3053.
- [4] Karagulian, F.; Lea, A. S.; Dilbeck, C. W.; Finlayson-Pitts, B. J. *Phys. Chem. Chem. Phys.* **2008**, 10, 528-541.
- [5] Roepstorff, P.; Fohlman, J. *Biomedical Mass Spectrometry* **1984**, 11, 601-601.
- [6] Clauser, K. R.; Hall, S. C.; Smith, D. M.; Webb, J. W.; Andrews, L. E.; Tran, H. M.; Epstein, L. B.; Burlingame, A. L. *Proc. Natl. Acad. Sci. U. S. A.* **1995**, 92, 5072-5076.
- [7] Qin, J.; Chait, B. T. *Anal. Chem.* **1997**, 69, 4002-4009.
- [8] Bruni, R.; Taeusch, H. W.; Waring, A. J. *Proc. Natl. Acad. Sci. U. S. A.* **1991**, 88, 7451-7455.
- [9] Berlett, B. S.; Stadtman, E. R. *J. Biol. Chem.* **1997**, 272, 20313-20316.